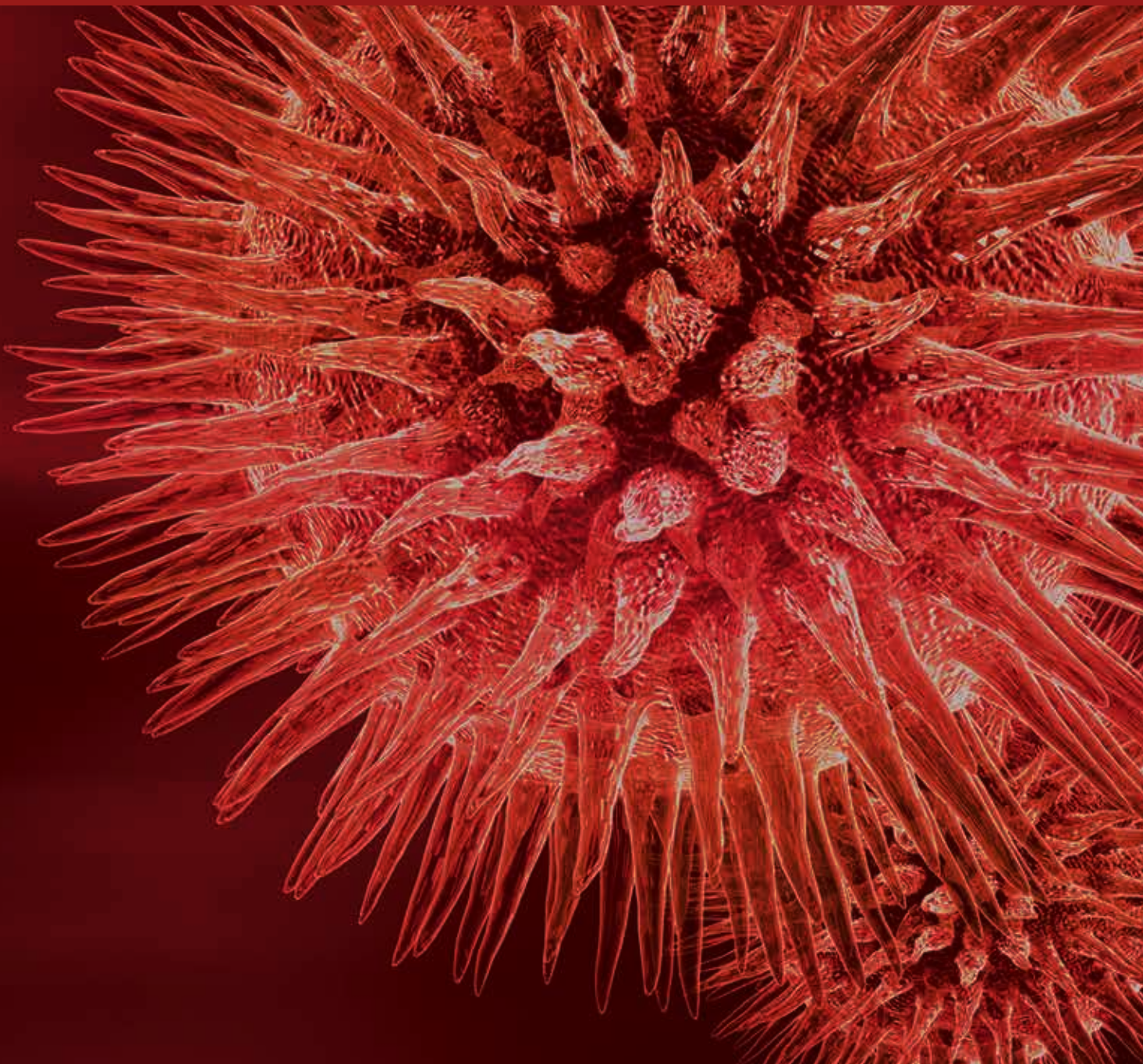


Neuroimaging of Brain Networks and Function

Guest Editors: Hengyi Rao, Danny Jiongjiong Wang, Yihong Yang, and Yong He





Neuroimaging of Brain Networks and Function

BioMed Research International

Neuroimaging of Brain Networks and Function

Guest Editors: Hengyi Rao, Danny Jiongjiong Wang,
Yihong Yang, and Yong He



Copyright © 2015 Hindawi Publishing Corporation. All rights reserved.

This is a special issue published in “BioMed Research International.” All articles are open access articles distributed under the Creative Commons Attribution License, which permits unrestricted use, distribution, and reproduction in any medium, provided the original work is properly cited.

Contents

Neuroimaging of Brain Networks and Function, Hengyi Rao, Danny Jiongjiong Wang, Yihong Yang, and Yong He
Volume 2015, Article ID 509141, 2 pages

Gender Differences in Cerebral Regional Homogeneity of Adult Healthy Volunteers: A Resting-State fMRI Study, Chunsheng Xu, Chuanfu Li, Hongli Wu, Yuanyuan Wu, Sheng Hu, Yifang Zhu, Wei Zhang, Linying Wang, Senhua Zhu, Junping Liu, Qingping Zhang, Jun Yang, and Xiaochu Zhang
Volume 2015, Article ID 183074, 8 pages

Highlighting the Structure-Function Relationship of the Brain with the Ising Model and Graph Theory, T. K. Das, P. M. Abeyasinghe, J. S. Crone, A. Sosnowski, S. Laureys, A. M. Owen, and A. Soddu
Volume 2014, Article ID 237898, 14 pages

Abnormal Functional Resting-State Networks in ADHD: Graph Theory and Pattern Recognition Analysis of fMRI Data, Anderson dos Santos Siqueira, Claudinei Eduardo Biazoli Junior, William Edgar Comfort, Luis Augusto Rohde, and João Ricardo Sato
Volume 2014, Article ID 380531, 10 pages

Visual Learning Alters the Spontaneous Activity of the Resting Human Brain: An fNIRS Study, Haijing Niu, Hao Li, Li Sun, Yongming Su, Jing Huang, and Yan Song
Volume 2014, Article ID 631425, 9 pages

Alteration of Interictal Brain Activity in Patients with Temporal Lobe Epilepsy in the Left Dominant Hemisphere: A Resting-State MEG Study, Haitao Zhu, Jinlong Zhu, Tiezhu Zhao, Yong Wu, Hongyi Liu, Ting Wu, Lu Yang, Yuanjie Zou, Rui Zhang, and Gang Zheng
Volume 2014, Article ID 171487, 8 pages

Altered Modular Organization of Functional Connectivity Networks in Cirrhotic Patients without Overt Hepatic Encephalopathy, Gang Zheng, Liping Zhang, Long Jiang Zhang, Qiang Li, Zhiying Pan, Xue Liang, Donghong Shi, and Guang Ming Lu
Volume 2014, Article ID 727452, 11 pages

Intrinsic Functional Connectivity Networks in Healthy Elderly Subjects: A Multiparametric Approach with Structural Connectivity Analysis, Martin Gorges, Hans-Peter Müller, Albert C. Ludolph, Volker Rasche, and Jan Kassubek
Volume 2014, Article ID 947252, 14 pages

A Functional Polymorphism of the MAOA Gene Modulates Spontaneous Brain Activity in Pons, Hui Lei, Xiaocui Zhang, Xin Di, Hengyi Rao, Qingsen Ming, Jibiao Zhang, Xiao Guo, Yali Jiang, Yidian Gao, Jinyao Yi, Xiongzhaoh Zhu, and Shuqiao Yao
Volume 2014, Article ID 243280, 6 pages

Quantifying Cerebellum Grey Matter and White Matter Perfusion Using Pulsed Arterial Spin Labeling, Xiufeng Li, Subhendra N. Sarkar, David E. Purdy, and Richard W. Briggs
Volume 2014, Article ID 108691, 12 pages

Tract-Based Spatial Statistics: Application to Mild Cognitive Impairment, Yau-Yau Wai, Wen-Chuin Hsu, Hon-Chung Fung, Jiann-Der Lee, Hsiao-Lung Chan, Ming-Lun Tsai, Yu-Chun Lin, Yih-Ru Wu, Leslie Ying, and Jiun-Jie Wang
Volume 2014, Article ID 713079, 8 pages

Editorial

Neuroimaging of Brain Networks and Function

Hengyi Rao,¹ Danny Jiongjiong Wang,² Yihong Yang,³ and Yong He⁴

¹*Center of Functional Neuroimaging, Department of Neurology, Perelman School of Medicine, University of Pennsylvania, Philadelphia, PA 19104, USA*

²*Department of Neurology, Ahmanson-Lovelace Brain Mapping Center, University of California, Los Angeles, Los Angeles, CA 90095, USA*

³*Magnetic Resonance Imaging and Spectroscopy Section, National Institute on Drug Abuse, Baltimore, MD 21224, USA*

⁴*National Key Laboratory of Cognitive Neuroscience and Learning and IDG/McGovern Institute for Brain Research, Beijing Normal University, Beijing 100875, China*

Correspondence should be addressed to Hengyi Rao; hengyi@mail.med.upenn.edu

Received 17 December 2014; Accepted 17 December 2014

Copyright © 2015 Hengyi Rao et al. This is an open access article distributed under the Creative Commons Attribution License, which permits unrestricted use, distribution, and reproduction in any medium, provided the original work is properly cited.

The human brain consists of multiple interconnected large scale networks. Recent advances in structural and functional neuroimaging techniques have introduced new concepts and approaches to noninvasively assess brain networks, which has attracted enormous research interest. To examine human brain function, traditional neuroimaging research typically focuses on localizing neural responses to varying external stimuli or task demands. However, task-induced phasic neuronal responses account for less than 5% of the brain's energy budget, while the majority of the brain's energy is used for intrinsic spontaneous brain activities. Although the number of human brain imaging studies and the knowledge obtained from these studies are growing exponentially, there are many more unanswered questions regarding the structural organization and the function of brain networks. In this special issue, we have invited a few papers that studied structural and functional brain networks using various neuroimaging methods including resting-state fMRI, diffusion tensor imaging (DTI), arterial spin labeling (ASL) perfusion MRI, functional near-infrared spectroscopy (fNIRS), magnetoencephalogram (MEG), and imaging genetics. These studies involve healthy populations as well as multiple clinical populations, including patients with cirrhosis, mild cognitive impairment (MCI) and Alzheimer's disease (AD), attention deficit hyperactivity disorder (ADHD), and epilepsy.

This specific issue includes several studies focusing on clinical populations. In one study by G. Zheng and colleagues, resting-state fMRI was used to examine functional

connectivity changes in the progression of minimal hepatic encephalopathy and found continuously impaired intra- and intermodular connectivity in patients with cirrhosis. In another study, Y.-Y. Wai and colleagues used tract-based spatial statistics of DTI to characterize white matter integrity in different subtypes of MCI, including amnesic MCI, dysexecutive MCI, AD, and healthy controls. They found that amnesic MCI and AD patients share significant white matter damage, whereas dysexecutive MCI patients appear to have a distinct pathogenesis. In the third study, A. dos Santos Siqueira and colleagues used graph theory and analyzed a resting-state fMRI data set from healthy children and ADHD patients in the ADHD-200 database. Distinct patterns of network dysfunction were evident for both inattentive and combined ADHD subtypes. However, the authors observed that the classification scores for discriminating between ADHD and healthy subjects were close to chance and that functional connectivity estimations were strongly dependent on the sample characteristics. In the final study, H. Zhu and colleagues used resting-state MEG to identify the epileptogenic and other abnormal regions in patients with left temporal lobe epilepsy (TLE) and provided further evidence supporting the notion that TLE is not a focal focus but a multifocus disease.

A few other studies in this specific issue examined brain networks and function in normal population. In one study by H. Lei and colleagues, resting-state fMRI was integrated with genetics to examine the effect of genetic variation of the

MAOA gene on resting brain activity in healthy male adolescents. Those with the low-activity MAOA genotype exhibited lower amplitude of low-frequency fluctuation (ALFF) in the pons compared to those with the high-activity MAOA genotype. Moreover, there was a significant genotype by ALFF interaction effect on impulsivity scores. In another study, H. Niu and colleagues examined the effects of learning on resting brain activity using fNIRS and demonstrated that 5 days of visual perceptual learning significantly altered resting oxygenated hemoglobin functional connectivity between visual cortex and frontal/central areas. In the study by C. Xu and colleagues, the regional homogeneity (ReHo) approach was used as an index in the resting-state fMRI to investigate gender differences in spontaneous brain activity among a large sample of young healthy adults. This study found significant ReHo differences in multiple cortical regions and resting-state networks between male and female subjects.

This specific issue also includes two studies on neuroimaging methods and one review paper. In one study, X. Li and colleagues compared FAIR and PICORE sequences and systematically optimized ASL imaging parameters for measuring cerebellum grey matter and white matter perfusion. In another study, M. Gorges and colleagues demonstrated a potential framework for multiparametric functional connectivity mapping through combination of resting-state fMRI with DTI. Finally, in the review paper, T. K. Das and colleagues highlighted the structure-function relationship of the brain networks using the Ising model and graph theory.

In summary, studies published in this specific issue demonstrate a few examples of continuous efforts to integrate structural and functional neuroimaging methods as well as other research modalities in order to elucidate brain networks and their function in both normal healthy population and clinical patients.

*Hengyi Rao
Danny Jiongjiong Wang
Yihong Yang
Yong He*

Research Article

Gender Differences in Cerebral Regional Homogeneity of Adult Healthy Volunteers: A Resting-State fMRI Study

Chunsheng Xu,^{1,2,3} Chuanfu Li,^{1,2,3} Hongli Wu,^{2,3} Yuanyuan Wu,⁴ Sheng Hu,⁵
Yifang Zhu,^{1,2} Wei Zhang,¹ Linying Wang,⁴ Senhua Zhu,⁶ Junping Liu,^{1,2} Qingping Zhang,⁷
Jun Yang,⁸ and Xiaochu Zhang^{9,10}

¹ Medical Imaging Center, The First Affiliated Hospital of Anhui University of Chinese Medicine, Anhui 230031, China

² Laboratory of Digital Medical Imaging, The First Affiliated Hospital of Anhui University of Chinese Medicine, Anhui 230031, China

³ Institute of Computer Application of Chinese Medicine, Anhui Academy of Chinese Medicine, Anhui 230038, China

⁴ Graduate School, Anhui University of Chinese Medicine, Anhui 230038, China

⁵ Department of Electronic Science and Technology, University of Science & Technology of China, Anhui 230027, China

⁶ Institute of Biophysics, Chinese Academy of Sciences, Beijing 100101, China

⁷ School of Acupuncture & Osteology, Anhui University of Chinese Medicine, Anhui 230038, China

⁸ Department of Acupuncture and Moxibustion, The First Affiliated Hospital of Anhui University of Chinese Medicine, Anhui 230031, China

⁹ CAS Key Laboratory of Brain Function & Disease and School of Life Sciences, University of Science & Technology of China, Anhui 230027, China

¹⁰ Center of Medical Physics and Technology, Hefei Institutes of Physical Science, CAS, Anhui 230031, China

Correspondence should be addressed to Chuanfu Li; 13956078816@126.com, Jun Yang; yangzyun@yahoo.cn and Xiaochu Zhang; zxcustc@ustc.edu.cn

Received 14 May 2014; Revised 7 September 2014; Accepted 30 September 2014

Academic Editor: Hengyi Rao

Copyright © 2015 Chunsheng Xu et al. This is an open access article distributed under the Creative Commons Attribution License, which permits unrestricted use, distribution, and reproduction in any medium, provided the original work is properly cited.

Objective. We sought to use the regional homogeneity (ReHo) approach as an index in the resting-state functional MRI to investigate the gender differences of spontaneous brain activity within cerebral cortex and resting-state networks (RSNs) in young adult healthy volunteers. **Methods.** One hundred and twelve healthy volunteers (56 males, 56 females) participated in the resting-state fMRI scan. The ReHo mappings in the cerebral cortex and twelve RSNs of the male and female groups were compared. **Results.** We found statistically significant gender differences in the primary visual network (PVN) ($P < 0.004$, with Bonferroni correction) and left attention network (LAtN), default mode network (DMN), sensorimotor network (SMN), executive network (EN), and dorsal medial prefrontal network (DMPFC) as well ($P < 0.05$, uncorrected). The male group showed higher ReHo in the left precuneus, while the female group showed higher ReHo in the right middle cingulate gyrus, fusiform gyrus, left inferior parietal lobule, precentral gyrus, supramarginal gyrus, and postcentral gyrus. **Conclusions.** Our results suggested that men and women had regional specific differences during the resting-state. The findings may improve our understanding of the gender differences in behavior and cognition from the perspective of resting-state brain function.

1. Introduction

A large number of postmortem and imaging investigations on gender differences were dedicated to the human brain [1–7]. Previous structural neuroimaging studies showed that the brain size is larger in men than in women and revealed that the anatomical gender differences of the brain in the cortex

are region-specific [8, 9]. Women usually have larger relative volumes in frontal and medial paralimbic cortices, while men have larger frontomedial, amygdala, and hypothalamus relative to cerebrum size [9, 10]. Apart from these anatomical differences, gender differences also exist in many behavioral and cognitive domains. Men generally perform better in visual and spatial processing as well as mathematics [11–13],

whereas women tend to outperform men in verbal skills and memory [14, 15], facial emotion recognition [16], fine motor skills [4], and emotion processing [4, 17].

Not only is magnetic resonance imaging a significant imaging modality in clinical diagnosis and treatment planning, but it also provides detailed knowledge of physiological and pathological brain functions for medical research [18]. By taking the advantages of fMRI technique, many studies have reported gender differences in the functions of the brain, such as the sex-related hemispheric lateralization in language processing [19] and emotional memory [17], suggesting that male and female brains might have some different neural mechanisms to conduct certain tasks [20]. However, compared with these task state studies, there are still few studies on the difference in the resting-state of the brain. The resting-state function reflects the neuronal baseline activity of the brain when the subject is not performing an explicit task, representing the state of the human brain in the absence of goal-directed neuronal action and external input. Biswal et al. [21] investigated sex effects using amplitude of low-frequency fluctuation (ALFF) in a large-scale resting-state fMRI cohort ($n = 1414$, across 35 imaging centers) and suggested that sex emerged as a significant determinant. Wang et al. [13] employed a support vector machine-based multivariate pattern analysis (MVPA) approach and found men showed higher regional homogeneity (ReHo) in the right hemisphere and women tended to show greater ReHo in the left.

The ReHo is defined as the regional synchrony of spontaneous fMRI signals and can be used to map the resting-state brain function [22]. To investigate the gender difference in the brain functions, the first question is whether there is any gender difference in ReHo within the resting-state networks (RSNs). There are about twelve RSNs in the brain as previously reported, such as the default mode network (DMN), the sensorimotor network (SMN), the visual network (VN), the auditory network (AN), the salience network (SN), and the attention and executive function networks [23, 24]. The second question will be what specific brain areas are. To address these two questions, we analyzed the gender difference of ReHo in twelve RSNs and whole cerebral cortex of adult healthy volunteers. We hypothesized that men and women might have different ReHo in some of the RSNs and cerebral cortices, which might be related to the gender differences in cognitive domains as previously reported [1–7].

2. Materials and Methods

2.1. Subjects. One hundred and twelve healthy volunteers (56 males, 56 females) were recruited to take part in this experiment. All the procedures were fully explained to the participants and informed consents were obtained from all subjects before they took part in the experiment. All volunteers were the college students in the university, right-handed with no history of mental or neurological disease, with no history of psychiatric and neurological disorders or drug use, and with no obvious abnormality in brain structure. This study was approved by the Ethics Board at the First Affiliated Hospital of Anhui University of Chinese Medicine.

2.2. Data Acquisition. Before the experiment, the participants were requested to change clothes, rest, and then enter into the scanning room after the whole body had been relaxed. The subjects were told to close their eyes and their ears were stuffed with cotton balls during scanning. The lights in the scanning room were turned off to reduce visual stimulation. During the entire scanning process, the subjects were asked to avoid psychological activity as far as possible.

All fMRI experiments were completed at the MR room of the Medical Imaging Center, the First Affiliated Hospital of Anhui University of Chinese Medicine. The Siemens Symphony 1.5T MRI whole body scanner (Siemens Medical Systems, Germany) and standard head coil were used. A total of 4 sequences were scanned, which were as follows. (1) The first sequence was pilot images. (2) T2-weighted images: this sequence lasted for 1 minute 30 seconds. The goal of this sequence was to find whether or not there was any obvious structural abnormality of the brain. (3) Resting-state fMRI data acquisition: this sequence lasted for 10 minutes. Take the axial position parallel to the AC-PC line, with 36 slices that covered the whole brain. EPI-BOLD sequences were used, with TR/TE/FA of 3000 ms/30 ms/90°, FOV of 192 mm × 192 mm, and matrix of 64 × 64. (4) T1-weighted 3D anatomical images: this sequence lasted for 8 minutes 59 seconds. Sagittal position was taken and 176 slices were scanned which covered the whole brain. Spoiled gradient echo sequence was used, with TR/TE/FA of 2100 mm/3.93 mm/13°, FOV of 250 mm × 250 mm, slice thickness/spacing of 1.0 mm/0.5 mm, and matrix of 256 × 256. It took about 21 minutes to complete all the data acquisition.

2.3. Data Preprocessing. All preprocessing procedures were performed using the AFNI software (<http://afni.nimh.nih.gov/>) in the Laboratory of Digital Medical Imaging, the First Affiliated Hospital of Anhui University of Chinese Medicine. The first 4 volumes of the functional images were discarded for the signal equilibrium and participants' adaptation to the scanning circumstance. After excluding the first 4 volumes, all fMRI volumes were slice corrected and then realigned to the first volume. Data was included if the subject's head movement during fMRI scanning was less than 2 mm translation and less than 2° angular rotation in any axis. Six motion parameters, linear drift, and the mean time series of all voxels within the white matter and the cerebrospinal fluid were removed from the data by linear regression to reduce the effects of confounding factors. After that, a temporal filter (0.01–0.08 Hz) was applied to reduce the effect of low-frequency drift and high-frequency physiological respiratory and cardiac noise signals.

2.4. ReHo Analysis. The ReHo analysis was performed in each subject with the program of 3dReHo in the AFNI software. Kendall's coefficient of concordance (KCC) value (also called ReHo value) was calculated to measure the similarity of the ranked time series of a given voxel to its nearest 26 neighbor voxels [22]. By calculating the KCC value of every voxel in the whole brain, an individual ReHo map

TABLE 1: Cerebral gender differences in ReHo between males and females.

Regions	Brodmann area	Side	Coordinate (Talairach)			Voxels	z-value
			Peak x	Peak y	Peak z		
Female > male							
Inferior parietal lobule	BA40	L	-46.5	-31.5	32.5	43	4.83
			-40.5	-34.5	32.5	8	4.26
Precentral gyrus	BA6	L	-37.5	-10.5	29.5	17	4.32
Supramarginal gyrus	BA40	L	-46.5	-52.5	32.5	13	4.2
Middle cingulate gyrus	BA24	R	1.5	-19.5	32.5	10	4.17
Fusiform gyrus	BA20	R	52.5	-22.5	-24.5	4	4.09
Postcentral gyrus	BA2	L	-46.5	-25.5	35.5	4	4.43
Male > female							
Precuneus	BA7	L	-4.5	-67.5	47.5	4	-4.09

Note: BA, Brodmann area; L, left; R, right. The threshold was set to $P < 0.0001$, $\alpha < 0.05$, and cluster ≥ 4 (Monte Carlo simulation program AlphaSim).

was obtained for each subject. All individual voxel-wise ReHo values were computed and standardized into ReHo z -values by subtracting the mean ReHo obtained from the entire brain (i.e., global ReHo, male 0.1632 ± 0.0205 , female 0.1578 ± 0.0113 , $P > 0.05$) and then dividing by the standard deviation [25–27]. Spatial smoothing was then performed with a Gaussian filter of 8 mm full-width half-maximum (FWHM) kernel in order to manage the anatomical variability and to improve the signal-to-noise ratio [13]. Before the intergroup comparison, all ReHo maps were spatially normalized to the standard Talairach atlas template.

2.5. Intergroup Analysis. To explore the ReHo differences between the male and the female groups, a second-level, random-effect, two-sample two-tailed t -test was performed on the individual normalized ReHo maps in a voxel-by-voxel manner within the brain. Although age was not significantly different between groups, it was still included as a covariate to avoid any possible influence. The AFNI Monte Carlo simulation program AlphaSim was used to obtain a corrected significance level of $P < 0.0001$ and a minimum cluster size of 4 voxels (108 mm^3) in the group difference maps. The anatomical localization and labeling of the functional data was determined by both Talairach coordinates and three radiologists.

2.6. RSNs Analysis. For RSNs analysis, the regions of interest (ROIs) of 12 RSNs were derived from our previous study [24]. Using ICA analysis, the preprocessed time series of BOLD after head motion correction, smoothing, and spatial normalization were concatenated along time to form a 4-dimensional (4D) dataset. GIFT-toolbox [28] was used to decompose the 4D BOLD data into 20 mutually independent components. These analyses identified 12 RSNs for BOLD data. There were the DMN, left attention networks (LAtN), right attention network (RAtN), primary visual network (PVN), secondary visual network (SVN), SMN, AN, executive network (EN), dorsal medial prefrontal network (DMPFC), ventral medial prefrontal network (VMPFC), salience network (SN), and medial temporal limbic network

(MTLN). The ROIs' ReHo of each subject was extracted from the individual normalized ReHo maps, and the mean ReHo of each subject was calculated by the program of 3dROIstats in the AFNI software. The ReHo of 12 RSNs was statistically compared between males and females using independent samples t -test approach. The threshold was defined as the Bonferroni correction of $P < 0.05$ (i.e., $P < 0.05/12 = 0.00417$). Further, we also did an exploratory analysis (the threshold was set as $P < 0.05$), which reflects the exploratory nature.

3. Results

3.1. General Information. Fifty-six cases of males (mean age: 25.93 years, range 20–43 years) and fifty-six cases of females (mean age: 26.46 years, range 18–44 years) were finally included in the second-level analysis. Age was not significantly different between groups. All subjects in this study had less than 2 mm translation and 2° of rotation in any of the x -, y -, and z -axes. Therefore, no subjects were removed from the data analysis.

3.2. Cerebral ReHo Differences between Males and Females. It was showed that there existed significant differences in the intergroup comparison between genders. Significantly higher ReHo in the left precuneus was found in the males, and significantly higher ReHo in the right middle cingulate gyrus, right fusiform gyrus, left inferior parietal lobule, left precentral gyrus, left supramarginal gyrus, and left postcentral gyrus was found in the females (Table 1 and Figure 1).

3.3. ReHo Differences of RSNs between Males and Females. The ReHo of PVN was found higher in males than females ($P < 0.004$). In the exploratory analysis, we further found higher ReHo of the DMN, LAtN, PVN, SMN, EN, and DMPFC in females compared to males ($P < 0.05$). No gender differences were found in the other 6 RSNs (Table 2 and Figure 2).

TABLE 2: Comparison of ReHo in RSNs between males and females.

	DMN	LAtN	RAtN	PVN	SVN	SMN	AN	EN	DMPFC	VMPFC	SN	MTLN
Male	0.411	-0.982	-0.759	4.390	3.737	0.356	-3.922	0.412	-0.003	-3.314	-0.637	-2.838
Female	1.780	0.226	0.069	0.810	3.257	2.475	-4.904	2.021	1.157	-3.387	-0.007	-3.245
<i>t</i>	2.258	2.741	1.803	-2.974	-0.538	2.186	-1.215	2.47	1.988	-0.095	1.243	-0.757
<i>P</i>	0.026*	0.007**	0.074	0.004*	0.592	0.031*	0.227	0.015*	0.049*	0.925	0.217	0.451

Note: DMN, default mode network; LAtN, left attention networks; RAtN, right attention network; PVN, primary visual network; SVN, secondary visual network; SMN, sensorimotor network; AN, auditory network; EN, executive network; DMPFC, dorsal medial prefrontal network; VMPFC, ventral medial prefrontal network; SN, salience network; MTLN, medial temporal limbic network. #Independent samples *t*-test, significance threshold $P < 0.004$ (with Bonferroni correction). *Independent samples *t*-test, significance threshold $P < 0.05$ (uncorrected).

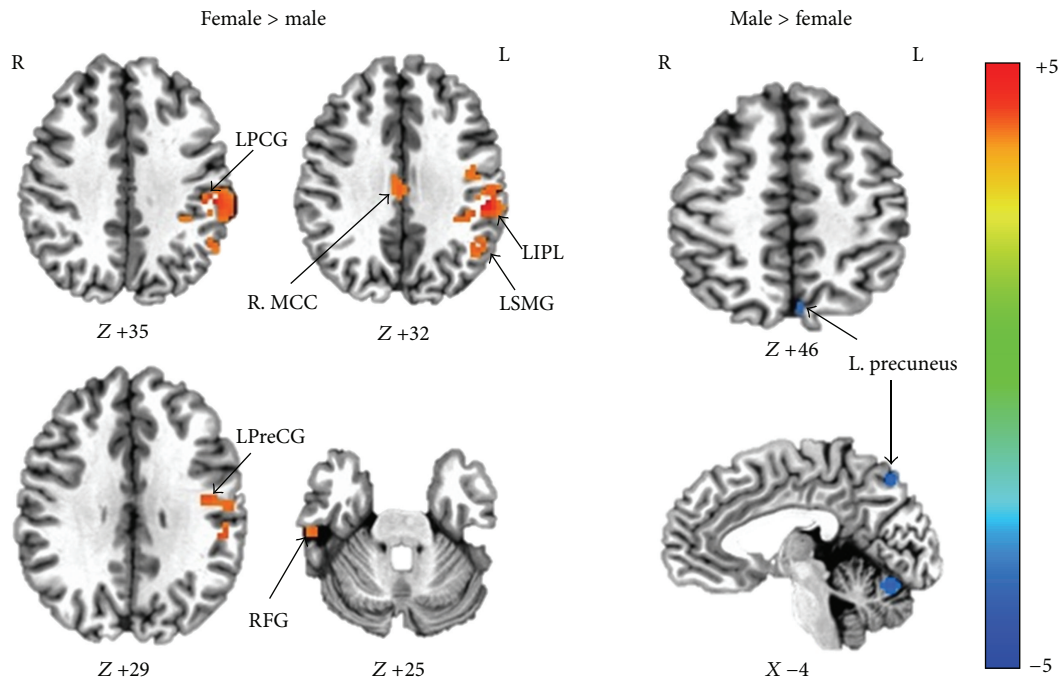


FIGURE 1: ReHo differences of cerebral regions between males and females (Monte Carlo simulation program AlphaSim, $P < 0.0001$, cluster size ≥ 4 , and $\alpha < 0.05$). Women showed greater ReHo than men in areas of the right middle cingulate gyrus (R. MCC), right fusiform gyrus (RFG), left inferior parietal lobule (LIPL), left precentral gyrus (LPreG), left supramarginal gyrus (LSMG), and left postcentral gyrus (LPG), while men showed greater ReHo in the left precuneus. L, left; R, right.

4. Discussion

This study applied ReHo analysis approach to investigate gender differences of resting-state in a large sample of adult healthy individuals. It was found that there existed gender difference in the PVN, LAtN, and some brain areas functionally related to gender differences in cognitive and behavior domains. These results suggest that males and females might have regional specific differences during the resting-state.

In the 12 RSNs, the higher ReHo of PVN was found in males than females, which showed significant gender difference between males and females after Bonferroni correction. PVN is associated with visual processing and SMN is related to motor function [23]. The higher ReHo of PVN in males might imply that males do better in visuospatial processing than females, which is consistent with previous anatomical and behavioral researches [11–13]. In the exploratory analysis, females had higher ReHo of DMN,

LAtN, SMN, EN, and DMPFC than males. As previous studies reported, DMN, LAtN, EN, and DMPFC are involved in a wide range of cognitive processes and memory function [29, 30]. The results might suggest that women outperform men in some cognitive domains and emotion recognition processing, which is in line with previous researches [4, 17]. Several previous studies have reported the gender differences of functional brain networks during rest [30–32]. However, there were some consistency and some inconsistency as well. Our findings were consistent with the fact that there were no significant differences between sexes in the functional connectivity of the brain areas within the SN reported by Weissman-Fogel et al. [30], but they were inconsistent with our results of exploratory analysis that the EN and the DMN which they reported had no significant differences between genders. Another report [32] demonstrated that significant gender differences of resting-state activity were found in all networks. We suggested that the discrepancy might mainly

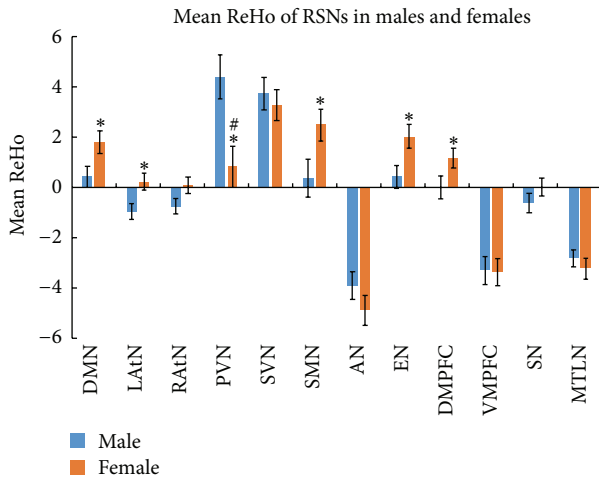


FIGURE 2: Mean ReHo of 12 RSNs between males and females. Significant differences were observed in the PVN (with Bonferroni correction, $^*P < 0.004$). In the exploratory analysis, significant differences were observed in the DMN, LAtN, PVN, SMN, EN, and DMPFC as well as PVN (uncorrected, $^*P < 0.05$). Error bar represented standard error.

result from the different methods they had used in their data analysis.

The specific brain areas in which gender difference of ReHo was found could be classified into two kinds. One kind was that female had higher ReHo and another kind was that male had higher ReHo. Six regions of greater ReHo were shown in females than males, including the right middle cingulate gyrus, right fusiform gyrus, left inferior parietal lobule, left precentral gyrus, left supramarginal gyrus, and left postcentral gyrus in the females. The inferior parietal lobule is a part of left attention network, which was identified from BOLD data using ICA analysis. It is concerned with multiple aspects of sensory processing and sensorimotor integration [33], especially in the perception of emotions in facial stimuli [34], and also, it is concerned with language and body image [35–38]. The middle cingulate cortex is involved in many different functions, including negative affect, pain, and cognitive control [39]. It has also reported that middle cingulate cortex receives widespread inputs, both directly and indirectly, from emotion-related brain regions [40] and may be a pivotal node of emotion and motor integration [41, 42]. Mann et al. [43] observed that women had relatively larger cingulate gray matter volume than men and showed different patterns of age-related volume decline between men and women. Although there are still some disputes on the functionalities of fusiform gyrus, a relative convergent point is related to various cognitive functions [44], such as face and body recognition [45–48], orthography and reading [49–51], word recognition [52], and processing of color information [53–56]. Therefore, the higher ReHo of the above areas in females is consistent with the behavioral sex difference that women generally excel in language [14, 15], facial emotion recognition [16], and emotional memory tasks [4, 17]. Furthermore, the different ReHo areas of the precentral gyrus between genders were located in its inferior

part, which represents the primary motor area of hand and orofacial area [57]. The anterior supramarginal gyrus, which showed regional specific differences between genders in the present study, is also a component of left attention network in our results of ICA processing. It is involved in tool action observation [58]. Consistent with the previous studies [4, 14–17], these results might suggest that women excel better in hand and orofacial related tasks, something like fine motor skills, facial expression, and verbal fluency.

Meanwhile, we found that higher ReHo in the specific region of the left precuneus in men than in women. The precuneus is a part of PVN in our network-wise analysis ROIs. It is strongly interconnected with the parietooccipital visual and oculomotor-related cortices [59]. The precuneus is involved with visuospatial processing [60–62], episodic memory [63], reflections upon self [64, 65], and awareness and conscious information processing [66, 67]. These different processes may be selectively related to different subregions within the precuneus [61]; for example, the posterior subregion, a part of PVN, was related to visual area [68]. In this study, the posterior subregion of left precuneus showed higher regional homogeneity in men, which was consistent with the previous report [61]. In addition, we also found the higher ReHo of the PVN in males than females. Therefore, it might reflect that there existed difference in visuospatial processing between men and women [11, 12] and provided further evidence to a converging point suggested by previous behavioral study; that is, men generally perform better in visuospatial processing than women [11–13].

A gender difference in cerebral regional homogeneity of adult healthy volunteers was also reported by Wang et al. [13]. There were some consistency and inconsistency between their results and ours. The consistency was that both Wang and we found gender difference in resting-state function of healthy volunteers and women mainly exhibited higher ReHo in their left hemispheres. In this study, we adopted the independent samples and repeated the results of left hemispheres preponderance of ReHo in females, which strengthened the conclusion of the higher ReHo in females' left hemispheres concluded by Wang et al. [13]. However, the specific brain regions showing gender differences were not exactly the same. We thought the discrepancy mainly resulted from the difference in methodology. In Wang's study, a support vector machine-based MVPA approach was employed to identify the complex patterns of sex differences in brain structure and resting-state function, but in our study, the ReHo maps were compared between the males and the females using *t*-test. Different data analysis methods can demonstrate different results [69, 70], and the threshold selection can also influence the results [71]. Thus, the result difference between this study and Wang's study might indicate different aspects of resting-state brain function via different analysis methods. In addition, age range may have an effect on resting-state homogeneity [21, 72, 73]. Therefore, we would use different analysis methods and pay more attention to the effect of age in future studies in order to make the results more comprehensive.

Potential limitations of this study should be noted. First, in our study, age range of subjects is a little broader for men

than women. As previous researchers reported [21, 72, 73], age range is critical as it may have an effect on resting-state homogeneity. Although age was not significantly different between our groups and we had included age as a covariate to avoid any possible influence, it would be better to increase the sample size and minimize the age range in the future investigations. Second, the present study had not correlated the ReHo value with the behavioral data for no such data were collected in the experiment. In the future study, this factor should be taken into account. Third, although it is a general practice that global signal of ReHo was removed when doing group level analysis, Zuo et al. [25] reported that removing global effect would reduce reliability of ReHo. Therefore, we should improve our data processing methods in the future. Fourth, the results of DMN, LATN, SMN, EN, and DMPFC in the present study are based on the exploratory analysis (i.e., it did not reach the threshold after Bonferroni correction although some of them are close). Therefore, these results should be replicated in the future.

In summary, the present study found gender differences in regional homogeneity of adult healthy volunteers within some of RSNs and cerebral cortices and indicated that men and women might have regional specific differences during the resting-state. Many of the specific regions showed in voxel-wise analysis belong to the RSNs that showed gender differences in the present study. These regional specific regions are mostly related to the functions of behavior and cognition. The findings are consistent with the gender differences in behavioral and cognitive domains and might improve our understanding of the gender differences from the perspective of brain function.

Conflict of Interests

The authors declare that there is no conflict of interests regarding the publication of this paper.

Acknowledgments

The authors sincerely thank all the volunteers for their participation in this study. This study was supported by grants from the National Key Basic Research and Development Program (973) under Grant no. 2010CB530500, the National Natural Science Foundation of China under Grant nos. 81202768, 31171083, 31230032, and 31471071, Anhui Provincial Natural Science Foundation under Grant no. 1208085MH147, Major Scientific Projects of Anhui Provincial Education Commission under Grant no. KJ2011ZD05, the Fundamental Research Funds for the Central Universities of China (WK2070000033), and 100 Talents Program of the Chinese Academy of Sciences (BJ2070000047).

References

- [1] K. P. Cosgrove, C. M. Mazure, and J. K. Staley, "Evolving knowledge of sex differences in brain structure, function, and chemistry," *Biological Psychiatry*, vol. 62, no. 8, pp. 847–855, 2007.
- [2] J. S. Allen, H. Damasio, T. J. Grabowski, J. Bruss, and W. Zhang, "Sexual dimorphism and asymmetries in the gray-white composition of the human cerebrum," *NeuroImage*, vol. 18, no. 4, pp. 880–894, 2003.
- [3] C. D. Good, I. Johnsrude, J. Ashburner, R. N. A. Henson, K. J. Friston, and R. S. J. Frackowiak, "Cerebral asymmetry and the effects of sex and handedness on brain structure: a voxel-based morphometric analysis of 465 normal adult human brains," *NeuroImage*, vol. 14, no. 3, pp. 685–700, 2001.
- [4] B. Crespo-Facorro, R. Roiz-Santiáñez, R. Pérez-Iglesias et al., "Sex-specific variation of MRI-based cortical morphometry in adult healthy volunteers: the effect on cognitive functioning," *Progress in Neuro-Psychopharmacology and Biological Psychiatry*, vol. 35, no. 2, pp. 616–623, 2011.
- [5] L. Fan, Y. Tang, B. Sun et al., "Sexual dimorphism and asymmetry in human cerebellum: an MRI-based morphometric study," *Brain Research*, vol. 1353, pp. 60–73, 2010.
- [6] M. E. Frederikse, A. Lu, E. Aylward, P. Barta, and G. Pearlson, "Sex differences in the inferior parietal lobule," *Cerebral Cortex*, vol. 9, no. 8, pp. 896–901, 1999.
- [7] M. Ingalhalikar, A. Smith, and D. Parker, "Sex differences in the structural connectome of the human brain," *Proceedings of the National Academy of Sciences of the United States of America*, vol. 111, no. 2, pp. 823–828, 2013.
- [8] N. Raz, F. Gunning-Dixon, D. Head, K. M. Rodrigue, A. Williamson, and J. D. Acker, "Aging, sexual dimorphism, and hemispheric asymmetry of the cerebral cortex: Replicability of regional differences in volume," *Neurobiology of Aging*, vol. 25, no. 3, pp. 377–396, 2004.
- [9] J. M. Goldstein, L. J. Seidman, N. J. Horton et al., "Normal sexual dimorphism of the adult human brain assessed by in vivo magnetic resonance imaging," *Cerebral Cortex*, vol. 11, no. 6, pp. 490–497, 2001.
- [10] R. C. Gur, F. Gunning-Dixon, W. B. Bilker, and R. E. Gur, "Sex differences in temporo-limbic and frontal brain volumes of healthy adults," *Cerebral Cortex*, vol. 12, no. 9, pp. 998–1003, 2002.
- [11] A. M. Rizk-Jackson, S. F. Acevedo, D. Inman, D. Howieson, T. S. Benice, and J. Raber, "Effects of sex on object recognition and spatial navigation in humans," *Behavioural Brain Research*, vol. 173, no. 2, pp. 181–190, 2006.
- [12] D. Voyer, S. Voyer, and M. P. Bryden, "Magnitude of sex differences in spatial abilities: a meta-analysis and consideration of critical variables," *Psychological Bulletin*, vol. 117, no. 2, pp. 250–270, 1995.
- [13] L. Wang, H. Shen, F. Tang, Y. Zang, and D. Hu, "Combined structural and resting-state functional MRI analysis of sexual dimorphism in the young adult human brain: an MVPA approach," *NeuroImage*, vol. 61, no. 4, pp. 931–940, 2012.
- [14] D. Kimura, "Sex, sexual orientation and sex hormones influence human cognitive function," *Current Opinion in Neurobiology*, vol. 6, no. 2, pp. 259–263, 1996.
- [15] J. S. Hyde and M. C. Linn, "Gender differences in verbal ability: a meta-analysis," *Psychological Bulletin*, vol. 104, no. 1, pp. 53–69, 1988.
- [16] Q. Rahman, G. D. Wilson, and S. Abrahams, "Sex, sexual orientation, and identification of positive and negative facial affect," *Brain and Cognition*, vol. 54, no. 3, pp. 179–185, 2004.
- [17] T. Canli, J. E. Desmond, Z. Zhao, and J. D. E. Gabrieli, "Sex differences in the neural basis of emotional memories," *Proceedings of the National Academy of Sciences of the United States of America*, vol. 99, no. 16, pp. 10789–10794, 2002.

- [18] N. Sharma, A. K. Ray, K. K. Shukla et al., "Automated medical image segmentation techniques," *Journal of Medical Physics*, vol. 35, no. 1, pp. 3–14, 2010.
- [19] B. A. Shaywitz, S. E. Shaywitz, K. R. Pugh et al., "Sex differences in the functional organization of the brain for language," *Nature*, vol. 373, no. 6515, pp. 607–609, 1995.
- [20] L. Cahill, "Why sex matters for neuroscience," *Nature Reviews Neuroscience*, vol. 7, no. 6, pp. 477–484, 2006.
- [21] B. B. Biswal, M. Mennes, X.-N. Zuo et al., "Toward discovery science of human brain function," *Proceedings of the National Academy of Sciences of the United States of America*, vol. 107, no. 10, pp. 4734–4739, 2010.
- [22] Y. Zang, T. Jiang, Y. Lu, Y. He, and L. Tian, "Regional homogeneity approach to fMRI data analysis," *NeuroImage*, vol. 22, no. 1, pp. 394–400, 2004.
- [23] J. S. Damoiseaux, S. A. R. B. Rombouts, F. Barkhof et al., "Consistent resting-state networks across healthy subjects," *Proceedings of the National Academy of Sciences of the United States of America*, vol. 103, no. 37, pp. 13848–13853, 2006.
- [24] S. Zhu, Z. Fang, S. Hu, Z. Wang, and H. Rao, "Resting state brain function analysis using concurrent BOLD in ASL perfusion fMRI," *PLoS ONE*, vol. 8, no. 6, Article ID e65884, 2013.
- [25] X.-N. Zuo, T. Xu, L. Jiang et al., "Toward reliable characterization of functional homogeneity in the human brain: preprocessing, scan duration, imaging resolution and computational space," *NeuroImage*, vol. 65, pp. 374–386, 2013.
- [26] S. Zheng, M. Zhang, X. Wang et al., "Functional MRI study of working memory impairment in patients with symptomatic carotid artery disease," *BioMed Research International*, vol. 2014, Article ID 327270, 6 pages, 2014.
- [27] M. Dong, W. Qin, L. Zhao et al., "Expertise modulates local regional homogeneity of spontaneous brain activity in the resting brain: an fMRI study using the model of skilled acupuncturists," *Human Brain Mapping*, vol. 35, no. 3, pp. 1074–1084, 2014.
- [28] X. Wang, Z. Feng, D. Zhou et al., "Dissociable self effects for emotion regulation: a study of chinese major depressive outpatients," *BioMed Research International*, vol. 2014, Article ID 390865, 11 pages, 2014.
- [29] R. L. Buckner, J. R. Andrews-Hanna, and D. L. Schacter, "The brain's default network: anatomy, function, and relevance to disease," *Annals of the New York Academy of Sciences*, vol. 1124, no. 1, pp. 1–38, 2008.
- [30] I. Weissman-Fogel, M. Moayed, K. S. Taylor, G. Pope, and K. D. Davis, "Cognitive and default-mode resting state networks: do male and female brains 'rest' differently?" *Human Brain Mapping*, vol. 31, no. 11, pp. 1713–1726, 2010.
- [31] K. Wu, Y. Taki, K. Sato et al., "Topological organization of functional brain networks in healthy children: differences in relation to age, sex, and intelligence," *PLoS ONE*, vol. 8, no. 2, Article ID e55347, 2013.
- [32] M. Filippi, P. Valsasina, P. Misci, A. Falini, G. Comi, and M. A. Rocca, "The organization of intrinsic brain activity differs between genders: a resting-state fMRI study in a large cohort of young healthy subjects," *Human Brain Mapping*, vol. 34, no. 6, pp. 1330–1343, 2013.
- [33] D. M. Clower, R. A. West, J. C. Lynch, and P. L. Strick, "The inferior parietal lobule is the target of output from the superior colliculus, hippocampus, and cerebellum," *Journal of Neuroscience*, vol. 21, no. 16, pp. 6283–6291, 2001.
- [34] J. Radua, M. L. Phillips, T. Russell et al., "Neural response to specific components of fearful faces in healthy and schizophrenic adults," *NeuroImage*, vol. 49, no. 1, pp. 939–946, 2010.
- [35] K. Schulze and S. Koelsch, "Working memory for speech and music," *Annals of the New York Academy of Sciences*, vol. 1252, no. 1, pp. 229–236, 2012.
- [36] C. Y. Wu, M. H. Ho, and S. H. Chen, "A meta-analysis of fMRI studies on Chinese orthographic, phonological, and semantic processing," *NeuroImage*, vol. 63, no. 1, pp. 381–391, 2012.
- [37] O. Felician and P. Romain, "Your body and mine: a neuropsychological perspective," *Neurophysiologie Clinique*, vol. 38, no. 3, pp. 183–187, 2008.
- [38] E. F. Torrey, "Schizophrenia and the inferior parietal lobule," *Schizophrenia Research*, vol. 97, no. 1–3, pp. 215–225, 2007.
- [39] Q. He, C. Chen, Q. Dong, G. Xue, Z.-L. Lu, and A. Bechara, "Gray and white matter structures in the midcingulate cortex region contribute to body mass index in Chinese young adults," *Brain Structure and Function*, 2013.
- [40] T. Paus, "Primate anterior cingulate cortex: where motor control, drive and cognition interface," *Nature Reviews Neuroscience*, vol. 2, no. 6, pp. 417–424, 2001.
- [41] R. J. Morecraft and G. W. van Hoesen, "Cingulate input to the primary and supplementary motor cortices in the rhesus monkey: evidence for somatotopy in areas 24c and 23c," *Journal of Comparative Neurology*, vol. 322, no. 4, pp. 471–489, 1992.
- [42] M. G. Pereira, L. de Oliveira, F. S. Erthal et al., "Emotion affects action: midcingulate cortex as a pivotal node of interaction between negative emotion and motor signals," *Cognitive, Affective and Behavioral Neuroscience*, vol. 10, no. 1, pp. 94–106, 2010.
- [43] S. L. Mann, E. A. Hazlett, W. Byne et al., "Anterior and posterior cingulate cortex volume in healthy adults: effects of aging and gender differences," *Brain Research*, vol. 1401, pp. 18–29, 2011.
- [44] N. M. Schenker-Ahmed and J. Annese, "Cortical mapping by magnetic resonance imaging (MRI) and quantitative cytological analysis in the human brain: a feasibility study in the fusiform gyrus," *Journal of Neuroscience Methods*, vol. 218, no. 1, pp. 9–16, 2013.
- [45] V. Natu and A. J. O'Toole, "The neural processing of familiar and unfamiliar faces: a review and synopsis," *British Journal of Psychology*, vol. 102, no. 4, pp. 726–747, 2011.
- [46] M. Meng, T. Cherian, G. Singal, and P. Sinha, "Lateralization of face processing in the human brain," *Proceedings of the Royal Society B: Biological Sciences*, vol. 279, no. 1735, pp. 2052–2061, 2012.
- [47] J. M. Contreras, M. R. Banaji, and J. P. Mitchell, "Multivoxel patterns in fusiform face area differentiate faces by sex and race," *PLoS ONE*, vol. 8, no. 7, Article ID e69684, 2013.
- [48] R. Bruffaerts, P. Dupont, S. De Grauwe et al., "Right fusiform response patterns reflect visual object identity rather than semantic similarity," *NeuroImage*, vol. 83, pp. 87–97, 2013.
- [49] K. Tsapkini and B. Rapp, "The orthography-specific functions of the left fusiform gyrus: evidence of modality and category specificity," *Cortex*, vol. 46, no. 2, pp. 185–205, 2010.
- [50] J. T. Devlin, H. L. Jamison, L. M. Gonnerman, and P. M. Matthews, "The role of the posterior fusiform gyrus in reading," *Journal of Cognitive Neuroscience*, vol. 18, no. 6, pp. 911–922, 2006.
- [51] B. D. McCandliss, L. Cohen, and S. Dehaene, "The visual word form area: expertise for reading in the fusiform gyrus," *Trends in Cognitive Sciences*, vol. 7, no. 7, pp. 293–299, 2003.

- [52] D. J. Sharp, M. Awad, J. E. Warren, R. J. S. Wise, G. Vigliocco, and S. K. Scott, "The neural response to changing semantic and perceptual complexity during language processing," *Human Brain Mapping*, vol. 31, no. 3, pp. 365–377, 2010.
- [53] T. Allison, G. McCarthy, A. Nobre, A. Puce, and A. Belger, "Human extrastriate visual cortex and the perception of faces, words, numbers, and colors," *Cerebral Cortex*, vol. 4, no. 5, pp. 544–554, 1994.
- [54] W. K. Simmons, V. Ramjee, M. S. Beauchamp, K. McRae, A. Martin, and L. W. Barsalou, "A common neural substrate for perceiving and knowing about color," *Neuropsychologia*, vol. 45, no. 12, pp. 2802–2810, 2007.
- [55] A. Martin, J. V. Haxby, F. M. Lalonde, C. L. Wiggs, and L. G. Ungerleider, "Discrete cortical regions associated with knowledge of color and knowledge of action," *Science*, vol. 270, no. 5233, pp. 102–105, 1995.
- [56] X. Wang, Z. Han, Y. He, A. Caramazza, L. Song, and Y. Bi, "Where color rests: spontaneous brain activity of bilateral fusiform and lingual regions predicts object color knowledge performance," *NeuroImage*, vol. 76, pp. 252–263, 2013.
- [57] C. R. Noback, N. L. Strominger, R. J. Demarest, and D. A. Ruggiero, *The Human Nervous System: Structure and Function*, Humana Press, 6th edition, 2005.
- [58] R. R. Peeters, G. Rizzolatti, and G. A. Orban, "Functional properties of the left parietal tool use region," *NeuroImage*, vol. 78, pp. 83–93, 2013.
- [59] G. R. Leichnetz, "Connections of the medial posterior parietal cortex (area 7m) in the monkey," *Anatomical Record*, vol. 263, no. 2, pp. 215–236, 2001.
- [60] R. Kawashima, P. E. Roland, and B. T. O'Sullivan, "Functional anatomy of reaching and visuomotor learning: a positron emission tomography study," *Cerebral Cortex*, vol. 5, no. 2, pp. 111–122, 1995.
- [61] S. Zhang and C.-S. R. Li, "Functional connectivity mapping of the human precuneus by resting state fMRI," *NeuroImage*, vol. 59, no. 4, pp. 3548–3562, 2012.
- [62] M. Wallentin, E. Weed, L. Østergaard, K. Mouridsen, and A. Roepstorff, "Accessing the mental space—spatial working memory processes for language and vision overlap in precuneus," *Human Brain Mapping*, vol. 29, no. 5, pp. 524–532, 2008.
- [63] D. Dörfel, A. Werner, M. Schaefer, R. von Kummer, and A. Karl, "Distinct brain networks in recognition memory share a defined region in the precuneus," *European Journal of Neuroscience*, vol. 30, no. 10, pp. 1947–1959, 2009.
- [64] M. Freton, C. Lemogne, L. Bergouignan, P. Delaveau, S. Lehericy, and P. Fossati, "The eye of the self: precuneus volume and visual perspective during autobiographical memory retrieval," *Brain Structure and Function*, vol. 219, no. 3, pp. 959–968, 2013.
- [65] M. Cabanis, M. Pyka, S. Mehl et al., "The precuneus and the insula in self-attributional processes," *Cognitive, Affective and Behavioral Neuroscience*, vol. 13, no. 2, pp. 330–345, 2013.
- [66] A. E. Cavanna and M. R. Trimble, "The precuneus: a review of its functional anatomy and behavioural correlates," *Brain*, vol. 129, no. 3, pp. 564–583, 2006.
- [67] B. A. Vogt and S. Laureys, "Posterior cingulate, precuneal and retrosplenial cortices: cytology and components of the neural network correlates of consciousness," *Progress in Brain Research*, vol. 150, pp. 205–217, 2005.
- [68] C. L. Colby, R. Gattass, C. R. Olson, and C. G. Gross, "Topographical organization of cortical afferents to extrastriate visual area PO in the macaque: a dual tracer study," *Journal of Comparative Neurology*, vol. 269, no. 3, pp. 392–413, 1988.
- [69] D. Rubin, T. Fekete, and L. R. Mujica-Parodi, "Optimizing complexity measures for fMRI data: algorithm, artifact, and sensitivity," *PLoS ONE*, vol. 8, no. 5, Article ID e63448, 2013.
- [70] S. M. Smith, D. Vidaurre, C. F. Beckmann et al., "Functional connectomics from resting-state fMRI," *Trends in Cognitive Sciences*, vol. 17, no. 12, pp. 666–682, 2013.
- [71] M. T. R. Stevens, R. C. N. D'Arcy, G. Stroink, D. B. Clarke, and S. D. Beyea, "Thresholds in fMRI studies: reliable for single subjects?" *Journal of Neuroscience Methods*, vol. 219, no. 2, pp. 312–323, 2013.
- [72] M. P. Lopez-Larson, J. S. Anderson, M. A. Ferguson, and D. Yurgelun-Todd, "Local brain connectivity and associations with gender and age," *Developmental Cognitive Neuroscience*, vol. 1, no. 2, pp. 187–197, 2011.
- [73] W. Koch, S. Teipel, S. Mueller et al., "Effects of aging on default mode network activity in resting state fMRI: does the method of analysis matter?" *NeuroImage*, vol. 51, no. 1, pp. 280–287, 2010.

Review Article

Highlighting the Structure-Function Relationship of the Brain with the Ising Model and Graph Theory

T. K. Das,¹ P. M. Abeyasinghe,¹ J. S. Crone,^{2,3,4} A. Sosnowski,¹ S. Laureys,^{5,6}
A. M. Owen,⁷ and A. Soddu¹

¹ Physics & Astronomy Department, Brain & Mind Institute, Western University, London, ON, Canada N6A 3K7

² Neuroscience Institute & Centre for Neurocognitive Research, Christian Doppler Klinik, Paracelsus Medical University, 5020 Salzburg, Austria

³ Centre for Neurocognitive Research & Department of Psychology, University of Salzburg, 5020 Salzburg, Austria

⁴ Department of Neurology, Christian Doppler Klinik, Paracelsus Medical University, 5020 Salzburg, Austria

⁵ Cyclotron Research Center and University Hospital of Liège, University of Liège, 4000 Liège, Belgium

⁶ Department of Neurology, CHU Sart Tilman Hospital, University of Liège, 4000 Liège, Belgium

⁷ Department of Psychology, Brain & Mind Institute, Western University, London, ON, Canada N6A 5B7

Correspondence should be addressed to T. K. Das; tdas2@uwo.ca

Received 13 May 2014; Revised 17 July 2014; Accepted 17 July 2014; Published 4 September 2014

Academic Editor: Yong He

Copyright © 2014 T. K. Das et al. This is an open access article distributed under the Creative Commons Attribution License, which permits unrestricted use, distribution, and reproduction in any medium, provided the original work is properly cited.

With the advent of neuroimaging techniques, it becomes feasible to explore the structure-function relationships in the brain. When the brain is not involved in any cognitive task or stimulated by any external output, it preserves important activities which follow well-defined spatial distribution patterns. Understanding the self-organization of the brain from its anatomical structure, it has been recently suggested to model the observed functional pattern from the structure of white matter fiber bundles. Different models which study synchronization (e.g., the Kuramoto model) or global dynamics (e.g., the Ising model) have shown success in capturing fundamental properties of the brain. In particular, these models can explain the competition between modularity and specialization and the need for integration in the brain. Graphing the functional and structural brain organization supports the model and can also highlight the strategy used to process and organize large amount of information traveling between the different modules. How the flow of information can be prevented or partially destroyed in pathological states, like in severe brain injured patients with disorders of consciousness or by pharmacological induction like in anaesthesia, will also help us to better understand how global or integrated behavior can emerge from local and modular interactions.

1. Introduction

Despite decades of research focusing on network based brain activities, the anatomical structure of the observed brain networks and the functional aspects of spatiotemporal brain dynamics remain mysterious [1]. Several recent functional magnetic resonance imaging (fMRI) studies on the wakeful resting brain have showed the existence of different brain networks—resting-state networks (RSNs), for example, the default mode network (DMN), salience network (SN), auditory network (AN), three distinct visual networks (VN), sensorimotor network (SMN), and left and right executive

control (ECN), which are considered to be unperturbed, nonstimulated functional networks, which at baseline activity are performing complex cognitive tasks [2–6]. The balance between segregation and integration of well-segmented and separated brain regions is essential for efficient information processing and rapid information transfer within and between the networks [7, 8]. A human brain consists of around 100 billion neurons, and each of these neurons forms approximately 1000 trillion electrical as well as chemical synaptic and nonsynaptic connections with other neurons in a brain network [9]. As a result, the importance of studying neurobiological implications of the complex neural wiring

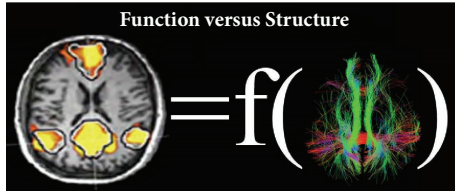


FIGURE 1: Default mode network in a healthy control as extracted from resting state functional magnetic resonance imaging using independent component analysis and the fibers reconstructed using a tractography technique applied to diffusion tensor imaging data and subsequently filtered by the regions functionally connected in the default mode network.

structure of these aforementioned functional networks has always been proven to be critical. The state of the art in neuroimaging techniques is already offering us the possibility to assess structural and functional connectivity of these brain networks. However, there is still a gap in finding more convincing structure-function relationships that could be predicted by the optimal neural activity in the network. This limits our current understanding of the mechanisms governing the base of emergent spatiotemporal brain dynamics, and their relation to complex evolutionary cognitive assessments of brain networks [10].

Starting from the Hodgkin-Huxley conductance-based model [11], the field of computational neuroscience has been playing a significant role in replicating the functional characteristics of spontaneous neuronal activity from the modular brain network [12–16]. This could provide new insights into network dynamics along with the advancement of neuroimaging experiments [17–20]. Neuroimaging observations are strongly supporting a relationship between the structural architecture of the brain and its functional networking (see Figure 1 as an example for the DMN functional pattern and its structural support) [21–23]. The emergence of spontaneous network dynamics in the resting brain was simulated from the heterogeneous structural connectivity of the human brain and then compared with the spatiotemporal dynamics of BOLD low-frequency signals during rest [19]. In their study, oscillatory neural populations were found to be synchronized through the phase dynamics of coupled oscillators in a generalized Kuramoto model. This synchronization model could offer a detailed comparison of functional networks among the structural connectivity. With increasing global coupling strength of oscillators, clusters of oscillator nodes progressively integrate to form larger clusters with positive and negative correlations between them, and the corresponding network dynamics exhibit a phase transition from a desynchronized phase to a partially synchronized phase. In contrast to homogeneous or randomly coupled networks, the transition from a partially synchronized to a fully synchronized phase was found to be less probable due to the role of possible delay in transmission in the resting brain network. Despite this, a good agreement of “emergent” properties between simulated functional connectivity and empirical functional connectivity was demonstrated through the measurement of individual seed-based

correlation in RSNs. Mechanisms behind cluster formations (or integration), intra- and inter-regional interactions, and the emergence of intercluster correlations/anticorrelations remain unexplored [19, 22]. Their studies suggest the need for more computational modeling-based research on the structure-function dependencies in brain networks.

In the context of the complex structure-function relationships in the brain network, self-organized neural dynamics have been shown to exhibit random behaviour which can become very similar to systems studied in statistical physics (e.g., the Ising model) [24–26]. In the past, neural dynamics in the resting brain had been considered as quasistationary states without introducing the structural information and without a direct correspondence between lattice size and brain positions [12, 27]. In order to investigate dynamics of the resting brain, a collective phenomenon based 2-dimensional (2D) Ising model was simulated numerically at different temperatures [18, 28]. Their simulated results allow an assessment of the cooperative emergent properties and the universality classes of network dynamics [18, 20, 27] as well as the biological plausibility of RSNs [2]. Under these mechanisms, the collective spin dynamics exhibit long-range spatiotemporal correlations with second order phase transitions between ordered and disordered magnetic states at the critical temperature [12, 29]. Compared to subcritical ($T < T_c$) and supercritical ($T > T_c$) temperature regions, their simulated results at this critical point highlighted a balance between positive and negative correlated networks and were comparable with the correlation and anticorrelation obtained from resting state fMRI. The universal mechanisms underlying the spontaneous emergent phenomena of the 2D Ising model can explain self-organized criticality of neural dynamics in large scale RSNs [28, 30]. Functional activation patterns of neural networks largely depend on the underlying structure of fiber pathways connecting all regions of the cortical and subcortical brain area [23, 31]. In a recent study [32], the functional neural activity of resting brain networks was also simulated from the generalized Ising model, replacing equal spin coupling with the structural network of the human connectome. The structural based collective neural dynamics were able to explain correlation-based networks that were comparable with the RSNs extracted from fMRI. Their findings confirmed that the second order phase transition and self-organized criticality of the 2D Ising model at critical temperature [27] might not be enough to explain the complex organization of information transfer in resting brain networks. This raises more puzzling questions about functional RSNs in various conditions including the involvement of cognitive tasks on the resting brain or altered states of consciousness like physiological (sleep), pharmacological (anesthesia), and pathophysiological (disorder of consciousness) states of brain networks [33].

In addition to the aforementioned Kuramoto model of coupled oscillators and Ising model of magnetization, Honey et al. presented a neuronal mass model based analysis that could predict the functional connectivity from the human anatomical structure [21]. Following conductance-based neuronal dynamics, the neuronal mass model simulates a population of highly interconnected excitatory and inhibitory

neurons. Three dynamic variables (membrane potential of pyramidal cells, average number of open potassium channels, and inhibitory interneurons) are used to describe the time-course of local field potentials for a neuron mass. Each mass represents a node of cortex, which is interconnected to other nodes through the structural connectivity matrix via the mean firing rate. Along with these variables there are multiple microscopic quantities (ion channel conductance, fraction of channels open, and the ratio of NMDA to AMPA receptors), being used to describe the dynamics of neural masses. The number of intraconnected neurons, as well as the net effect of these microscopic constants, remain unknown for each node. There is an additional fitting parameter describing the excitatory coupling between nodes in the network. Utilizing all parameters, global resting brain dynamics are modelled and compared with empirical results [21, 34, 35]. In comparison, the Ising model uses one parameter, temperature, to simulate global brain activity. More research on the Ising model, taking into account the structural and functional interrelationships seen in the neural mass model, could resolve many unknowns in large-scale brain networks.

Modern neuroimaging techniques like fMRI and diffusion tensor imaging (DTI), along with methodological advances in both spatial pattern detection and anatomical tracing, has made it possible to extract the functional patterns and the structures of neuroanatomical circuitry at different spatial scales [36–38]. With the development of graph theory, we have witnessed an unprecedented growth of applications to understand the structural and functional complexity of the human brain connectome [39] due to its relative simplicity, highly generalized, and easily interpretable nature. In a graph, structural (i.e., synaptic, axonal, and dendritic) and functional (i.e., spontaneous or evoked neuronal response based dynamic interactions) network connectivity of brains is typically represented by a set of nodes which carries neuronal information at the scale of interest and a set of edges that represents either functional relationships or structural connections among individual nodes [10, 40, 41]. Correlated nodes in patches of the cortex (gray matter) were used to demonstrate dynamic interaction of neural circuitry, in which functionally clustered regions of small-world networks were governed by specific features, for example, high clustering, small path length, high efficiency, and repeated network motifs in a particular class [42, 43]. In the Watts-Strogatz model, probability of increasing rewiring demonstrates the transition of a random network from a periodic ring shaped lattice of the small-world topology [44]. Several pathological states of brain networks were also investigated, in which any disturbance of structural connectivity in neural networks could increase the probability of rewiring and reduce the functionally organized brain activity, for example, the Erdős-Rényi type networking [34, 45–47]. Based on anatomical connectivity patterns and physiological interactions of neurons in mammalian brains, a statistical model of canonical microcircuits was able to describe cortical dynamics dependent on the large-scale “average connectivity” [14, 48]. The linked long-range projections in this model demonstrated nonrandom coherent features and large-scale spatiotemporal organizations of complex brain functionality.

Recently, an electroencephalogram (EEG) study providing a high temporal resolution has been performed on large-scale network dynamics to investigate the loss of consciousness and cognitive deficits in patients with disorders of consciousness (DOC) after severe brain injury. This study provides information about further diagnosis and physiological mechanisms [49]. In large-scale brain networks, however, nodes keep being defined a priori, which is not always justified due to the limitation in sensitivity of detecting complex axonal fiber architecture [49, 50] and also due to the lack of appropriate parcellation procedures in order to establish short- and long-range functional relationships among highly coherent brain regions [51, 52].

The performance of self-organized criticality, and its relation to efficient information processing in conscious brains, is solely determined by maintaining an optimal balance between axonal lengths and synaptic costs in neuronal circuitry [53]. Axonal wiring cost is considered as the source of functional integration, which is mostly spent forming long-range communications among spatially distant brain regions. On the other hand, the strength of short-ranged intraregional connectivity is improved with an increase of synaptic costs, implying a segregation effect on global dynamic patterns. There are also other factors, for example, the metabolic cost, glia cells, and myelination that play a role in neuronal communications. According to the economic principle of the brain, minimizing wiring and metabolic energy costs results in a more “profitable” and efficient tradeoff between wiring costs and the maximum structural and/or functional connectivity among spatially distinct brain regions. Balancing neuronal communication cost and highly conserved global connectome organization, the functional network topology in the healthy human brain demonstrates small-worldness [45]. The computational efficiency and functional integration of this type of brain network lie in the intermediate regime between the lattice-type topological networking (efficiency = low, cost = low) and random networking (efficiency = high, cost = high) [54]. Series of earlier fMRI studies on the anaesthetized human and monkey brains demonstrated a breakdown of cortical and subcortical functional connectivity in all resting networks when subjects were in a state of anesthesia-induced loss of consciousness [55–58]. This effect on functional connectivity altered intra- and inter-cortical connectivity, preventing the efficiency of information flow that was present in the small-world network of wakeful healthy brains. Their findings on imbalanced functional connectivity in the segmented cortical network also highlighted the requirement of maintaining the economic principle in order to perform the active cross-modal functional interactions during network communications.

In this paper, we focus on reviewing the functional organization of brain dynamics and its underlying structure-function relationship in a wakeful and conscious resting brain, followed by a brief discussion of its alterations under pharmacological and pathological states of consciousness [33]. Recent work on the Ising model and graph theory is explored to help understanding the global and local organization of brain communication at a spatiotemporal scale [20, 32, 59, 60] and its structural-functional interdependencies.

Comparing both theoretical insights and fMRI empirical results, the notion of criticality, metastability, and phase transitions in self-organized brain dynamics are demonstrated, taking into account the emergence of macrostates under cooperative processes [13, 61].

2. Ising Model and Its Application to Brain Dynamics

The Ising model of ferromagnetism was firstly introduced by Ernst Ising in 1925 as a statistical model of ferromagnetism [62]. A 2D square lattice version was further explored to explain the existence of ferro/paramagnetic transitions and was exactly solved in statistical physics by Onsager in 1944 [63]. Essentially, the model consists of discrete magnetic moments with their spins $s_i = +1$ pointing upward and $s_i = -1$ pointing in downward directions. In the brain, local increase (or decrease) in BOLD activity from its baseline could also be represented by “+1” (or “-1”) spin state [18, 64]. According to the model, each of these spins has the tendency to align with its neighbours in the square lattice through the nearest-neighbour, interaction energy, or coupling constant J_{ij} . In the absence of any external field, the energy of a state t is expressed by $E(t) = -(1/2) \sum_{\langle i,j \rangle} J_{ij} s_i s_j$, where $\langle i, j \rangle$ denotes the nearest neighbour interaction between nodes i and j . Furthermore, the strength of interactions always competes against the effect of the temperature of the thermal bath with which the spin lattice is in contact. According to the formalism of statistical physics [65], the probability of finding the system in a configuration t is $P(t) = \exp[-E(t)/kT]/z$. Here $z = \sum e^{-E(t)/kT}$ is called the partition function, k is the Boltzman constant, and T is the temperature. E measures the integrated energy of a spin configuration, in which the interaction between spins wants to minimize which can be used to quantify the global spin organization. kT instead measures the kinetic energy randomly transferred between the thermal bath and the spin lattice, which produces the segregation effect in spin clusters. Numerical approaches have been developed to simulate the dynamics of an Ising model. The combination of Metropolis algorithm and classical Monte Carlo simulation with periodic boundary conditions establishes the thermalization procedure of magnetic spins when the system is placed in touch with a heat bath of temperature T [66]. With increasing T , the spontaneous fluctuation of Ising spins increases. When the temperature reaches a certain critical value (T_c), there is a qualitative change in the organization of the spin clusters as a whole, and the correlation length between neighbouring spins within the cluster (which captures the size of the formed clusters) diverges. The outcome of spin organizations from a 2D Ising model simulation at three different T values is presented in Figure 2 after being projected on a 1015 parcellation of the brain [67] (notice that the relation between physical position in the brain and the 2D lattice is completely arbitrary, even if nearest neighbour interaction distribution is maintained).

At low T , the spontaneous Monte Carlo spin flips are less probable, and spins in a given configuration are mostly aligned to contribute the minimum energy or ground state

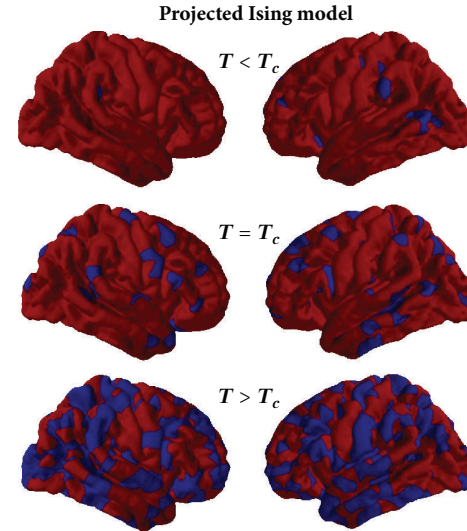


FIGURE 2: Three different 2D Ising model configurations after thermalization for, respectively, $T < T_c$, $T = T_c$, and $T > T_c$. A 32×32 square lattice configuration has been projected on a 1015 parcellated brain keeping the nearest neighbour interaction structure.

energy of the system. A quantity called the magnetization, which is the average of total spins over the whole lattice, determines the magnetic ordering of the system, that is, its ferromagnetic behaviour. When all spins are aligned along the same direction, a magnetization of magnitude “+1” or “-1” will be generated corresponding to a complete order configuration. The large amount of integrated magnetic ordering in this low temperature regime is accompanied by a small information content of the organized spin clusters. At high T , the magnetic ordering is completely lost due to significantly increasing number of spontaneous spin flips and the magnetization tends to “0,” which can be used to characterize the paramagnetic phase. In this case, a large number of laws of nature do not hold due to spontaneous symmetry breaking under global spin flips, and this disordered phase can be seen as the result of the dominating segregation effect over the cluster integration [66]. The information content is very high, in this case, but without integration. For the intermediate regime of T , the self-organized criticality, as well as a second order phase transition, are observed in the 2D Ising model through the maximum fluctuation in the magnetization and the susceptibility peak when T reaches a critical value T_c [18]. In this case, a balance between integration and segregation effects is recognized and revealed by the divergence of the correlation length through the formation of long-range ordering within the correlated functional networks of spin clusters. The global ordering of magnetization is preserved in the $T < T_c$ regime and is destroyed above the critical temperature T_c . In Figure 3, four different states of 2D spin configurations are shown for $T < T_c$, $T = T_c$, and $T > T_c$. These four different configurations correspond to the same four different time points at three different temperatures. Due to its simplicity of simulating two state spin systems and the richness of its dynamic behaviour in self-organized criticality,

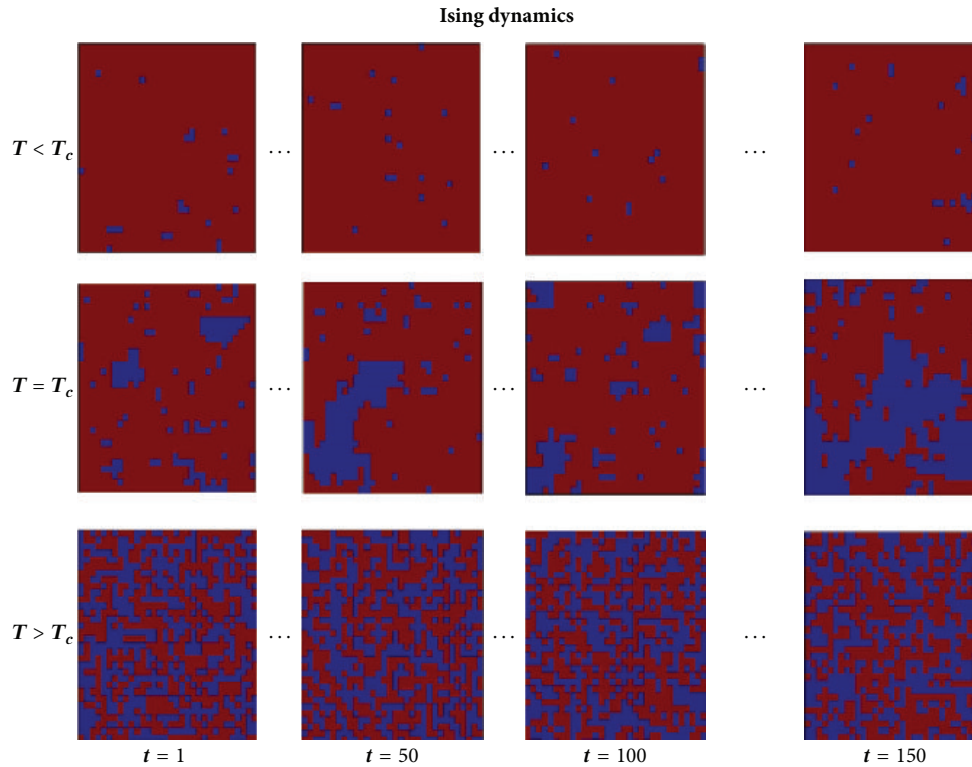


FIGURE 3: Dynamics of a 2D Ising model with lattice size 32×32 after thermalization. For the three different temperatures $T < T_c$, $T = T_c$, and $T > T_c$ the Ising model is simulated generating 150 time data points. Each time point corresponds to a new configuration in which all spins have been tested for flip through the Metropolis algorithm. Configurations of the same four time points are reported for the three different temperatures.

the Ising model has been demonstrating unprecedented growth of applications in physics as in many other fields, including computational neuroscience [18, 28, 30].

In neuroscience, electrophysiological brain activity in the presence or absence of sensory stimulation can be described by two states: (1) active states in which randomly generated neuronal action potentials collectively process information and provide neuronal communications with each other via functional networking and (2) inactive states in which neurons do not cross the threshold value to fire action potentials [12]. In the brain at rest, when a large number of neurons are functionally connected with each other, the resultant interaction of all other neurons on a given neuron can always be considered as its single averaged form [68, 69]. This situation can often be realized in the mean field theory, in which an effective interaction (e.g., exchange coupling in the Ising model) substitutes the many body interactions, involving the long-range ordering in the functional network [64, 70]. Reduction of many degrees of freedom in neural dynamics can therefore be simplified in an asymptotic form that results as the emergence of activated functional patterns [71]. The stability of these synchronous dynamic patterns in a network represents a neuronal firing state based on cooperative activity. In addition to four different spin configurations at the critical temperature (T_c), mean functional organizations of neural dynamics, sampled at four different times and based on the resting state fMRI of 14 healthy

subjects is shown in Figure 4. The baseline for the fMRI signal has been separately calculated for each parcellated region as the mean of the time-course for that region. All values above (or below) the baseline are represented in “Red” (or “Blue”).

Series of earlier studies on fMRI, multielectrode local field potential (LFP), and magnetoencephalography (MEG) [72] profoundly highlighted the spontaneous emergence of cortical and sub-cortical resting brain activity in human and non-human primates [73]. In their analyses, collective functional organization of RSNs were found to be very similar to the emergence of simulated organizations poised in 2D Ising model near the critical temperature (see previous section). Along with the simulated spatiotemporal brain activity near or at the critical point, brain functionality in RSNs encountered the maximization of information processing, taking into account the input sensitivity and dynamic range of activity patterns [26, 73]. Besides prominent matching of the long-range correlations in large-scale cortical networks, power law behaviour with a slope value $-3/2$ (represents the fractal dimension) and neuronal avalanches in small-scale networks were indicated in empirical and simulated data of the resting brain [18, 74].

In addition to this earlier work, there has been considerable growing attention on simulating the brain dynamics and its relation to self-organized criticality using the structure of human connectome from the DTI based measurements [32]. The fiber distributions between each pair of cortex parcellated

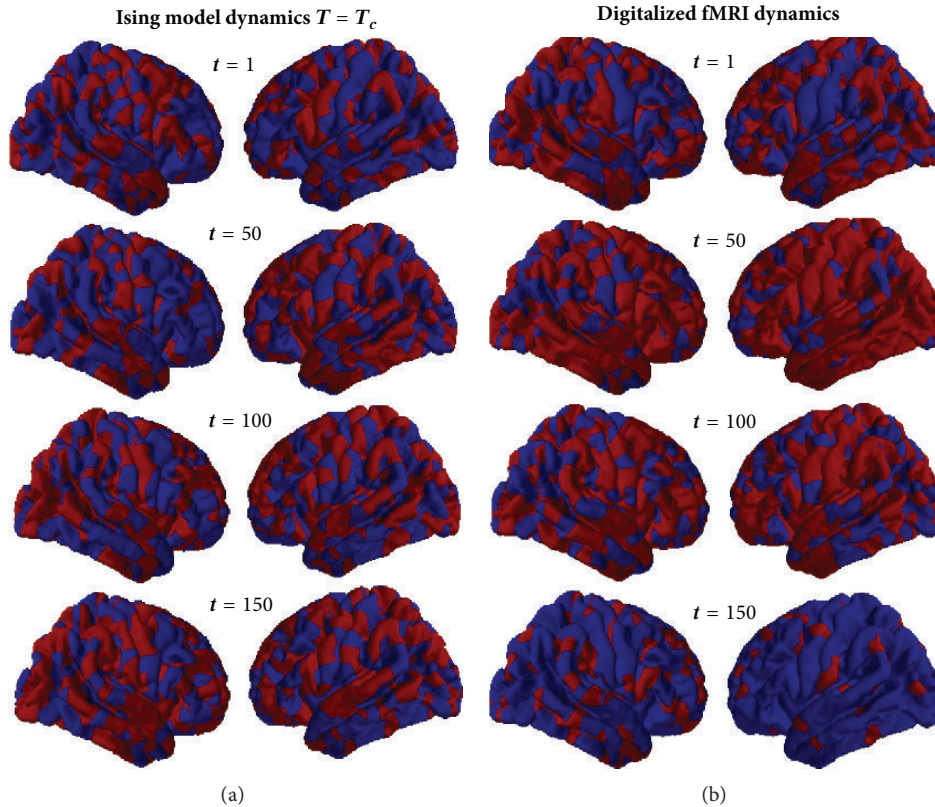


FIGURE 4: Simulated and functional imaging maps generated for four different time points. (a) shows the equilibrium spin configurations at $T = T_c$. In (b), digital maps are created by setting a threshold as the baseline value of the BOLD time course for each corresponding parcellated region. Red corresponds to a value of above baseline (or spin “+1”) and blue below (or spin “-1”). Maps are created after averaging BOLD signal over 14 healthy subjects.

regions could be in fact used as the input for the coupling J_{ij} between spin i and spin j in a generalized Ising model. In this way, all nodes including left and right hemispheres are interacting with each other, implying that any spin sees all the other spins as nearest neighbor even if with different couplings. Recently, a study on simulating the resting functional activity in monkeys and humans [73, 75] attempted to emphasize the finite size, scaling, and universality of brain dynamics. Along with the measurement of maximum information processing at criticality, their calculations on T_c (not in line with earlier findings) as well as critical exponents of magnetization, specific heat and susceptibility, could explore collective brain activities in different spatial scales [75]. In the next section, functional organizations of spontaneous brain activity will be reviewed in the light of dynamic phase transitions, while the phenomena of self-organized criticality and metastability will help to characterize the similar behaviour of organized activity patterns observed in the empirical data [72, 76].

3. Self-Organized Criticality, Phase Transition, and Metastability in Brain Networks

Criticality in any dynamic system, including the brain, can be characterized by a threshold that describes the boundary

of phase transition between ordered and disordered patterns. In order to understand experimental findings of human functional brain activity, for example, the resting state fMRI, a large number of interacting spin systems has been modeled successfully as self-organized criticality [77]. Recently, the correlation networks of resting state fMRI data were compared with the correlation matrix of a 2D Ising model at different temperatures, in which spins were connected with the short ranged nearest-neighbour interactions [28]. In the Ising model, the self-organized dynamic patterns are formed through the spontaneous fluctuation of random spins, reducing degrees of freedom through non-linear interactions among functional units of spin clusters [65]. These functional units are characterized by reduced degrees of freedom and are represented by order parameters (e.g., the magnetization) [66]. With increasing T , the spontaneous fluctuation of spin-flips increases, and at critical temperature the dynamic phase transition replicates the long-range ordering in the spin dynamics. This effect of long-range ordering can provide the maximum information flow, which is reduced down abruptly either in the phase of ordered ($T < T_c$ in subcritical phase) or completely disordered ($T > T_c$ in supercritical phase) spin states. This has been considered as the self-organized criticality of a 2D Ising model, in which the maximum occurrence of metastable states [76] can mimic

almost all fascinating properties in the wakeful resting brain. Self-organization in the resting brain is also the result of spontaneous neural dynamics that have shown features such as metastability in order to explain the efficient information processing in the network. It is only in the critical regime of the Ising model that we can retain these properties and simulate brain functionality effectively [13, 20, 73].

Starting from Turing instabilities in dynamical systems (1950), it has been shown that macrostates of brain wave oscillations can be formed out of cooperative processes, instabilities, rapid transitions between coherent states, pattern formations, and so forth [13, 78]. Due to the variability of synaptic couplings among large groups of neurons in an input-output based brain network, the ability to process and transfer information depends solely on integrating several functional counter-parts of the neural circuits of cortical and subcortical structures [79]. Taking into account the cooperation and competition in spontaneous neuronal oscillations, the basis of conscious brain activity lies in the state of metastability [80]. The dynamic states of brain oscillations lie in far-from-equilibrium regions, but it stabilizes over a long time period, explaining the ability to perform brain activities out of many random inputs from the external world [81]. The emergence of simulated spin dynamics in the Ising model and brain dynamics in level of consciousness, exhibit features of dynamic transitions between metastable states [18, 76]. Due to the limitation on appropriate fiber-tract modeling, the structural connectivity used in current neuroscience research seemed to overlook long-range projections and the polarization of fiber tracts. Insufficient information on the anatomical structure of the brain limits the current findings of simulated brain activity with the Ising model. Further research on fiber-tract connectivity in brain networks will improve simulations of self-organized criticality and metastability of functional brain activity. This will lead to a better understanding of complex brain phenomena such as cognition or generating consciousness. While simulating the Ising model provided the opportunity to characterize the structure-function relationship in emergence of complicated brain organizations, the research on graph theoretical approaches (see next section) could offer a better insight to understand the information traffic, and the integration properties of the network.

4. A Brief Review of Graph Theory

4.1. Current Progress on Graph Theory. Initial approaches of the network structures based on graph theory have developed a growing interest among the researchers involved in investigating the neuronal systems of the brain. Graph theory is providing a simplified and more generalized approach to studying the complex neuronal structures (e.g., Brain network) in neuroscience [82]. Furthermore, it has been proposed that the structure of the global brain network enhances the interaction between the segregation and integration of functionally specialized areas in the brain [83]. Even though the functional networks are restrained by the limitations of the structural connections, context-sensitive

integration during cognition tasks necessarily requires a divergence between structural and functional networks. This essential idea is well explained by the “small-world” networks in graph theory which deals with highly clustered, yet globally interconnected networks [84]. The higher the clustering, the greater is the ability of being connected with groups of neurons in the brain network, resulting in network hubs. Thus, it describes the strong functional organization of the brain network and it is also evident in networks which have been extracted in resting state fMRI [84]. In addition, such networks have been described in cortical structure [42, 85] and in EEG and MEG (magnetoencephalogram) studies. Therefore, it is important to compare the parallel behaviour of the organization of functional and structural neuronal anatomy in the brain, and the complex networks of graph theory.

4.2. Fundamentals of Graph Theory. Graph theory is an outstanding basis from which to study the functional and anatomical connections in the brain. A graph related to the brain network is a model of the neurons or group of neurons in patches of cortex (nodes/vertices in graph theoretical nomenclature) which are interconnected by a set of edges. The edges represent functional or structural connections between cortical and subcortical regional nodes based on analysis of human neuroimaging data [39]. Nodes in large scale brain networks usually represent brain regions, whereas the edges represent anatomical, effective or functional connections. In a graph, the number of connections a node has is called degree k [86]. The distribution of the degree $P(k)$ gives the information about the fraction of nodes having k number of edges and is, therefore, the probability distribution of the degree over the whole network. Clustering coefficient of a graph is another commonly used characteristic which gives the ratio of the number of existing connections to the number of all possible connections [44, 87], whereas the characteristic path length is the average of the shortest path lengths between the nodes. In addition, the global efficiency gives the inverse of the harmonic mean of the minimum path length, between each pair of nodes [88–90] and it indicates the amount of traffic that the network can handle. The local efficiency indicates a measure of the fault tolerance of the network [88] which gives information about handling traffic by each node in the network. In another perspective, efficiency is a useful network measure, which can be used to distinguish between highly active networks or otherwise. Moreover, the strength of divisions of a network in clusters is given by the modularity [91]. High modularity could establish strong connectivity of nodes within clusters and sparse connectivity between nodes of different clusters in the network. The complex networks, which are fundamentally characterized by these network metrics, are complex not only by the means of the size of the network, but also due to the interaction architecture and dynamics of the network [92].

The networks have been classified, according to their topology, under three categories designated random network, small-world network, and scale-free network. Random graphs can be constructed by assigning connections between

pairs of nodes with uniform probability. For most of the complex network systems, a random network is a poor estimate. The probability distribution of the degree of a random graph follows a normal distribution as the connections are made randomly between the nodes [92]. The clustering coefficient of random graphs is much smaller compared to that of scale-free and small-world networks. On the other hand, the small-world network is highly clustered yet comprises a smaller characteristic path length compared to random networks [44]. Small-world networks maintain a balance between network segregation and integration, providing a high global and local efficiency of information transfer between nodes of a network [39]. In scale free networks, the nodes are connected in a way that there are few nodes which have very many connections, and many nodes which have few connections [92] implying low efficiency. This is in contrast to with small-world networks where the efficiency is comparatively high, supporting high information transfer between the nodes. On the other hand, the low efficiency of the scale free networks will give the impression of mostly unconnected network structures as well [93]. Although this characterization among the network structures is common, in relation to brain dynamics, a brain network can also be characterized with respect to its regional anatomical connectivity.

4.3. Types of Topological Connectivity. Topological connectivity of the brain may characterize different features of dynamic organization. This organization can be expressed by weighted or unweighted graphs. In weighted graphs, nodes represent the regions of interest and edges encode the strength of their correlation (functional) or the density of the fibers connecting them (anatomical) [94], while in unweighted graphs edges only represent the presence of connectivity exceeding a specific threshold. However, this binarization does not provide any information on important differences between weak and strong connections. For specific metrics such as the characteristic path length, the strength of connection is critical for interpretation since it determines the functional distance of connectivity, which is important to characterize long-distance shortcuts. By comparing functional and anatomical connectivity, a broader understanding of the way the brain functions with respect to its structural connectivity can be gained.

4.3.1. Anatomical Connectivity. Anatomical/Structural connectivity between cortical regions of the brain is represented by the connections of axonal fibers. It ranges from inter-neuronal connectivity to inter-regional connectivity in the brain [10]. In MRI analysis, the anatomical connectivity is being tracked using DTI data. Graph theory offers a quantitative description of the anatomical patterns by producing a graph for the anatomical network of the brain. Mapping the anatomical connections of the human brain using graph theory has revealed small-world attributes with local clusters of brain regions [10]. This pattern of finding indicates that the structural organization of the brain demonstrates the most efficient type of network.

4.3.2. Functional Connectivity. Although studying the anatomical connections of the brain allows us to understand the basic structural connectivity throughout the brain, investigating the functional connectivity provides us the knowledge of how this structural architecture relates to brain function. However, functional connectivity is based on statistical computations representing only correlations between nodes exceeding a specific threshold [31, 94]. In fMRI analysis, functional connectivity is analyzed using the BOLD signals. Therefore, functional connectivity emphasizes highly functionally correlated regions. As a result of that, the network can be presented as a fully connected graph among functionally active regions [94]. Thus, measure of efficiency of a network is always a relative quantity dependent on the graphical analysis itself and the choice of threshold.

4.3.3. Effective Connectivity. Effective connectivity refers to the effect that one neural system or element influences another neural system or element [10, 31]. Using effective connectivity, the causal interactions between the elements of the network can be better understood. In this case, a directed graph can be generated to represent the effective connectivity between multiple regions of the brain network [10]. Applying directed graphs is a more sophisticated approach since it also provides information about the direction of connectivity. However, this adds statistically relevant issues when computing fMRI data because temporal aspects of interaction have to be considered which are problematic when measuring the BOLD signal (for further discussion, see [95–98]).

4.4. Neurobiological Implications of Graph Theory

4.4.1. The Network Properties in Ising Model and the Brain Network. Studying network properties in graph theory allows a comparison of networks using Ising model data and empirical fMRI data. An important measure in this comparison is the distribution of the degree for the two types of data sets, along with the distribution of the correlation. This will provide the basis to compare the functional behaviour of the brain network in resting state with the critical phenomena of the Ising model.

After calculating, for each given temperature, configurations of the 2D Ising model at a chosen number of time points, a correlation matrix can be extracted and compared with the correlation of the empirical data from the resting brain (Figure 5). In Figure 5(a), the correlation distribution of empirical and simulated data is showing an important similarity when the Ising model is simulated at the critical temperature. Figure 5(b) represents the degree distribution for the graphs generated by the corresponding correlation matrices after setting a threshold to zero (using the Brain Connectivity Toolbox [86]). Beyond the critical temperature, the correlation of the simulated data tends to go to zero. At the critical temperature, the 2D Ising model, which does not assess the quality or quantity of information processing, is reflecting the distribution of correlation values of experimental data relevant to brain dynamics [28]. In addition, the distribution of the degree for the 2D Ising model at the critical

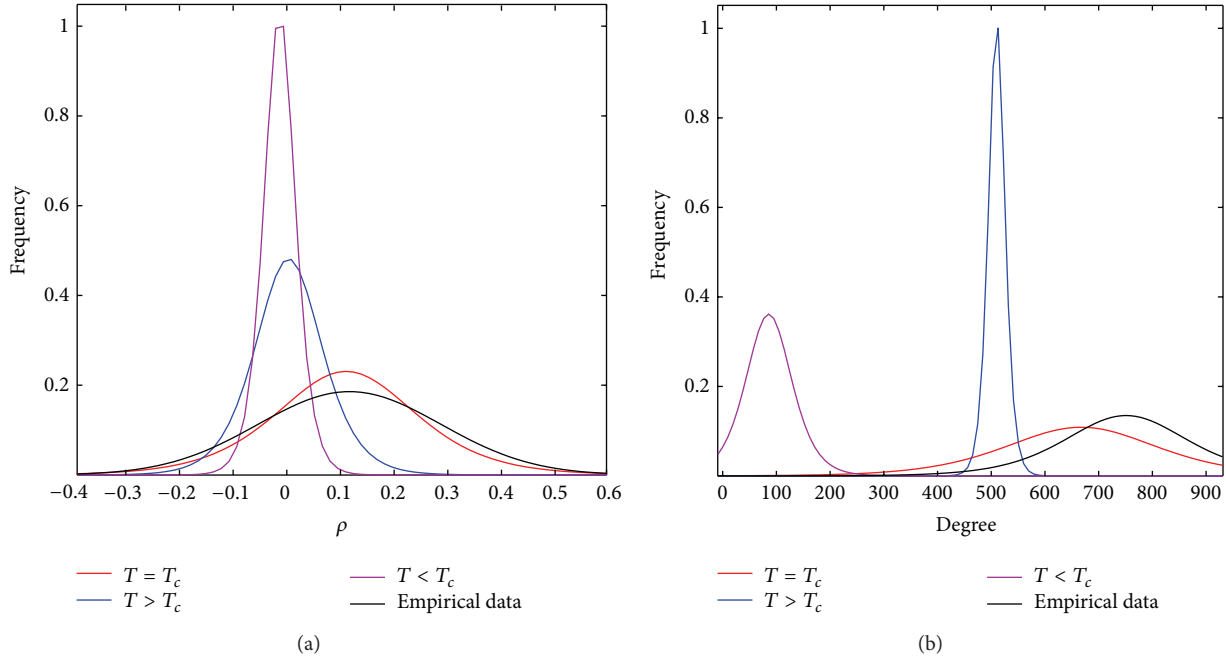


FIGURE 5: (a) shows the correlation values (ρ) distribution for three different simulations of the 2D Ising model at $T < T_c$, $T = T_c$, and $T > T_c$ together with the empirical data from resting state fMRI. (b) shows the degree distribution of the graphs obtained from the corresponding correlation matrices after setting a threshold equal to zero.

temperature follows a similar behavior as the experimental data. At temperatures below the critical temperature, the average degree is found at a smaller value compared to that of the resting fMRI degree distribution, which implies lower functional connectivity of the nodes in the Ising model.

The brain network follows small-world behaviour with higher efficiency and a higher clustering coefficient with respect to random or scale-free networks [84]. Moreover, it has shorter average path lengths and most of the connections are made among the neighbouring nodes, while few long-range connections are made in order to create short cuts. In the case of the Ising model, the variation of the degree distribution along with the temperature, allows extraction of valuable information about the network. Below the critical temperature the degree of connectivity of most nodes lies around 10% of the highest possible degree while at higher temperatures it is around 50% of the highest possible degree. These two cases, sub- and supercritical regimes, show a low efficiency in the network, suggesting that the critical behavior for the Ising model is predicting the highest information transfer in accordance with the resting brain data. As the brain network shows small-world network behaviour with lower characteristic path length and higher clustering coefficients in controls, under pathological or pharmacological conditions these properties could be altered depending on the structural or functional modulations of the network.

To understand the structural organization of the brain network and its functional interaction, research has focused on brain alterations. Patients with severe brain injury are especially interesting to investigate, as alterations in structural connectivity can be isolated and compared to loss of

function to further explore the relationship between structural and functional connectivity. Moreover, severe brain injury is characterized by a large-scale network disconnection which is the prime mechanism for the underlying cognitive impairment [99]. A prominent impairment in patients with severe brain injury is altered consciousness. In severe chronic states this is defined as disorders of consciousness (DOC) and comprises coma, vegetative state/unresponsive wakeful syndrome (VS/UWS), minimally consciousness states (MCS), and locked-in syndrome (LIS) [100]. In the presence of severe brain injury, the structure of the brain network can be crucially affected. This may lead to a disruption in the functional connectivity of the brain network, which can be captured by their graphical properties [101]. It has been observed by Crone et al. [91] that the functional brain networks of patients with DOC demonstrate a higher clustering coefficient compared to random networks, but a similar characteristic path length, which verifies the small-world attributes in both healthy controls as well as patients with DOC. In comparison to healthy subjects though, the patients show reduced modularity at the global level that implies a shift in the ratio of the connection density within and between clusters. This indicates a disturbance in the optimal balance between integration and segregation.

Altered states of consciousness can also be observed without changes in the structural connectivity as induced, for example, by the anesthetic propofol. In anesthesia-induced loss of consciousness, functional connectivity is disturbed while the structural connectivity is preserved. In respect to graph theory, this can be interpreted as a decrement of the number of functional connections. Graph theoretical

analyses revealed significant changes in the distribution of degree and local functional organizations of brain networks during propofol-induced loss of consciousness [102]. Recently, Monti et al. investigated the increase in clustering and characteristic path length and the decrease in efficiency of global information flow in propofol-induced unconscious brain networks, compared to wakefulness, mild-sedation, and recovery states of the brain [103]. In their studies, loss of consciousness in the sedation state was characterized as the result of increasing the segregation effect in functional brain organizations.

5. Conclusions and Discussion

Throughout this paper, we have reviewed the structure-function relationship in the brain network with recent ongoing analyses, focusing on the Ising model and graph theory. The Ising model together with graph theory proved to be effective approaches to studying brain dynamics. In particular, the Ising model is involved in characterizing the emergent properties of functional network organizations at the critical temperature and the changes in organization when temperature is departing from its critical value. Three significant temperature values are taken into account as the critical, subcritical, and supercritical temperatures. Much of the earlier efforts have compared brain dynamics with the behaviour of self-organized criticality at the critical point of the Ising model. However, the recent finding of characterising brain dynamics in the Griffith phase has started diminishing the hallmark of self-organized criticality in brain networks, unless the network becomes highly efficient and optimized [104]. Their analyses provide the opportunity to look into the behaviour of functional networks based on Ising model simulation in subcritical and supercritical temperature regions in order to understand the macroscopic brain mechanisms. On the other hand, graph theory has been providing another platform to characterize the structural and functional connectivity of the brain. Underpinning results of graph theoretical metrics reveal that the brain network follows a small-world behaviour with a high efficiency and low wiring cost [54, 84]. Furthermore, graph theoretical measures provide additional understanding about the information transfer among the nodes of the Ising model at the critical temperature and in the sub- and supercritical regimes.

The brain is one of the most complex networks in nature due to its sophisticated structure-function relationships. Understanding the optimized information processing and transfer in its cortical networks is the prime focus of much current neuroscience research. With recent advancements in neuroimaging techniques like fMRI (with high spatial resolution), EEG, and MEG (with high temporal resolution), any functional activity based measurements could quantify global correlation patterns in wakeful resting brains [5] or altered states of consciousness as induced by anaesthesia or severe brain injury [33]. Current neuroimaging techniques enable us to explore multiple functional networks within the resting brain with resolution of the order of 10^5 neurons in a cubic millimeter of neuronal tissue [105]. With this in mind, neuroimaging studies are limited in their characterization

of individuals' functionality within any correlated network. However, several of the macroscopic brain phenomena, for example, consciousness, mind, human cognition, global information processing, have recently been investigated in the resting brain with multidimensional analyses of the brain organization in various spatial and temporal scales. With the aid of mean field theory, the functional connectivity of these networks has also been compared with the simulated self-organized criticality of the Ising model in absence/presence of anatomical connectivity.

Nowadays, multimodal neuroimaging is applied to patients with DOC in order to find diagnostic tools [106]. In Figure 6, DTI, fMRI, and FDG-PET are presented for a patient in vegetative state (VS/UWS) and a patient in minimally conscious state (MCS) together with a healthy subject [107]. While the resting-state fMRI and FDG-PET images present a functionally preserved right hemisphere for both patients, DTI shows underlying differences in structural connectivity. In VS and MCS patients, these neuroimaging methods complement each other to provide information of structural and functional connectivity. In recent years, DOC, which could be a result of impaired regulation of arousal and awareness due to connectivity disruptions among different anatomical brain regions [108], have been extensively studied [103, 109, 110]. Their findings highlighted the strong dependency of structure and function in brain networks. Applications of structural and functional neuroimaging, together with computational modeling like the Ising model may allow accessing the spatiotemporal organization of the resting brain and its possible reorganization or disruption in altered states of consciousness.

A recent review also highlighted the fact that structural brain damage after traumatic brain injury (TBI) could disrupt the functional activity of large-scale intrinsic connectivity networks as well as interactions of the damaged structure with neuroinflammation and neurodegeneration as in Alzheimer disease and chronic traumatic encephalopathy [99]. Traumatic focal brain injury may disconnect large-scale brain networks that might result in network dysfunction and cognitive impairment. Their investigations on structural and functional integrity within intrinsic connectivity networks may help to improve diagnosis at the individual network level and clinical treatment in future research. However, the difficulty of accessing long-term human brain data after TBI constrains current studies of DOC, which are mostly treated on the basis of "trial" and "error." In patients with TBI, diffuse axonal injury may damage structural network connectivity via white matter fibers, which is difficult to investigate through the current tractography technique [111, 112]. This demands the necessity of studying computational models that may help to understand in vivo structure-function relations as well as neuronal intercommunication in large scale brain networks [10].

Graph theory is a useful tool for understanding the organization of brain networks in different spatial and temporal scales. In the healthy brain during rest, the organization within and between RSNs demonstrates small-world features which maximize the information transfer by a relative low level of wiring cost [10]. Together with findings from Ising

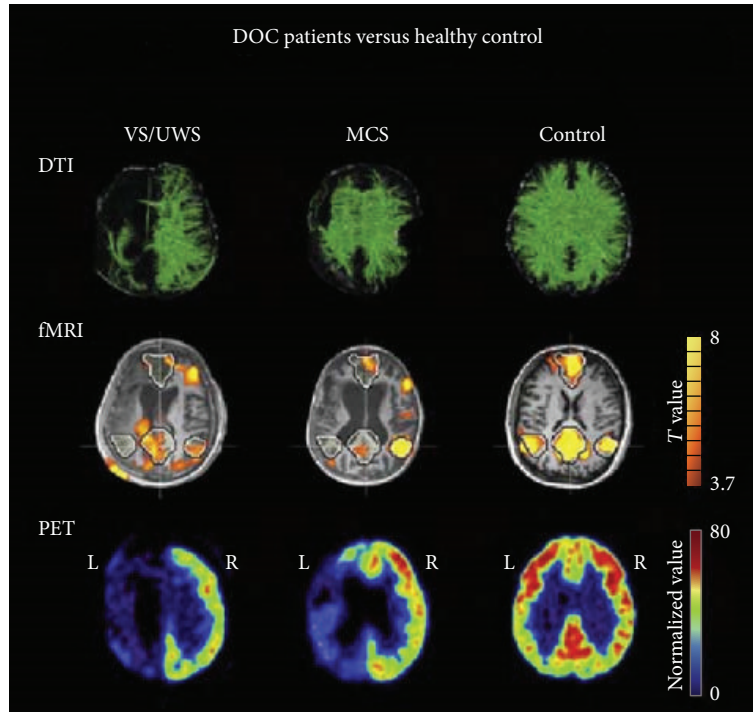


FIGURE 6: Diffusion tensor imaging, default mode network as extracted from resting state functional magnetic resonance imaging and 18F-fluorodeoxyglucose positron emission tomography in a vegetative patient, a minimally conscious patient, and a healthy control. This figure was modified by Bruno et al. [107].

model simulations explaining the self-organized criticality of brain dynamics, graph theory has opened the door to understand specific properties of organization among these self-organized functional modules [8]. This knowledge can now be used to explore neurobiological mechanisms of the brain network and its alterations in pathological or pharmacological states to better understand how brain phenomena such as cognition or consciousness emerge [1]. This knowledge can then be used to improve innovative biomarkers for the diagnosis and prognosis of disease.

Conflict of Interests

The authors declare that there is no conflict of interests regarding the publication of this paper.

Acknowledgments

This work was supported by the Canada Excellence Research Chair (CERC), the James McDonnell Foundation (JMF) programs (AMO), and a discovery grant (AS) from the Natural Sciences and Engineering Research Council (NSERC). Authors would like to thank Erik Ziegler for producing the fibers' skeleton of the DMN of Figure 1.

References

- [1] O. Sporns, "Contributions and challenges for network models in cognitive neuroscience," *Nature Neuroscience*, vol. 17, pp. 652–660, 2014.
- [2] M. D. Greicius, B. Krasnow, A. L. Reiss, and V. Menon, "Functional connectivity in the resting brain: a network analysis of the default mode hypothesis," *Proceedings of the National Academy of Sciences of the United States of America*, vol. 100, no. 1, pp. 253–258, 2003.
- [3] B. B. Biswal, "Resting state fMRI: a personal history," *NeuroImage*, vol. 62, no. 2, pp. 938–944, 2012.
- [4] M. P. van den Heuvel and H. E. Hulshoff Pol, "Exploring the brain network: a review on resting-state fMRI functional connectivity," *European Neuropsychopharmacology*, vol. 20, no. 8, pp. 519–534, 2010.
- [5] M. D. Greicius, K. Supekar, V. Menon, and R. F. Dougherty, "Resting-state functional connectivity reflects structural connectivity in the default mode network," *Cerebral Cortex*, vol. 19, no. 1, pp. 72–78, 2009.
- [6] D. M. Cole, S. M. Smith, and C. F. Beckmann, "Advances and pitfalls in the analysis and interpretation of resting-state FMRI data," *Frontiers in Systems Neuroscience*, vol. 4, p. 8, 2010.
- [7] Y. Liu, M. Liang, Y. Zhou et al., "Disrupted small-world networks in schizophrenia," *Brain*, vol. 131, no. 4, pp. 945–961, 2008.
- [8] O. Sporns, *Networks of the Brain*, MIT Press, Boston, Mass, USA, 2011.
- [9] C. R. Noback, N. L. Strominger, R. J. Demarest, and D. A. Ruggiero, *The Human Nervous System: Structure and Function*, Springer, New York, NY, USA, 2005.
- [10] E. Bullmore and O. Sporns, "Complex brain networks: graph theoretical analysis of structural and functional systems," *Nature Reviews Neuroscience*, vol. 10, no. 3, pp. 186–198, 2009.
- [11] A. L. Hodgkin and A. F. Huxley, "A quantitative description of membrane current and its application to conduction and

- excitation in nerve," *The Journal of Physiology*, vol. 117, no. 4, pp. 500–544, 1952.
- [12] D. J. Amit, *Modeling Brain Function: The World of Attractor Neural Networks*, Cambridge University Press, 1992.
- [13] J. S. Kelso, *Dynamic Patterns: The Self-Organization of Brain and Behavior*, MIT Press, 1995.
- [14] E. M. Izhikevich, *Dynamical Systems in Neuroscience*, The MIT Press, Boston, Mass, USA, 2007.
- [15] M. Ozer, M. Perc, and M. Uzuntarla, "Controlling the spontaneous spiking regularity via channel blocking on Newman-Watts networks of Hodgkin-Huxley neurons," *EPL*, vol. 86, no. 4, Article ID 40008, 2009.
- [16] M. Breakspear, S. Heitmann, and A. Daffertshofer, "Generative models of cortical oscillations: neurobiological implications of the Kuramoto model," *Frontiers in Human Neuroscience*, vol. 4, article 190, 2010.
- [17] M. D. Fox and M. E. Raichle, "Spontaneous fluctuations in brain activity observed with functional magnetic resonance imaging," *Nature Reviews Neuroscience*, vol. 8, no. 9, pp. 700–711, 2007.
- [18] D. R. Chialvo, "Emergent complex neural dynamics," *Nature Physics*, vol. 6, no. 10, pp. 744–750, 2010.
- [19] J. Cabral, E. Hugues, O. Sporns, and G. Deco, "Role of local network oscillations in resting-state functional connectivity," *NeuroImage*, vol. 57, no. 1, pp. 130–139, 2011.
- [20] G. Deco, V. K. Jirsa, and A. R. McIntosh, "Emerging concepts for the dynamical organization of resting-state activity in the brain," *Nature Reviews Neuroscience*, vol. 12, no. 1, pp. 43–56, 2011.
- [21] C. J. Honey, O. Sporns, L. Cammoun et al., "Predicting human resting-state functional connectivity from structural connectivity," *Proceedings of the National Academy of Sciences of the United States of America*, vol. 106, no. 6, pp. 2035–2040, 2009.
- [22] J. Cabral, E. Hugues, M. L. Kringselbach, and G. Deco, "Modeling the outcome of structural disconnection on resting-state functional connectivity," *NeuroImage*, vol. 62, no. 3, pp. 1342–1353, 2012.
- [23] E. Ziegler, A. Foret, L. Mascetti et al., "Altered white matter architecture in BDNF Met carriers," *PLoS ONE*, vol. 8, no. 7, Article ID e69290, 2013.
- [24] D. R. Chialvo, "Critical brain networks," *Physica A: Statistical Mechanics and Its Applications*, vol. 340, no. 4, pp. 756–765, 2004.
- [25] A. Levina, J. M. Herrmann, and T. Geisel, "Dynamical synapses causing self-organized criticality in neural networks," *Nature Physics*, vol. 3, no. 12, pp. 857–860, 2007.
- [26] A. Haimovici, E. Tagliazucchi, P. Balenzuela, and D. R. Chialvo, "Brain organization into resting state networks emerges at criticality on a model of the human connectome," *Physical Review Letters*, vol. 110, no. 17, Article ID 178101, 2013.
- [27] D. R. Chialvo, P. Balenzuela, and D. Fraiman, "The brain: what is critical about it?" *American Institute of Physics Conference Proceedings*, vol. 1028, pp. 28–45, 2008.
- [28] D. Fraiman, P. Balenzuela, J. Foss, and D. R. Chialvo, "Ising-like dynamics in large-scale functional brain networks," *Physical Review E*, vol. 79, no. 6, Article ID 061922, 2009.
- [29] S. Istrail, "Statistical mechanics, three-dimensionality and NP-completeness. I. Universality of intractability for the partition function of the ISIng model across non-planar surfaces (extended abstract)," in *Proceedings of the 32nd Annual ACM Symposium on Theory of Computing*, pp. 87–96, ACM, New York, NY, USA.
- [30] J. M. Beggs and N. Timme, "Being critical of criticality in the brain," *Frontiers in Physiology*, vol. 3, article 163, 2012.
- [31] K. J. Friston, "Functional and effective connectivity: a review," *Brain Connectivity*, vol. 1, no. 1, pp. 13–36, 2011.
- [32] D. Marinazzo, M. Pellicoro, and S. Stramaglia, "Information transfer of an Ising model on a brain network," *BMC Neuroscience*, vol. 14, article P376, supplement 1, 2013.
- [33] L. Heine, A. Soddu, F. Gómez et al., "Resting state networks and consciousness: alterations of multiple resting state network connectivity in physiological, pharmacological, and pathological consciousness states," *Frontiers in Psychology*, vol. 3, Article ID Article 295, 2012.
- [34] C. J. Honey, R. Kötter, M. Breakspear, and O. Sporns, "Network structure of cerebral cortex shapes functional connectivity on multiple time scales," *Proceedings of the National Academy of Sciences of the United States of America*, vol. 104, no. 24, pp. 10240–10245, 2007.
- [35] R. Almeida and M. Stetter, "Modeling the link between functional imaging and neuronal activity: synaptic metabolic demand and spike rates," *NeuroImage*, vol. 17, no. 2, pp. 1065–1079, 2002.
- [36] J. Scholz, M. C. Klein, T. E. J. Behrens, and H. Johansen-Berg, "Training induces changes in white-matter architecture," *Nature Neuroscience*, vol. 12, no. 11, pp. 1370–1371, 2009.
- [37] M. E. Raichle, "A paradigm shift in functional brain imaging," *The Journal of Neuroscience*, vol. 29, no. 41, pp. 12729–12734, 2009.
- [38] P. Hagmann, O. Sporns, N. Madan et al., "White matter maturation reshapes structural connectivity in the late developing human brain," *Proceedings of the National Academy of Sciences of the United States of America*, vol. 107, no. 44, pp. 19067–19072, 2010.
- [39] E. T. Bullmore and D. S. Bassett, "Brain graphs: graphical models of the human brain connectome," *Annual Review of Clinical Psychology*, vol. 7, pp. 113–140, 2011.
- [40] B. Horwitz, "The elusive concept of brain connectivity," *NeuroImage*, vol. 19, no. 2, pp. 466–470, 2003.
- [41] G. Gong, Y. He, L. Concha et al., "Mapping anatomical connectivity patterns of human cerebral cortex using in vivo diffusion tensor imaging tractography," *Cerebral Cortex*, vol. 19, no. 3, pp. 524–536, 2009.
- [42] Y. He, Z. J. Chen, and A. C. Evans, "Small-world anatomical networks in the human brain revealed by cortical thickness from MRI," *Cerebral Cortex*, vol. 17, no. 10, pp. 2407–2419, 2007.
- [43] Z. J. Chen, Y. He, P. Rosa-Neto, J. Germann, and A. C. Evans, "Revealing modular architecture of human brain structural networks by using cortical thickness from MRI," *Cerebral Cortex*, vol. 18, no. 10, pp. 2374–2381, 2008.
- [44] D. J. Watts and S. H. Strogatz, "Collective dynamics of "small-world" networks," *Nature*, vol. 393, no. 6684, pp. 440–442, 1998.
- [45] O. Sporns, "The non-random brain: efficiency, economy, and complex dynamics," *Frontiers in Computational Neuroscience*, vol. 5, article 5, 2011.
- [46] J. Alstott, M. Breakspear, P. Hagmann, L. Cammoun, and O. Sporns, "Modeling the impact of lesions in the human brain," *PLoS Computational Biology*, vol. 5, no. 6, Article ID e1000408, 2009.
- [47] C. J. Honey and O. Sporns, "Dynamical consequences of lesions in cortical networks," *Human Brain Mapping*, vol. 29, no. 7, pp. 802–809, 2008.

- [48] T. Binzegger, R. J. Douglas, and K. A. Martin, "A quantitative map of the circuit of cat primary visual cortex," *The Journal of Neuroscience*, vol. 24, no. 39, pp. 8441–8453, 2004.
- [49] S. J. Schiff, *Neural Control Engineering: The Emerging Intersection between Control Theory and Neuroscience*, MIT Press, Boston, Mass, USA, 2012.
- [50] J. Schmahmann, "The primary motor cerebellum is in the anterior lobe but not the posterior lobe. Evidence from stroke patients," in *Neurology*, Lippincott Williams & Wilkins, Philadelphia, Pa, USA, 2007.
- [51] D. A. Fair, A. L. Cohen, N. U. F. Dosenbach et al., "The maturing architecture of the brain's default network," *Proceedings of the National Academy of Sciences of the United States of America*, vol. 105, no. 10, pp. 4028–4032, 2008.
- [52] S. M. Nelson, A. L. Cohen, J. D. Power et al., "A parcellation scheme for human left lateral parietal cortex," *Neuron*, vol. 67, no. 1, pp. 156–170, 2010.
- [53] G. Buzsáki, "Large-scale recording of neuronal ensembles," *Nature Neuroscience*, vol. 7, no. 5, pp. 446–451, 2004.
- [54] E. Bullmore and O. Sporns, "The economy of brain network organization," *Nature Reviews Neuroscience*, vol. 13, no. 5, pp. 336–349, 2012.
- [55] P. Boveroux, A. Vanhaudenhuyse, M. Bruno et al., "Breakdown of within- and between-network resting state functional magnetic resonance imaging connectivity during propofol-induced loss of consciousness," *Anesthesiology*, vol. 113, no. 5, pp. 1038–1053, 2010.
- [56] J. L. Vincent, G. H. Patel, M. D. Fox et al., "Intrinsic functional architecture in the anaesthetized monkey brain," *Nature*, vol. 447, no. 7140, pp. 83–86, 2007.
- [57] M. M. Monti, "Dynamic change of global and local information processing in propofol-induced loss and recovery of consciousness," *PLoS Computational Biology*, vol. 9, no. 10, Article ID e1003271, 2013.
- [58] P. Guldenmund, A. Demertzi, P. Boveroux et al., "Thalamus, brainstem and salience network connectivity changes during propofol-induced sedation and unconsciousness," *Brain connectivity*, vol. 3, no. 3, pp. 273–285, 2013.
- [59] M. Tschernegg, J. S. Crone, T. Eigenberger et al., "Abnormalities of functional brain networks in pathological gambling: a graph-theoretical approach," *Frontiers in Human Neuroscience*, vol. 7, article 625, 2013.
- [60] O. Sporns, "Structure and function of complex brain networks," *Dialogues in Clinical Neuroscience*, vol. 15, no. 3, pp. 247–262, 2013.
- [61] G. Werner, "Metastability, criticality and phase transitions in brain and its models," *BioSystems*, vol. 90, no. 2, pp. 496–508, 2007.
- [62] S. G. Brush, "History of the Lenz-Ising model," *Reviews of Modern Physics*, vol. 39, no. 4, pp. 883–893, 1967.
- [63] L. Onsager, "Crystal statistics. I. A two-dimensional model with an order-disorder transition," *Physical Review*, vol. 65, article 117, 1944.
- [64] M. G. Kitzbichler, M. L. Smith, S. R. Christensen, and E. Bullmore, "Broadband criticality of human brain network synchronization," *PLoS Computational Biology*, vol. 5, no. 3, Article ID e1000314, 2009.
- [65] L. E. Reichl and I. Prigogine, *A Modern Course in Statistical Physics*, vol. 71, University of Texas Press, 1980.
- [66] D. P. Landau and K. Binder, *A Guide to Monte Carlo Simulations in Statistical Physics*, Cambridge University Press, Cambridge, 3rd edition, 2009.
- [67] B. Fischl, "FreeSurfer," *NeuroImage*, vol. 62, no. 2, pp. 774–781, 2012.
- [68] H. B. Barlow, "Single units and sensation: a neuron doctrine for perceptual psychology?" *Perception*, vol. 1, no. 4, pp. 371–394, 1972.
- [69] C. Koch, *Biophysics of Computation: Information Processing in Single Neurons*, Oxford University Press, 2004.
- [70] E. Schneidman, M. J. Berry II, R. Segev, and W. Bialek, "Weak pairwise correlations imply strongly correlated network states in a neural population," *Nature*, vol. 440, no. 7087, pp. 1007–1012, 2006.
- [71] J. J. Hopfield, "Neural networks and physical systems with emergent collective computational abilities," *Proceedings of the National Academy of Sciences of the United States of America*, vol. 79, no. 8, pp. 2554–2558, 1982.
- [72] R. Kozma, M. Puljic, and W. J. Freeman, "Thermodynamic model of criticality in the cortex based on EEG/ECOG data," *Criticality in Neural Systems*, 2014.
- [73] S. Yu, H. Yang, O. Shriki, and D. Plenz, "Universal organization of resting brain activity at the thermodynamic critical point," *Frontiers in Systems Neuroscience*, vol. 7, article 42, 2013.
- [74] S. N. Dorogovtsev and J. F. F. Mendes, *Evolution of Networks: From Biological Nets to the Internet and WWW*, Oxford University Press, Oxford, UK, 2013.
- [75] H. G. Schuster, D. Plenz, and E. Niebur, *Criticality in Neural Systems*, John Wiley & Sons, 2014.
- [76] J. A. Scott Kelso, "Multistability and metastability: understanding dynamic coordination in the brain," *Philosophical Transactions of the Royal Society B: Biological Sciences*, vol. 367, no. 1591, pp. 906–918, 2012.
- [77] J. Hidalgo, J. Grilli, S. Suweis, M. A. Munoz, J. R. Banavar, and A. Maritan, "Emergence of criticality in living systems through adaptation and evolution: practice makes critical," 2013, <http://arxiv.org/abs/1307.4325>.
- [78] T. Froese, A. Woodward, and T. Ikegami, "Turing instabilities in biology, culture, and consciousness? On the enactive origins of symbolic material culture," *Adaptive Behavior*, vol. 21, no. 3, pp. 199–214, 2013.
- [79] M. I. Rabinovich, V. S. Afraimovich, C. Bick, and P. Varona, "Information flow dynamics in the brain," *Physics of Life Reviews*, vol. 9, no. 1, pp. 51–73, 2012.
- [80] J. S. Kelso and E. Tognoli, "Toward a complementary neuroscience: metastable coordination dynamics of the brain," in *Downward Causation and the Neurobiology of Free Will*, pp. 103–124, Springer, 2009.
- [81] G. Deco and M. Corbetta, "The dynamical balance of the brain at rest," *The Neuroscientist*, vol. 17, no. 1, pp. 107–123, 2011.
- [82] B. C. M. van Wijk, C. J. Stam, and A. Daffertshofer, "Comparing brain networks of different size and connectivity density using graph theory," *PLoS ONE*, vol. 5, no. 10, Article ID e13701, 2010.
- [83] H.-J. Park and K. Friston, "Structural and functional brain networks: from connections to cognition," *Science*, vol. 342, no. 6158, Article ID 1238411, 2013.
- [84] K. Supekar, V. Menon, D. Rubin, M. Musen, and M. D. Greicius, "Network analysis of intrinsic functional brain connectivity in Alzheimer's disease," *PLoS Computational Biology*, vol. 4, no. 6, Article ID e1000100, 2008.
- [85] O. Sporns and J. D. Zwi, "The small world of the cerebral cortex," *Neuroinformatics*, vol. 2, no. 2, pp. 145–162, 2004.
- [86] M. Rubinov and O. Sporns, "Complex network measures of brain connectivity: uses and interpretations," *NeuroImage*, vol. 52, no. 3, pp. 1059–1069, 2010.

- [87] S. H. Strogatz, "Exploring complex networks," *Nature*, vol. 410, no. 6825, pp. 268–276, 2001.
- [88] S. Achard and E. Bullmore, "Efficiency and cost of economical brain functional networks," *PLoS Computational Biology*, vol. 3, no. 2, p. e17, 2007.
- [89] V. Latora and M. Marchiori, "Efficient behavior of small-world networks," *Physical Review Letters*, vol. 87, no. 19, Article ID 198701, 2001.
- [90] V. Latora and M. Marchiori, "Economic small-world behavior in weighted networks," *The European Physical Journal B :Condensed Matter and Complex Systems*, vol. 32, no. 2, pp. 249–263, 2003.
- [91] J. Sophia Crone, A. Soddu, Y. Höller et al., "Altered network properties of the fronto-parietal network and the thalamus in impaired consciousness," *NeuroImage: Clinical*, vol. 4, pp. 240–248, 2014.
- [92] O. Sporns and R. Kötter, "Motifs in brain networks," *PLoS Biology*, vol. 2, no. 11, article e369, 2004.
- [93] P. Crucittia, V. Latorab, M. Marchioric, and A. Rapisarda, "Efficiency of scale-free networks: error and attack tolerance," *Physica A*, vol. 320, pp. 622–642, 2003.
- [94] B. Alper, B. Bach, N. H. Riche, T. Isenberg, and J. Fekete, "Weighted graph comparison techniques for brain connectivity analysis," in *Proceedings of the SIGCHI Conference on Human Factors in Computing Systems (CHI '13)*, pp. 483–492, May 2013.
- [95] A. Roebroek, E. Formisano, and R. Goebel, "The identification of interacting networks in the brain using fMRI: model selection, causality and deconvolution," *NeuroImage*, vol. 58, no. 2, pp. 296–302, 2011.
- [96] W. D. Penny, K. E. Stephan, A. Mechelli, and K. J. Friston, "Modelling functional integration: a comparison of structural equation and dynamic causal models," *NeuroImage*, vol. 23, no. 1, pp. S264–S274, 2004.
- [97] K. Friston, "Causal modelling and brain connectivity in functional magnetic resonance imaging," *PLoS Biology*, vol. 7, no. 2, Article ID e1000033, 2009.
- [98] K. Friston, "Dynamic causal modeling and granger causality comments on: the identification of interacting networks in the brain using fMRI: model selection, causality and deconvolution," *NeuroImage*, vol. 58, no. 2, pp. 303–305, 2011.
- [99] D. J. Sharp, G. Scott, and R. Leech, "Network dysfunction after traumatic brain injury," *Nature Reviews Neurology*, vol. 10, pp. 156–166, 2014.
- [100] S. Laureys, A. M. Owen, and N. D. Schiff, "Brain function in coma, vegetative state, and related disorders," *The Lancet Neurology*, vol. 3, no. 9, pp. 537–546, 2004.
- [101] A. Soddu, A. Vanhauzenhuysse, M. A. Bahri et al., "Identifying the default-mode component in spatial IC analyses of patients with disorders of consciousness," *Human Brain Mapping*, vol. 33, no. 4, pp. 778–796, 2012.
- [102] M. S. Schröter, V. I. Spoormaker, A. Schorer et al., "Spatiotemporal reconfiguration of large-scale brain functional networks during propofol-induced loss of consciousness," *The Journal of Neuroscience*, vol. 32, no. 37, pp. 12832–12840, 2012.
- [103] M. M. Monti, A. Vanhauzenhuysse, M. R. Coleman et al., "Willful modulation of brain activity in disorders of consciousness," *The New England Journal of Medicine*, vol. 362, no. 7, pp. 579–589, 2010.
- [104] P. Moretti, M. A. Mu, and M. A. Muñoz, "Griffiths phases and the stretching of criticality in brain networks," *Nature Communications*, vol. 4, Article ID 2521, 2013.
- [105] A. L. Roskies, "Brain-mind and structure-function relationships: a methodological response to coltheart," *Philosophy of Science*, vol. 76, no. 5, pp. 927–939, 2010.
- [106] A. Demertzi, F. Gómez, J. S. Crone et al., "Multiple fMRI system-level baseline connectivity is disrupted in patients with consciousness alterations," *Cortex*, vol. 52, pp. 35–46, 2014.
- [107] M. A. Bruno, D. Fernández-Espejo, R. Lehenbre et al., "Multimodal neuroimaging in patients with disorders of consciousness showing "functional hemispherectomy""", *Progress in Brain Research*, vol. 193, pp. 323–333, 2011.
- [108] A. Soddu, A. Vanhauzenhuysse, A. Demertzi et al., "Resting state activity in patients with disorders of consciousness," *Functional Neurology*, vol. 26, no. 1, pp. 37–43, 2011.
- [109] A. M. Owen and M. R. Coleman, "Functional MRI in disorders of consciousness: advantages and limitations," *Current Opinion in Neurology*, vol. 20, no. 6, pp. 632–637, 2007.
- [110] J. T. Giacino, J. J. Fins, S. Laureys, and N. D. Schiff, "Disorders of consciousness after acquired brain injury: the state of the science," *Nature Reviews Neurology*, vol. 10, pp. 99–114, 2014.
- [111] R. W. van Boven, G. S. Harrington, D. B. Hackney et al., "Advances in neuroimaging of traumatic brain injury and post-traumatic stress disorder," *Journal of Rehabilitation Research and Development*, vol. 46, no. 6, pp. 717–756, 2009.
- [112] M. Inglese, S. Makani, G. Johnson et al., "Diffuse axonal injury in mild traumatic brain injury: a diffusion tensor imaging study," *Journal of Neurosurgery*, vol. 103, no. 2, pp. 298–303, 2005.

Research Article

Abnormal Functional Resting-State Networks in ADHD: Graph Theory and Pattern Recognition Analysis of fMRI Data

Anderson dos Santos Siqueira,¹ Claudinei Eduardo Biazoli Junior,^{1,2}
William Edgar Comfort,¹ Luis Augusto Rohde,^{3,4} and João Ricardo Sato^{1,2,4}

¹ Center of Mathematics, Computation and Cognition, Universidade Federal do ABC, Avenida dos Estados 5001, 09210-580 Santo Andre, SP, Brazil

² NIF-LIM44, Institute of Radiology, Hospital das Clinicas, University of Sao Paulo, Avenida Dr. Enéas de Carvalho Aguiar, 05403-900 Sao Paulo, SP, Brazil

³ Department of Psychiatry, Federal University of Rio Grande do Sul, Rua Ramiro Barcelos 2350, 90035-903 Porto Alegre, RS, Brazil

⁴ National Institute of Developmental Psychiatry for Children and Adolescents, Brazil

Correspondence should be addressed to João Ricardo Sato; joao.sato@ufabc.edu.br

Received 16 May 2014; Revised 1 August 2014; Accepted 1 August 2014; Published 31 August 2014

Academic Editor: Yihong Yang

Copyright © 2014 Anderson dos Santos Siqueira et al. This is an open access article distributed under the Creative Commons Attribution License, which permits unrestricted use, distribution, and reproduction in any medium, provided the original work is properly cited.

The framework of graph theory provides useful tools for investigating the neural substrates of neuropsychiatric disorders. Graph description measures may be useful as predictor variables in classification procedures. Here, we consider several centrality measures as predictor features in a classification algorithm to identify nodes of resting-state networks containing predictive information that can discriminate between typical developing children and patients with attention-deficit/hyperactivity disorder (ADHD). The prediction was based on a support vector machines classifier. The analyses were performed in a multisite and publicly available resting-state fMRI dataset of healthy children and ADHD patients: the ADHD-200 database. Network centrality measures contained little predictive information for the discrimination between ADHD patients and healthy subjects. However, the classification between inattentive and combined ADHD subtypes was more promising, achieving accuracies higher than 65% (balance between sensitivity and specificity) in some sites. Finally, brain regions were ranked according to the amount of discriminant information and the most relevant were mapped. As hypothesized, we found that brain regions in motor, frontoparietal, and default mode networks contained the most predictive information. We concluded that the functional connectivity estimations are strongly dependent on the sample characteristics. Thus different acquisition protocols and clinical heterogeneity decrease the predictive values of the graph descriptors.

1. Introduction

Attention-deficit/hyperactive disorder (ADHD) is a neurodevelopmental disorder with a prevalence of around 5.3% in children and adolescents [1]. It is characterized by cognitive and behavioral impairments associated with inattention and/or hyperactivity and impulsivity symptoms [2]. The most frequent and investigated ADHD phenotypes are the ones with predominance of inattentive symptoms and a group that combines inattention and hyperactivity/impulsivity. As for most mental disorders, the etiological bases and neural substrates of ADHD are far from being fully understood.

The search for structural or functional neural correlates of ADHD, and consequently for potential biomarkers of the disorder, is crucial in the pursuit of its prevention, early detection and more effective treatment [3, 4]. For this purpose, the combination of machine-learning techniques for pattern recognition and resting-state functional neuroimaging data is a particularly promising approach [5].

Graph theoretical analysis is an emerging component in the field of connectomics and brain network analysis based on neuroimaging data [6, 7]. Descriptors derived from graph theory are measurements quantifying different characteristics of the network organization. When applied to

resting-state fMRI data, graph theoretical measures may be used to enhance the understanding of resting-state network (RSN) dynamics [8]. RSNs are characterized by consistent correlations with the spontaneous fluctuations of the BOLD signal among certain brain regions. Among the diffuse RSNs identified via fMRI analysis, specifically sensory-motor, frontoparietal, basal ganglia, and default mode networks have been implicated in ADHD pathophysiology [9]. Currently, abnormal interactions within distinct RSNs have been identified as a key factor in contributing to various neuropsychiatric disorders [10], in particular within the default mode network (DMN) [11, 12].

Pattern recognition methods based on machine learning techniques have shown to be a promising approach to the analysis of neuroimaging data [13]. Support vector machines (SVMs) [14] are one of the most frequently used methods in this field, given their robust properties when dealing with high dimensional multivariate data in addition to providing predictions for each individual case. In other words, given a set of features (e.g., brain measurements) and a label (e.g., healthy and patient), SVMs are used to learn a function, which maps the set of features to their respective labels within a training dataset. Thus, given a new set of features produced from an unseen observation, SVMs are able to provide a predicted label for this novel observation.

Graph theory descriptors can be used as predictor variables (i.e., features) in a machine-learning framework. Merging graph theoretical approaches and machine learning techniques might provide a better-adjusted way to scrutinize the impairment of RSNs in ADHD as well as mapping predictions to a single individual case. In this study, we investigated the use of network centrality measures as predictive features to discriminate between typical developing children and ADHD patients with both inattentive and combined presentations. In addition, we investigated possible differences between inattentive and combined ADHD groups. The ADHD-200 dataset [15] formed the basis of our analysis. We aimed at evaluating three issues: (i) the mean classification score ($(\text{sensitivity} + \text{specificity})/2$) across distinct acquisition sites; (ii) the classification score site-by-site (i.e., only the data within each site are used to train and test the classifier) with a global classification (i.e., using the data of all sites in a joint analysis); (iii) brain regions (i.e., network nodes) containing the greater amount of predictive information to discriminate between the groups. We hypothesize that frontoparietal, sensory-motor, and default mode network nodes will have a more relevant predictive value in the classification. This hypothesis relies on the potential association between abnormalities in resting-state networks and the main symptoms of ADHD.

2. Materials and Methods

2.1. Data and Image Preprocessing. The publicly available resting-state fMRI data from the ADHD-200 Consortium were used in the present study. The images were acquired at five different sites: Peking University, Kennedy Krieger Institute, NeuroIMAGE sample, New York University Child Study Center, and Oregon Health & Science University

(OHSU). The subject sample consisted of 609 subjects, 340 controls (mean age [standard deviation] – 11.59 [2.86] years; 180 males), and 269 patients with ADHD according to DSM-IV-TR criteria (mean age [s.d.] – 11.58 [2.88] years; 215 males). Among the total number of ADHD patients, 159 fulfilled the criteria for the inattentive type (mean age [s.d.] – 11.24 [3.05] years, 130 males), while 110 were classified as the combined type (mean age [s.d.] – 12.08 [2.55] years, 85 males).

All research protocols from institutes contributing to the ADHD-200 Consortium received local approval by their respective IRB. All the data distributed via the International Neuroimaging Data-sharing Initiative (INDI) are fully anonymized in accordance with HIPAA Privacy Rules. Further details concerning the sample and scanning parameters can be obtained by request to the ADHD-200 Consortium.

Step-wise data preprocessing was previously conducted by the NeuroBureau community using the Athena pipeline and consisted in the systematic and homogeneous processing of all resting-state fMRI data. The following steps were carried out: exclusion of the first four EPI volumes; slice time correction; deobliquity of the dataset; head motion correction using the first volume as a reference; exclusion of voxels in non-brain regions by masking the volumes; averaging the EPI volumes to obtain a mean functional image; coregistration of this mean functional image to the subjects' correspondent anatomical image; spatial transformation of functional data into template space; extraction of BOLD time series from white matter and cerebrospinal fluid using masks obtained from segmenting the structural data; removing trend and motion effects through linear multiple regression; temporal band-pass filtering; spatial smoothing using a Gaussian filter. All preprocessed images are available at the website <http://neurobureau.projects.nitrc.org>.

2.2. Connectivity Analysis and Graphs. A representative set of 400 brain-wide regions of interest (ROIs) was chosen for defining the network nodes used for connectivity analysis and the construction of the graphs. The ROIs were determined by using the method developed by Craddock et al. [16] based on the fMRI data of 650 subjects. This atlas is publicly available at <http://www.nitrc.org/plugins/mwiki/index.php/neurobureau:AthenaPipeline>. The Pearson correlation coefficient between each pair of ROIs was calculated and regarded as a proxy of functional connectivity. The correlation matrix was equated with the adjacency matrix of an undirected and weighted graph. Meanwhile, binary adjacency matrices were built for each subject by applying three different cut-off values (0.1, 0.15 and 0.25) to the correlation matrix. The cut-offs were defined within this particular range since the network becomes too fragmented and granular to allow a proper graph analysis for higher cut-off values [17]. We evaluated the predictive power from both weighted and unweighted graphs. The following centrality measures of the nodes in the weighted graph were calculated: degree, closeness [18], betweenness [19], eigenvector, and Burt's constraint [20]. The degree, closeness, and betweenness were also calculated for the unweighted graphs.

The mathematical definitions of these measures are described in Table 1 where N is the set of all nodes and

TABLE 1

Measure	Definition
Degree (k)	$k_i = \sum_{j \in N} a_{ij}$
Closeness (L^{-1})	$L_i^{-1} = \frac{1}{\sum_{j \in N, j \neq i} d_{ij}}$
Betweenness (b)	$b_i = \frac{1}{(n-1)(n-2)} \sum_{\substack{h, j \in N \\ h \neq j, h \neq i, j \neq i}} \frac{\rho_{hj}(i)}{\rho_{hj}}$
Eigenvector (x)	$x_i = \frac{1}{l} \sum_{j \in N} a_{ij} x_j$
Burt's constraint (C)	$C_i = \sum_{j \in N \setminus \{i\}} \left(a_{ij} + \sum_{q \in N \setminus \{i, j\}} a_{iq} a_{ij} \right)^2$

edges within a network and n is the number of nodes. An edge between two nodes i and j is represented by $a_{i,j}$. In the undirected graph case, $a_{ij} = 1$ if there is a connection between the nodes i and j ; otherwise, $a_{ij} = 0$. In betweenness definition, ρ_{hj} is the number of shortest paths between h and j , and $\rho_{hj}(i)$ is the number of shortest paths between h and j passing through i . In eigenvector definition, l is a constant. Note that eigenvector and Burt's constraint are definable only for weighted graphs.

Degree is a straight and intuitive way to quantify nodes centrality, and it is defined as the number of edges connected to a particular node. The closeness centrality is the average distance between a given node and all other nodes of the network. Betweenness quantifies the influence of a node and is defined as the number of shortest paths passing through it. The basic rationale underlying eigenvector centrality is that connections with more central nodes increase the nodes influence in the network. Hence, different weights are attributed to a vertex depending on the centrality of the connected nodes. Finally, Burt's constraint value is inversely proportional to the number of connections of a node and increases with the number of strong mutual connections [20]. The uses and interpretations of graph theoretical measures in the context of fMRI studies were the central topic in an excellent previous review [7]. All analyses were performed in the *R* platform for Computational Statistics (*R* Project for Statistical Computing) (<http://www.r-project.org/>) using the *R igraph* package.

2.3. Classifier Implementation and Identification of Discriminative ROIs. The centrality measures of each graph's nodes were used as features (i.e., predictor variables) in an independent classification analysis. Classification was performed using a linear support vector machine (SVM) algorithm [14]. The rationale behind SVM is that the determination of the boundary defined by the predictor variables should maximize the separation margin between the two groups to be classified. Accuracy of the classification model was estimated via a leave-one-subject out cross-validation procedure. The classifications were based on the discrimination between typical developing children compared to ADHD patients (both inattentive and combined, and a comparison between the ADHD-inattentive and ADHD-combined types. For each

graph descriptor, two distinct analyses were carried out: (i) an independent site-by-site classification using the data within a single site to train and test the SVM (leave-one-subject-out score) and (ii) a joint analysis concatenating the data strings from all sites into a single classification.

Finally, in order to identify the most discriminative regions, we built brain maps highlighting the 5% brain regions with greater predictive values. We used the approach proposed by Mourão-Miranda et al. [21] and Sato et al. [22]. In brief, the decision function of the linear SVM used to predict the group of each subject is a hyperplane equation. This equation is defined by a constant and a set of coefficients, each one associated to an input feature (i.e., a brain region defined by the ROIs). During the classifier training, these parameters are tuned in order to define the optimum hyperplane for separating the data. We then used the absolute values of these hyperplane coefficients (taking into account the training with all subjects and not the leave-one-out procedure) to rank the features and highlight the top 5% most discriminative brain regions.

3. Results

3.1. Classifier Accuracy. Table 2 depicts the scores for the between-group condition comparing typical developing children with ADHD patients. The highest score obtained via site-by-site analysis was 73% using weighted betweenness at the OHSU site. However, this finding was not replicated at the other sites. In the whole-sample analysis the highest score was 58%, achieved with eigenvector centrality.

Table 3 shows the scores for the discrimination analysis between inattentive and combined ADHD subtypes. This analysis was more promising and several measures achieved scores greater than 65% across multiple sites. The highest score obtained via site-by-site analysis was 77% when using the degree measure with unweighted graphs (with a 0.15 cut-off) at OHSU. The highest score in whole-sample analysis was 61%, achieved when using unweighted degree (with a 0.25 cut-off).

Interestingly, the mean score (across sites) and the score from whole-sample classification were very similar, except when using betweenness and degree in unweighted graphs (Figure 1). In this exception, the mean score was greater than the whole sample classification score.

3.2. Brain Regions with Higher Predictive Value. Regarding the identification of the brain regions with greater contribution to prediction, we chose only the classifications with accuracy above 70%. Figure 2 illustrates the discriminant regions for weighted betweenness centrality in healthy versus ADHD groups at OHSU. Several cerebellar and cortical regions were observed including left cerebellum, cerebellar vermis, bilateral occipital cortex, left inferior temporal gyrus, left parietal cortex, right dorsolateral prefrontal cortex, and left frontal pole.

Figure 3 depicts the regions in which centrality measures contributed to the classification of the ADHD types in the OHSU sample. Betweenness centrality contributed most

TABLE 3: ADHD types classification: sensitivity, specificity, and score for each centrality descriptor. Note: the accuracy measures could not be obtained at the NeuroIMAGE site due to the small number of ADHD-combined subjects.

Descriptor	Cut-off	Inattentive ADHD versus Combined ADHD																		
		Peking			Kennedy Krieger			NeuroIMAGE			New York			OHSU			All sites			
		Spec	Sens	Score	Spec	Sens	Score	Spec	Sens	Score	Spec	Sens	Score	Spec	Sens	Score	Spec	Sens	Score	
Closeness	0.1	100%	0%	50%	100%	0%	50%	—	—	—	100%	0%	50%	100%	0%	50%	0%	100%	0%	50%
	0.15	100%	0%	50%	100%	0%	50%	—	—	—	100%	0%	50%	100%	0%	50%	100%	0%	50%	100%
	0.25	100%	0%	50%	100%	0%	50%	—	—	—	100%	0%	50%	100%	0%	50%	100%	0%	50%	100%
Unweighted graph Between	0.1	34%	69%	52%	94%	40%	67%	—	—	—	63%	37%	50%	96%	42%	69%	62%	45%	54%	54%
	0.15	31%	71%	51%	94%	40%	67%	—	—	—	58%	33%	45%	96%	50%	73%	58%	47%	53%	53%
	0.25	41%	69%	55%	88%	0%	44%	—	—	—	63%	37%	50%	91%	42%	66%	64%	46%	55%	55%
Degree	0.1	45%	61%	53%	94%	40%	67%	—	—	—	63%	35%	49%	87%	58%	73%	60%	49%	54%	54%
	0.15	28%	71%	50%	94%	20%	57%	—	—	—	66%	33%	49%	78%	75%	77%	60%	55%	58%	58%
	0.25	34%	71%	53%	88%	20%	54%	—	—	—	64%	42%	53%	74%	58%	66%	67%	55%	61%	61%
Weighted graph Closeness Between Degree EVC Burt	—	34%	71%	53%	100%	40%	70%	—	—	—	63%	35%	49%	74%	33%	54%	60%	37%	49%	49%
	—	28%	78%	53%	100%	0%	50%	—	—	—	66%	37%	51%	74%	17%	45%	58%	46%	52%	52%
	—	31%	73%	52%	88%	20%	54%	—	—	—	64%	37%	51%	78%	67%	72%	59%	51%	55%	55%
—	34%	71%	53%	69%	0%	34%	—	—	—	66%	37%	51%	87%	58%	73%	65%	46%	56%	56%	
—	100%	0%	50%	100%	0%	50%	—	—	—	100%	0%	50%	100%	0%	50%	100%	0%	50%	100%	0%

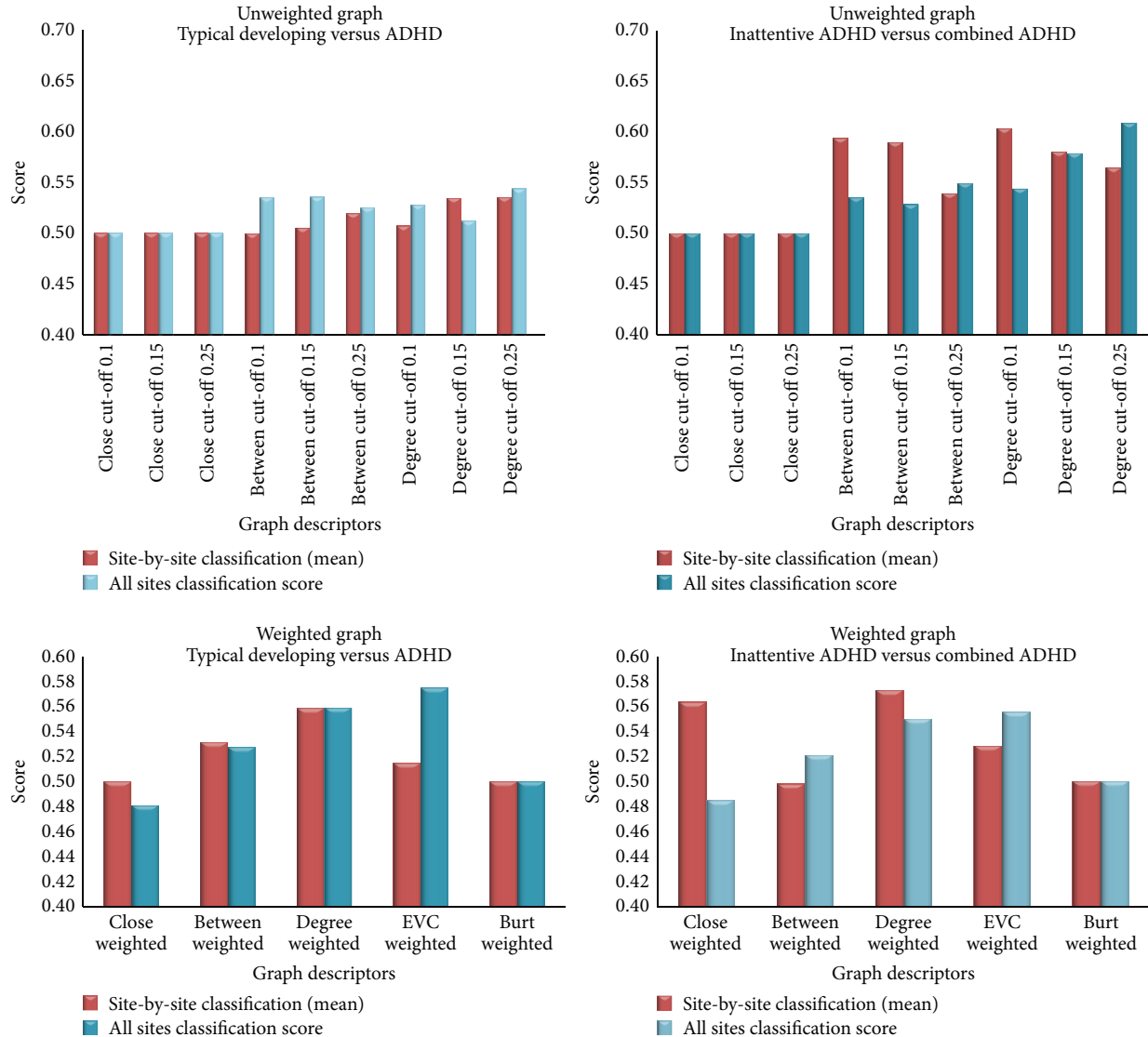


FIGURE 1: Classification scores ($(\text{specificity} + \text{sensitivity})/2$) for each centrality measure.

to classification in the following brain regions: thalamus, left cerebellar cortex, right occipital cortex, right temporal cortex, right precuneus, and right dorsomedial prefrontal and parietal cortices. The brain regions in which degree centrality contributed mostly to classification of ADHD types are also depicted in Figure 3. They include the right temporal and frontal cortices, precuneus and bilateral sensory-motor cortex, dorsal anterior cingulate cortex (dACC), and bilateral parietal regions. In the case of eigenvector centrality, the highest classification scores were obtained in orbitofrontal cortex (OFC), dACC, bilateral temporal cortex, right parietal cortex, motor areas, basal ganglia, and bilateral cerebellum.

4. Discussion

At present, resting-state fMRI is a well-established tool for the assessment of spontaneous brain activity. Graph theoretical measures provide a suitable framework for the investigation

of the structures of complex neural networks. In addition, the application of machine-learning algorithms has been of great impact on developing more advanced neuroimaging studies of psychiatric disorders [13]. In the present work, we aimed to explore the use of graph-derived measures of resting-state BOLD signal as features to discriminate between ADHD types and healthy subjects. In order to estimate the “real-world” reproducibility of the classification procedure, we analyzed data collected at five distinct sites, which differed in terms of MRI scan specifications and acquisition parameters. Finally, we mapped the brain regions in which centrality graph-derived measures showed the greatest contribution to classification. This mapping could provide some insight into the pathophysiological mechanisms of ADHD from a network analysis perspective.

When the whole sample was used, none of the centrality measures had a relevant predictive power beyond chance. However, significant prediction values were observed at the

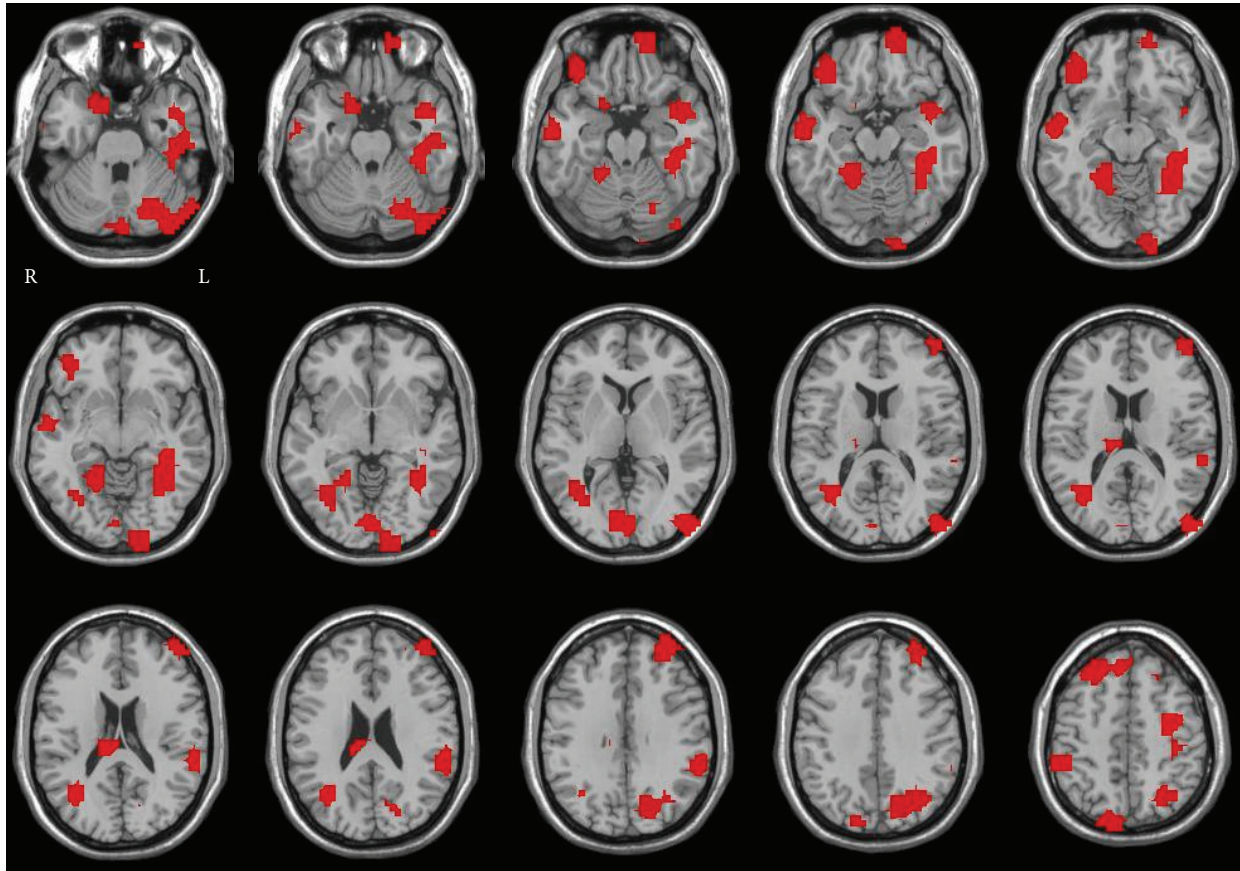


FIGURE 2: Discriminant regions for betweenness centrality (weighted graph) in typical developing versus ADHD classification at OHSU.

OHSU site. Thus both within- and between-site variability have a negative impact on the extraction of predictive information and consequently on classification. In the OHSU sample, betweenness centrality measures contained predictive information for the classification of ADHD and control subjects with a score of 73%. After an extensive analysis of sample characteristics and acquisition parameters, we hypothesize that the classification score at OHSU was higher than the other scores for two main reasons: (i) the sample was approximately balanced between typically developing controls (42 subjects) and ADHD patients (35 subjects), while the group sizes were very different at the other sites; (ii) OHSU EPI acquisition has the largest voxel size (3.8 mm) and the 3T system was equipped with a 12 channels head coil (as opposed to 8) which increases the signal-to-noise ratio.

When the 5% nodes with greater predictive values were mapped, a sparse pattern of brain regions was observed. In fact, widespread brain alterations in ADHD are supported by findings of impaired interregional connectivity between the nodes of large-scale functional networks (reviewed in [9]), and both task-related and resting-state fMRI studies described atypical activations in frontal, temporal, and parietal lobes as well as in cerebellum [23–25].

A promising finding was observed for the degree centrality in the whole sample analysis on the classification

of the disorder types. In the within-site analyses, relatively high scores were observed for degree, betweenness, and eigenvector centralities. However, as the sample size is smaller in these cases, variability is increased. Moreover, the mean scores of within-site analyses were almost identical to the ones from the whole sample analysis. Brain regions mapped for betweenness measures included nodes of the right frontoparietal network. This network has been implicated in attentional and executive processes and is thought to be impaired in ADHD. Cubillo et al. [23] have shown reduced interregional functional connectivity between frontoparietal network nodes during a stop and switching task in ADHD patients when compared to control subjects. Of particular note is the thalamus, which forms part of this attentional network [26, 27], and consequently may play a key role in ADHD. In fact, reduced regional activations in bilateral thalami have been reported in ADHD. Additionally, reduced connectivity between the thalamus and right prefrontal region, occurring concurrently with increased connectivity between the thalamus and occipital lobes, has been found in ADHD in an fMRI study using a sustained attention task [28]. Interestingly, betweenness is the number of shortest path lengths that pass through a node, which is consistent with the purported structural position of the thalamus as a relay to the whole cortex sheet. We speculate that a high

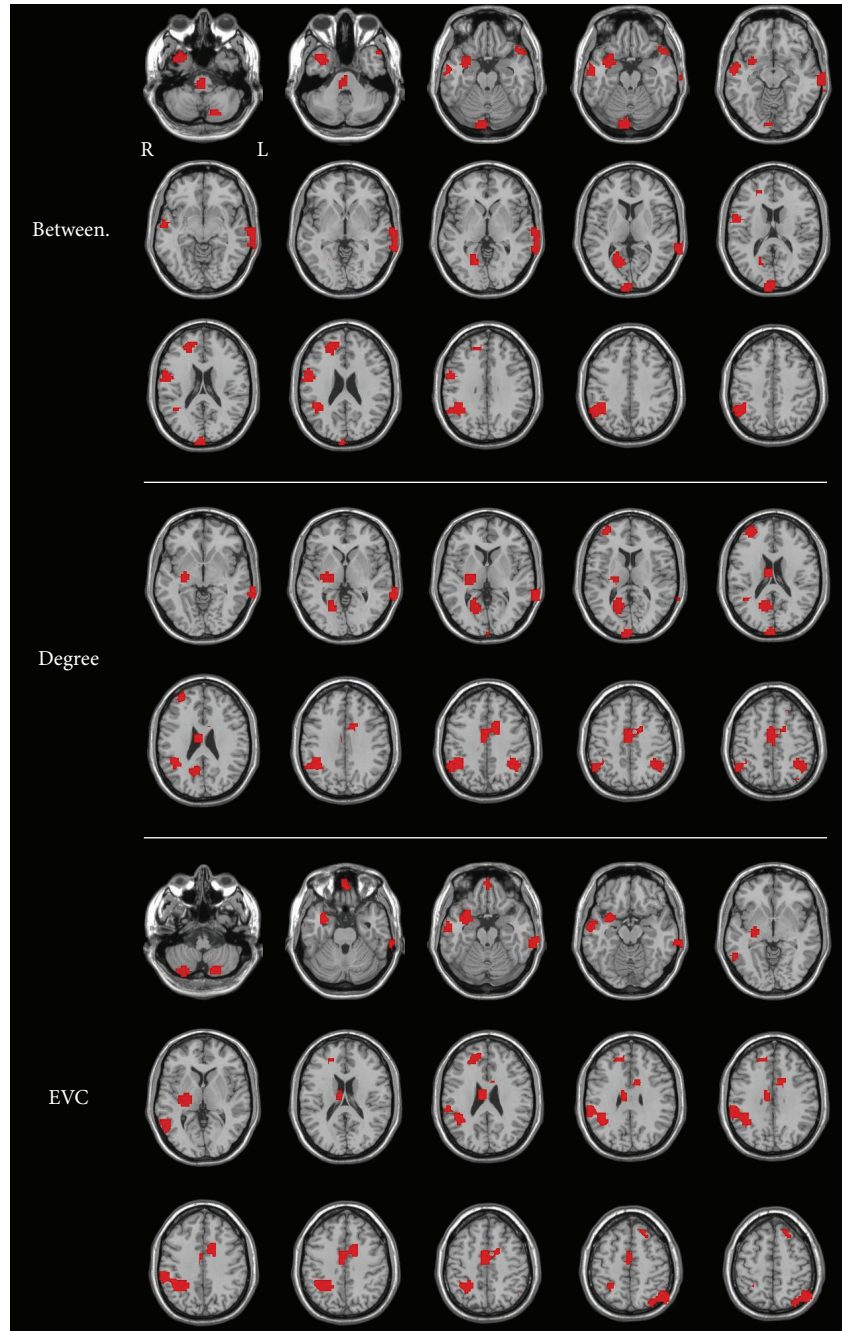


FIGURE 3: Discriminant regions for unweighted betweenness, weighted degree, and weighted eigenvector centrality in the classification between ADHD types at OHSU.

betweenness value for the nodes of the attentional network is compatible with the function of switching attention focus to different stimuli or tasks.

The measure of degree centrality, when applied to the separation between ADHD types, produced the highest classification scores in areas of the sensory-motor network and of the DMN, mainly in parietal cortex and the precuneus. These findings are in agreement with our hypothesis, based on consistent results in the literature [9]. In fact, it is quite intuitive that motor network connectivity should be

altered in a disorder characterized by hyperactivity. It is coherent that the measure of degree centrality (the number of nodes that connect to a given node) contains more discriminative information in these areas, since the motor network fundamentally comprises the output of the central nervous system. It is also expected that motor regions contain information which enables discrimination between inattention with or without hyperactivity. The eigenvector centrality was also found to contribute more to classification within the motor network, as well as within orbitofrontal

cortex, dorsal anterior cingulate cortex, parietal regions, basal ganglia, and the cerebellum. Orbitofrontal areas have been classically implicated in impulse control mechanisms and appear to have impaired activation in ADHD patients [26]. Finally, alterations of DMN activity have also been proposed as a key part of ADHD pathophysiology [29]. In summary, functional networks implicated in attention, hyperactivity, and impulsivity contained predictive information for the discrimination between ADHD inattentive and combined subtypes.

In conclusion, a novel approach of applying graph theoretical measures was shown to be useful for testing our hypothesis regarding resting-state network impairment in ADHD disorder. In particular, distinct patterns of network dysfunction were evident for both inattentive and combined ADHD subtypes. The classification scores for discriminating between ADHD and healthy subjects were close to chance. Clearly, within-site analysis improves prediction levels when compared to whole sample analysis, suggesting that heterogeneity across the sites may strongly limit the application of the method as a potential clinical support. The functional connectivity estimation is strongly dependent on the samples' characteristics. Thus, in order to advance the pathophysiological knowledge of ADHD, we emphasize the importance of further multicentric studies with more homogeneous acquisitions.

Disclosure

Dr. Luis Augusto Rohde has been a member of the speakers' bureau/advisory board and/or acted as a consultant for Eli-Lilly, Janssen-Cilag, Novartis, and Shire in the last three years. He receives authorship royalties from Oxford Press and ArtMed. He has also received travel awards from Shire for his participation of the 2014 APA meeting. The ADHD and Juvenile Bipolar Disorder Outpatient Programs chaired by him received unrestricted educational and research support from the following pharmaceutical companies in the last three years: Eli-Lilly, Janssen-Cilag, Novartis, and Shire.

Conflict of Interests

The authors declare that there is no conflict of interests regarding the publication of this paper.

Acknowledgments

The authors are grateful to the Sao Paulo Research Foundation—FAPESP (Grants 2012/13390-9, 2013/10498-6, and 2013/00506-1) and to CAPES Brazil. The authors would also like to thank the institutes funding the ADHD-200 Consortium: The Commonwealth Sciences Foundation, Ministry of Health, China (200802073); The National Foundation, Ministry of Science and Technology, China (2007BAI17B03); The National Natural Sciences Foundation, China (30970802); The Funds for International Cooperation of the National Natural Science Foundation of China (81020108022); The National Natural Science Foundation

of China (8100059); the Open Research Fund of the State Key Laboratory of Cognitive Neuroscience and Learning; The Autism Speaks Foundation and the (National Institutes of Health) NIH (R01 NS048527, R01MH078160, and R01MH085328); the Johns Hopkins General Clinical Research Center (M01 RR00052); the National Center for Research Resources (P41 RR15241); the Intellectual and Developmental Disabilities Research Center (HD-24061); the (Netherlands Organisation for Scientific Research) NWO-Groot, the (National Institutes of Mental Health) NIMH (R01MH083246); Autism Speaks; The Stavros Niarchos Foundation; The Leon Levy Foundation; An endowment provided by Phyllis Green and Randolph Cöwen; K99/R00 MH091238 (Fair); R01 MH086654 (Nigg); the Oregon Clinical and Translational Research Institute (Fair); the Medical Research Foundation (Fair); UNCF/Merck (Fair); the Ford Foundation (Fair); Cognitive & Brain Systems Maturation (5R01 MH067924, Luna); Reward Processing in Adolescence (1R01 MH080243, Luna); Functional Anatomy of Adolescent ADHD: Defining markers of recovery (K01MH82123, Velanova); The Brooks Family Fund; R01 HD057076 (Schlaggar); R01 NS046424; NIH NINDS NRSA (Church); NIH NIMH R21 (Schlaggar) and TSA (Schlaggar); TSA (Church).

References

- [1] G. Polanczyk, M. S. De Lima, B. L. Horta, J. Biederman, and L. A. Rohde, "The worldwide prevalence of ADHD: a systematic review and meta-regression analysis," *American Journal of Psychiatry*, vol. 164, no. 6, pp. 942–948, 2007.
- [2] American Psychiatric Association, *Diagnostic and Statistical Manual of Mental Disorders*, American Psychiatric Publishing, Arlington, Va, USA, 2013.
- [3] B. N. Cuthbert and T. R. Insel, "Toward the future of psychiatric diagnosis: the seven pillars of RDoC," *BMC Medicine*, vol. 11, no. 1, article 126, 2013.
- [4] T. Insel, B. Cuthbert, M. Garvey et al., "Research Domain Criteria (RDoC): toward a new classification framework for research on mental disorders," *American Journal of Psychiatry*, vol. 167, no. 7, pp. 748–751, 2010.
- [5] D. E. J. Linden, "The challenges and promise of neuroimaging in psychiatry," *Neuron*, vol. 73, no. 1, pp. 8–22, 2012.
- [6] E. Bullmore and O. Sporns, "Complex brain networks: graph theoretical analysis of structural and functional systems," *Nature Reviews Neuroscience*, vol. 10, no. 3, pp. 186–198, 2009.
- [7] M. Rubinov and O. Sporns, "Complex network measures of brain connectivity: Uses and interpretations," *NeuroImage*, vol. 52, no. 3, pp. 1059–1069, 2010.
- [8] J. S. Damoiseaux, S. A. R. B. Rombouts, F. Barkhof et al., "Consistent resting-state networks across healthy subjects," *Proceedings of the National Academy of Sciences of the United States of America*, vol. 103, no. 37, pp. 13848–13853, 2006.
- [9] A. de La Fuente, S. Xia, C. Branch, and X. Li, "A review of attention-deficit/hyperactivity disorder from the perspective of brain networks," *Frontiers in Human Neuroscience*, vol. 7, article 192, 2013.
- [10] M. Greicius, "Resting-state functional connectivity in neuropsychiatric disorders," *Current Opinion in Neurology*, vol. 21, no. 4, pp. 424–430, 2008.

- [11] B. Biswal, F. Z. Yetkin, V. M. Haughton, and J. S. Hyde, "Functional connectivity in the motor cortex of resting human brain using echo-planar MRI," *Magnetic Resonance in Medicine*, vol. 34, no. 4, pp. 537–541, 1995.
- [12] R. L. Buckner, J. R. Andrews-Hanna, and D. L. Schacter, "The brain's default network: anatomy, function, and relevance to disease," *Annals of the New York Academy of Sciences*, vol. 1124, pp. 1–38, 2008.
- [13] S. Klöppel, A. Abdulkadir, C. R. Jack Jr., N. Koutsouleris, J. Mourão-Miranda, and P. Vemuri, "Diagnostic neuroimaging across diseases," *NeuroImage*, vol. 61, no. 2, pp. 457–463, 2012.
- [14] V. N. Vapnik, *The Statistical Learning Theory*, Springer, 1998.
- [15] HD-Consortium, "The ADHD-200 consortium: a model to advance the translational potential of neuroimaging in clinical neuroscience," *Frontiers in Systems Neuroscience*, vol. 6, article 62, 2012.
- [16] R. C. Craddock, G. A. James, P. E. Holtzheimer, X. P. Hu, and H. S. Mayberg, "A whole brain fMRI atlas generated via spatially constrained spectral clustering," *Human Brain Mapping*, vol. 33, no. 8, pp. 1914–1928, 2012.
- [17] J. D. Power, D. A. Fair, B. L. Schlaggar, and S. E. Petersen, "The development of Human Functional Brain Networks," *Neuron*, vol. 67, no. 5, pp. 735–748, 2010.
- [18] L. C. Freeman, "Centrality in social networks conceptual clarification," *Social Networks*, vol. 1, no. 3, pp. 215–239, 1979.
- [19] L. C. Freeman, "A set of measures of centrality based on betweenness," *Sociometry*, vol. 40, no. 1, pp. 35–41, 1977.
- [20] R. S. Burt, "Structural holes and good ideas," *The American Journal of Sociology*, vol. 110, no. 2, pp. 349–399, 2004.
- [21] J. Mourão-Miranda, A. L. W. Bokde, C. Born, H. Hampel, and M. Stetter, "Classifying brain states and determining the discriminating activation patterns: Support Vector Machine on functional MRI data," *NeuroImage*, vol. 28, no. 4, pp. 980–995, 2005.
- [22] J. R. Sato, A. Fujita, C. E. Thomaz et al., "Evaluating SVM and MLDA in the extraction of discriminant regions for mental state prediction," *NeuroImage*, vol. 46, no. 1, pp. 105–114, 2009.
- [23] A. Cubillo, R. Halari, C. Ecker, V. Giampietro, E. Taylor, and K. Rubia, "Reduced activation and inter-regional functional connectivity of fronto-striatal networks in adults with childhood Attention-Deficit Hyperactivity Disorder (ADHD) and persisting symptoms during tasks of motor inhibition and cognitive switching," *Journal of Psychiatric Research*, vol. 44, no. 10, pp. 629–639, 2010.
- [24] K. Rubia, A. Cubillo, A. B. Smith, J. Woolley, I. Heyman, and M. J. Brammer, "Disorder-specific dysfunction in right inferior prefrontal cortex during two inhibition tasks in boys with attention-deficit hyperactivity disorder compared to boys with obsessive-compulsive disorder," *Human Brain Mapping*, vol. 31, no. 2, pp. 287–299, 2010.
- [25] P. Shaw, "Attention-deficit/hyperactivity disorder and the battle for control of attention," *Journal of the American Academy of Child and Adolescent Psychiatry*, vol. 51, no. 11, pp. 1116–1118, 2012.
- [26] G. Bush, "Attention-deficit/hyperactivity disorder and attention networks," *Neuropsychopharmacology*, vol. 35, no. 1, pp. 278–300, 2010.
- [27] G. Bush, "Cingulate, frontal, and parietal cortical dysfunction in attention-deficit/hyperactivity disorder," *Biological Psychiatry*, vol. 69, no. 12, pp. 1160–1167, 2011.
- [28] X. Li, A. Sroubek, M. S. Kelly et al., "Atypical pulvinar-cortical pathways during sustained attention performance in children with attention-deficit/hyperactivity disorder," *Journal of the American Academy of Child and Adolescent Psychiatry*, vol. 51, no. 11, pp. 1197–1207, 2012.
- [29] F. X. Castellanos and E. Proal, "Large-scale brain systems in ADHD: beyond the prefrontal-striatal model," *Trends in Cognitive Sciences*, vol. 16, no. 1, pp. 17–26, 2012.

Research Article

Visual Learning Alters the Spontaneous Activity of the Resting Human Brain: An fNIRS Study

Haijing Niu,^{1,2} Hao Li,^{1,2} Li Sun,³ Yongming Su,^{1,2} Jing Huang,^{1,2} and Yan Song^{1,2}

¹ State Key Laboratory of Cognitive Neuroscience and Learning and IDG/McGovern Institute for Brain Research, Beijing Normal University, Beijing 100875, China

² Center for Collaboration and Innovation in Brain and Learning Sciences, Beijing Normal University, Beijing 100875, China

³ Peking University Sixth Hospital/Institute of Mental Health, Key Laboratory of Ministry of Health, Peking University, Beijing 100191, China

Correspondence should be addressed to Yan Song; songyan@bnu.edu.cn

Received 6 March 2014; Revised 1 August 2014; Accepted 1 August 2014; Published 28 August 2014

Academic Editor: Yihong Yang

Copyright © 2014 Haijing Niu et al. This is an open access article distributed under the Creative Commons Attribution License, which permits unrestricted use, distribution, and reproduction in any medium, provided the original work is properly cited.

Resting-state functional connectivity (RSFC) has been widely used to investigate spontaneous brain activity that exhibits correlated fluctuations. RSFC has been found to be changed along the developmental course and after learning. Here, we investigated whether and how visual learning modified the resting oxygenated hemoglobin (HbO) functional brain connectivity by using functional near-infrared spectroscopy (fNIRS). We demonstrate that after five days of training on an orientation discrimination task constrained to the right visual field, resting HbO functional connectivity and directed mutual interaction between high-level visual cortex and frontal/central areas involved in the top-down control were significantly modified. Moreover, these changes, which correlated with the degree of perceptual learning, were not limited to the trained left visual cortex. We conclude that the resting oxygenated hemoglobin functional connectivity could be used as a predictor of visual learning, supporting the involvement of high-level visual cortex and the involvement of frontal/central cortex during visual perceptual learning.

1. Introduction

Perceptual learning (PL) refers to the relatively permanent modification of perception and behavior following a sensory experience. The orientation discrimination task is one of the most intensively studied PL tasks. In this task, subjects need to decide whether a grating or a line is tilted clockwise or anticlockwise with respect to the reference. Performance on this task dramatically improves with practice; moreover, this learning effect is specific to the position and orientation of the stimuli [1]. In typical PL models, this specificity is interpreted as an indicator of the retinotopic early visual cortical locus of learning, where different orientations are processed separately [2–4]. Indeed, significant modulation of learning on V1/V2 activity has been found in single-unit recording studies of animals and functional magnetic resonance imaging (fMRI) studies in humans [5, 6]. On the other hand, some researchers have proposed that visual PL

occurs at the middle visual stages, such as the extrastriate cortex including V2–V4, where neurons are characterized by both orientation/location selectivity and more complex properties [7, 8]. Recent neuroimaging studies even proposed that the higher central mechanism, rather than the early visual processing itself, may account for orientation discrimination learning [9–11]. Therefore, the emerging view is that a single cortical area or process is not likely to be exclusively responsible for PL. Perceptual learning might be a refinement of synergistic processes in multiple stages and cortical areas, including those dedicated to sensory processing, engaged in top-down control, and involved in decision-making and memory. This hypothesis was consistent with two recent works, which showed that the resting-state blood oxygenation level-dependent (BOLD) signal functional connectivity and directed mutual interaction between trained visual cortex and frontal-parietal areas involved in the control of spatial attention were significantly modified after extensive practice

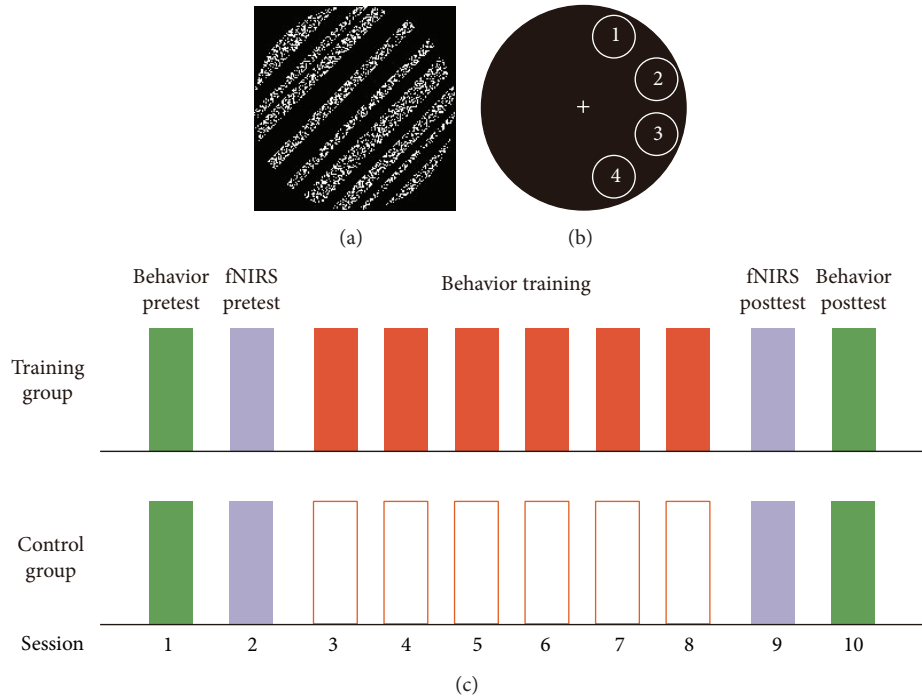


FIGURE 1: (a) Example of the stimulus used in the current study. (b) The stimulus presented at one of the four locations in the right visual field and the location of the grating were fixed for each participant during the whole experiment. The four locations were counterbalanced across participants. (c) Experiment design for the “training” group and “control” group.

on a shape-identification task [11, 12]. Critically, postlearning modulations in functional connectivity correlated with individual measures of improvement. These findings suggest that the change in spontaneous functional connectivity could encode or support the encoding of behavioral visual learning.

In the present study, we investigated whether and how classical orientation discrimination learning modified the resting oxygenated hemoglobin (HbO) functional connectivity brain activity by using functional near-infrared spectroscopy (fNIRS). We acquired resting-state fNIRS before and after intense training on the classical orientation discrimination task at a specific location in the right visual field. Compared with the fMRI that records signals based on the paramagnetic properties of deoxygenated hemoglobin (HbR), fNIRS detects changes in the optical properties of the cortical surface mediated by variations in local hemodynamic activity and can estimate variations in the concentration of both HbR and HbO at a higher temporal resolution. As an emerging neuroimaging tool, fNIRS has been successfully used to identify functional connectivity during resting-state brain activity [13–19]. If functional connectivity is related to the neural changes that occur during the orientation discrimination learning, then training-specific plasticity in functional connectivity should be observed.

2. Materials and Methods

2.1. Participants. Thirty undergraduate and graduate students (22 males; 20–25 years old) with normal or correct-to-normal vision participated in this study as paid volunteers.

Subjects were randomly arranged into two groups: the “training” group (six males and nine females) and the “control” group (eight males and seven females). In addition to these thirty subjects, two subjects were excluded because of the low signal-to-noise ratio in several channels (less than 25% of the mean signal-to-noise ratio of all the channels) due to failures in source/detector placement. Four subjects were excluded due to large head movement during their fNIRS recording [15, 16]. All of the subjects signed the informed consent before the experiment, and the experimental protocol was approved by the Beijing Normal University Institutional Review Board.

2.2. Stimuli and Procedure. The stimuli were generated using MATLAB with the Psychtoolbox extension and were presented on a 21-inch ViewSonic G220f color monitor (1024 pixel \times 768 pixel resolution, 0.39 mm \times 0.39 mm pixel size, 120 Hz frame rate, and 50 cd/m² mean luminance). The stimulus, called a “solid noisy grating,” was a circular field (diameter = 3.8°) consisting of one-dimensional white noise (white and black bars with width varying from 0.077° to 0.312° which were reset in each trial; Figure 1(a)). Each trial started with the presentation of a white fixation cross at the center of the screen for 500 ms. Subsequently, a “solid noisy grating” would appear in one of the four locations centered at 5° eccentricity from the fixation in the right visual field for 100 ms. The location of the grating was fixed for each participant during the whole experiment, and the four locations were counterbalanced across participants. Finally, an infinite central cross was presented until a response was detected. Subjects were instructed to judge whether the

grating orientation had a more clockwise or anticlockwise orientation relative to 36° by pressing one of the two buttons with their right hand. Auditory feedback would be given if the response was incorrect. A standard 3-down-1-up staircase was used in the grating orientation discrimination threshold testing, which resulted in a 79.4% convergence level. That is, when subjects' responses were correct for 3 consecutive trials, the difference between the grating and the reference 36° was decreased by one step. When subjects provided an incorrect response, the difference between the grating and the reference 36° was increased by one step. The steps of the staircase were separated by 0.05 log units. If the orientation variation trend changed, then there was a reversal. Each staircase consisted of ten reversals, four preliminary reversals and six experimental reversals. The geometric mean of the experimental reversals was taken as the threshold for each staircase, and the average of all of the thresholds in one session was taken as the threshold of this session. Therefore, the threshold in our study means the lowest difference angle at which the grating orientation can be discriminated from the reference 36° . To make sure that subjects focused their eyes on the fixation throughout the experiment, an EyeLink 1000 Long Range Mount system was used to monitor their eye movement during pretest, training, and posttest. In addition, a piece of black cardboard with a circular aperture (diameter = 17°) was used to cover the monitor to exclude the possibility that subject could utilize the edges of the monitor to perform the orientation discrimination task. Experiments were performed in a dimly lit room. Subjects sat in a chair with their heads on a chin-and-head rest to keep still at a distance of 1 m from the monitor.

For the "training" group, the experiment consisted of nine sessions on nine successive days (Figure 1(c)). First, subjects performed a behavioral pretest in session 1 (including five staircases of an orientation discrimination task) and a resting fNIRS pretest in session 2 (12 min). Then, subjects were trained with the same orientation discrimination task in session 3 to session 7 (including 100 staircases in total, 20 staircases for each session). After five sessions of training, subjects had a resting fNIRS posttest in session 8 (the same as the fNIRS pretest) and a behavioral posttest in session 9 (the same as the behavioral pretest in session 1). All training and test sessions were performed in a 36° orientation.

To determine whether the changes in functional connectivity were induced by the training or the simple passage of time, participants in the "control" group did not take part in any type of training and participated in only the same behavioral and fNIRS measurements in the pre- and posttests (session 1, session 2, session 8, and session 9; Figure 1(c)).

2.3. fNIRS Measurement. The resting-state fNIRS measurements were conducted using a continuous wave system (ETG-4000, Hitachi Medical Co., Japan). The system generated two wavelengths of near-infrared light (690 and 830 nm) and collected the hemoglobin concentration at 10 Hz sampling rate. Two 3×5 optode probe sets (consisting of 7 photodetectors and 8 light emitters, 3×3 cm probe configuration) were used to produce 44 measurement channels to allow for the measurement of frontal/central and posterior

cortices (Figure 2). Specifically, channel 16 was placed at Cz according to the international 10–20 system, and the middle point of channels 42 and 43 was placed at theinion. The probe sets were examined and adjusted to ensure the consistency of the positions across the participants.

All fNIRS channels were marked on one participant's scalp by vitamin E capsules which are visible in structural MR imaging (Figure 2(b), top). NIRS-SPM was used to project the measurement channels onto the cortical surface and to further determine the anatomical localization of each fNIRS measurement channel (Figure 2(b), bottom).

During the fNIRS measurements, subjects sat in a comfortable chair with their eyes fixed on a black cross presented on a gray background for 12 min. They were instructed to relax and keep motionless as much as possible.

The structural MRI data were acquired using a SIEMENS TRIO 3-Tesla scanner in the Imaging Center for Brain Research, Beijing Normal University. During MRI data acquisition, the participant was supine in the MRI scanner with the two probes placed on the subject's head, which was fixed by straps. The T1-weighted structural image was acquired using a magnetization-prepared rapid gradient echo (MPRAGE) sequence: 206 slices, TR = 2530 ms, TE = 3.39 ms, slice thickness = 1 mm, FA = 7° , FOV = 256×256 mm², and in-plane resolution = 256×256 .

2.4. Data Processing. The psychophysical data of two groups were analyzed with a repeated-measure ANOVA with the two factors being "group" (training versus control group, between-subject factor) and "test" (pretest versus posttest, within-subject factor).

For fNIRS data processing, optical data were first converted from relative changes in light intensities to HbO and HbR for each channel based on the modified Beer-Lambert law using HomER [20]. The converted data were visually checked and excluded from subsequent processing once the pre- or posttest data included large motion artifacts or a low signal-to-noise ratio. Then, a band-pass filter (0.009–0.08 Hz) was adopted to remove the high-frequency physiological noises and low-frequency baseline drifts. Finally, for each subject, we cut 10 min low-frequency oxyhemoglobin signals to be used as functional connectivity analysis at resting state.

For each subject and each test, we calculated the Pearson correlation coefficients of every two channels' time course to produce a correlation matrix. Then, the coefficients were z-transformed through the function $z = (1/2) \log((1+r)/(1-r))$. Next, we applied a one-tailed paired *t*-test between the pretest and posttest for each group to determine whether there were significant changes in functional connectivity. Among them, we further identified the ones which could significantly predict the behavioral improvement by computing correlation coefficient.

3. Results

3.1. Psychophysical Data. Figure 3 shows the learning curve and mean data obtained from the psychophysical threshold measured in the training and control groups. The 2×2 repeated-measure ANOVA shows that the main effect of

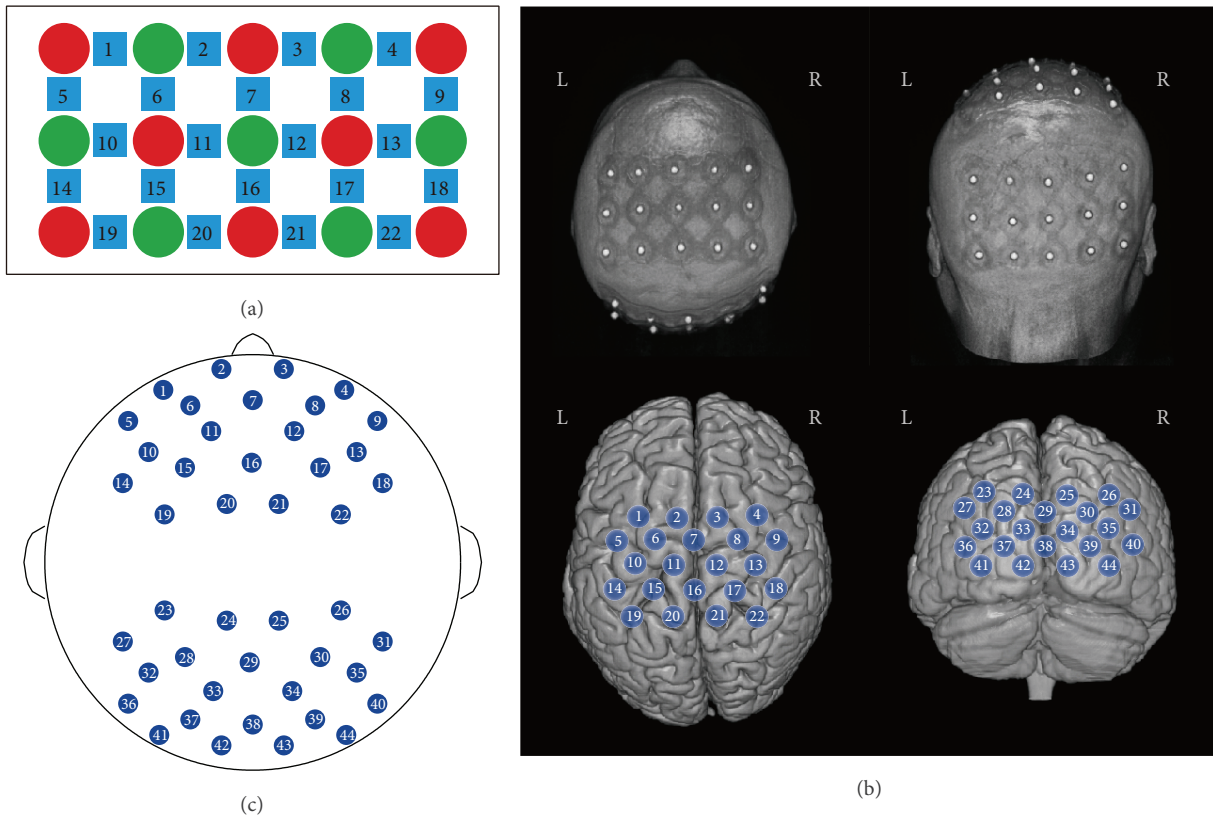


FIGURE 2: (a) The 3 × 5 optode probe set with seven detectors (green) and eight sources (red), resulting in 22 channels (blue). (b) Cerebral projections of light sources and detectors overlaid on the participants’ scalp (top). The two 22 channels (total 44 channels) were fitted on the frontal/central and posterior cortex of the head, respectively (bottom). (c) The total 44 channels on the head model.

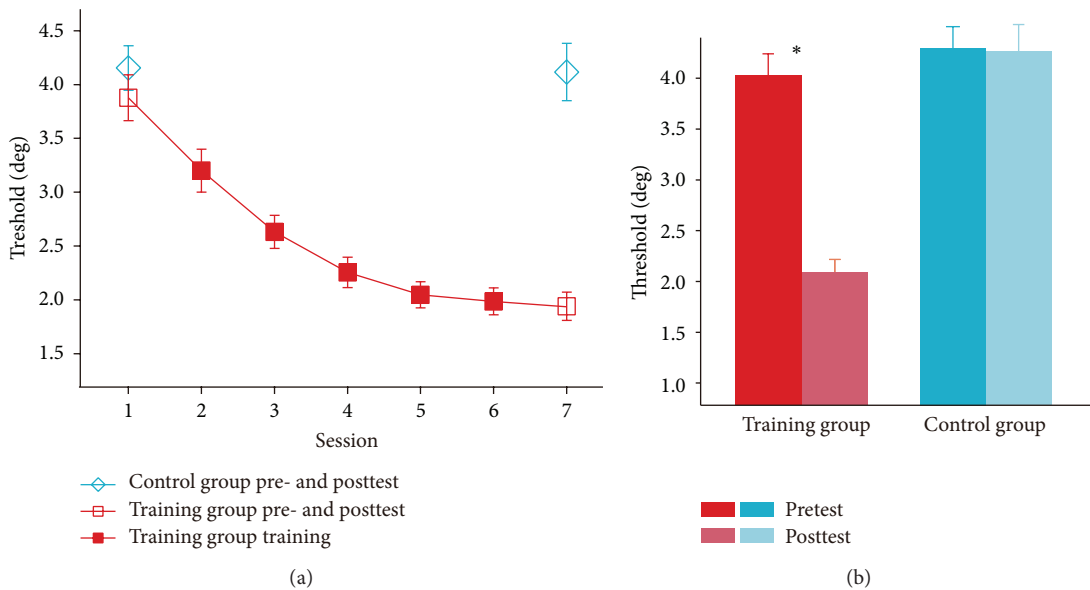


FIGURE 3: (a) The learning curves of the “training” group (solid red squares), the pre- and posttest thresholds for the “training” group (hollow red squares), and the “control” group (hollow blue diamonds). (b) The pre- and posttest thresholds for the “training” group (red columns) and the “control” group (blue columns).

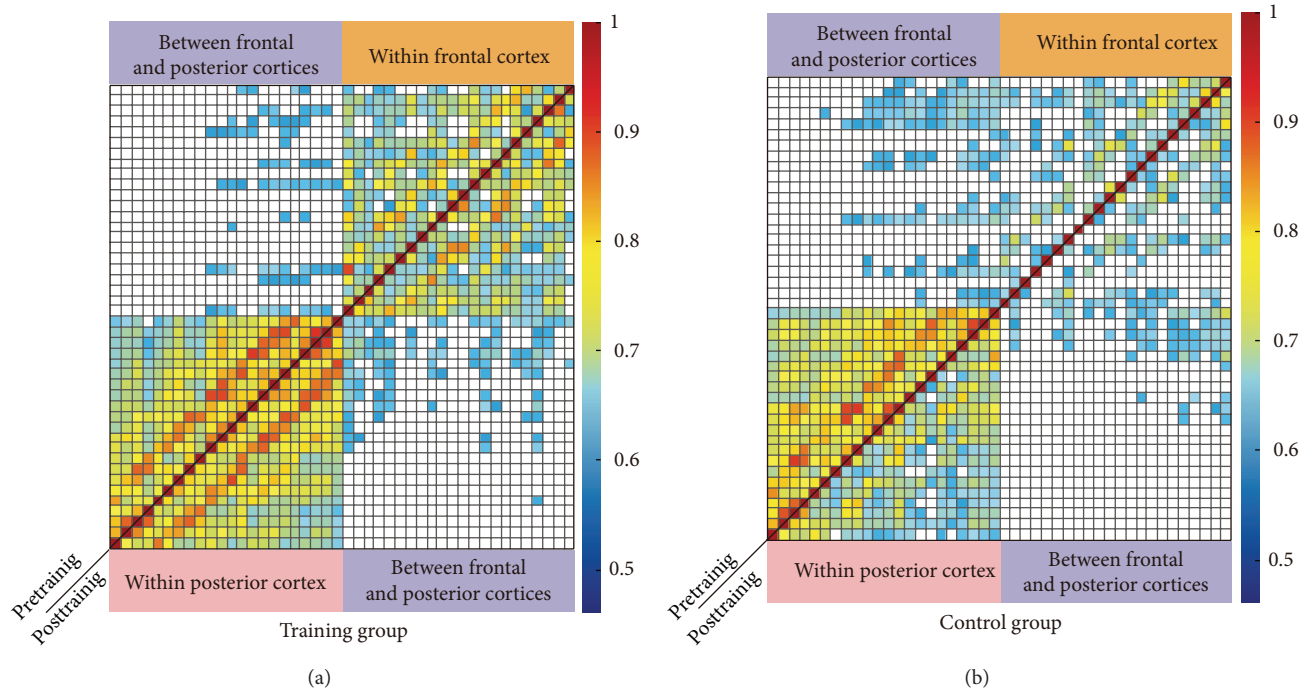


FIGURE 4: Pre- and posttest spontaneous HbO functional connectivity correlation matrix for the “training” group (a) and the “control” group (b). Color bar indicates correlation values for each channel. Note the stability of the correlation matrix across tests, indicating that within-probe functional connectivity is very stable over time.

the group was significant ($F(1, 59) = 7.958, P < 0.05$), and the interaction of group \times test was also significant ($F(1, 59) = 4.772, P < 0.05$). Simple effect analysis showed that, for the “training” group, psychophysical thresholds in the behavioral posttest were significantly lower than those in the behavioral pretest ($P < 0.01$, Figure 3(b)). For the “control” group, however, psychophysical thresholds did not significantly differ between two tests ($P > 0.9$; Figure 3(b)). In addition, the “training” and “control” groups had similar pretest thresholds ($P > 0.5$), Therefore the observers in two groups were homogeneous in the behavioral dimension before the training.

3.2. RSFC Changes. For the HbO responses, the functional connectivity correlation matrix of the pre- and posttest is illustrated in Figure 4. Regardless of the group, it was obvious that both pre- and posttests had stronger functional connectivity within probes than between the two probes.

Then, we examined the changes of the connectivity patterns induced by perceptual learning. Although the functional connectivity patterns for the “training” group showed a high degree of similarity between the pre- and posttests, the one-tailed t -test results showed that the strength of a large number of connections was improved after learning (Figure 5(a)), and most were between-probes rather than within-probes. It is also worth noting that the changes in functional connectivity were centered at the right superior frontal area (CH12) and the right postcentral area (CH21). For the “control” group, however, the change pattern of functional connectivity was less obvious and the strength of only a few connections was significantly improved (Figure 4(b)).

We further checked whether the connectivity strength was decreased; however, no such connectivity was found in both groups.

3.3. Correlation between RSFC Changes and Learning. For each functional connectivity that changed significantly after learning, correlation analyses were carried out to determine if there was a relationship between the change in behavioral performance (the threshold difference between post- and pretest) and the change in functional connectivity (the strength difference between post- and pretest). For the “training” group, the changes in functional connectivity between the right postcentral area (CH21) and the following regions significantly predicted participants’ behavioral performance: left middle occipital gyrus (CH32), right middle occipital gyrus (CH26), left superior occipital gyrus (CH23, CH28), right superior occipital gyrus (CH25), and right angular gyrus (Figures 5(c) and 6; Tables 1 and 2). In addition, the strength of functional connectivity between the right postcentral gyrus (CH22) and right middle occipital gyrus (CH26), between the right postcentral gyrus (CH22) and the right angular gyrus (CH31), between the left precuneus (CH20) and occipital lobe (CH23, CH26), and between right paracentral lobule (CH16) and right angular (CH31) also positively correlated with the behavioral improvement. These measures involved the channels adjacent to CH21 (Figures 5(c) and 6; Tables 1 and 2). All of these results indicated that the stronger the long functional connectivity became, the more the improvement the subjects would make. More importantly, although the gratings were only presented to the right visual field (hence the visual information was mainly projected to the left visual cortex) during the whole training,

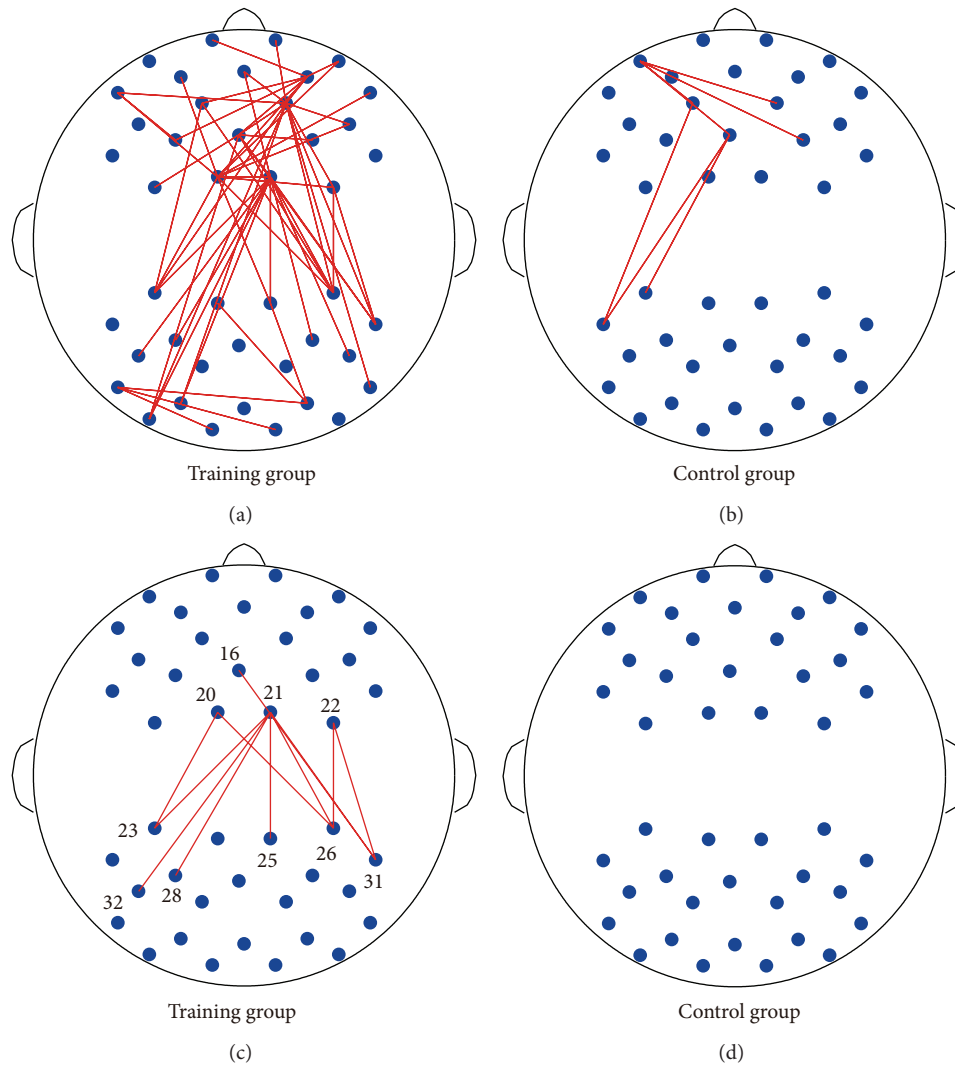


FIGURE 5: Clusters for the significantly strengthened functional connectivity after training (a, b). Clusters for which the strengthened functional connectivity significantly predicted behavioral improvement (c, d).

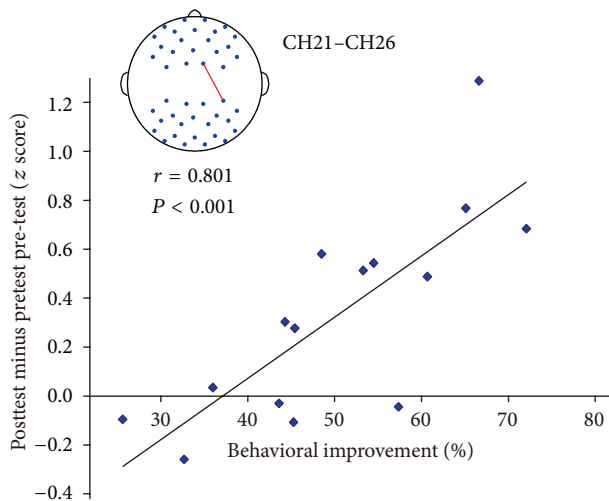


FIGURE 6: The strengthened CH21-CH26 functional connectivity significantly predicted behavioral improvement.

the connectivity between frontal channels and right posterior channels not directly stimulated by the grating stimuli was also significantly increased. Furthermore, those changes had a strong correlation with behavioral improvement.

For the “control” group, however, none of the changes in functional connectivity were reliably correlated with the behavioral performance improvement (Figure 5(d)).

Lastly, we analyzed HbR concentration data by using the same methods applied to the HbO. Neither the significantly changed connectivity nor reliable correlation between the HbR and behavioral performance was found in either group, supporting the conclusion that HbO was the most sensitive indicator of changes in regional cerebral blood flow in fNIRS measurements [21].

4. Discussion

By investigating the spontaneous HbO connectivity changes in observers who were trained with grating orientation

TABLE 1: The MNI coordinate, region, and BA for some NIRS channels.

Channel	MNI			Region	BA
	<i>x</i>	<i>y</i>	<i>z</i>		
CH16	4	-29	78	Paracentral_Lobule_R	4
CH20	-9	-45	79	Precuneus_L	5
CH21	15	-43	80	Postcentral_R	5
CH22	36	-41	71	Postcentral_R	3
CH23	-27	-89	39	Occipital_Sup_L	19
CH25	20	-92	38	Occipital_Sup_R	19
CH26	41	-81	40	Occipital_Mid_R	19
CH28	-16	-98	29	Occipital_Sup_L	18
CH31	52	-75	32	Angular_R	39
CH32	-27	-98	21	Occipital_Mid_L	18

TABLE 2: Clusters for which the strengthened functional connectivity can predict the behavioral improvement.

Connectivity	Correlation with behavioral improvement	
	<i>r</i>	<i>P</i> value
CH21-CH26	0.801	<0.001
CH21-CH23	0.791	<0.001
CH21-CH31	0.772	<0.001
CH20-CH23	0.665	<0.01
CH21-CH28	0.637	<0.05
CH20-CH26	0.631	<0.05
CH21-CH25	0.598	<0.05
CH21-CH32	0.596	<0.05
CH22-CH26	0.591	<0.05
CH22-CH31	0.572	<0.05
CH16-CH31	0.556	<0.05

discrimination, we demonstrated that orientation discrimination learning is associated with stronger functional connectivity. Critically, these changes correlated with the individual degree of perceptual learning, suggesting that visual perceptual learning can change the pattern of spontaneous cortical activity between different brain networks in specific ways. The specific learning-related modulation in resting HbO connectivity was not induced by the simple passage of time because these effects disappeared in the control group.

Visual perceptual learning is often taken as evidence of neural plasticity in the retinotopic early visual cortex [1, 22, 23]. However, recent psychophysical studies suggest that perceptual learning is a high-level learning process beyond the retinotopic early visual areas [24–28]. Our results showed that when the task is performed only at the right visual field, the functional connectivity was significantly increased in both left and right high-level visual cortex. This nonretinotopic effect suggests the involvement of top-down influence. Single-unit and fMRI studies have shown that not only the retinotopic early visual cortex, but also the nonretinotopic higher brain areas that are more related to attention and decision-making are involved in visual discrimination [29, 30]. Recent neurophysiological and fMRI

evidence has further shown that the brain areas responsible for decision-making, such as LIP and ACC, are also involved in visual perceptual learning [10, 31]. Therefore, it is not surprising to find that the increased functional connectivity mainly involved the frontal/central cortex and high-level visual cortex in this study, suggesting the top-down modulation in higher-order decision-making or attention systems [32–34].

Resting-state measures have been correlated with individual performance variability in several cognitive domains, such as working memory [35], executive control [36], reading competence [37], and face perception [38]. In the domain of visual learning, fMRI has been used to examine the mechanism of learning-induced changes in resting functional connectivity. For example, Lewis et al. showed that resting-state blood oxygenation level-dependent (BOLD) functional connectivity between visual cortex and task-relevant cortical networks changed after learning on a shape-identification task [11]. Different from our results, the BOLD functional connectivity between trained visual cortex and dorsal attention regions became weaker after learning, and this decrement in functional connectivity strength was positively correlated with behavioral improvement.

Our results provide evidence for the functional role of spontaneous HbO coherence in cortical networks as identified by fNIRS. The finding that most relevant changes in our study occur between, rather than within, networks indicates that this signal may be especially important in linking large-scale cortical networks, which is consistent with the work of Lewis et al. [11]. This is also consistent with the suggestion that coherence is related to low-frequency fluctuations of neuronal activity that are deemed very important for long-distance cortical communication [39].

In conclusion, we used fNIRS to explore RSFC changes during visual learning and proved that resting oxygenated hemoglobin functional connectivity could be used as a predictor of visual learning. Our results provide further support that the coordinated activation of cortical networks during behavior shapes the organized pattern of correlated spontaneous activity at rest. The individual degree of orientation discrimination learning was mainly related to the changes in functional connectivity between high-level visual cortex and frontal/central association areas but not within portions of visual cortex.

Conflict of Interests

The authors declare that no conflict of interests exists.

Authors' Contribution

Haijing Niu, Hao Li, and Li Sun contributed equally to this work.

Acknowledgments

The present research was supported by the National Key Basic Research Program of China (2014CB846103 and

2011CB711000), NSFC (31271203 and 81201122), and the Open Project Grant of the State Key Laboratory of Cognitive Neuroscience and Learning (CNLZD1301).

References

- [1] A. A. Schoups, R. Vogels, and G. A. Orban, "Human perceptual learning in identifying the oblique orientation: retinotopy, orientation specificity and monocularly," *The Journal of Physiology*, vol. 483, no. 3, pp. 797–810, 1995.
- [2] Y. Adini, D. Sagi, and M. Tsodyks, "Context-enabled learning in the human visual system," *Nature*, vol. 415, no. 6873, pp. 790–793, 2002.
- [3] E. Freeman, J. Driver, D. Sagi, and L. Zhaoping, "Top-down modulation of lateral interactions in early vision: does attention affect integration of the whole or just perception of the parts?" *Current Biology*, vol. 13, no. 11, pp. 985–989, 2003.
- [4] A. F. Teich and N. Qian, "Learning and adaptation in a recurrent model of V1 orientation selectivity," *Journal of Neurophysiology*, vol. 89, no. 4, pp. 2086–2100, 2003.
- [5] A. Schoups, R. Vogels, N. Qian, and G. Orban, "Practising orientation identification improves orientation coding in V1 neurons," *Nature*, vol. 412, no. 6846, pp. 549–553, 2001.
- [6] Y. Yotsumoto, T. Watanabe, and Y. Sasaki, "Different dynamics of performance and brain activation in the time course of perceptual learning," *Neuron*, vol. 57, no. 6, pp. 827–833, 2008.
- [7] T. Yang and J. H. R. Maunsell, "The effect of perceptual learning on neuronal responses in monkey visual area V4," *The Journal of Neuroscience*, vol. 24, no. 7, pp. 1617–1626, 2004.
- [8] S. Raiguel, R. Vogels, S. G. Mysore, and G. A. Orban, "Learning to see the difference specifically alters the most informative V4 neurons," *Journal of Neuroscience*, vol. 26, no. 24, pp. 6589–6602, 2006.
- [9] M. Bartolucci and A. T. Smith, "Attentional modulation in visual cortex is modified during perceptual learning," *Neuropsychologia*, vol. 49, no. 14, pp. 3898–3907, 2011.
- [10] T. Kahnt, M. Grueschow, O. Speck, and J. Haynes, "Perceptual learning and decision-making in human medial frontal cortex," *Neuron*, vol. 70, no. 3, pp. 549–559, 2011.
- [11] C. M. Lewis, A. Baldassarre, G. Committeri, G. L. Romani, and M. Corbetta, "Learning sculpts the spontaneous activity of the resting human brain," *Proceedings of the National Academy of Sciences of the United States of America*, vol. 106, no. 41, pp. 17558–17563, 2009.
- [12] A. Baldassarre, C. M. Lewis, G. Committeri, A. Z. Snyder, G. L. Romani, and M. Corbetta, "Individual variability in functional connectivity predicts performance of a perceptual task," *Proceedings of the National Academy of Sciences of the United States of America*, vol. 109, no. 9, pp. 3516–3521, 2012.
- [13] F. Homae, H. Watanabe, T. Otobe et al., "Development of global cortical networks in early infancy," *The Journal of Neuroscience*, vol. 30, no. 14, pp. 4877–4882, 2010.
- [14] C. Lu, Y. Zhang, B. B. Biswal, Y. Zang, D. Peng, and C. Zhu, "Use of fNIRS to assess resting state functional connectivity," *Journal of Neuroscience Methods*, vol. 186, no. 2, pp. 242–249, 2010.
- [15] R. C. Mesquita, M. A. Franceschini, and D. A. Boas, "Resting state functional connectivity of the whole head with near-infrared spectroscopy," *Biomedical Optics Express*, vol. 1, no. 1, pp. 324–336, 2010.
- [16] H. Niu, J. Wang, T. Zhao, N. Shu, and Y. He, "Revealing topological organization of human brain functional networks with resting-state functional near infrared spectroscopy," *PLoS ONE*, vol. 7, no. 9, Article ID e45771, 2012.
- [17] S. Sasai, F. Homae, H. Watanabe, and G. Taga, "Frequency-specific functional connectivity in the brain during resting state revealed by NIRS," *NeuroImage*, vol. 56, no. 1, pp. 252–257, 2011.
- [18] B. R. White, A. Z. Snyder, A. L. Cohen et al., "Resting-state functional connectivity in the human brain revealed with diffuse optical tomography," *NeuroImage*, vol. 47, no. 1, pp. 148–156, 2009.
- [19] H. Zhang, Y.-J. Zhang, C.-M. Lu, S.-Y. Ma, Y.-F. Zang, and C.-Z. Zhu, "Functional connectivity as revealed by independent component analysis of resting-state fNIRS measurements," *NeuroImage*, vol. 51, no. 3, pp. 1150–1161, 2010.
- [20] T. J. Huppert, S. G. Diamond, M. A. Franceschini, and D. A. Boas, "HomER: a review of time-series analysis methods for near-infrared spectroscopy of the brain," *Applied Optics*, vol. 48, no. 10, pp. D280–D298, 2009.
- [21] X. Cui, D. M. Bryant, and A. L. Reiss, "NIRS-based hyper-scanning reveals increased interpersonal coherence in superior frontal cortex during cooperation," *NeuroImage*, vol. 59, no. 3, pp. 2430–2437, 2012.
- [22] A. Karni and D. Sagi, "Where practice makes perfect in texture discrimination: evidence for primary visual cortex plasticity," *Proceedings of the National Academy of Sciences of the United States of America*, vol. 88, no. 11, pp. 4966–4970, 1991.
- [23] V. R. Bejjanki, J. M. Beck, Z. Lu, and A. Pouget, "Perceptual learning as improved probabilistic inference in early sensory areas," *Nature Neuroscience*, vol. 14, no. 5, pp. 642–650, 2011.
- [24] K. C. Aberg, E. M. Tartaglia, and M. H. Herzog, "Perceptual learning with Chevrons requires a minimal number of trials, transfers to untrained directions, but does not require sleep," *Vision Research*, vol. 49, no. 16, pp. 2087–2094, 2009.
- [25] P. E. Jeter, B. A. Doshier, S. Liu, and Z. Lu, "Specificity of perceptual learning increases with increased training," *Vision Research*, vol. 50, no. 19, pp. 1928–1940, 2010.
- [26] R. Wang, J. Zhang, S. A. Klein, D. M. Levi, and C. Yu, "Task relevancy and demand modulate double-training enabled transfer of perceptual learning," *Vision Research*, vol. 61, pp. 33–38, 2012.
- [27] L. Q. Xiao, J. Y. Zhang, R. Wang, S. A. Klein, D. M. Levi, and C. Yu, "Complete transfer of perceptual learning across retinal locations enabled by double training," *Current Biology*, vol. 18, no. 24, pp. 1922–1926, 2008.
- [28] J. Zhang, G. Zhang, L. Xiao, S. A. Klein, D. M. Levi, and C. Yu, "Rule-based learning explains visual perceptual learning and its specificity and transfer," *The Journal of Neuroscience*, vol. 30, no. 37, pp. 12323–12328, 2010.
- [29] I. Mukai, D. Kim, M. Fukunaga, S. Japee, S. Marrett, and L. G. Ungerleider, "Activations in visual and attention-related areas predict and correlate with the degree of perceptual learning," *The Journal of Neuroscience*, vol. 27, no. 42, pp. 11401–11411, 2007.
- [30] J. I. Gold and M. N. Shadlen, "The neural basis of decision making," *Annual Review of Neuroscience*, vol. 30, pp. 535–574, 2007.
- [31] C. Law and J. I. Gold, "Neural correlates of perceptual learning in a sensory-motor, but not a sensory, cortical area," *Nature Neuroscience*, vol. 11, no. 4, pp. 505–513, 2008.
- [32] M. H. Herzog and M. Fahle, "Modeling perceptual learning: difficulties and how they can be overcome," *Biological Cybernetics*, vol. 78, no. 2, pp. 107–117, 1998.

- [33] M. Sigman, H. Pan, Y. Yang, E. Stern, D. Silbersweig, and C. D. Gilbert, "Top-down reorganization of activity in the visual pathway after learning a shape identification task," *Neuron*, vol. 46, no. 5, pp. 823–835, 2005.
- [34] M. Fahle, "Perceptual learning and sensorimotor flexibility: cortical plasticity under attentional control?" *Philosophical Transactions of the Royal Society B: Biological Sciences*, vol. 364, no. 1515, pp. 313–319, 2009.
- [35] M. Hampson, N. R. Driesen, P. Skudlarski, J. C. Gore, and R. T. Constable, "Brain connectivity related to working memory performance," *Journal of Neuroscience*, vol. 26, no. 51, pp. 13338–13343, 2006.
- [36] W. W. Seeley, V. Menon, A. F. Schatzberg et al., "Dissociable intrinsic connectivity networks for salience processing and executive control," *Journal of Neuroscience*, vol. 27, no. 9, pp. 2349–2356, 2007.
- [37] M. S. Koyama, A. di Martino, X. Zuo et al., "Resting-state functional connectivity indexes reading competence in children and adults," *The Journal of Neuroscience*, vol. 31, no. 23, pp. 8617–8624, 2011.
- [38] Q. Zhu, J. Zhang, Y. L. L. Luo, D. D. Dilks, and J. Liu, "Resting-state neural activity across face-selective cortical regions is behaviorally relevant," *The Journal of Neuroscience*, vol. 31, no. 28, pp. 10323–10330, 2011.
- [39] D. A. Leopold, Y. Murayama, and N. K. Logothetis, "Very slow activity fluctuations in monkey visual cortex: implications for functional brain imaging," *Cerebral Cortex*, vol. 13, no. 4, pp. 422–433, 2003.

Research Article

Alteration of Interictal Brain Activity in Patients with Temporal Lobe Epilepsy in the Left Dominant Hemisphere: A Resting-State MEG Study

Haitao Zhu,¹ Jinlong Zhu,¹ Tiezhu Zhao,² Yong Wu,¹ Hongyi Liu,¹ Ting Wu,³ Lu Yang,³ Yuanjie Zou,¹ Rui Zhang,¹ and Gang Zheng^{2,4}

¹ Department of Neurosurgery, Nanjing Brain Hospital Affiliated to Nanjing Medical University, Nanjing, Jiangsu 210029, China

² College of Civil Aviation, Nanjing University of Aeronautics and Astronautics, Nanjing, Jiangsu 210016, China

³ MEG Center, Nanjing Brain Hospital Affiliated to Nanjing Medical University, Nanjing, Jiangsu 210029, China

⁴ Department of Medical Imaging, Jinling Hospital, Medical School of Nanjing University, Nanjing, Jiangsu 210002, China

Correspondence should be addressed to Rui Zhang; neurosurgeonzr@njmu.edu.cn and Gang Zheng; zg431193@gmail.com

Received 16 May 2014; Revised 3 July 2014; Accepted 5 July 2014; Published 21 July 2014

Academic Editor: Danny Jiongjiong Wang

Copyright © 2014 Haitao Zhu et al. This is an open access article distributed under the Creative Commons Attribution License, which permits unrestricted use, distribution, and reproduction in any medium, provided the original work is properly cited.

Resting MEG activities were compared between patients with left temporal lobe epilepsy (LTLE) and normal controls. Using SAMg2, the activities of MEG data were reconstructed and normalized. Significantly elevated SAMg2 signals were found in LTLE patients in the left temporal lobe and medial structures. Marked decreases of SAMg2 signals were found in the wide extratemporal lobe regions, such as the bilateral visual cortex. The study also demonstrated a positive correlation between the seizure frequency and brain activities of the abnormal regions after the multiple linear regression analysis. These results suggested that the aberrant brain activities not only were related to the epileptogenic zones, but also existed in other extratemporal regions in patients with LTLE. The activities of the aberrant regions could be further damaged with the increase of the seizure frequency. Our findings indicated that LTLE could be a multifocal disease, including complex epileptic networks and brain dysfunction networks.

1. Introduction

Epilepsy is a common neurological disorder, characterized by hypersynchronous neuronal activity as shown from electrophysiological recordings [1, 2]. Many patients have excellent or good surgical outcomes after the resection of epileptogenic zone. However, the generation and spread of focal onset epileptic seizures involve a large network of brain areas that extended beyond the seizure onset zone (SOZ). Traditionally, the epileptogenic zone was thought to be singular. However, this has been challenged in favor of a network model, in which the focus (or foci) would be widely distributed [3].

During the past decade, there have been an increasing number of studies using structural or functional connectivity methods to research the clinical impact of temporal lobe epilepsy (TLE) on neural networks [4, 5]. Many studies have shown that connectivity abnormalities not only are restricted to the ipsilateral or contralateral temporal lobes,

but also involved the extratemporal regions, such as thalamus, cerebellum, frontal lobe areas and cingulate gyrus, and occipital regions [6, 7]. Activity of the regions functionally or anatomically connected to the temporal lobe or hippocampus probably results in complex cognitive and behavioral conditions. These findings have led to the notion of TLE as a “network disease” [3]. Surgical resection is the gold standard for the localization of SOZ and the evaluation of brain function recovery in TLE patients. However, few cases were confirmed by the surgery and histopathological examinations. Furthermore, the relationship between the epileptogenic zone and other altered brain regions in the TLE network is still unclear.

With the development of medical imaging, there are many advanced image techniques used to study the epileptogenic zone and other brain activities. MEG, a non-invasive detection technology, detects neuronal activity directly with millisecond temporal resolution. Compared

to electroencephalograph (EEG), which is strongly influenced by conductivity in different organizations within the head, the propagation of magnetic fields is not distorted by the brain, skull, and scalp [8]. Therefore, localizing sources from MEG data is relatively simpler than locating the sources of electric field from EEG data. Previous studies have shown that MEG is a clinically valuable diagnostic tool in presurgical evaluation for both the localization of the epileptogenic zone and the prognosis of surgical outcome [9, 10].

In this study, our hypotheses were as follows: (1) the resting-state brain activity may be different across numerous brain regions, rather than only in SOZs, in left temporal lobe epilepsy (LTLE) patients and healthy controls; (2) these differences could be related to the clinical variables of LTLE; (3) the brain abnormalities of LTLE patients could benefit from surgery of the epileptogenic zone. To confirm SOZs, LTLE patients who planned to undergo surgical treatments were included in our study. Factors such as age at onset (year), seizure frequency (per month), and duration of seizure (month) were recorded and followed up with after surgery. To noninvasively assess resting-state brain activity, resting-state MEG (rsMEG) data were acquired in all subjects and quantified based on the SAMg2 method. The SAMg2 values were compared between two groups to detect altered brain regions in LTLE patients and controls. The correlations were calculated to find the relationships between altered brain regions and clinical records of the LTLE patients.

2. Materials and Methods

2.1. Subjects. The study was approved by the Medical Ethics Committee of the hospital. Informed consent for the study was obtained from all participants.

From the period of January 2007 to December 2012, 122 patients with refractory epilepsy were admitted to the epilepsy center of the Brain Hospital of Nanjing Medical University (Nanjing, China) and underwent presurgical evaluation. Ninety-eight patients (80.3%) ultimately had cortical resection to treat their epilepsy. Twenty LTLE patients (all right-handed, 7 female and 13 male, mean age 25.25 ± 6.90 yrs) were recruited from the patients who underwent surgical resection for medically intractable epilepsy. Inclusion criteria included (1) seizures with typical temporal lobe semiology that were not controlled with antiepileptic drugs (AEDs); (2) an epileptogenic zone that was located in the left temporal lobe; (3) left hemispheric dominance for language determined by neuropsychological evaluations (etomidate speech and memory test, eSAM, when indicated); (4) patients who underwent surgery for resection of epileptogenic zone; and (5) follow-up time >12 months. General information of the patients is summarized in Table 1.

We assessed the clinical factors including the age at onset (year), seizure frequency (per month), and duration of the seizure (month). The seizure frequency was calculated based on the long-term EEG recordings. Two or more seizures were captured during VEEG monitoring. Seizure semiology, ictal, and interictal EEG data were interpreted by an epileptologist and an electrophysiologist to exclude the pseudoepileptic

seizures and other interferences. In our study, the mean monitoring time was 257.70 ± 150.33 hours, ranging from 96 to 764 hours.

Twenty healthy volunteers (all right-handed, 8 females and 12 males, mean age 25.60 ± 5.64 yrs) were recruited as controls, from local community by advertising in the Brain Hospital of Nanjing Medical University. Healthy controls were interviewed and confirmed to have no history of neurological disorders or psychiatric illnesses and no gross abnormalities in brain MRI images. To control the effects of the sleep deprivation in patients, all of our healthy subjects were asked to sleep after 12:00 pm.

2.2. Methods

2.2.1. Data Acquisition. All patients had MRI scans with a GE Sigma scanner (GE Healthcare, Milwaukee, WI, USA) before the MEG recording. Three fiducial points were placed in identical locations as the ones used in the MEG recordings so that the 3D MRI and MEG data could be coregistered precisely to yield an MSI using these three landmarks. Three markers, nasion, left ear, and right ear, were stamped on each subject's head. The protocol included the following sequences: axial and sagittal T1 weighted, axial and coronal T2 weighted, axial and coronal fluid-attenuated inversion recovery (FLAIR) images, and three-dimensional (3D) spoiled gradient recalled (SPGR).

rsMEG data acquisitions were performed using a 275-channel whole-head system (CTF VSM MedTech Systems Inc., Coquitlam, BC, Canada) in a magnetically shielded room (MSR) (Vacuumschmelze, Hanau, Germany) that was designed to reduce environmental magnetic noise. Before the MEG scan, there was no reduction in the antiepileptic medication due to the potential risk factor. To increase the likelihood of capturing spike events, we used sleep deprivation. The head position relative to the sensor arrays for each patient was measured using three coils affixed to the nasion and preauricular points before MEG data recording. During MEG recording, all subjects were instructed to rest with their eyes closed and heads still. For each subject, 120-second MEG data was recorded. If the head movement during the recording was greater than 5 millimeters (mm), the epoch was recorded again.

2.2.2. Data Processing. rsMEG data were preprocessed by CTF software (VSM MedTech Systems Inc., Canada, Version CTF-5.2.1). The frequency ranging from 20 Hz to 70 Hz was used in several studies and is outside the range of alpha-band activity that would tend to drive the excess kurtosis negative [11–13]. To eliminate the background activity and contrast the interictal spike activity, we performed SAM(g2) analysis localized the epileptic zone in clinical [12, 14, 15]. First, MEG data were filtered (20–70 Hz). Then, the SAMg2 Z-map of each subject was calculated by the SAMg2 script of the CTF software. After the calculation, the SAMg2 Z-map of each subject was registered with its corresponding 3D MRI by the markers on the nasion, left ear, and right ear. The registered SAMg2 Z-maps were spatially normalized

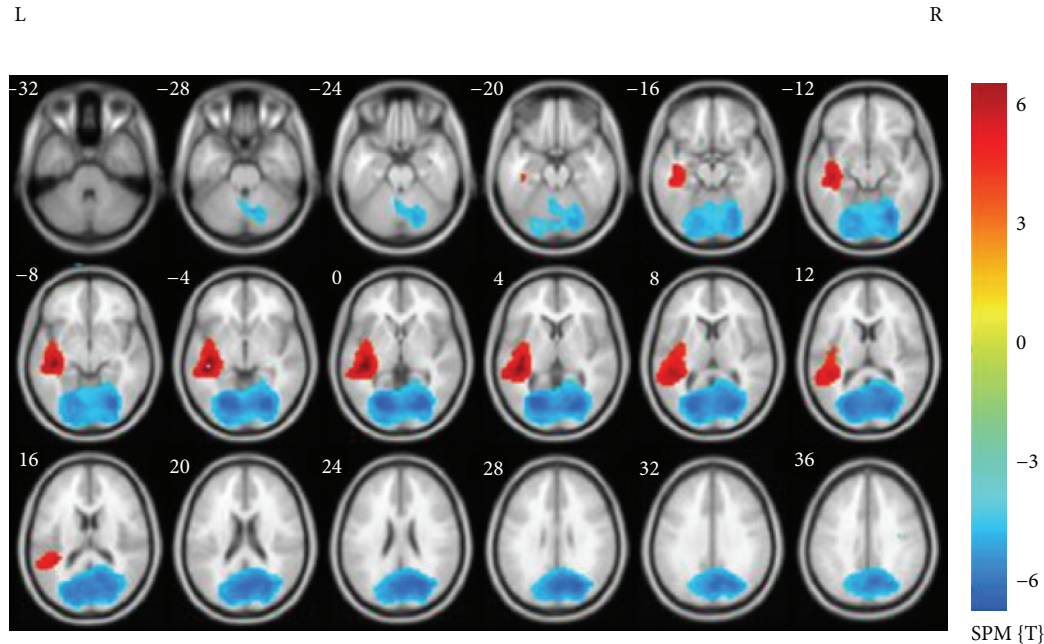


FIGURE 1: Statistical parametric maps depict SAMg2 increases (warm colors) and decreases (cool colors) in LTLE compared with controls. Significant increases occur in left side hippocampal gyrus, insula, superior temporal gyrus, middle temporal gyrus, inferior temporal gyrus, and Heschl gyrus, while decreases occur in the bilateral calcarine, cerebellum, cuneus, fusiform, lingual gyrus, occipital lobe, precuneus, left parietal gyrus, and contralateral precentral gyrus.

to the Montreal Neurological Institute (MNI) template and resampled to $3 \times 3 \times 3 \text{ mm}^3$. Finally, spatial smoothing was conducted on the Z-maps with an isotropic Gaussian kernel of 6mm of full width at half maximum.

2.2.3. Statistical Analysis. One way analysis of covariance (ANCOVA) with age and gender as covariates was used to compare SAMg2 maps of healthy controls and those of LTLE patients. The voxel-wise ANCOVA P values were less than 0.05 after false discovery rate (FDR) correction was considered significant.

According to the voxel-wise significant differences between two groups, regions with suprathreshold clusters were defined as regions of interests (ROIs) for further analyses. Mean SAMg2 Z values of these regions were calculated using Automated Anatomical Labeling atlas [16]. Correlations between ROIs and clinical variables of LTLE (seizure onset, seizure frequency, and duration of seizure) were calculated. All data were shown as mean \pm SD. An FDR-corrected P values less than 0.05 were considered significant.

3. Results

There was no significant difference in age and gender between the two groups ($P > 0.05$).

3.1. Brain Regions with Abnormal Brain Activity between Two Groups. In the LTLE patients compared to gender and age matched healthy subjects, there was a significant reduction in

SAM g2 signals in the bilateral calcarine, cerebellum, cuneus, fusiform, lingual gyrus, occipital lobe (superior, middle, and inferior gyrus), precuneus, left parietal gyrus, and contralateral precentral gyrus. Patients also showed increased SAM g2 signals in the ipsilateral (left side) hippocampal gyrus, insula, superior temporal gyrus, middle temporal gyrus, inferior temporal gyrus, and Heschl gyri ($P < 0.05$, FDR corrected) (Table 2 and Figure 1).

3.2. Correlation Analysis of Abnormal Activity and Clinical Variables. The relationship between the above abnormal regions and clinical variables (age at seizure onset, frequency of seizures, and duration of epilepsy) was evaluated using multiple linear regression analysis. We found that multiple abnormal regions were significantly associated with frequency of seizures (Table 3). Duration of epilepsy and age at seizure onset did not significantly influence brain activity.

4. Discussion

In this study, the difference in the SAMg2 signals between patients with LTLE and healthy subjects was used to measure the disruption of neuronal activity in epileptic and distant brain regions during the interictal period. Significant differences were observed in the spatial pattern and intensity of SAMg2 signals in the two groups. These findings are discussed further below. The special changes of the resting-state brain activity may be potential noninvasive biomarkers for understanding, diagnosing, and potentially treating the LTLE patients.

TABLE 1: Demographic and clinical characteristics of the patients.

Number	Age (Y)/gender	Age at onset (Y)	Seizure frequency/Mo	Duration of seizure (Mo)	MRI (lesion location)	Interictal MEG (SAMg2)	EEG (intro/extroperation)	Surgical procedure	Pathology	Follow-up (months)/outcome (Engle)
1	35/M	23	4	12	LT	LT	LT	Lesionectomy + ATL	LT cortical dysplasia	35/IA
2	30/M	14	25	16	NM	LT	LT (ant)	ATL	LT neurodegeneration	46/IA
3	23/F	13	5	10	LT	LT, LH	LT (ant, bas-lat)	ATL + SAH	LT neurodegeneration; LH HS	35/IA
4	21/M	4	3	17.5	LT, LH	LT, LH	LT (bas-lat)	ATL + SAH	LT gliosis; LH Atrophy	29/IIA
5	36/M	32	4	4.5	LT	LT	LT (lesion-pos)	Lesionectomy + ATL	LT angiomatosis	39/IA
6	21/F	6	5	15	LT	LT	LT (ant, bas-lat)	ATL + SAH	LT neurodegeneration; LH atrophy	65/IB
7	32/F	22	12	10.5	NM	LT, LH	LT (ant, bas-lat)	ATL + SAH	LT neurodegeneration; LH atrophy	24/IA
8	18/M	9	5	9	LT	LT	LT (lat, mid-inf)	Lesionectomy + ATL	LT ganglioneuroma	60/IB
9	38/F	30	30	8.5	LT	LT	LT (perilesion)	Lesionectomy + ATL	LT cortical dysplasia	58/IA
10	22/F	2	4	20	NM	LFT	LAT	ALT	NM	37/IIA
11	25/M	16	7	9.5	LT	LT	LT (lesion-pos)	Lesionectomy + ATL	LT cortical dysplasia	26/IB
12	29/M	8	11	21	NM	LT	LAT	ALT	LT neurodegeneration	17/IIIB
13	16/M	2	3	14.5	LT, LH	LT, LH	LT (ant, bas-lat)	ATL + SAH	LT neurodegeneration; LH atrophy	22/IA
14	22/F	6	15	16	LT	LT	LT	Lesionectomy + ATL	LT cortical dysplasia	44/IA
15	21/M	11	22	10	LT, LH	LT, LH	LT (ant, bas-lat)	ATL + SAH	LT gliosis; LH atrophy	16/IA
16	33/M	27	28	6	LT, LH	LTP, LH	LT (ant, bas-lat)	ATL + SAH	LT neurodegeneration; LH HS	21/IA
17	16/M	4	6	12	NM	LT, LH	LT (ant, bas-lat)	ATL + SAH	LT gliosis; LH atrophy	15/IA
18	25/M	13	8	12	LT	LT	LT	Lesionectomy + ATL	LT cortical dysplasia	33/IA
19	16/F	3	2	13	LT, LI	LT, LI	LAT, LI	ATL + SAH	LT neurodegeneration; LI atrophy	38/IIIC
20	26/M	15	6	11	NM	LFT	LT (perilesion)	Lesionectomy + ATL	LT cortical dysplasia	49/IB

M: male; F: female; LT: left temporal; NM: normal; LH: left hippocampus; LI: left insular; LFT: left frontal-temporal; ant: anterior; bas: basal; lat: lateral; mid: middle; pos: post; inf: inferior; ATL: anterior temporal lobectomy; SAH: selective amygdalohippocampectomy; HS: hippocampal sclerosis.

TABLE 2: Brain regions with increased and decreased activations in the patient group.

Brain ROI	Voxels	T value	MNI coordinate		
			X	Y	Z
Temporal_Mid_L	270	4.15	-48	-33	0
Hippocampus_L	75	4.11	-36	-27	-6
Temporal_Sup_L	179	4.1	-45	-36	6
Temporal_Inf_L	36	4.04	-42	-30	-12
Heschl_L	38	3.96	-39	-21	6
Insula_L	87	3.89	-39	-18	0
Fusiform_L	92	-2.03	-24	-75	-3
Precentral_R	68	-3.67	45	-3	51
Cerebellum_L	310	-3.71	-18	-72	-12
Cerebellum_R	424	-3.82	24	-81	-18
Parietal_Sup_L	38	-3.86	-15	-69	42
Precuneus_L	242	-4	0	-66	30
Occipital_Sup_L	210	-4.03	-18	-81	12
Occipital_Inf_R	129	-4.04	30	-81	-6
Occipital_Inf_L	115	-4.06	-27	-81	0
Occipital_Mid_L	295	-4.07	-27	-75	0
Precuneus_R	405	-4.14	15	-66	24
Occipital_Mid_R	262	-4.15	27	-72	27
Lingual_R	554	-4.19	24	-75	-3
Calcarine_L	533	-4.3	-21	-72	6
Occipital_Sup_R	226	-4.32	27	-69	27
Cuneus_L	322	-4.33	0	-72	24
Lingual_L	456	-4.37	-21	-72	3
Fusiform_R	159	-4.44	27	-75	-6
Calcarine_R	474	-4.44	24	-75	9
Cuneus_R	335	-4.49	21	-69	27

L: left; R: right; Mid: middle; Sup: superior; Inf: inferior.

Compared to the healthy control group, SAMg2 values increased in the ipsilateral (left side) hippocampal gyrus, insula, superior temporal gyrus, middle temporal gyrus, inferior temporal gyrus, and Heschl gyri of the patients. These results revealed that the irritated areas were beyond the SOZ but restricted to the ipsilateral temporal lobe and mesial structure. We propose that the increased SAMg2 signals in specific regions may form irritated areas that might be responsible for seizure genesis and propagation. The removal of the irritated areas may be an effective treatment for the LTLE patients.

The role of the neurosurgeon in the surgical treatment of TLE had evolved from doing so-called standard anterior temporal lobectomies (TLR) to selective amygdalohippocampectomy (SAH) and temporal resection guided by intraoperative electrocorticography. A number of studies were devoted to the comparison of seizure results from temporal lobectomy (TLR) with selective amygdalohippocampectomy (SAH) [17, 18]. And several studies have reported that seizure outcomes are irrespective of the extent of mesial and lateral resection [19, 20], while others state that seizure outcomes are better if larger volumes or specific substructures are removed [21].

TABLE 3: Results of correlation analysis between the abnormal activity and the seizure frequency ($P < 0.05$ with FDR correction).

Brain ROI	P value	R value
Precentral_R	0.025	0.377
Hippocampus_L	0.025	0.406
Calcarine_L	0.025	0.373
Calcarine_R	0.027	0.349
Cuneus_L	0.021	0.474
Cuneus_R	0.026	0.357
Lingual_R	0.026	0.409
Occipital_Sup_L	0.031	0.488
Occipital_Sup_R	0.021	0.454
Occipital_Mid_L	0.025	0.383
Occipital_Mid_R	0.040	0.520
Occipital_Inf_L	0.022	0.441
Occipital_Inf_R	0.023	0.478
Fusiform_L	0.027	0.481
Fusiform_R	0.026	0.388
Parietal_Sup_L	0.022	0.431
Precuneus_L	0.022	0.459
Precuneus_R	0.027	0.389
Temporal_Mid_L	0.024	0.370
Temporal_Inf_L	0.033	0.577
Cerebellum_L	0.035	0.313
Cerebellum_R	0.028	0.517

L: left; R: right; Mid: middle; Sup: superior; Inf: inferior.

Comparing TLR and SAH, McKhann pointed out, “neither SAH nor TLR could be recommended over the other option as a standard or guideline in the surgical management of TLE” [22]. The Spencer type of resection [23], which consists of a small anterior partial lobectomy combined with a more extensive mesial resection, may be an ideal method for the treatment of TLE. Our study reveals that the irritated areas of LTLE involve not only the lateral neocortical structures but also the ipsilateral nearby structures, such as the hippocampus (HC), insula, and Heschl gyri. These interictal irritated zones may be involved in the LTLE network formation. The Spencer type of resection would be sufficient enough to resect or interrupt a large enough part of the mesial structures to render the mesiobasal network between the HC, parahippocampal gyrus, and amygdalum unable to build up and sustain a seizure. Abosch et al. [24] referred to this as “severing a critical proportion of the connections” when they discussed the variability in extent of resection described by McKhann et al. [22].

In this study, all of the patients were diagnosed with LTLE and eleven of them underwent the Spencer type of resection (left anterior temporal lobectomy combined with partial amygdalohippocampectomy). The seizure freedom (Engel class I) of them was 72.7% (8/11) better than the group of the remainder 55.6% (5/9). The results from this study have further proved that the refractory LTLE is not a focal disease but a network disease and can be cured by extensive surgical resection.

The appearance of the insula is also significant because of its particular interconnection with the amygdalohippocampal structures. Isnard et al. found that seizure activity invaded the insular cortex in all temporal lobe epilepsy patients studied with chronic depth stereotactic recordings [25]. This may explain the persistence of seizures after selective amygdalohippocampectomy. This study also had its own limitations; we have removed the anterior temporal lobe and the mesial structures except the insula during surgery.

The reduction in SAMg2 values is thought to reflect deactivated brain activity or dysfunction in the special regions. Compared with healthy controls, LTLE patients showed multifocal dysfunction in the bilateral calcarine, cerebellum, cuneus, fusiform, lingual gyrus, occipital lobe (superior, middle, and inferior gyri), and precuneus brain regions. The ipsilateral superior parietal gyrus and contralateral precentral gyrus also displayed reduction. The deactivated areas extend widely beyond the ipsilateral hemisphere to the contralateral or bilateral areas in patients with LTLE.

A relatively large dysfunctional area was observed in the bilateral visual cortex, including the bilateral calcarine, fusiform, lingual gyrus, and occipital lobe (superior, middle, and inferior gyri) in this study. Van Paesschen et al. used SPECT to study the cerebral perfusion changes in complex partial seizures patients with hippocampal sclerosis. They found bilateral occipital hyperperfusion during complex partial seizure and relative occipital hypoactivation during interictal period [26].

The cause of interictal bilateral visual cortex dysfunction is unknown, but propagating epileptiform discharges through the branches of the inferior longitudinal fasciculus (ILF) may play a role. Catani et al. [27] used tractography in the living human brain to address the connections between occipital and temporal lobe and found direct fiber connections between the occipital and anterior temporal cortex in a bundle labeled the ILF. In our study, the dysfunctional regions also involved the three origin branches of the ILF: a lingual branch, a lateral occipital branch, and a cuneal branch. Moreover, a recent study combining fMRI and tractography has visualized the propagation of epileptic activity from the temporal epileptogenic focus to the occipital lobe in mesial temporal lobe epilepsy [28]. The involved cortices lie along the occipitotemporal connections supplied by the inferior longitudinal fasciculus, suggesting a direct propagation pathway from the anterotemporal to the occipital lobe [29]. However, in line with previous brain imaging studies we take our data to suggest that the left side epileptic interictal discharges may influence the activity of the bilateral visual cortex in the patients with left temporal lobe epilepsy.

Our study just focuses on the reduced active regions of the default mode network (DMN) within the bilateral precuneus, ipsilateral superior parietal gyrus, while the other regions of the DMN are normal. Decreased SAMg2 signals within the DMN are considered to result from the disruption of neuronal activity and are commonly used to reflect associated impairments in brain disorders. The lateral parietal cortex is involved in spatial attention aspects of word reading [30]. The precuneus (PCUN) has been reported to be involved in consciousness, engaged in self-related mental

representations during rest [31], and related to the late recovery of consciousness in epilepsy patients [32]. The posterior cingulate cortex/precuneus (PCC/PCUN) is activated during tasks that involve autobiographic memory and self-referential processes [33]. TLE patients often present a few abnormal psychological and psychiatric symptoms associated with the functionalities of the DMN [34], such as absence of self-awareness, emotional and psychic experiences, and social cognitive impairments.

The motor impairment of LTLE patients has been demonstrated by this study. Our MEG study revealed that the deactivated region involved the contralateral precentral gyrus and the bilateral cerebellum. The contralateral precentral gyrus is dominated by the control of limb movement ipsilateral to the epileptic focus, while the cerebellum is by sensory-motor integration, motor coordination, and so forth. Nelissen et al., using SPECT and PET to study the brain blood perfusion in TLE, found interictal hypometabolism in the frontal lobe cortex. They suggested a dynamic process of frontal lobe function inhibition, which not only could represent protection against epileptiform-discharge propagation, but could also be responsible for the functional deficits presented by these patients. In this study, we also found more serious damages in bilateral cerebellum lobe in our LTLE patients. This phenomenon was so-called "crossed cerebellar diaschisis" and was considered an indication of disconnection of the glutamatergic corticopontocerebellar tracts [35]. The decreased SAMg2 values of the bilateral cerebellum lobe could be a sign of decreased motor coordination.

In our study, sleep deprivation was used to increase the likelihood of capturing spike events which were performed in all epilepsy patients in our epilepsy center. Many studies also adopted the similar sleep deprivation method to increase the likelihood of capturing spike events in clinical [36, 37]. A lack of sleep has been demonstrated to produce performance deficits in experimental tasks of alertness, attention, memory, cognition, learning, and motor responses [38]. While the neurophysiological effects of sleep deprivation remain incompletely understood, a few recent studies have begun to provide guidance on where and what neurophysiological changes occur as a function of sleep deprivation. Thomas et al. quantified and characterized global and regional brain activity changes implicated in sleep deprivation-induced neurobehavioral impairment during cumulative, extended sleep loss [39]. Significant decreases in CMRglu were reported in the thalamus, prefrontal and posterior parietal cortices. Alertness and cognitive performance declined in association with these brain deactivations. This study provides evidence that short-term sleep deprivation produces global and regional decreases in brain activity, with larger reductions in activity in the distributed cortical-thalamic network mediating attention and higher-order cognitive processes. The results from sleep deprivation were different than the hyperactivity and dysfunctional regions which were due to epilepsy in our study. In our study, the healthy volunteers were demanded to sleep after twelve o'clock before MEG examinations to control the additional effects of the sleep loss in LTLE patients. The decreased brain activities detected in our patients were caused by the long-term effects of epilepsy

rather than sleep loss. Considering the complex effects of sleep deprivation on brain activity, further study should be performed to control sleep loss in patients with epilepsy.

In our study, we used the SAMg2 signals to study how brain activity in LTLE patients differs from brain activity in healthy controls. Specifically, seizure frequency was strongly associated with intensity of abnormal activity in the LTLE patients. In the study, we further confirmed that TLE is not a focal focus, but a multifocal disease. The mechanism of these extensive abnormal activities needs further study.

5. Limitations

In the study, we did not compare the preoperative brain activities of TLE with the changes of postoperative patients. Further, this study was limited by not comparing abnormal activities with neuropsychological findings and prognostic factor. To make up the difference between TLE patients and controls in the sleep loss, all our health subjects were asked to sleep later. Though sleep loss was not totally controlled, our findings were quite different from those in sleep deprivation, indicating that our study was less affected by sleep deprivation. However, it is difficult to exclude the potential impact of the sleep deprivation to the brain activity of the patients and the normal subjects. Further study should be conducted to specify the effects of sleep loss in TLE patients.

Conflict of Interests

The authors disclose no conflicts.

Acknowledgments

This paper is supported by Grants from National Natural Science Foundation of China (Grant no. 81101039 to G. Zheng) and from Natural Science Foundation of Jiangsu Province (Grant no. BK20131081 to R. Zhang).

References

- [1] C. A. Schevon, J. Cappell, R. Emerson et al., "Cortical abnormalities in epilepsy revealed by local EEG synchrony," *NeuroImage*, vol. 35, no. 1, pp. 140–148, 2007.
- [2] G. J. Ortega, L. Menendez de la Prida, R. G. Sola, and J. Pastor, "synchronization clusters of interictal activity in the lateral temporal cortex of epileptic patients: Intraoperative electrocorticographic analysis," *Epilepsia*, vol. 49, no. 2, pp. 269–280, 2008.
- [3] L. Bonilha, T. Nesland, G. U. Martz et al., "Medial temporal lobe epilepsy is associated with neuronal fibre loss and paradoxical increase in structural connectivity of limbic structures," *Journal of Neurology, Neurosurgery and Psychiatry*, vol. 83, no. 9, pp. 903–909, 2012.
- [4] G. Bettus, E. Guedj, F. Joyeux et al., "Decreased basal fMRI functional connectivity in epileptogenic networks and contralateral compensatory mechanisms," *Human Brain Mapping*, vol. 30, no. 5, pp. 1580–1591, 2009.
- [5] G. Doucet, K. Osipowicz, A. Sharan, M. R. Sperling, and J. I. Tracy, "Extratemporal functional connectivity impairments at rest are related to memory performance in mesial temporal epilepsy," *Human Brain Mapping*, vol. 34, no. 9, pp. 2202–2216, 2013.
- [6] N. Bernasconi, S. Duchesne, A. Janke, J. Lerch, D. L. Collins, and A. Bernasconi, "Whole-brain voxel-based statistical analysis of gray matter and white matter in temporal lobe epilepsy," *NeuroImage*, vol. 23, no. 2, pp. 717–723, 2004.
- [7] F. Riederer, R. Lanzenberger, M. Kaya, D. Prayer, W. Serles, and C. Baumgartner, "Network atrophy in temporal lobe epilepsy: a voxel-based morphometry study," *Neurology*, vol. 71, no. 6, pp. 419–425, 2008.
- [8] M. S. Hamalainen, "Magnetoencephalography: a tool for functional brain imaging," *Brain Topography*, vol. 5, no. 2, pp. 95–102, 1992.
- [9] R. Ramachandranair, H. Otsubo, M. M. Shroff et al., "MEG predicts outcome following surgery for intractable epilepsy in children with normal or nonfocal MRI findings," *Epilepsia*, vol. 48, no. 1, pp. 149–157, 2007.
- [10] M. J. M. Fischer, G. Scheler, and H. Stefan, "Utilization of magnetoencephalography results to obtain favourable outcomes in epilepsy surgery," *Brain*, vol. 128, no. 1, pp. 153–157, 2005.
- [11] R. Ishii, L. Canuet, A. Ochi et al., "Spatially filtered magnetoencephalography compared with electrocorticography to identify intrinsically epileptogenic focal cortical dysplasia," *Epilepsy Research*, vol. 81, no. 2–3, pp. 228–232, 2008.
- [12] H. E. Kirsch, S. E. Robinson, M. Mantle, and S. Nagarajan, "Automated localization of magnetoencephalographic interictal spikes by adaptive spatial filtering," *Clinical Neurophysiology*, vol. 117, no. 10, pp. 2264–2271, 2006.
- [13] D. F. Rose, H. Fujiwara, K. Holland-Bouley, H. M. Greiner, T. Arthur, and F. T. Mangano, "Focal peak activities in spread of interictal-ictal discharges in epilepsy with beamformer meg: Evidence for an epileptic network?" *Frontiers in Neurology*, vol. 4, article 56, Article ID Article 56, 2013.
- [14] S. E. Robinson, S. S. Nagarajan, M. Mantle, V. Gibbons, and H. Kirsch, "Localization of interictal spikes using SAM(g2) and dipole fit," *Neurology & Clinical Neurophysiology*, vol. 2004, article 74, 2004.
- [15] I. Sugiyama, K. Imai, Y. Yamaguchi et al., "Localization of epileptic foci in children with intractable epilepsy secondary to multiple cortical tubers by using synthetic aperture magnetometry kurtosis," *Journal of Neurosurgery: Pediatrics*, vol. 4, no. 6, pp. 515–522, 2009.
- [16] N. Tzourio-Mazoyer, B. Landeau, D. Papathanassiou et al., "Automated anatomical labeling of activations in SPM using a macroscopic anatomical parcellation of the MNI MRI single-subject brain," *NeuroImage*, vol. 15, no. 1, pp. 273–289, 2002.
- [17] E. Paglioli, A. Palmi, M. Portuguez et al., "Seizure and memory outcome following temporal lobe surgery: selective compared with nonselective approaches for hippocampal sclerosis," *Journal of Neurosurgery*, vol. 104, no. 1, pp. 70–78, 2006.
- [18] H. Bate, P. Eldridge, T. Varma, and U. C. Wiesmann, "The seizure outcome after amygdalohippocampectomy and temporal lobectomy," *European Journal of Neurology*, vol. 14, no. 1, pp. 90–94, 2007.
- [19] V. Salanova, O. Markand, and R. Worth, "Temporal lobe epilepsy: analysis of failures and the role of reoperation," *Acta Neurologica Scandinavica*, vol. 111, no. 2, pp. 126–133, 2005.
- [20] M. J. Hennessy, R. D. C. Elwes, C. D. Binnie, and C. E. Polkey, "Failed surgery for epilepsy: a study of persistence and recurrence of seizures following temporal resection," *Brain*, vol. 123, no. 12, pp. 2445–2466, 2000.

- [21] C. Tonini, E. Beghi, A. T. Berg et al., "Predictors of epilepsy surgery outcome: a meta-analysis," *Epilepsy Research*, vol. 62, no. 1, pp. 75–87, 2004.
- [22] G. M. McKhann II, J. Schoenfeld-McNeill, D. E. Born, M. M. Haglund, and G. A. Ojemann, "Intraoperative hippocampal electrocorticography to predict the extent of hippocampal resection in temporal lobe epilepsy surgery," *Journal of Neurosurgery*, vol. 93, no. 1, pp. 44–52, 2000.
- [23] D. D. Spencer, S. S. Spencer, R. H. Mattson, P. D. Williamson, and R. A. Novelly, "Access to the posterior medial temporal lobe structures in the surgical treatment of temporal lobe epilepsy," *Neurosurgery*, vol. 15, no. 5, pp. 667–671, 1984.
- [24] A. Abosch, N. Bernasconi, W. Boling et al., "Factors predictive of suboptimal seizure control following selective amygdalohippocampectomy," *Journal of Neurosurgery*, vol. 97, no. 5, pp. 1142–1151, 2002.
- [25] J. Isnard, M. Guenot, K. Ostrowsky, M. Sindou, and F. Mauguiere, "The role of the insular cortex in temporal lobe epilepsy," *Annals of Neurology*, vol. 48, pp. 614–623, 2000.
- [26] W. Van Paesschen, P. Dupont, G. van Driel, H. van Billoen, and A. Maes, "SPECT perfusion changes during complex partial seizures in patients with hippocampal sclerosis," *Brain*, vol. 126, no. 5, pp. 1103–1111, 2003.
- [27] M. Catani, D. K. Jones, R. Donato, and D. H. Ffytche, "Occipito-temporal connections in the human brain," *Brain*, vol. 126, no. 9, pp. 2093–2107, 2003.
- [28] K. Hamandi, H. W. R. Powell, H. Laufs et al., "Combined EEG-fMRI and tractography to visualise propagation of epileptic activity," *Journal of Neurology, Neurosurgery and Psychiatry*, vol. 79, no. 5, pp. 594–597, 2008.
- [29] R. Wiest, L. Estermann, O. Scheidegger et al., "Widespread grey matter changes and hemodynamic correlates to interictal epileptiform discharges in pharmacoresistant mesial temporal epilepsy," *Journal of Neurology*, vol. 260, no. 6, pp. 1601–1610, 2013.
- [30] T. Bitan, D. Manor, I. A. Morocz, and A. Karni, "Effects of alphabeticality, practice and type of instruction on reading an artificial script: an fMRI study," *Cognitive Brain Research*, vol. 25, no. 1, pp. 90–106, 2005.
- [31] A. E. Cavanna and M. R. Trimble, "The precuneus: a review of its functional anatomy and behavioural correlates," *Brain*, vol. 129, no. 3, pp. 564–583, 2006.
- [32] P. Dupont, J. J. Zaknun, A. Maes et al., "Dynamic perfusion patterns in temporal lobe epilepsy," *European Journal of Nuclear Medicine and Molecular Imaging*, vol. 36, no. 5, pp. 823–830, 2009.
- [33] R. L. Buckner and D. C. Carroll, "Self-projection and the brain," *Trends in Cognitive Sciences*, vol. 11, pp. 49–57, 2007.
- [34] R. L. Buckner, J. R. Andrews-Hanna, and D. L. Schacter, "The brain's default network: anatomy, function, and relevance to disease," *Annals of the New York Academy of Sciences*, vol. 1124, pp. 1–38, 2008.
- [35] N. Nelissen, W. van Paesschen, K. Baete et al., "Correlations of interictal FDG-PET metabolism and ictal SPECT perfusion changes in human temporal lobe epilepsy with hippocampal sclerosis," *NeuroImage*, vol. 32, no. 2, pp. 684–695, 2006.
- [36] Z. Xiao, J. Xiang, S. Holowka et al., "Volumetric localization of epileptic activities in tuberous sclerosis using synthetic aperture magnetometry," *Pediatric Radiology*, vol. 36, no. 1, pp. 16–21, 2006.
- [37] J. S. Archer, D. F. Abbott, A. B. Waites, and G. D. Jackson, "fMRI "deactivation" of the posterior cingulate during generalized spike and wave," *NeuroImage*, vol. 20, no. 4, pp. 1915–1922, 2003.
- [38] Y. Harrison and J. A. Horne, "The impact of sleep deprivation on decision making: a review," *Journal of Experimental Psychology: Applied*, vol. 6, no. 3, pp. 236–249, 2000.
- [39] M. Thomas, H. Sing, G. Belenky et al., "Neural basis of alertness and cognitive performance impairments during sleepiness. I. Effects of 24 h of sleep deprivation on waking human regional brain activity," *Journal of Sleep Research*, vol. 9, no. 4, pp. 335–352, 2000.

Research Article

Altered Modular Organization of Functional Connectivity Networks in Cirrhotic Patients without Overt Hepatic Encephalopathy

Gang Zheng,^{1,2} Liping Zhang,³ Long Jiang Zhang,¹ Qiang Li,^{1,3} Zhiying Pan,^{1,2} Xue Liang,¹ Donghong Shi,¹ and Guang Ming Lu¹

¹ Department of Medical Imaging, Jinling Hospital, Clinical School of Medical College, Nanjing University, Nanjing, Jiangsu 210002, China

² College of Civil Aviation, Nanjing University of Aeronautics and Astronautics, Nanjing, Jiangsu 210016, China

³ College of Natural Science, Nanjing University of Aeronautics and Astronautics, Nanjing, Jiangsu 210016, China

Correspondence should be addressed to Long Jiang Zhang; kevinzhjl@163.com and Guang Ming Lu; cjr.luguangming@vip.163.com

Received 6 November 2013; Revised 6 April 2014; Accepted 10 April 2014; Published 5 June 2014

Academic Editor: Hengyi Rao

Copyright © 2014 Gang Zheng et al. This is an open access article distributed under the Creative Commons Attribution License, which permits unrestricted use, distribution, and reproduction in any medium, provided the original work is properly cited.

Minimal hepatic encephalopathy (MHE) is associated with changes in functional connectivity. To investigate the patterns of modular changes of the functional connectivity in the progression of MHE, resting-state functional magnetic resonance imaging was acquired in 24 MHE patients, 31 cirrhotic patients without minimal hepatic encephalopathy (non-HE), and 38 healthy controls. Newman's metric, the modularity Q value, was maximized and compared in three groups. Topological roles with the progression of MHE were illustrated by intra- and intermodular connectivity changes. Results showed that the Q value of MHE patients was significantly lower than that of controls ($P < 0.01$) rather than that of non-HE patients ($P > 0.05$), which was correlated with neuropsychological test scores rather than the ammonia level and Child-Pugh score. Less intrasubcortical connections and more isolated subcortical modules were found with the progression of MHE. The non-HE patients had the same numbers of connect nodes as controls and had more hubs compared with MHE patients and healthy controls. Our findings supported that both intra- and intermodular connectivity, especially those related to subcortical regions, were continuously impaired in cirrhotic patients. The adjustments of hubs and connector nodes in non-HE patients could be a compensation for the decreased modularity in their functional connectivity networks.

1. Introduction

The human brain can be regarded as a complex network, which is organized intrinsically as highly modular architectures with inter- and intramodular links between brain regions [1–5]. The modules or communities of a complex network are subsets of nodes [4, 6–8]. Modularity in the human brain has been identified by both structural and functional MRI studies [1, 2]. Detection and characterization of modular structure in the brain system can help identify groups of anatomically and/or functionally associated components performing specific biological functions [3]. Modular structure is crucial for the robustness of network stability and optimal network functions [9], and modular structure is related to the

balance of functional segregation and integration and high resilience to network node or edge damage. It has been shown that modularity of brain networks may play a critical role in the evolution and neurodevelopment [2]. Some studies have shown the disruptions of functional brain network modularity in patients with childhood-onset schizophrenia [10], schizophrenia [11, 12], epilepsy [13, 14], and chronic back pain [15].

Hepatic encephalopathy (HE) is a serious neuropsychiatric complication of both acute and chronic hepatic dysfunctions [16], which is characterized by a wide clinical spectrum, ranging from mild cognitive impairment to coma and death. Minimal hepatic encephalopathy (MHE), the mildest form of the spectrum of HE, usually has no

recognizable clinical symptoms of HE but has mild cognitive, motor control, and concentration attention deficits [17, 18]. In recent years, the diagnosis, pathophysiological mechanisms, and treatment of MHE have drawn wide attention. Many functional MRI (fMRI) studies have been performed to clarify the pathophysiological mechanisms of MHE. Some fMRI studies focus on the analysis of regional brain networks, supporting that the regional functional connectivity modules (e.g., cognitive, motor control, and concentration attention) of cirrhotic patients were impaired [19–21]. Different from those studies based on regional brain networks, Zhang et al. investigated patterns of whole-brain functional connectivity in cirrhotic patients with MHE and found widespread cortical and subcortical network connectivity changes, suggesting that not only functional connectivities within regions but also those between functional modules were impaired in MHE patients [22]. In particular, the impairment in the basal ganglia-thalamocortical circuit was found which could play an important role in mediating neurocognitive dysfunctions, especially for psychomotor speed and attention deficits in patients with MHE [22, 23, 37]. However, it is still unclear how functional connectivity within and between modules changes during the progression of MHE.

Based on the previous findings of widespread decreased cortical and subcortical network connectivity in MHE patients, we hypothesize that the community structure itself, including inter- and intramodular links between brain regions, is impaired in MHE patients, and functional connectivity change in the modular organized brain is associated with the development of MHE. The aim of this study was to quantitatively evaluate the modularity changes of functional connectivity network in healthy subjects, cirrhotic patients without minimal HE (non-HE), and MHE patients and to illustrate the patterns of spatial change of modular community structure in the development of MHE. Additionally, we aimed to evaluate the relationship between quantitative measures of modular community structure and the venous ammonia level, Child-Pugh score, and neuropsychological test scores in cirrhosis patients.

2. Materials and Methods

2.1. Subjects. This study was approved by local institutional review board and was conducted in compliance with Health Insurance Portability and Accountability Act. All subjects gave written informed consent before fMRI or neuropsychologic evaluation. 61 adult patients with cirrhosis (45 males and 16 females; mean age 49.3 ± 10.5 years) were recruited from our inpatient or outpatient departments during June of 2009 and June of 2013. The patients MHE was defined and classified according to the final report of the working party at the 11th World Congresses of Gastroenterology in Vienna in 1998 [16]. The inclusion criteria for recruitment of the patients were as follows: the patients have no clinically proven HE; the patients do not have any MRI contraindication, such as artificial tooth or other foreign bodies in the head causing significant artifacts, which would affect the fMRI exam; all patients had no other diseases affecting brain function, such as drug abuse, psychiatric diseases, and trauma. Thirty-nine age- and

gender-matched healthy volunteers were recruited from local community as controls (25 males and 14 females, mean age 49.1 ± 12.8 years). All healthy subjects had neither psychiatric nor neurological history and also no diseases affecting brain structure and functions. Abdominal ultrasound scans revealed no abnormal findings for all healthy subjects. For evaluation of MHE, two typical neuropsychiatric tests, number connection test type A (NCT-A) and digit symbol test (DST), were given to all subjects before MRI studies. A test result was considered abnormal if 2SD is above the mean score of healthy subjects in NCT-A and/or 2SD is below the mean score of healthy subjects in DST. The subject demographics and clinical data are summarized in Table 1.

2.2. Laboratory Examinations. Blood biochemistry tests, including prothrombin time, protein metabolism tests (including total protein, globulin, albumin, and the ration of albumin and globulin), bilirubin metabolism tests (including total bilirubin, direct bilirubin, and indirect bilirubin), glutamic pyruvic transaminase, and glutamic oxaloacetic transaminase, were performed within 24 hours before MRI scanning for all patients. Some of the tests above were used to calculate the Child-Pugh score to assess the severity of cirrhosis. The scoring system considered five variables selected by clinical experience, that is, ascites, encephalopathy, prothrombin time, and serum levels of bilirubin and albumin. A score ranging from 1 to 3 was assigned to each variable. Patients were classified into class A (scores 5–6), B (scores 7–9), or C (scores 10–15). Thirteen outpatients did not have the venous blood ammonia test. Laboratory tests were not prescribed to the normal subjects.

2.3. Magnetic Resonance Imaging and Preprocessing of fMRI Data. All experiments were performed using a clinical 3T whole-body scanner (TIM Trio, Siemens Medical Solutions, Erlangen, Germany) using a standard birdcage head transmit/receive coil. The head coil was positioned carefully to reduce head movement. A total of 250 volumes of EPI images were obtained axially and the parameters were as follows: field-of-view (FOV) = $240 \times 240 \text{ mm}^2$, matrix size = 64×64 , flip angle = 90° , TR = 2000 ms, TE = 30 ms, slice thickness = 4 mm, distance factor = 10%, slices = 30. For each subject, a magnetization-prepared, rapid acquisition gradient echo image with isotropic resolution of 1 mm was acquired to obtain high-resolution, T1-weighted anatomical images for spatial normalization. During MRI scans, all subjects were instructed to rest with their eyes closed and heads still.

Resting-state fMRI (rs-fMRI) data were preprocessed by SPM8 (Statistical Parametric Mapping, <http://www.fil.ion.ucl.ac.uk/spm/>). The first 10 volumes were discarded to allow for T1 equilibration effects. Then, slice timing and realignments were performed on the remaining 240 measures. The time course of head motion was obtained by estimating the translation in each direction and the rotation in angular motion on each axis for all 240 consecutive volumes. Six patients (4 males) and one healthy subject were excluded because either translation or rotation exceeded $+1 \text{ mm}$ or $+1$. We also evaluated the differences in translation and rotation

TABLE 1: Demographical and clinical data of the healthy controls and cirrhotic patients.

Variable	Healthy controls ($n = 38$)	non-HE patients ($n = 31$)	MHE patients ($n = 24$)	P value
Age (Y)	48.6 ± 12.7	46.6 ± 10.2	52.3 ± 9.2	0.187 [†]
Gender (M/F)	25/13	24/7	19/5	0.411 [~]
NCT-A (s) ^{*#}	45.1 ± 12.7	42.7 ± 9.6	69.5 ± 17.4	<0.001 [†]
DST (score) ^{**§}	49.8 ± 9.8	42.5 ± 9.6	25.6 ± 7.7	<0.001 [†]
Posthepatic cirrhosis (n)	—	21	17	—
Biliary cirrhosis (n)	—	3	3	—
Schistosomal cirrhosis (n)	—	0	1	—
Alcoholic cirrhosis (n)	—	1	1	—
Budd-Chiari syndrome (n)	—	1	0	—
Unknown aetiology (n)	—	5	2	—
Child-Pugh scores (score)	—	6.4 ± 1.5	6.8 ± 1.7	0.40 [†]
Child-Pugh scale (A/B/C)	—	20/10/1	11/12/1	—
Ammonia level (umol/L) [@]	—	52.8 ± 34.6 ($n = 26$)	61.2 ± 28.8 ($n = 19$)	0.398 [†]

Values are mean ± SD or number of patients; MHE: minimal hepatic encephalopathy; NCT-A: number connection test type A; DST: digit symbol test.

[@] Ammonia is obtained in 19 MHE patients and 26 non-HE patients.

[†] stands for the results of two-sample t -test.

[‡] stands for the result of the one-way ANOVA.

[~] stands for the result of the Chi-Square test.

^{*} stands for significant difference between MHE and non-HE patients (post hoc $P < 0.05$, Bonferroni-corrected).

[#] stands for significant difference between MHE patients and controls (post hoc $P < 0.05$, Bonferroni-corrected).

[§] stands for significant differences between non-HE patients and controls (post hoc $P < 0.05$, Bonferroni-corrected).

of head motion between cirrhotic patients and controls according to the following formula [24]:

$$\frac{\text{Head motion}}{\text{rotation}} = \frac{1}{1-L} \sum_{i=2}^L \sqrt{(x_i - x_{i-1})^2 + (y_i - y_{i-1})^2 + (z_i - z_{i-1})^2}, \quad (1)$$

where L is the length of the time series ($L = 240$ in this study) and x_i , y_i , and z_i are translations/rotations at the i th time point in the x , y , and z directions, respectively. The results showed that the two groups had no significant differences (two-sample t -test, both $P > 0.05$). The functional data were spatially normalized to the Montreal Neurological Institute (MNI) template and resampled to $3 * 3 * 3 \text{ mm}^3$. After spatial normalization, the BOLD signal was detrended to abandon linear trend and then filtered (0.01–0.08 Hz) to reduce the effects of low-frequency drift and high-frequency physiological noise. Nuisance covariates including global mean signals, white matter signals, cerebrospinal fluid signals, and head motion parameters were regressed out from the rs-fMRI data. Finally, we obtained mean time series of 90 regions of interests (ROIs) defined by Automated Anatomical Labeling (AAL) atlas [25] for each individual by averaging the rs-fMRI time series over all voxels in each ROI. To demonstrate module changes of functional regions, we mainly computed the functional connectivity networks and their corresponding graph analysis features based on AAL 90 template in this study.

Considering that the range of nodal scales and the difference in template parcellations may result in considerable variation of graph theoretical parameters of functional

connectivity networks, we also applied a high-resolution parcellation network with 1024 regions of interest [26] to verify the modularity changes in cirrhotic patients' brain functional connectivity networks.

2.4. Functional Connectivity Network and Its Modularity. The Pearson correlation coefficient between any pair of regional time series is computed to form a $90 * 90$ matrix of the functional connectivity network. In each subject, the node amount N is 90 and the total number of functional connectivities (or edges) is 4005 ($C_{90}^2 = 90 * 89/2 = 4005$). Fisher's r -to- z transform is used on the correlation matrix R_{ij} ($i, j = 1, \dots, N$) of each subject to improve the normality of the correlation coefficients [27]. Both positive and negative connections are connectivity in brain network. The absolute value of correlation coefficient is calculated to create the non-negative matrix M_{ij} [2]. For simplification, M_{ij} of each subject is thresholded to create a binarized matrix A_{ij} in a range of sparsity, comprising between 5% and 10% of the 4,005 possible edges in a network with 90 nodes [28].

In our study, Newman's metric [5] is used as a measure of modularity. The correlation matrices were processed by a code developed by Clauset et al. based on the greedy optimization [29]. Modularity can be regarded as the quantity for measuring the quality of a partition PA of a network. If we define the degree $k_i = \sum_j A_{ij}$ of a node i as the number of connections to the node, the modularity Q of each subject can be expressed by

$$Q = \frac{1}{2m} \sum_{C \in PA} \sum_{i, j \in C} \left(A_{ij} - \frac{k_i k_j}{2m} \right), \quad (2)$$

where m is the total edges in the network; the indices i and j run over the N nodes of the graph; the index C runs over the modules of the partition PA .

To display the functional modules of healthy control, non-HE and MHE groups, the weighted matrix M_{ij} is first averaged within each group by

$$\text{Group } M_{ij} = \frac{1}{n_{\text{Group}}} \sum_{n=1}^{n_{\text{Group}}} \text{Group } M_{ij}^n, \quad (3)$$

where Group = Control, non-HE, or MHE represents the healthy control, non-HE or MHE group and n_{Group} is the total subject number of healthy controls, non-HE or MHE groups. Then, the averaged matrix of each group is thresholded at a sparsity to obtain the binarized matrix $\text{Group}_{\text{Sparsity}} A_{ij}$. Finally, the module of each group can be achieved by finding the partition having the largest value of $\text{Group}_{\text{Sparsity}} Q$ in $\text{Group}_{\text{Sparsity}} A_{ij}$.

Whenever $\text{Group}_{\text{Sparsity}} Q$ of a network reaches maximum, topological principles to each node in group level can be obtained based on the density of intra- and intermodular functional connectivity [30]. Intramodular connectivity is measured by the normalized intramodular degree:

$$z_i = \frac{k_{s_i} - \bar{k}_s}{\sigma_{k_s}}, \quad (4)$$

where k_{s_i} is the degree connecting the i th node to other nodes in the s th module, \bar{k}_s is the average of k_{s_i} in the module s , and σ_{k_s} is the standard deviation of the intramodular degrees in the s th module.

Intermodular connectivity can be measured by the participation coefficient:

$$PC_i = 1 - \sum_{s=1}^{N_s} \frac{k_{s_i}}{k_i}, \quad (5)$$

where k_{s_i} is the intramodular degree as defined above, k_i is the total degree of the i th node, and N_s is the number of modules. A node with large Z value will have a large number of intramodular connections relative to other nodes in the same module. If a node is linked exclusively to all other modules in the community, its PC value will be close to one; if it is extensively linked in its own module to other nodes, its PC value will be zero.

Based on the PC and Z values, nodes of a given functional connectivity network can be partitioned into four categories: connector hub, connector nonhub, provincial hub, and provincial nonhub [2]. A node with PC value greater than 0.05 is regarded as a connector node; otherwise, it is a provincial one. A node with Z value larger than 1.0 is defined as a hub; otherwise, it is defined as a nonhub. Graphs with different types of nodes are visualized using Pajek (<http://vlado.fmf.uni-lj.si/pub/networks/pajek/>).

2.5. Statistical Analysis. Statistical analysis was performed by using the software SPSS version 13.0 (SPSS Inc. Chicago, IL, USA). One way analysis of covariance (ANCOVA) with

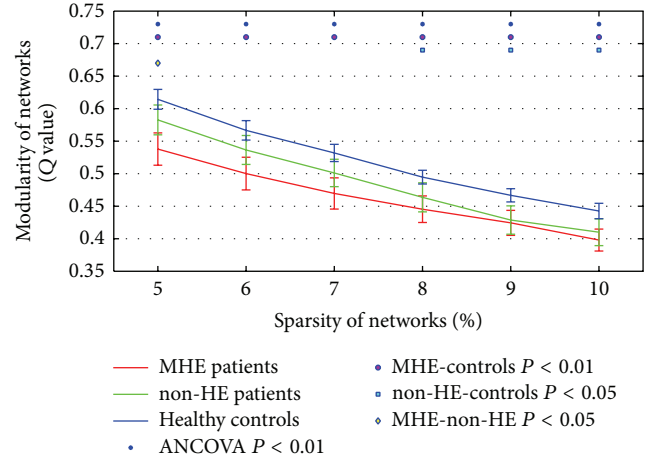


FIGURE 1: The network modularity Q values of healthy controls, non-HE and MHE patients from sparsity of 5% to sparsity of 10% at 1% intervals.

age and gender as covariates was used to analyze the difference of the modularity measure Q among healthy controls, non-HE and MHE patients. Post hoc comparisons (Sidak-corrected) were performed between every two groups at each sparsity. Correlations between Q values and the venous blood ammonia level, Child-Pugh score, and neuropsychological test scores were calculated. All data were shown as mean \pm SD. A P value less than 0.05 was considered statistically significant.

3. Results

3.1. Demographical and Clinical Data. Fifty-five patients (43 males and 12 females, mean age, 49.1 ± 10.1 years) and 38 controls (26 males and 12 females, mean age, 48.6 ± 12.7 years), matched for age ($P = 0.995$, two-sample t -test) and gender ($P = 0.216$, Mann-Whitney U test), were included for further analysis. Healthy subjects had a NCT-A score of 45.1 ± 12.7 s and a DST score of 49.8 ± 9.8 . These scores were used to differentiate MHE patients from non-HE patients. Thirty-one patients (24 males and 7 females, mean age, 46.6 ± 10.2 years) with normal NCT-A scores and DST scores were classified as non-HE patients and twenty-four patients (19 males and 5 females, mean age, 52.3 ± 9.2 years) with abnormal NCT-A or DST test scores were identified as MHE (Table 1). No correlation was found between the venous blood ammonia level, Child-Pugh score, and the neuropsychiatric tests (both $P > 0.05$) in cirrhotic patients.

3.2. The Modularity Q Values of Healthy Control, non-HE and MHE Patients. The modularity Q values of healthy control, non-HE and MHE patients were illustrated from sparsity of 5% to sparsity of 10% at 1% intervals in Figure 1. One-way ANCOVA results showed significant differences in the Q value among healthy controls, non-HE and MHE patients ($P < 0.01$). For three groups, the Q value declined monotonically as a function of increasing sparsity; that is,

TABLE 2: Correlations between the modularity Q values and the venous ammonia level, Child-Pugh score, and neuropsychological test scores.

Sparsity	5%	6%	7%	8%	9%	10%
NCT-A (s) ^a	0.393***	0.379***	0.341***	0.330**	0.283**	0.339***
DST (score) ^a	-0.342***	-0.288**	-0.250*	-0.194	-0.148	-0.201
Child-Pugh score ^b	-0.072	-0.086	-0.078	-0.022	0.034	0.035
Ammonia level (umol/L) ^b	0.050	-0.006	-0.051	0.054	0.065	0.047

NCT-A: number connection test type A; DST: digit symbol test.

^aCorrelations were performed in all subjects.

^bCorrelations were performed in cirrhotic patients.

* $P < 0.05$, ** $P < 0.01$, and *** $P < 0.001$.

maximum modularity would be greatest for networks with highest sparsity. Post hoc analysis showed that the modularity of brain networks in MHE patients was significantly lower than those in healthy controls over the entire range of sparsity ($P < 0.01$). Moreover, the modularity of non-HE patients was markedly lower than controls at $8\% \leq \text{sparsity} \leq 10\%$ ($P < 0.05$). In addition, the modularity of MHE patients was significantly lower than non-HE patients only at sparsity of 5% ($P < 0.05$). Correlation coefficients between the modularity Q values and the venous blood ammonia level, Child-Pugh score, and neuropsychological test scores were shown in Table 2. The Q values were positively correlated with NCT-A scores in all selected sparsity and were negatively correlated with DST score at $5\% \leq \text{sparsity} \leq 7\%$. No correlation was found between Q values and the venous blood ammonia level and Child-Pugh score (all $P > 0.05$).

We also verified the modularity Q values of three groups using 1024 template (see Supplementary Figure 1 available online at <http://dx.doi.org/10.1155/2014/727452>). The modularity results based on high-resolution parcellation were consistent with our findings using AAL 90 template.

3.3. The Total Number of Modules and the Selection of the Sparsity of Functional Connectivity Networks. Figure 2 shows the total number of modules of each group's mean network over the entire range of sparsity. The modules of three groups' mean networks nearly decreased as a function of increase in connection density. The number of modules in the MHE group was greater than that in the non-HE and healthy control group over the entire sparsities. The number of modules of non-HE group was higher than that of controls at $6\% \leq \text{sparsity} \leq 8\%$.

Salvador et al. suggested that 90 cortical and subcortical regions could be partitioned by cluster analysis into 6 major systems of anatomically and functionally related regions in healthy subjects [30]. If the density is high, many small modules might immigrate into a large module. At $9\% \leq \text{sparsity} \leq 10\%$, there were only five modules in our healthy controls which would limit the illustration of modules of three groups. Hence, low connection densities, for example, sparsity $\leq 8\%$, should be chosen to calculate the modules. However, if the density is too low, the binary networks would be too sparse to ensure the full connection of nodes. In normal subjects, the brain network was a fully connected one [2, 29, 30]. We found that there were isolated nodes in our

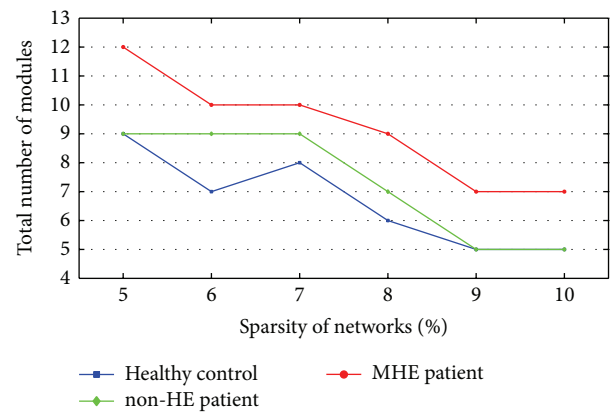


FIGURE 2: The total numbers of modules of healthy controls, non-HE and MHE groups from sparsity of 5% to sparsity of 10% at 1% intervals.

healthy controls when sparsity $\leq 7\%$. Considering the reasonable number of modules and connection of nodes in our healthy subjects, we mainly displayed the modules of healthy control, non-HE and MHE groups at sparsity = 8%, where our healthy control group had the same number of modules as that reported by Salvador et al. [30]. To show the consistent results at different thresholds, we also illustrated the modules of three groups at sparsities of 7% and 9%.

3.4. Modules Changes in Healthy Control, non-HE and MHE Groups. Figure 3 shows the community structures for three groups' brain functional networks at sparsity = 8%, respectively. To focus on the connectivity changes between cortical and subcortical regions and on the module changes of subcortical regions, only connections between cortical and subcortical regions and between subcortical regions were shown.

The healthy brain functional network comprised 6 connected modules at sparsity = 8%, which varied in size from 26 to 7 regional nodes (Figure 3(a)). Eight subcortical regions (e.g., bilateral caudate, putamens, pallidum, and thalami) were included in the second largest module containing 22 regions. Twenty-four edges were found between cortical and subcortical regions and between subcortical regions. Among 24 connections, 4 connectivities were found between cortical and subcortical regions, such as the connections between left insula and bilateral putamens, right insula and right putamen,

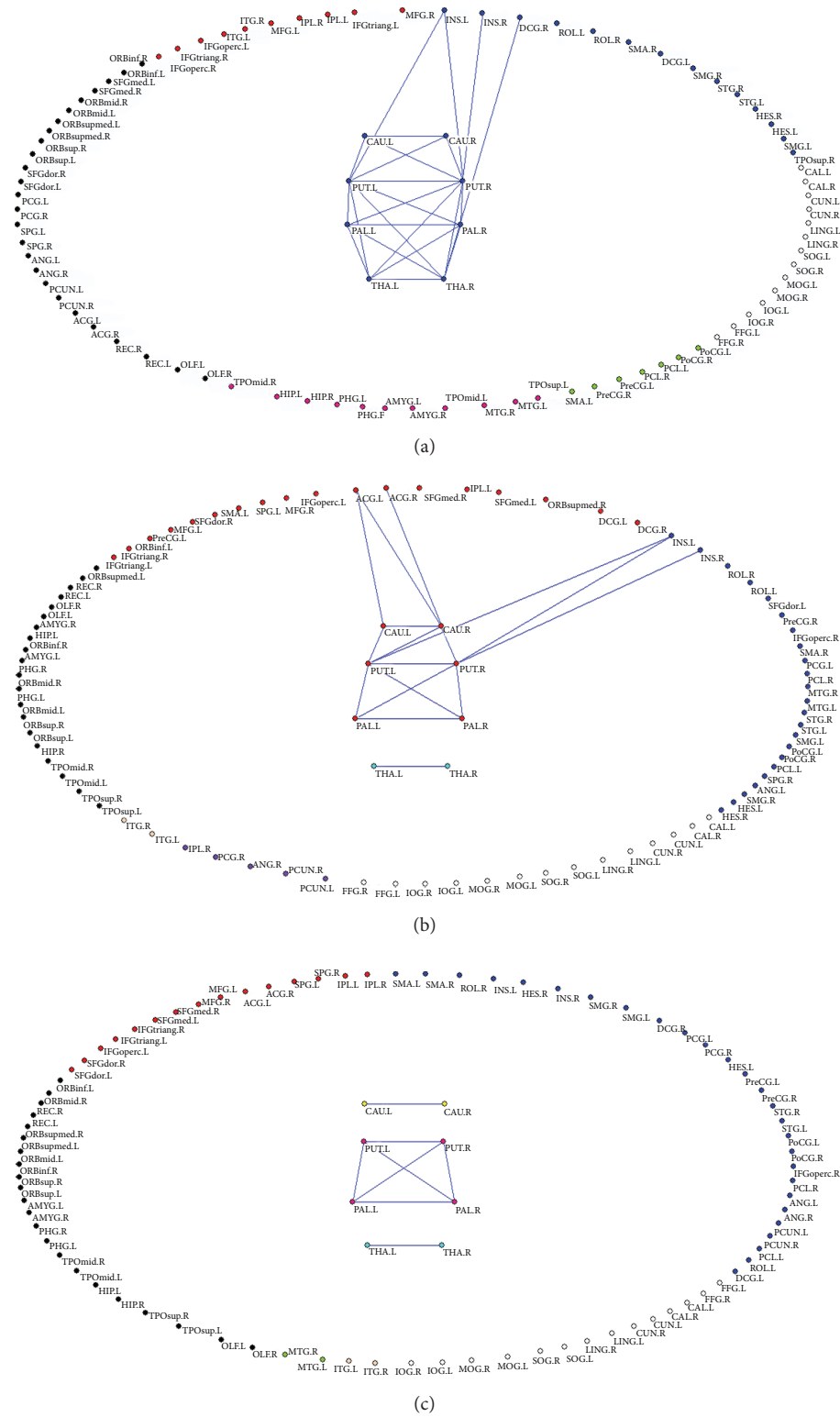


FIGURE 3: The community structures of healthy control, non-HE and MHE groups for mean functional networks at sparsity of 8%. (a) The community structure of healthy control group; (b) the community structure of non-HE group; (c) the community structure of MHE group.

and between right middle cingulum gyrus (DCG) and right thalamus; 20 ones were between subcortical regions, for example, the connections between left and right caudate, bilateral caudate and bilateral putamens, left and right putamen, bilateral putamens and bilateral pallidum, left and right pallidum, bilateral putamens and bilateral thalami, bilateral pallidum and bilateral thalami, and left and right thalamus.

The non-HE group had 7 modules at sparsity = 8%, among which bilateral thalami were isolated as an unconnected module (Figure 3(b)). There was a connection between left and right thalamus, while there was no connection between thalamus and other brain regions. Basal ganglia were involved in the largest module with 24 region nodes. Sixteen connections were detected between cortical regions and basal ganglia and between subregions of basal ganglia. Among 16 connections, 6 edges were between cortical regions and basal ganglia, such as the connections between left anterior cingulate gyrus (ACG) and bilateral caudate, right ACG and right caudate, left insula and bilateral putamens, and right insula and right putamen; 10 ones were between subregions of basal ganglia, such as the edges between left and right caudate, left and right putamen, left and right pallidum, bilateral putamens and bilateral pallidum, left caudate and left putamen, and right caudate and bilateral putamens.

In the MHE group, 9 modules were found at sparsity = 8% (Figure 3(c)). The subcortical region nodes were partitioned into three isolated modules and they were the caudate module composed of bilateral caudate, the thalamus module composed of bilateral thalami, and the putamen/pallidum module comprising bilateral putamens and pallidum. Among subcortical nodes, there were connections between left and right caudate, left and right thalamus, and bilateral putamens and pallidum. No connectivity was found between cortical and subcortical nodes.

3.5. Changes of Node Roles in Healthy Control, non-HE and MHE Groups. The node roles of healthy control, non-HE and MHE groups were displayed by connector hub, connector nonhub, provincial hub, and provincial nonhub and all connections between nodes were shown at sparsity = 8% (Figure 4).

In both healthy control and non-HE groups' mean networks (Figures 4(a) and 4(b)), over half of the whole-brain regions (51/90) were connector nodes which had numerous connections to other modules, while only 38 regions were connector nodes in MHE group (Figure 4(c)). The connector coefficients for healthy control, non-HE and MHE groups were 56.7% (51/90), 56.7% (51/90), and 42.2% (38/90), respectively. The total number of hubs in non-HE group (Hubs = 15) was greater than those in healthy control group (Hubs = 11) and in MHE group (Hubs = 12). Eight of the 15 hubs in non-HE group were categorized as connector hubs and 7 as provincial hubs, but only 5 connector hubs/7 provincial hubs in the healthy controls and 7 connector hubs/5 provincial hubs in the MHE group.

To verify our findings about the altered modular structures in cirrhotic patients, we also demonstrated the modules of three groups at the 7% and 9% sparsities (Supplementary Figures 2 and 3). The modules at the 7% sparsity were very

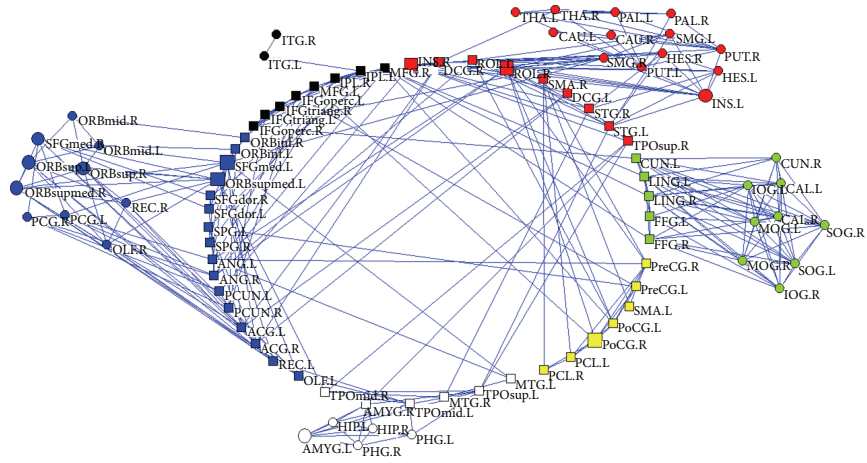
similar to those at 8% (Supplementary Figure 2). However, there was one isolated module in the healthy group. When the network sparsity was 9%, isolated modules in subcortical regions were also found in MHE patients (Supplementary Figure 3). However, modules with different brain functions were merged into large one, indicating that the brain regions were not well partitioned.

4. Discussion

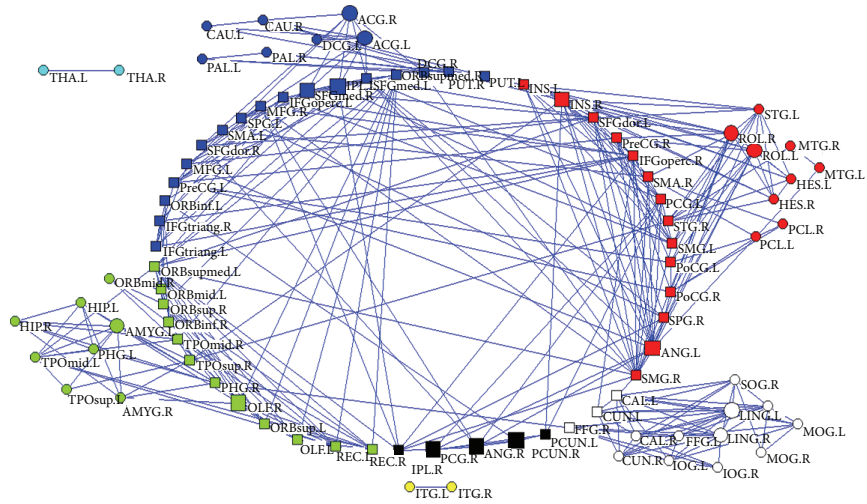
The present study showed (1) significantly decreased modularity of functional brain networks in cirrhotic patients, which depended on the severity of HE and was associated with neuropsychological test scores; (2) altered functional connectivity between cortical and subcortical modules, less intrasubcortical connection, and more isolated modules, related to the development of MHE; and (3) unchanged numbers of connect nodes and increased total hubs in non-HE patients.

Disrupted modularity of large-scale functional brain networks in cirrhotic patients within modules, reflected by decreased Q value, is expected because dysmetabolic neurotoxins were accumulated in patients' brains, resulting in the swelling of astrocytes and abnormal communication between neurons [31]. Since the modularity Q value is defined by the difference between the fraction of edges within each module and those random edges without regarding the community structure, it is able to represent the property of the connectivity structure within modules [5]. Networks with low modularity trend to be random graphs [2]. And hence, low Q values in cirrhotic patients, especially in MHE patients, supported that their functional connectivity networks lost self-organization properties within functional modules. Since the high clustering of connections between nodes in the same module will favor low wiring cost, modular networks may be of the property of small-worldness which is advantageous for nervous system design [32]. Previous small-world study in cirrhotic patients showed that small-worldness might decrease with the progression of HE [33]. Our modularity results supported that functional connectivity networks in cirrhotic patients were impaired in large-scale. Also, we found quantitative Q value correlated with neuropsychological test scores rather than with Child-Pugh score and venous blood ammonia level. Frontal dysfunction in MHE patients, such as attention [19, 21] and working memory impairment, has been consistently reported [34]. Our finding is consistent with these studies and indicates cognitive dysfunction can be associated with disrupted functional connectivity within modular structures in cirrhotic patients. Taken together, these support our disconnect hypothesis of HE; that is, disrupted regional brain connectivity network can be involved in the cognitive dysfunction in cirrhotic patients.

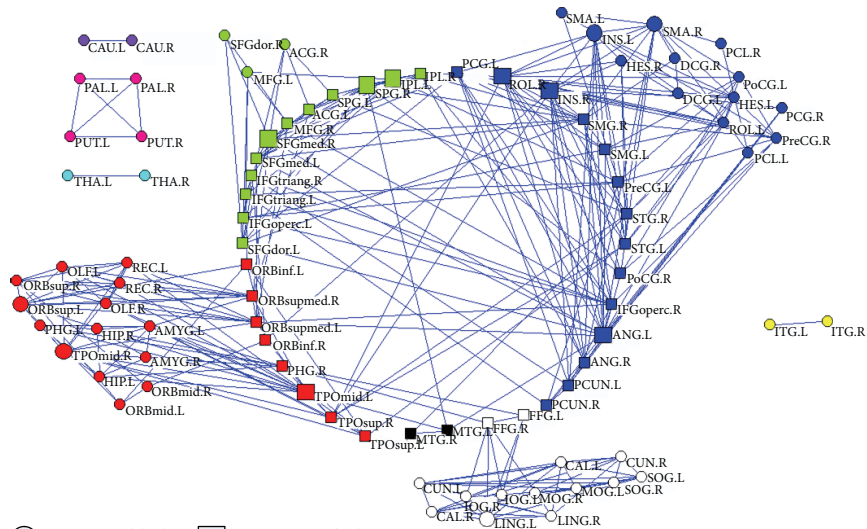
More modules in cirrhotic patients were found compared with those in controls, indicating that cirrhotic patients lost functional connectivity between modules. In particular, subcortical modularity loss, disrupted connections between cortical and subcortical modules, and less intrasubcortical connections occurred during the progression of the disease. Particularly in MHE patients, functional connectivity



(a)



(b)



(c)

FIGURE 4: The node roles of healthy control, non-HE and MHE groups. (a) The node role of healthy control group; (b) the node role of non-HE group; (c) the node role of MHE group.

between cortical and subcortical modules was disrupted, resulting in more isolated modules in these patients. These findings of more localized community structure in cirrhotic patients than in controls have been reported in previous literatures on aging, schizophrenia, epilepsy, and chronic back pain [2, 10–15]. We further found that more modules in cirrhotic patients can be associated with basal ganglia-thalamocortical circuit disruption because of lost community structure between these more localized subcortical communication structures (caudate nucleus, basal ganglia, and thalami) in MHE patients compared with healthy controls and non-HE patients, which depended on the severity of the disease as shown in Figure 3. This finding supported the important role of basal ganglia-thalamocortical circuit in the development of MHE [18]. Disrupted module organization of basal ganglia-thalamocortical circuit can be one of the key causes of more modules in cirrhotic patients than in controls. Histopathologically, Alzheimer type II astrocytes, the characteristic neuropathologic findings in cirrhotic patients, are predominantly found in the cortex, putamen, pallidum, and caudate nucleus [35]. Radiologically, the symmetrical hyperintensity of basal ganglia on T1-weighted images is often observed [36]. Recently fMRI studies indicated abnormal resting-state functional connectivity of this circuit in MHE patients [22, 23]. Disrupted effective connectivity network of the basal ganglia, anterior cingulate cortex, and striatum was also reported [37]. The decreased functional connectivity between thalamus, many cortices, and basal ganglia indicated reduced integrity of thalamic resting-state network in MHE. Taken together, we believe that disrupted modular structure and functional connectivity of basal ganglia-thalamocortical circuit could result in development of MHE.

Our study indicated non-HE patients had abnormal communication structures. The abnormal modularity findings in the non-HE patients included slightly decreased Q value and slightly increased modules. Importantly, in non-HE patients, the numbers of connect nodes did not change while the total numbers of hubs increased, indicating that there could be a compensation for the decreased modularity in their functional connectivity networks. Although more modules were found in non-HE patients compared with healthy subjects at the same sparsity, unchanged numbers of connect nodes could ensure the normal communications between functional modules. More connector and provincial hubs were found in non-HE patients, suggesting that more hubs were needed to make up the degradations of functional connectivity both between and within modules. In MHE patients, the numbers of connect nodes greatly decreased, which might not be sufficient for the basic information transmission between modules, explaining why more isolated modules were found in MHE patients. MHE patients were of less connector and provincial hubs compared with non-HE patients, indicating that their brain networks were seriously impaired and could not make up the normal communications between modules by increasing hubs.

We did not find correlation between the venous blood ammonia level and Child-Pugh score with modularity Q values in three groups, which could be related to the cirrhotic patients recruited in our study. Since only cirrhotic patients

without overt HE were included in this study, the ammonia level and Child-Pugh score in our patients were not very high, which might make it difficult to show the relationships between the factors and the modularity Q values. Future studies should include the cirrhotic patients with overt hepatic encephalopathy.

4.1. Limitations. There are still some limitations in our study. First, the sample size of patients with minimal HE was small and this would affect the validity of the statistical analysis of this preliminary study. Thus, a large-cohort study is needed. However, since a standard statistical processing pipeline was followed with accepted software and procedures in this study, we believe most findings are rational based on these analyses. Second, this study was not longitudinal and overt HE patients were not included in this study. Therefore, we cannot draw a conclusion on the progression pattern of brain functional connectivity modularity from MHE to overt HE, which needs to be further investigated. Additionally, no significant correlations were found between liver functions and the modularity Q values in this study, which might also be related to the selection of our patients because no overt HE patients were included in this study. Third, we used two neuropsychiatric tests to evaluate MHE which were recommended by the working party at the 11th World Congresses of Gastroenterology. Whole battery of neuropsychiatric tests should be performed in future study. Fourth, although we tried to pick up a reasonable threshold to demonstrate our findings, it is rather arbitrary for the selection of thresholds. Hence, we suggested that different thresholds should be tested to find if results are sensitive to them.

5. Conclusions

In conclusion, our study demonstrated that cirrhotic patients had disrupted modularity of functional brain networks associated with neurocognitive dysfunction, in accordance with the severity of HE. Subcortical modularity loss, disrupted connection between cortical and subcortical modules, and less intrasubcortical connection, especially, in basal ganglia-thalamocortical circuit were found with the development of MHE. Adjustment of hub and provincial nodes could be a compensation for the disrupted modularity in non-HE patients.

Abbreviations

NCT-A: Number connection test type A
DST: Digit symbol test
MHE: Minimal hepatic encephalopathy
OHE: Overt hepatic encephalopathy
non-HE: Cirrhotic patients without minimal hepatic encephalopathy.

Conflict of Interests

The authors declare that there is no conflict of interests regarding the publication of this paper.

Authors' Contribution

Gang Zheng and Liping Zhang participated to an equal extent in planning, analyzing, evaluating, and writing the paper. Long Jiang Zhang contributed to critical revision of the paper. Qiang Li and Zhiying Pan contributed to statistical analysis. Xue Liang and Donghong Shi contributed to acquisition of data. Long Jiang Zhang and Guang Ming Lu contributed to study concept and supervision.

Acknowledgments

This work is supported by Grants from the National Natural Science Foundation of China (Grant no. 81101039 to Gang Zheng and Grants nos. 81322020, 81230032, 81171313, and 30700194 to Long Jiang Zhang), China Postdoctoral Science Foundation of Jiangsu Province (Grant no. 1002083C to Gang Zheng), and Natural Science Foundation of Jiangsu Province (Grant no. BK2007572 to Long Jiang Zhang).

References

- [1] Z. J. Chen, Y. He, P. Rosa-Neto, J. Germann, and A. C. Evans, "Revealing modular architecture of human brain structural networks by using cortical thickness from MRI," *Cerebral Cortex*, vol. 18, no. 10, pp. 2374–2381, 2008.
- [2] D. Meunier, S. Achard, A. Morcom, and E. Bullmore, "Age-related changes in modular organization of human brain functional networks," *NeuroImage*, vol. 44, no. 3, pp. 715–723, 2009.
- [3] T.-W. Hsu, C. W. Wu, Y.-F. Cheng et al., "Impaired small-world network efficiency and dynamic functional distribution in patients with cirrhosis," *PLoS ONE*, vol. 7, no. 5, Article ID e35266, 2012.
- [4] M. E. J. Newman and M. Girvan, "Finding and evaluating community structure in networks," *Physical Review E: Statistical, Nonlinear, and Soft Matter Physics*, vol. 69, no. 2, part 2, Article ID 026113, 2004.
- [5] M. E. Newman, "Fast algorithm for detecting community structure in networks," *Physical Review E: Statistical, Nonlinear, and Soft Matter Physics*, vol. 69, no. 6, part 2, Article ID 066133, 2004.
- [6] G. Palla, I. Derényi, I. Farkas, and T. Vicsek, "Uncovering the overlapping community structure of complex networks in nature and society," *Nature*, vol. 435, no. 7043, pp. 814–818, 2005.
- [7] E. Bullmore and O. Sporns, "Complex brain networks: graph theoretical analysis of structural and functional systems," *Nature Reviews Neuroscience*, vol. 10, no. 3, pp. 186–198, 2009.
- [8] A. J. Schwarz, A. Gozzi, and A. Bifone, "Community structure and modularity in networks of correlated brain activity," *Magnetic Resonance Imaging*, vol. 26, no. 7, pp. 914–920, 2008.
- [9] Y. He, J. Wang, L. Wang et al., "Uncovering intrinsic modular organization of spontaneous brain activity in humans," *PLoS ONE*, vol. 4, no. 4, Article ID e5226, 2009.
- [10] A. F. Alexander-Bloch, N. Gogtay, D. Meunier et al., "Disrupted modularity and local connectivity of brain functional networks in childhood-onset schizophrenia," *Frontiers in Systems Neuroscience*, vol. 4, article 147, 2010.
- [11] A. Alexander-Bloch, R. Lambiotte, B. Roberts, J. Giedd, N. Gogtay, and E. Bullmore, "The discovery of population differences in network community structure: new methods and applications to brain functional networks in schizophrenia," *NeuroImage*, vol. 59, no. 4, pp. 3889–3900, 2012.
- [12] Q. Yu, S. M. Plis, E. B. Erhardt et al., "Modular organization of functional network connectivity in healthy controls and patients with schizophrenia during the resting state," *Frontiers in Systems Neuroscience*, vol. 5, article 103, 2012.
- [13] M. Chavez, M. Valencia, V. Navarro, V. Latora, and J. Martinerie, "Functional modularity of background activities in normal and epileptic brain networks," *Physical Review Letters*, vol. 104, no. 11, Article ID 118701, 2010.
- [14] M. J. Vaessen, H. M. Braakman, J. S. Heerink et al., "Abnormal modular organization of functional networks in cognitively impaired children with frontal lobe epilepsy," *Cerebral Cortex*, vol. 23, no. 8, pp. 1997–2006, 2013.
- [15] P. Balenzuela, A. Chernomoretz, D. Fraiman et al., "Modular organization of brain resting state networks in chronic back pain patients," *Frontiers in Neuroinformatics*, vol. 4, article 116, 2010.
- [16] P. Ferenci, A. Lockwood, K. Mullen, R. Tarter, K. Weissenborn, and A. T. Blei, "Hepatic encephalopathy—definition, nomenclature, diagnosis, and quantification: final report of the working party at the 11th world congresses of gastroenterology, Vienna, 1998," *Hepatology*, vol. 35, no. 3, pp. 716–721, 2002.
- [17] K. Weissenborn, "Diagnosis of encephalopathy," *Digestion*, vol. 59, supplement 2, pp. 22–24, 1998.
- [18] P. Amodio, S. Montagnese, A. Gatta, and M. Y. Morgan, "Characteristics of minimal hepatic encephalopathy," *Metabolic Brain Disease*, vol. 19, no. 3-4, pp. 253–267, 2004.
- [19] R. Qi, L. J. Zhang, Q. Xu et al., "Selective impairments of resting-state networks in minimal hepatic encephalopathy," *PLoS ONE*, vol. 7, no. 5, Article ID e37400, 2012.
- [20] L. Zhang, R. Qi, S. Wu et al., "Brain default-mode network abnormalities in hepatic encephalopathy: a resting-state functional MRI study," *Human Brain Mapping*, vol. 33, no. 6, pp. 1384–1392, 2012.
- [21] L. J. Zhang, R. Qi, J. Zhong et al., "Disrupted functional connectivity of the anterior cingulate cortex in cirrhotic patients without overt hepatic encephalopathy: a resting state fMRI study," *PLoS ONE*, vol. 8, no. 1, Article ID e53206, 2013.
- [22] L. J. Zhang, G. Zheng, L. Zhang et al., "Altered brain functional connectivity in patients with cirrhosis and minimal hepatic encephalopathy: a functional MR imaging study," *Radiology*, vol. 265, no. 2, pp. 528–536, 2012.
- [23] R. Qi, L. J. Zhang, J. Zhong et al., "Disrupted thalamic resting-state functional connectivity in patients with minimal hepatic encephalopathy," *European Journal of Radiology*, vol. 82, no. 5, pp. 850–856, 2013.
- [24] Y. Liu, M. Liang, Y. Zhou et al., "Disrupted small-world networks in schizophrenia," *Brain*, vol. 131, no. 4, pp. 945–961, 2008.
- [25] N. Tzourio-Mazoyer, B. Landeau, D. Papathanassiou et al., "Automated anatomical labeling of activations in SPM using a macroscopic anatomical parcellation of the MNI MRI single-subject brain," *NeuroImage*, vol. 15, no. 1, pp. 273–289, 2002.
- [26] M. Cao, J. Wang, Z. Dai, X. Cao, L. Jiang, and F. Fan, "Topological organization of the human brain functional connectome across the lifespan," *Developmental Cognitive Neuroscience*, vol. 7, pp. 76–93, 2014.
- [27] D. J. Watts and S. H. Strogatz, "Collective dynamics of "small-world" networks," *Nature*, vol. 393, no. 6684, pp. 440–442, 1998.
- [28] S. Achard and E. Bullmore, "Efficiency and cost of economical brain functional networks," *PLoS Computational Biology*, vol. 3, no. 2, article e17, 2007.

- [29] A. Clauset, M. E. J. Newman, and C. Moore, "Finding community structure in very large networks," *Physical Review E: Statistical, Nonlinear, and Soft Matter Physics*, vol. 70, part 2, no. 6, Article ID 066111, 2004.
- [30] R. Salvador, J. Suckling, M. R. Coleman, J. D. Pickard, D. Menon, and E. Bullmore, "Neurophysiological architecture of functional magnetic resonance images of human brain," *Cerebral Cortex*, vol. 15, no. 9, pp. 1332–2342, 2005.
- [31] M. D. Norenberg, "Astroglial dysfunction in hepatic encephalopathy," *Metabolic Brain Disease*, vol. 13, no. 4, pp. 319–335, 1998.
- [32] D. Meunier, R. Lambiotte, and E. T. Bullmore, "Modular and hierarchically modular organization of brain networks," *Frontiers in Neuroscience*, vol. 4, article 200, 2010.
- [33] W.-C. Lin, T.-W. Hsu, C.-L. Chen et al., "Connectivity of default-mode network is associated with cerebral edema in hepatic encephalopathy," *PLoS ONE*, vol. 7, no. 5, Article ID e36986, 2012.
- [34] L.-M. Liao, L.-X. Zhou, H.-B. Le, J.-J. Yin, and S.-H. Ma, "Spatial working memory dysfunction in minimal hepatic encephalopathy: an ethology and BOLD-fMRI study," *Brain Research*, vol. 1445, pp. 62–72, 2012.
- [35] L. Spahr, P. R. Burkhard, H. Gröttsch, and A. Hadengue, "Clinical significance of basal ganglia alterations at brain MRI and 1H MRS in cirrhosis and role in the pathogenesis of hepatic encephalopathy," *Metabolic Brain Disease*, vol. 17, no. 4, pp. 399–413, 2002.
- [36] R. F. Butterworth, "Complications of cirrhosis III. Hepatic encephalopathy," *Journal of Hepatology*, vol. 32, supplement 1, pp. 171–180, 2000.
- [37] R. Qi, L. J. Zhang, J. Zhong et al., "Altered effective connectivity network of the basal ganglia in low-grade hepatic encephalopathy: a resting-state fMRI study with Granger causality analysis," *PLoS ONE*, vol. 8, no. 1, Article ID e53677, 2013.

Research Article

Intrinsic Functional Connectivity Networks in Healthy Elderly Subjects: A Multiparametric Approach with Structural Connectivity Analysis

Martin Gorges,¹ Hans-Peter Müller,¹ Albert C. Ludolph,¹
Volker Rasche,² and Jan Kassubek¹

¹ Department of Neurology, University of Ulm, Oberer Eselsberg 45, 89081 Ulm, Germany

² Experimental Cardiovascular Imaging, Core Facility Small Animal MRI, University of Ulm, Albert-Einstein-Allee 23, 89081 Ulm, Germany

Correspondence should be addressed to Martin Gorges; martin.gorges@uni-ulm.de

Received 7 March 2014; Revised 1 May 2014; Accepted 3 May 2014; Published 29 May 2014

Academic Editor: Yong He

Copyright © 2014 Martin Gorges et al. This is an open access article distributed under the Creative Commons Attribution License, which permits unrestricted use, distribution, and reproduction in any medium, provided the original work is properly cited.

Intrinsic functional connectivity magnetic resonance imaging (iFCMRI) provides an encouraging approach for mapping large-scale intrinsic connectivity networks (ICNs) in the “resting” brain. Structural connections as measured by diffusion tensor imaging (DTI) are a major constraint on the identified ICNs. This study aimed at the combined investigation of ten well-defined ICNs in healthy elderly subjects at single subject level as well as at the group level, together with the underlying structural connectivity. IFCMRI and DTI data were acquired in twelve subjects (68 ± 7 years) at a 3T scanner and were studied using the *tensor imaging and fiber tracking* software package. The seed-based iFCMRI analysis approach was comprehensively performed with DTI analysis, following standardized procedures including an 8-step processing of iFCMRI data. Our findings demonstrated robust ICNs at the single subject level and conclusive brain maps at the group level in the healthy elderly sample, supported by the complementary fiber tractography. The findings demonstrated here provide a methodological framework for future comparisons of pathological (e.g., neurodegenerative) conditions with healthy controls on the basis of multiparametric functional connectivity mapping.

1. Introduction

Soon after the development of functional MRI [1], Biswal et al. described oscillatory hemodynamics in low frequency range (<0.1 Hz) within regions in the motor cortex by demonstrating spontaneous blood oxygenation level dependent (BOLD) fluctuations in a highly correlated manner between functionally associated brain areas when the brain is “at rest” [2]. Mapping the functional connectome of the human brain remains challenging [3], since intrinsic functional connectivity (iFC) analysis in the “resting-state” is only an indirect proxy of the “ongoing” brain’s hemodynamics. Besides the fact that the acquired data might be confounded by several factors such as respiratory, pulsatile, or cardiovascular artifacts [4, 5], shortcomings of postprocessing are assumed to influence the shape of the BOLD response [6]. There is growing awareness of a large scale functional brain architecture structured in a

topological manner [7] and attributed to specific functional explication [8]. Notably, the functionally interacting portions of the brain that were demonstrated in the absence of specific tasks (“task-free”) correspond to a large extent to those regions that reveal “task-induced” coactivations in task-based functional MRI [9]. Neural signaling between brain areas is markedly constrained by the brain’s anatomy and hence by axonal bundles (fibers) that interconnect different brain segments/regions [10], forming an efficient network and comprising interconnected hubs [11].

The probably most extensively studied intrinsic connectivity network (ICN) is the default mode network (DMN) [12–14] that has been initially described by Raichle et al. [15]. This large scale system includes areas revealing the highest coherent low frequency oscillations in the absence of a specific task [12]. In the past decade many ICNs

have emerged consistently identified by means of iFCMRI comprising the dorsal and ventral attention systems [16, 17], executive control and salience processing [18], primary visual and visual associative systems [8, 19], cerebellar network [8, 20], functional integrity of the cingulate cortex [21], and further networks [20]. These ICNs were identified using the “hypothesis-driven” seed-based approach. Additionally, “data-driven” independent component analysis exists which allow for the identification of a series of independent components that could be interpreted as an extract of distinct functionally organized networks [4, 19, 22].

A number of studies investigated the relationship between functional and structural connectivity (see e.g., [23] for a review), showing convergence between the strengths of resting-state functional connectivity and structural connectivity. Since it is commonly assumed that functional connectivity reflects structural connectivity in the brain [23–25], brain connectivity has been proven to play an essential role in the pathological state [12, 26–28] as well as in healthy aging where changes in functional [29] and structural connectivity [30] have been reported during the lifespan. Still, different connectivity measures as used in multiparametric approaches (e.g., BOLD fMRI and DTI measures) are a promising issue for further research and clinical applications.

This study aimed at the investigation of ten well-defined ICNs as functional brain maps in healthy elderly subjects together with the complementary analysis of the underlying structural connectivity. From the methodological view, the functional and structural connectivity analysis was performed by use of the in-house developed software package *tensor imaging and fiber tracking* (TIFT) [31, 32] that is well-established for diffusion tensor imaging (DTI) analysis procedures [31]. For the analysis of the iFCMRI data, a standardized data processing approach will be demonstrated on an item-by-item basis. We utilized a single-voxel seed-based approach in order to identify the ICNs at single subject level with subsequent group level computation of brain maps from individuals’ data. This way, we aimed at demonstrating our concept to combine iFCMRI with DTI data on the basis of recent studies [10]. These algorithms used in the TIFT software were evaluated in a group of healthy elderly. The investigation of the elderly adult has major impact when defining a control group for assessments in many studies in aged individuals such as in neurodegenerative conditions that commonly manifest in late life. Thus, a reference compilation of ICNs together with the underlying anatomical structure is of great interest for clinical comparisons.

2. Materials and Methods

2.1. Subjects. All subjects gave written informed consent for the MRI protocol according to institutional guidelines. The study had been approved by the Ethics Committee of the University of Ulm and was performed in accordance with the ethical standards laid down in the 1964 Declaration of Helsinki and its later amendments.

Twelve healthy volunteers (mean age 68 ± 7 years, M/F ratio 7/5) were recruited from the controls’ database of

TABLE 1: Demographic data of the subjects.

Parameter	Healthy elderly subjects
Number	12
Gender, M/F	7/5
Age/y	67.8 ± 6.8 (59.1–81.4)
MMSE	29.8 ± 0.5 (29.0–30.0)
DemTect	17 (10–13)
Years of education	12.5 (10.0–13.0)

Data are given as mean \pm std (min–max).

MMSE: mini-mental state examination; DemTect [34].

the Department of Neurology, University of Ulm. Detailed demographic data are listed in Table 1. The investigated group consisted of volunteers with higher education without any psychiatric disorders or history of neurological or other medical conditions and free of any cognitive problems. Overall cognitive performance was screened by mini-mental state examination (MMSE) [33] as well as by global dementia screening (DemTect) [34]. Exclusion criteria were cerebrovascular diseases, psychiatric abnormalities, severe hearing damage, or significant white matter lesion load such as periventricular or deep white matter hyperintensities [35].

2.2. MRI Acquisition. MRI scanning was performed at a 3-Tesla clinical scanner (Magnetom Allegra, Siemens, Erlangen, Germany; SyngoMRA30). The protocol included a “resting-state” iFCMRI sequence, a DTI sequence, and a T1-weighted 3D magnetization-prepared gradient echo sequence (MPRAGE). The iFCMRI scanning protocol consisted of 200 volumes (36 slices, 64×64 pixels, slice thickness 3.5 mm, and pixel size $3.5 \text{ mm} \times 3.5 \text{ mm}$). The echo time (TE) and repetition time (TR) were 30 ms and 2200 ms, respectively. All participants were instructed to keep relaxed and motionless with their eyes closed but awake in the absence of goal-directed attention during iFCMRI data acquisition. The DTI protocol consisted of 31 gradient directions (GD), including one $b = 0$ reference (72 slices, 128×128 pixels). The slice thickness was 2.0 mm; in-plane pixel size was $2.0 \text{ mm} \times 2.0 \text{ mm}$. TE and TR were 95 ms and 12700 ms; b was 1000 s/mm^2 . For the morphological background, a T1-weighted MPRAGE was recorded for each control subject (TR 2500 ms, TE 4.32 ms, matrix size 256×256 pixels, 192 slices, slice thickness 1.0 mm, and in-plane pixel size $1.0 \times 1.0 \text{ mm}^2$).

2.3. iFCMRI Data Preprocessing: Overview. All described algorithms and postprocessing were integrated in the previously described analysis software TIFT. A standardized preprocessing procedure was applied to all iFCMRI data, comprising the following components.

2.3.1. Preprocessing Step 1: Quality Control and Motion Correction. To insure sufficient image quality, all volumes of the EPI and MPRAGE images were visually inspected for proper registration. As head motion influences iFCMRI [36], motion corrected data were obtained from the scanner software (syngo MRVA30A, Siemens, Erlangen, Germany)

that provides a 3-dimensional elastic motion correction in all directions.

2.3.2. Preprocessing Step 2: Resampling on a Cubic 1 mm Grid. The data were resampled from $3.5 \times 3.5 \times 3.5 \text{ mm}^3$ to a cubic 1 mm grid of a $256 \times 256 \times 256$ matrix by means of a nonparametric k -nearest neighbor regression approach [37] using the average voxel intensity of the k -nearest neighbor voxels weighted by the inverse of their distance. Upsampling to a cubic 1 mm grid has already been performed in previous studies (e.g., [31]). The advantage of using the identical voxel resolution for multiparametric studies such as this bimodal approach (DTI, iFCMRI) is that in this way voxel locations could be easily and unambiguously transferred from one modality to another and vice versa. In addition, performing analysis in a cubic 1 mm grid provides a prerequisite for the utilized seed-voxel approach.

2.3.3. Preprocessing Step 3: Stereotaxic Normalization. Normalization of the rescaled EPI images ($1.0 \times 1.0 \times 1.0 \text{ mm}^3$) to the Montreal Neurological Institute (MNI) stereotaxic standard space [38] was accomplished [32]. First eight landmarks were defined in the EPI data in the first volume for each subject. A linear transformation in all 6 degrees of freedom (x , y , z , pitch, roll, and yaw) into MNI space was performed according to the coordinates of these landmarks. This procedure was applied separately for each MRI modality (iFCMRI, DTI, MPRAGE) for all subjects' data (first volume) included in this study in order to compute a modality specific template by arithmetically averaging the voxel intensities of all individual MNI transformed images. The deformation procedure was refined in the second iteration step by nonlinear normalization of the individual EPI data onto the study-specific template following the basic ideas of Ashburner and Friston [39] of minimizing the squared differences of regional intensities between the individual first EPI volume and the EPI template. Validation of the MNI normalization was performed by calculating Pearson's product correlation coefficient between each individual EPI image (first volume of data series) and the EPI template as a quantitative measure. The landmarks were refined for each subject whose normalization was unacceptable according to a correlation coefficient of $r < 0.8$. The same template-based normalization procedure was applied to the high-resolution MPRAGE images used for seed-voxel definition and for the display of results on a morphological background. Figure 1 displays templates for the different modalities in comparison to the MPRAGE template.

2.3.4. Preprocessing Step 4: Spatial Filtering. Spatial filtering was applied to the EPI series of each subject's data by using a 7 mm full-width at half maximum (FWHM) Gaussian blur filter (3-dimensional bell shape representing normal distribution). The filter width of 7 mm equals twice the recording voxel size of 3.5 mm which is a common choice according to the assumption that the Gaussian filter is designed as a "matched filter" [40]. The matched filter theorem states that the width of the filter used to process the data should be

tailored to the size of the structure under investigation [41]. None of the data sets for both modalities iFCMRI and DTI had to be excluded prior to the analysis due to unacceptable artefacts. The effect of spatial filtering is exemplified in Figure 2.

2.3.5. Preprocessing Step 5: Temporal Linear Detrending and Temporal Bandpass Filtering. Possible scanner drifts during the iFCMRI data acquisition were voxelwise removed over each volume by linear detrending [42]. Linear detrending was performed by subtracting the linear fit of the voxel time course. The time courses were further bandpass-filtered since iFCMRI data analysis is based on the coherence of low-frequency BOLD fluctuations. The frequency spectrum was band-limited for cutoff frequencies in the range of $0.01 < f < 0.08 \text{ Hz}$ [4, 6, 43] using a 6th-order Butterworth bandpass filter design. The first 15 out of 200 volumes of each time course were discarded due to the transient filter response (see Figure 2(c)) and due to scanner oscillations at the beginning of iFCMRI data acquisition. Moreover, this commonly applied procedure allows the participant to adapt to the experimental condition [44].

2.3.6. Processing Step 6: Seed-Based Correlation. Large scale correlation maps were computed according to the seed-based approach [2] in accordance with recent studies [7, 45, 46]. Ten well-defined ICNs [8, 20, 27] were computed by placing seed-voxels (i.e., encompassing one voxel only) into regions that had been consistently reported to serve as central hubs for the respective ICN as listed in Table 2. The exact location of the seed was manually refined based on the subjects' averaged high-resolution T1-images (MPRAGE) according to the standardized MNI atlas [38]. Figure 3 displays the DMN calculated for a representative single subject in the MNI space. As a novel aspect, the time series of one single voxel (i.e., the seed-voxel) was extracted in contrast to common approaches such as averaging the time series of voxels within a defined seed region [44, 47, 48] or taking each of the voxels within the given ROI as a seed-voxel [45]. The extracted time course of the seed-voxel or the averaged time course extracted from all voxels within the ROI spheres was correlated with the time series of all other voxels across the whole brain, yielding a corresponding correlation coefficient (r -value) for each voxel. The similarity of using a seed-voxel ($1.0 \times 1.0 \times 1.0 \text{ mm}^3$) or a spherical ROI with a radius of about 4 mm is shown in Figure 4. Nevertheless, using ROIs larger than 4 mm, the resulting brain maps slightly differ for "anatomically small" seed regions as exemplified for a 10 mm spherical ROI radius placed in the caudate in Figure 4(b) (right panel). Since the time courses were considered to be normally distributed, correlations were computed by use of the parametric Pearson's product moment correlation method.

2.3.7. Processing Step 7: $z(r)$ Transformation. Fisher's r - to z -transformation [54] was applied voxelwise to improve the normal distribution of the individual's connectivity maps as Z statistic images [55]. Each voxel corresponds to a $z(r)$ score

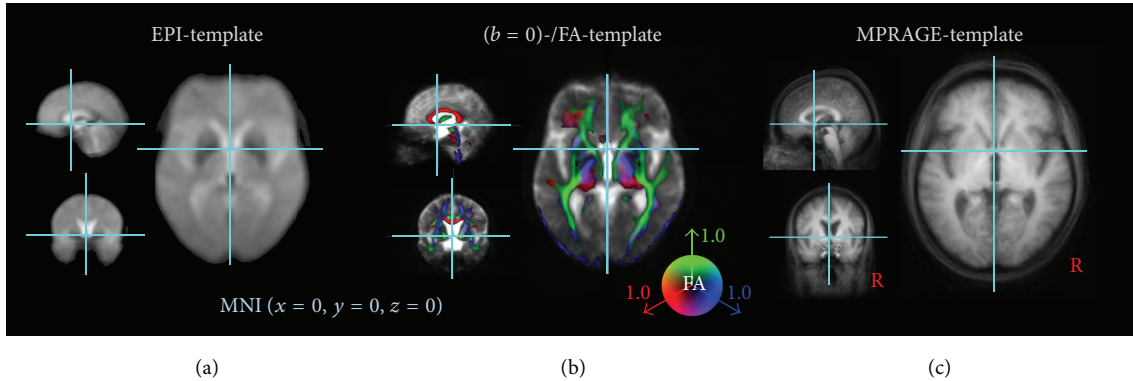


FIGURE 1: Templates in MNI stereotaxic space used for this study. (a) EPI template. (b) DTI templates (($b = 0$)-template and overlaid color-coded fractional anisotropy- (FA-) template), FA threshold 0.2. (c) MPRAGE template. Each template was computed for healthy elderly ($N = 12$) included in this study with display focus at the anterior commissure.

representing its connectivity strengths with respect to the seed-voxel of the respective ICN. As an example, Figure 3 displays the default mode network (DMN) calculated for a representative single subject on a cubic 1 mm grid in MNI coordinates.

2.3.8. Processing Step 8: Averaging Individual Brain Maps. In order to obtain the ICN at the group level, the $z(r)$ scores were arithmetically averaged voxelwise [45, 46, 49]. The brain maps at group level were statistically validated by also applying a two-sided one-sample t -test [44]. Arithmetical averaging and the application of one-sample t -test revealed similar results (Figure 5).

2.4. DTI Data Processing. The DTI analysis software TIFT was used for DTI data processing. In order to perform a spatial normalization in the MNI stereotaxic standard space, a study-specific ($b = 0$)-template and a fractional anisotropy- (FA-) template (see Figure 1(b)) had to be created [31]. As the nonaffine registration to an FA-template has the advantage of providing more contrast in comparison to ($b = 0$)-images [56], a FA-template was defined by averaging all individually derived FA maps for the healthy elderly.

Prior to averaging, DTI data were controlled for motion corrupted volumes by a recently described technique [57]; it was found that no volumes had to be excluded for further analysis. The subsequent averaging procedure requires careful treatment of the orientational information which is preserved during the normalization process [32, 58]. After this normalization procedure, all individual DTI data sets were used for the calculation of the second-rank diffusion tensor and the FA for quantification of the diffusion anisotropy, according to standard methods [59]. In order to apply group based fiber tracking (FT) algorithms, averaged DTI data sets were calculated from all subjects' data sets by arithmetic averaging of the MNI transformed data. In this manner, an averaged DTI data set was calculated while preserving directional information of individual data sets (for details, see [32, 60]). These averaged DTI data sets were then used to identify pathways for defined brain structures.

Tractography was performed by using a streamline tracking technique. Manually defined seed points were the basis for the consecutive FT [31]. In order to improve FT performance, additional control data sets with 49 GD were included in the study. Parameters for FT represented a dot product threshold between two FT steps of 0.9, a FA threshold of 0.2, and a seed-voxel radius of 5 mm. Seeds for the FT corresponding to the ICNs are listed in Table 3.

3. Results

Ten well-described ICNs were unambiguously identified by using seed-voxels placed into regions as listed in Table 2. In order to illustrate the performance of averaging, a representative single subject DMN was juxtaposed to the group-averaged DMN in Figure 3. More specifically, Figure 6 illustrates ten identified single subject ICNs in juxtaposition to the ten group-averaged ICNs according to Table 2 as follows.

(a) The *default mode network* (DMN) (Figure 6(a)) was identified by seeding the PCC with the adjacent precuneus region. The brain map covers the medial parietal cortex comprising bilateral temporal areas around their midline extending to inferior parietal regions. In addition, the medial frontal cortex reveals activity in ventromedial, anteriomedial, and dorsomedial areas, the frontal pole, and the anterior cingulate. Weaker activity was observed in the bilateral hippocampal formation and parts of dorsolateral prefrontal cortex.

(b, c) Figures 6(b) and 6(c) show the *left* and *right frontoparietal control* ICNs yielded by seeds in the left and right middle temporal area, respectively. Within these spatial maps, activity was observed in several frontoparietal areas comprising the dorsolateral prefrontal cortex, frontal pole as well as lateral occipital area, inferior parietal cortex, and parts of the posterior cingulate cortex. As a relay between cortical and subcortical areas, also bilateral thalamic activation was found.

(d) The *motor* ICN (Figure 6(d)) was computed for a seed region within the left motor cortex revealing similar

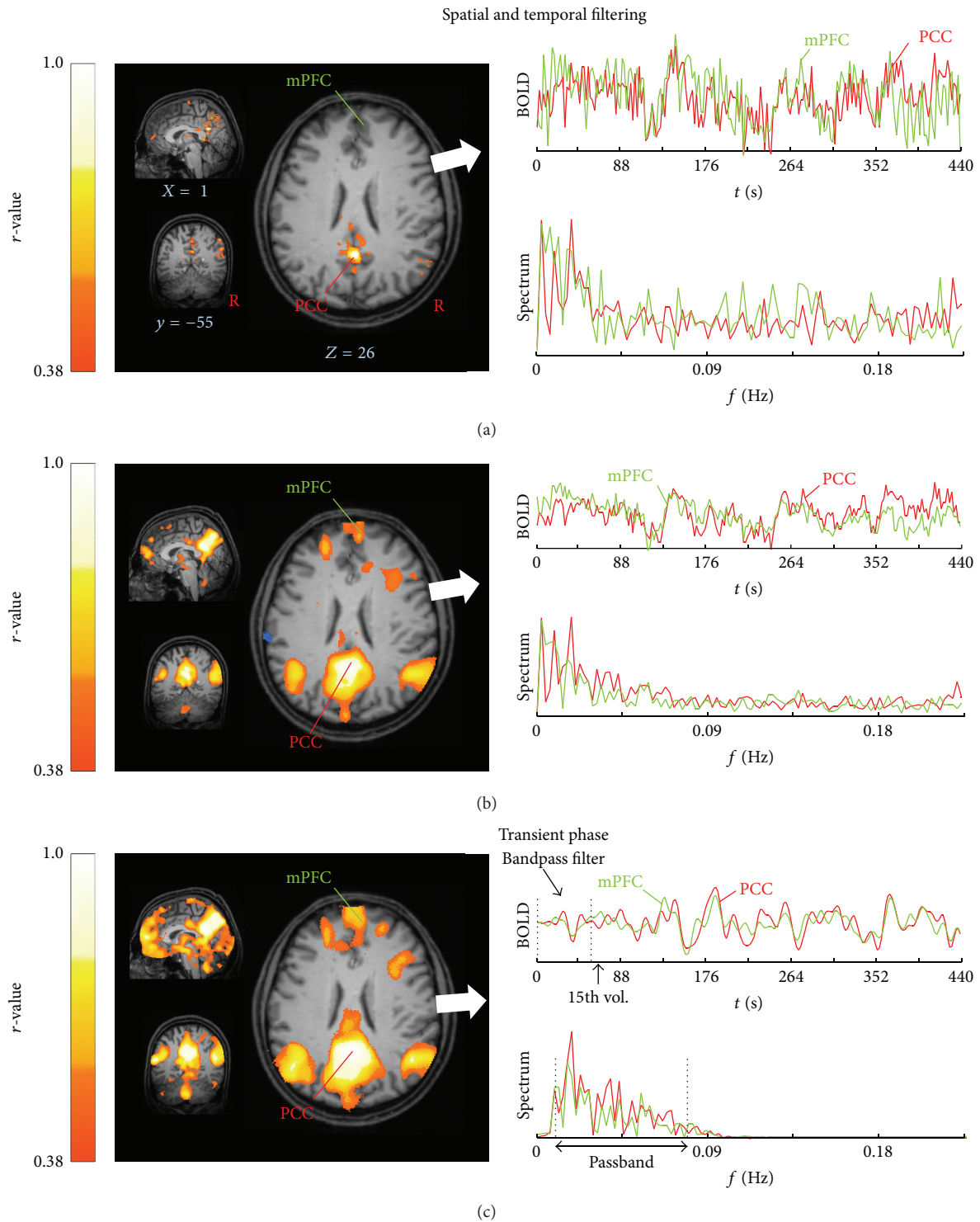


FIGURE 2: The effect of spatial and temporal filtering exemplified for one representative subject. Most informative orthogonal slices (left column) in the MNI stereotaxic space show the default mode network (DMN) computed for a seed-voxel in posterior cingulate cortex (PCC, $x\ y\ z, 0\ -55\ 26$) for (a) motion corrected and resampled data to 1 mm cubic grid, (b) after spatial smoothing with a 3D-Gaussian kernel (8 mm FWHM), and (c) after temporal linear detrending and bandpass filtering (0.01–0.08 Hz). Time rows with corresponding frequency spectrum (right column) for the seed-voxel (red trace) and a voxel-time course extracted from the medial prefrontal cortex (mPFC, green trace, $x\ y\ z, 1/50/22$). Connectivity strengths are shown in hot colors, thresholded for $|r| > 0.38$ corresponding to $P < 0.0000001$ and overlaid on the individual MPRAGE ($1.0 \times 1.0 \times 1.0\ \text{mm}^3$).

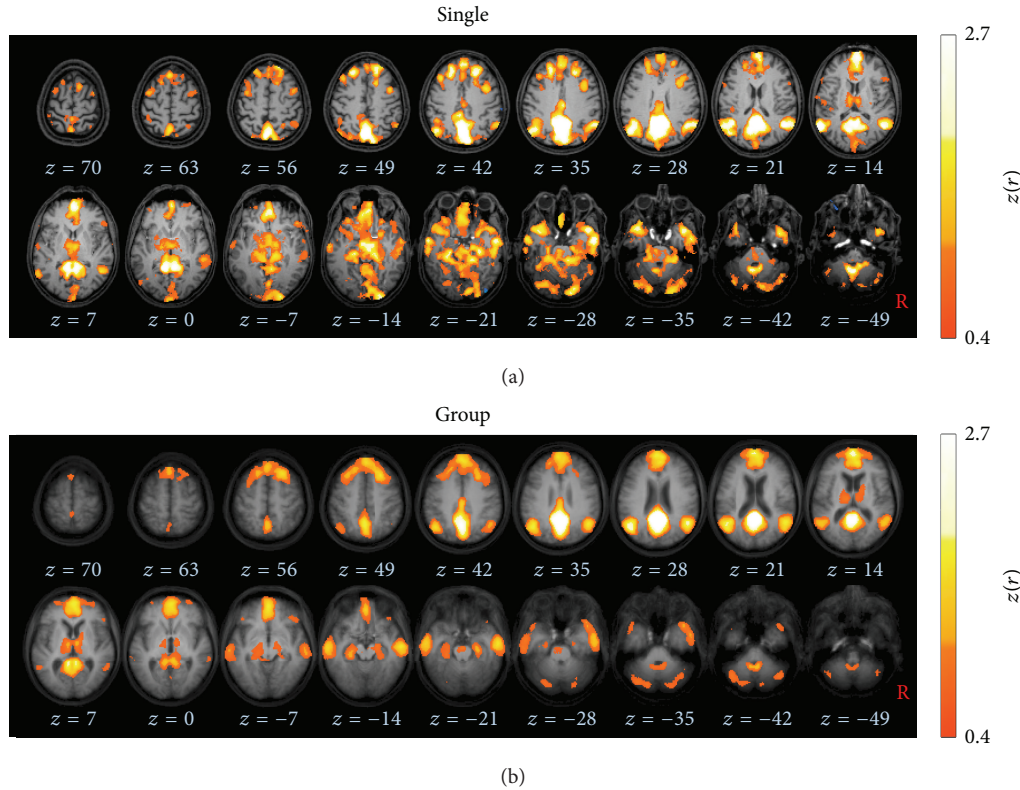


FIGURE 3: Axial slices in the MNI stereotaxic space show the default mode network (DMN) computed for a seed-voxel in posterior cingulate cortex (PCC, $x\ y\ z, 0\ -55\ 26$). Connectivity strengths are depicted in hot colors, thresholded for $|z(r)| > 0.4$ corresponding to $P < 0.0000001$. (a) Results for a representative subject (male, 60 years) overlaid on the individual MPRAGE images. (b) Group averaged brain map for all subjects ($N = 12$) displayed on the averaged MPRAGE background.

activation in both hemispheres comprising the sensory-motor and motor association systems. These included pre- and postcentral motor regions and the supplementary motor area. Moreover, weaker activation was found in the visual association areas in the occipital pole and the thalamus.

(e) The right extrastriatal seed corresponded to a symmetric brain map known as the *visuospatial* ICN (Figure 6(e)) that included middle and inferior temporal gyri as well as visual association structures at the temporooccipital junction and extending laterally towards the primary visual cortex in the posterior and lateral occipital cortices. Moreover, this ICN map encompasses superior dorsal parietal regions and extra-primary areas of the visual cortex.

(f) The frontal eye fields (FEF) served as the seed region for the *dorsal attention* system (Figure 6(f)), displaying a pronounced symmetric activity in both hemispheres. This brain map encompasses the supplementary eye fields, small portions of the dorsolateral prefrontal cortex, the intraparietal cortices including the parietal eye fields, associative motor areas, and middle temporal structures encompassing visual associative structures. The cingulate gyrus extending from posterior towards anterior portions including the cingulate eye fields revealed also activity. Striatal regions exhibited strong iFC with the FEF; in detail, the putamen displayed the strongest connectivity while the caudate nucleus with adjusting thalamus was found to be less strongly functionally

connected with the FEF. In summary, the dorsal attention ICN covers areas that are strongly associated with eye movement control.

(g) The *ventral attention* ICN (Figure 6(g)) has been computed by a basal ganglia seed in the right ventral striatum. Its iFC map covers large parts of the limbic system including the nucleus accumbens, the temporoparietal junction, and ventromedial prefrontal cortex.

(h) A second striatal seed within the caudate nucleus demonstrated strong activity in the basal ganglia and thalamus and is thus defined as the *basal ganglia thalamic* ICN (Figure 6(h)). The spatial pattern indicated weaker iFC with bilateral cerebellar regions and the right dorsolateral prefrontal cortex. Thus, the cortical activations were mainly found in the right hemisphere, with an overlap with the right frontoparietal control network.

(i) Placing a seed within the midbrain resulted in the *brainstem* ICN (Figure 6(i)) that included the brainstem extending from mesencephalic areas towards the medulla oblongata. The brainstem associated brain map encompasses bilateral thalamic areas. This resulting brain map is a mirror image with respect to the midline.

(j) The *cerebellar* ICN (Figure 6(j)) was identified by placing a seed in the right cerebellum. Weaker activations included middle temporal areas and bilateral thalamus.

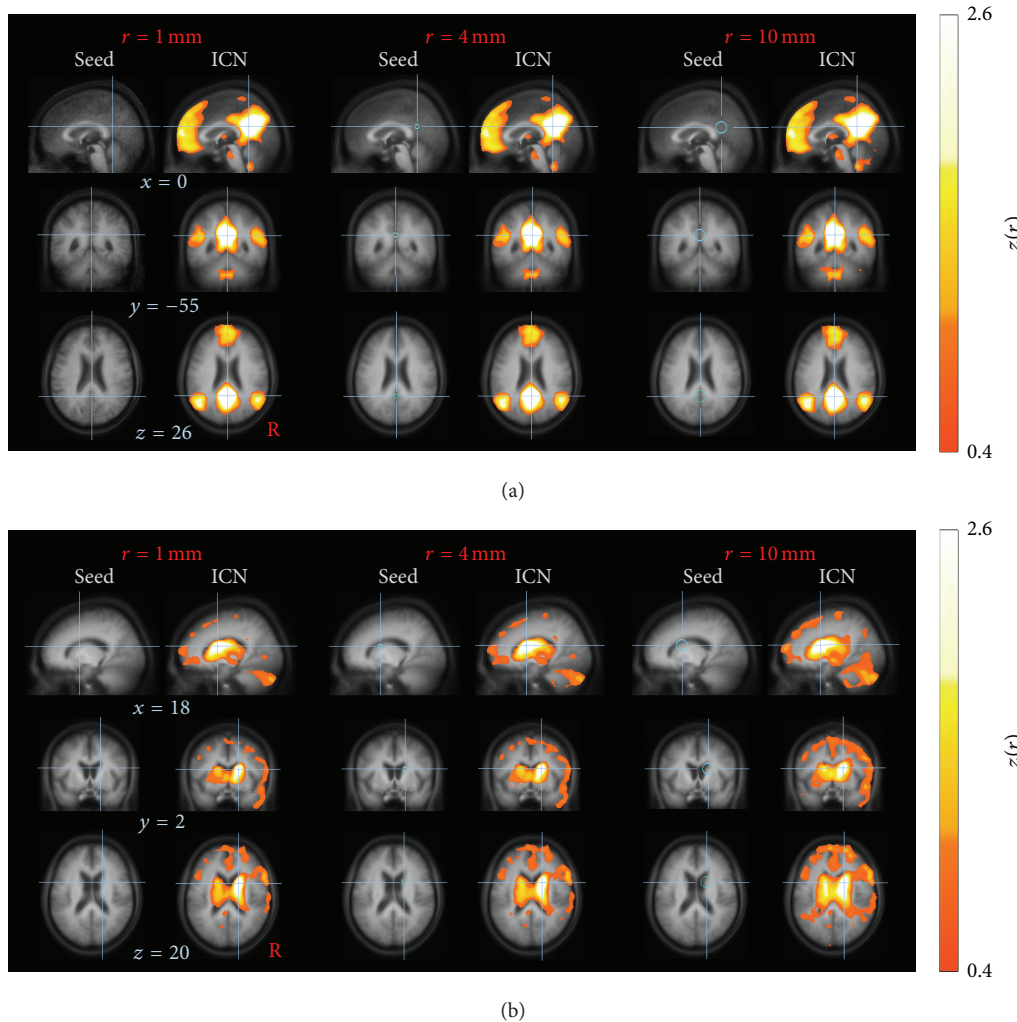


FIGURE 4: Effect of voxel-seed versus spherical ROI seeds at group level. (a) Default mode network (DMN) computed for a posterior cingulated cortex (PCC) seed. (b) Basal ganglia thalamic (BT) ICN computed for a caudate seed. Crosshairs on orthogonal slices indicate the voxel-seed location (left column), the center of the spherical ROI with 4 mm radius (center) and 10 mm radius (right). Data are shown in 1 mm cubic grid in the MNI space on the averaged MPAGE image. The computation of the ICNs (right column of each pair) revealed similar results for a seed-voxel compared to a spherical ROI for the PCC seed (a). However, for smaller structures such as the caudate, the resulting brain map pointed towards a slightly different and more diffuse pattern with spherical radii larger than 4 mm (b).

The resulting ICNs in the elderly subjects (see Figure 6 and Supplementary Figure available online at <http://dx.doi.org/10.1155/2014/947252>) show a similar spatial distribution of the brain maps as compared to ICNs of younger subjects. These ICNs have been previously identified, that is, the “task-negative” DMN [12, 15], as well as the “task-positive” ICNs, comprising left and right lateralized frontoparietal control [49, 50], visuospatial [8, 20], motor [2, 52, 68] dorsal attention [4, 49], ventral attention [53, 69], basal ganglia thalamic [53, 69, 70], brainstem [49, 50], and cerebellar [49, 50]. ICNs capture fundamental units of functional organization [7]; for a detailed synopsis see also Table 2. Notably, we did not observe significant anticorrelated regions in any of the identified ICNs at group level and on individual basis. At group level, this finding was consistent for both data

postprocessing approaches, that is, (i) arithmetically averaging of the individual brain maps and (ii) applying a one-sample *t*-test (including multiple comparison correction). The overall results of the investigated brain connectivity are illustrated in Figure 7 that shows the combination of the ten ICNs (Figure 6) with their corresponding DTI-based FTs: the DMN and the cingulum bundle [23], the left and right frontoparietal control ICNs and the inferior longitudinal fasciculus [61], the motor ICN and the corticospinal tracts [62, 63], the visuospatial ICN and the optic radiation [62, 63], the dorsal attention system and the callosal radiation originating from callosal segment II [63, 64], the ventral attention ICN and the callosal radiation originating from callosal segment I [63, 64], the basal ganglia thalamic and thalamic radiation [65], the brainstem ICN and the

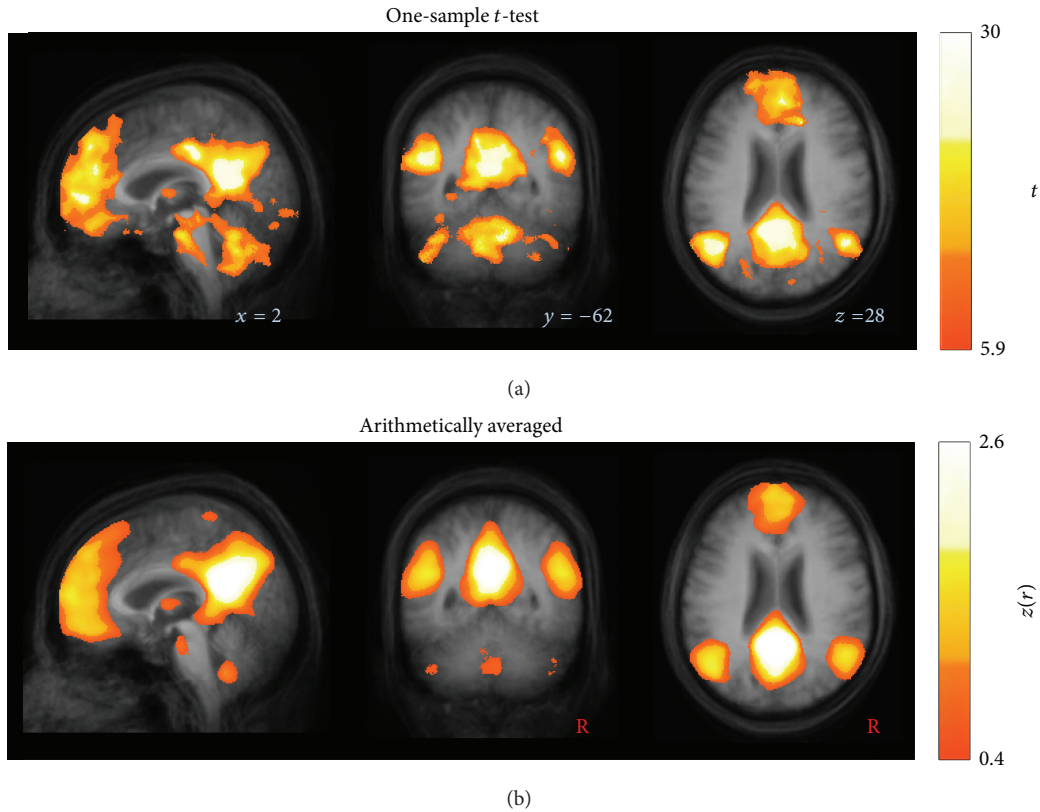


FIGURE 5: Similarity of ICNs at group level computed by (a) a one-sample t -test compared to (b) arithmetically averaged, as exemplified for the most informative orthogonal slices depicting the default mode network. The two-sided one-sample t -test was thresholded at $P < 0.001$, corrected for multiple comparisons using the false discovery rate. Data are shown in stereotaxic MNI space in a 1 mm^3 cubic grid.

TABLE 2: Definitions of seed-voxel location ($1.0 \times 1.0 \times 1.0 \text{ mm}^3$) in the MNI stereotaxic space with their corresponding intrinsic connectivity network (ICN). Given references provide the acknowledgement for the defined ICNs.

#	ICN	Seed-voxel			Seed-voxel region	Reference
		X	Y	Z		
A	Default mode network (DMN)	0	-55	26	Posterior cingulate cortex	Raichle et al., 2001 [15]; Greicius et al., 2003 [13]; Buckner et al., 2008 [12]
B	Left frontoparietal control (L-FPC)	-50	-52	49	Left Inferior parietal lobule	Vincent et al., 2008 [49]; Spormaker et al., 2012 [50]; Beckmann et al., 2005 [19]
C	Right frontoparietal control (R-FPC)	50	-54	49	Right inferior parietal lobule	
D	Motor (MOT)	-27	-27	68	Motor cortex	Biswal et al., 1995 [2]; Wu, et al., 2009 [51]; Wu et al., 2011 [52]
E	Visuospatial (VIS)	47	-72	15	Extrastriate cortex	Smith et al., 2009 [8]; Laird et al., 2011 [20]; Beckmann et al., 2005 [19]
F	Dorsal attention (DA)	30	-9	54	Frontal eye field	Vincent et al., 2008 [49]; van Dijk et al., 2010 [4]
G	Ventral attention (VA)	11	13	0	Ventral striatum	Di Martino et al., 2008 [53]; Hacker et al., 2012 [46]
H	Basal ganglia thalamic (BT)	18	2	20	Caudate nucleus	Di Martino et al., 2008 [53]; Laird et al., 2011 [20]
I	Brainstem (BS)	2	-31	-20	Midbrain	Laird et al., 2011 [20]; Hacker et al., 2012 [46]
J	Cerebellum (CB)	32	-79	-34	Cerebellum	Smith et al., 2009 [8]; Laird et al., 2011 [20]

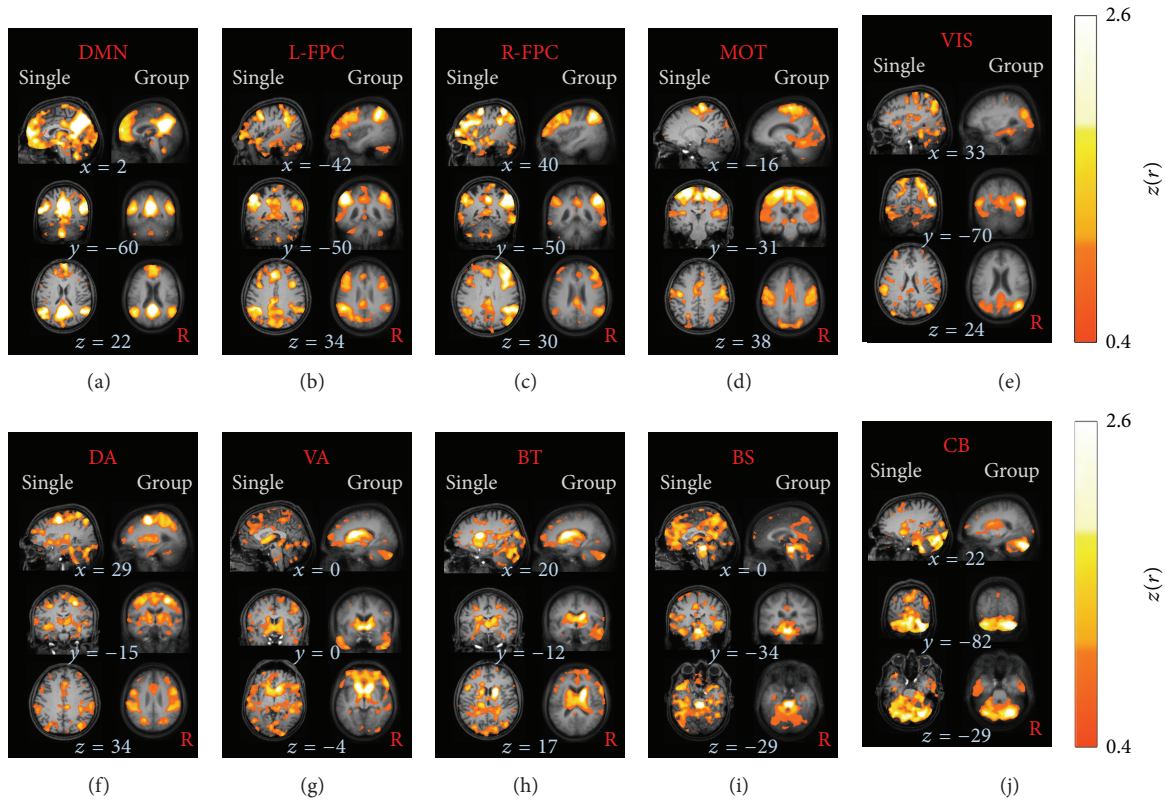


FIGURE 6: Orthogonal slices of ten well-matched pairs of ICNs ((a)–(j)) in the stereotaxic MNI space for a representative single subject (male, 60 years) overlaid on the individual MPRAGE (left columns) and for the complete healthy subject group ($N = 12$) displayed on their averaged MPRAGE (right columns). Connectivity strengths of brain maps are depicted in hot colors, thresholded for $|z(r)| > 0.4$ corresponding to $P < 0.0000001$. (a) The default mode ICN (DMN). ((b), (c)) The left and right frontoparietal control (FPC) ICNs. (d) The motor (MOT) ICN. (e) The visuospatial (VIS) ICN. (f) The dorsal attention (DA) system. (g) The ventral attention (VA) ICN. (h) The basal ganglia thalamic (BT) ICN. (i) The brainstem (BS) ICN. (j) The cerebellar (CB) ICN.

TABLE 3: Diffusion tensor imaging analysis: fiber tracking (FT) seeds in the MNI stereotaxic space corresponding to the intrinsic connectivity networks (ICNs).

#	ICN	FT seed			FT
		X	Y	Z	
A	Default mode network (DMN)	± 8	-16	38	Cingulum bundles [23]
B, C	Left frontoparietal control (L-FPC)	± 27	-40	53	Inferior longitudinal fasciculi [61]
D	Motor (MOT)	± 25	-14	21	Corticospinal tracts [62, 63]
E	Visuospatial (VIS)	0	-14	21	Optic radiation [62, 63]
F	Dorsal attention (DA)	0	1	25	Callosal radiation originating from callosal segment II [63, 64]
G	Ventral attention (VA)	± 18	-6	-8	Callosal radiation originating from callosal segment I [63, 64]
H	Basal ganglia thalamic (BT)	± 25	-10	28	Thalamic radiation [65]
I	Brainstem (BS)	± 4	-28	-13	Corticopontine pathway [62, 66]
J	Cerebellum (CB)	± 15	-38	-29	Superior cerebellar peduncle [67]

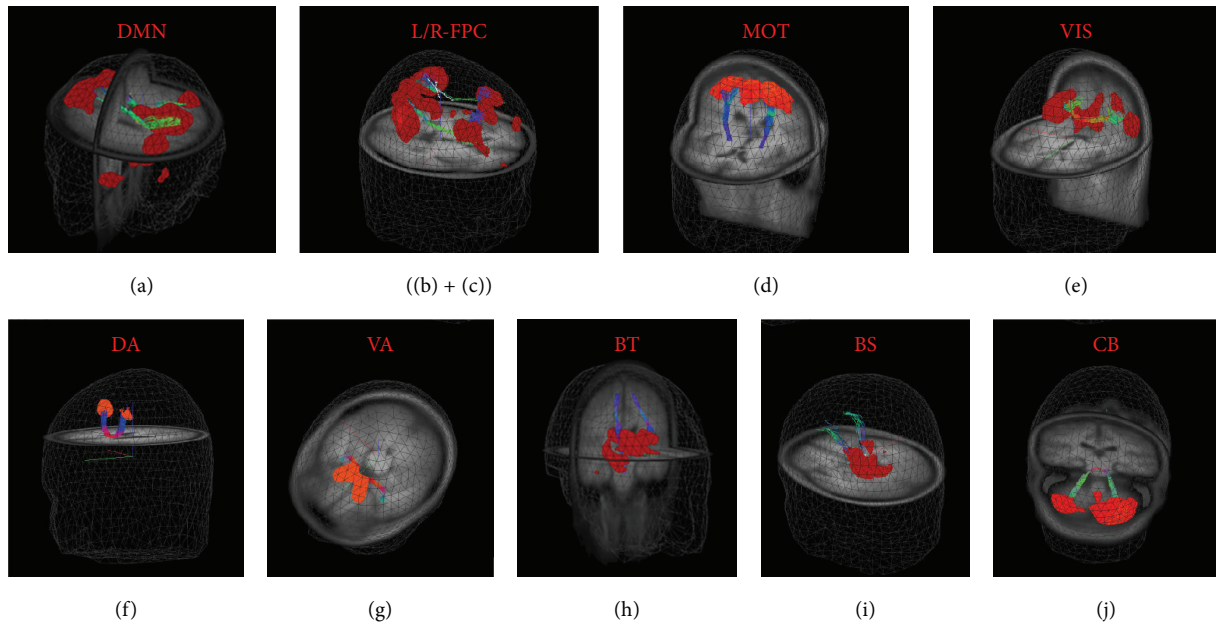


FIGURE 7: 3D representations on the averaged MPRAGE template of ten ICNs ((a)–(j)) in MNI space with corresponding fiber tracts (FTs). (a) The default mode ICN (DMN) and cingulum bundle. ((b), (c)) The left and right frontoparietal control (FPC) ICNs and inferior longitudinal fasciculus. (d) The motor (MOT) ICN and corticospinal tracts. (e) The visuospatial (VIS) ICN and optic radiation. (f) The dorsal attention (DA) system and callosal radiation originating from callosal segment II. (g) The ventral attention (VA) ICN and callosal radiation originating from callosal segment I. (h) The basal ganglia thalamic (BT) ICN and thalamic radiation. (i) The brainstem (BS) ICN and corticopontine pathway. (j) The cerebellar (CB) ICN and superior cerebellar peduncle. Color coding is for visualization only.

corticopontine pathway [62, 66], and the cerebellar ICN and the superior cerebellar peduncle [67].

4. Discussion

4.1. Methodological Approach

- (i) A framework has been presented that allows for iFC analysis and ICN identification by a five-item preprocessing followed by a three-step seed-based correlation analysis in order to obtain ICNs. The following algorithm implementations in the TIFT software [31] were adapted from DTI analysis and also applied for iFCMRI processing; data were resampled to a cubic 1 mm grid for further (complementary) analysis.
- (ii) Spatial Gaussian filtering was applied in order to optimize the sensitivity and specificity.
- (iii) Stereotaxic normalization to study-specific templates was performed both to an EPI-template for iFC and to ($b = 0$)- and FA-templates for DTI, respectively.

The parallels and cross-links to DTI analysis algorithms in a common software environment allow for further complementary iFC/DTI analysis at the group level targeting group comparisons [10].

4.2. Novelty of the Study. The novelty of this study comprises the following aspects.

- (i) ICN identification in a sample of elderly subjects which is in the age range of many studies addressing neurodegenerative diseases. This is all the more important since it could be shown that age-dependent changes of the cerebral vasculature exist which may alter the neuronal-vascular coupling and thus the BOLD signal (in task-based fMRI investigations) [71].
- (ii) One prerequisite of the seed-voxel approach for ICN identification is an upsampling to a cubic 1 mm grid. Compared with ROI-seed-based approaches [10, 16, 45], the presently applied seed-voxel approach is supposed to provide some advantages: first, spatial smoothing with sufficient kernel size improves highly correlated time courses of adjacent voxels [45] so that the location of the seed-voxel is assumed to be robust against displacements. Second, although the data were stereotaxically normalized in a two-step procedure, small discrepancies in normalization are a common but confounding side effect due to the slightly different individual's brain anatomy. In particular, for small anatomical ROIs, a larger seed radius may exceed the true ROI by encompassing structures outside. Instead, selecting a single voxel in a 1 mm cubic grid on the basis of the averaged high-resolution image (e.g. MPRAGE) [46] may overcome this problem. In order to emphasize this statement, Figure 4 illustratively exemplifies that the PCC seed is less vulnerable against increasing spherical seed radii compared with the smaller caudate seed.

- (iii) Although the ICN identification at the group level directly reflects reliable ICNs with excellent signal-to-noise ratio compared to single subject ICNs, single subject ICNs showed sufficient quality for further comprehensive analysis at single subject level.
- (iv) IFCMRI analysis algorithms were included in a well-established software package which allows for easy complementary iFCMRI/DTI analysis. That way, prerequisites for combined functional and structural network analysis at the group level in studies of, for example, neurodegenerative diseases, are prepared.
- (v) The eight-step proposed approach did not include any kind of brain masking (e.g., white matter mask or cerebrospinal fluid mask). No nuisance covariates such as whole brain signal, cerebrospinal fluid, white matter signals, or head motion parameters were regressed out, as addressed in the following.

4.3. Nuisance Covariates. In order to correct for nonneuronal BOLD signals [72], removing the effect of nuisance covariates is a common iFCMRI preprocessing step [47]. However, it remains unclear where the respective data for regressing out those covariates should be extracted [44]. In this study, no nuisance covariates were regressed out because the demonstrated ICNs in the elderly were unambiguously identified utilizing the proposed approach. The observed brain maps were remarkably similar compared to previous studies (e.g., [8, 20, 73]). The effect of regressing out movement, ventricle, and white matter covariates appears to be of minor impact which is in agreement with others [4, 74] who systematically investigated and illustrated these effects. However, those authors pointed out the strong influence of utilizing global signal regression that in turn induces the ongoing debated anticorrelated regions [5].

4.4. Anticorrelated Regions. The identified brain maps did not reveal anticorrelated regions, probably because we did not apply global mean regression in the data processing procedure. The commonly applied global mean regression is thought to induce anticorrelated regions [75] and is therefore still controversial in iFCMRI literature [44]. Hence, anticorrelated regions and their possible physiological interpretation are a matter of an ongoing debate [5, 76].

4.5. Prospects to Studies at the Group Level. While DTI-based comparisons at the group level require spatial smoothing (preferably by means of a Gaussian kernel with FWHM in the range of 6 mm to 12 mm or twice the scanner resolution [40]), statistical analysis of the ICNs can be directly applied to the iFCMRI- $z(r)$ maps of subjects' data by performing a two-sided parametric Student's t -test for unequal variances [77] in order to contrast voxelwise differences groups. The resulting P values have to be corrected for multiple comparisons (e.g., by utilizing the false discovery rate (FDR) [78]), followed by correction for multiple comparisons at cluster level [79].

The step-by-step procedure presented in this study is an approach to implement complementary iFCMRI/DTI

analysis at the group level (healthy controls' data as used in this study). The extension to comparisons of subject groups (consisting, e.g., of a patient and a control sample) could easily be performed. The complementary analysis in one single software environment allows for mapping structural damage (DTI metrics differences) in combination to detection of tract connections (DTI-based FT reconstructions) with functional alterations (hyper- or hypoconnectivity) of the corresponding networks.

The association between functional and structural connectivity in the brain at "rest" has been demonstrated for the DMN [10, 25]. More generally, functional components have been found to correspond to structural components for several portions of the brain [80]. This is one of the main goals of the human connectome project that aims at characterizing the brain function on the basis of functional and structural connectivity [81, 82]. The impact of both functional and structural components might be also important for the understanding of pathological conditions such as dementia [83]. In addition, the iFCMRI approach appears to be sensitive to characterize potential compensatory mechanisms [84]. Together, mapping the functional integrity of the human brain in neurological or psychiatric conditions emerges as a noninvasive sensitive approach to detect alterations in neuronal signaling.

4.6. Limitations. The healthy elderly participating in the present study were found to be free of any cognitive deficits; however, with respect to the years of education they were higher educated than the average adult population and may therefore be biased towards a somewhat higher cognitive reserve [85]. The limited number of included subjects ($N = 12$) can generally be considered as a limiting factor on the one hand. However, the low sample size might be of advantage for this specific investigation on the other hand because one aim was to identify consistent ICNs in a small number of cognitively sufficient characterized healthy adults.

With respect to data acquisition, the isometric recording resolution was 3 mm for iFCMRI and 2 mm for DTI, respectively; this limitation of different resolutions has been partially overcome by resampling to a 1 mm cubic grid. The DTI quality was further constrained by the minimum required number of gradients (i.e., $N = 30$) used for the structural analysis path. The ICNs comprised portions of the brain that may be coupled via complex fiber organizations. In order to track those axonal bundles and possibly cross-fibers, a higher number of gradient directions enable performing more subtle fiber tracking in optimized quality [31]. In addition, iFCMRI temporal resolution was typically low ($TR = 2.2$ s) which resulted, according to the sampling theorem, in aliasing effects caused by confounding frequency components $f > 13.7/\text{min}$ (corresponding to TR) such as cardiac or respiratory oscillations [6].

5. Conclusion

In this study, it has been shown that it is possible to compute ICNs at single subject level as well as at the group level

by use of a straightforward standardized procedure. Robust ICNs at the group level could be defined for a comparatively small number of contributing subjects ($N = 12$). With the parallel analysis approach of iFC and DTI in a single software environment (TIFFT), it was shown that comprehensive analyses between functional network mapping (as assessed by iFCMRI analysis at the group level) and structural network mapping (as assessed by DTI-based FT of corresponding network tract systems) could be performed. The findings demonstrated here provide a methodological framework for future investigations aiming at contrasting pathological (neurodegenerative) conditions with healthy controls on the basis of multiparametric brain connectivity mapping.

Conflict of Interests

The authors declare that there is no conflict of interests regarding the publication of this paper.

Authors' Contribution

Martin Gorges and Hans-Peter Müller contributed equally.

References

- [1] S. Ogawa, D. W. Tank, R. Menon et al., "Intrinsic signal changes accompanying sensory stimulation: functional brain mapping with magnetic resonance imaging," *Proceedings of the National Academy of Sciences of the United States of America*, vol. 89, no. 13, pp. 5951–5955, 1992.
- [2] B. Biswal, F. Z. Yetkin, V. M. Haughton, and J. S. Hyde, "Functional connectivity in the motor cortex of resting human brain using echo-planar MRI," *Magnetic Resonance in Medicine*, vol. 34, no. 4, pp. 537–541, 1995.
- [3] B. B. Biswal, M. Mennes, X.-N. Zuo et al., "Toward discovery science of human brain function," *Proceedings of the National Academy of Sciences of the United States of America*, vol. 107, no. 10, pp. 4734–4739, 2010.
- [4] K. R. A. Van Dijk, T. Hedden, A. Venkataraman, K. C. Evans, S. W. Lazar, and R. L. Buckner, "Intrinsic functional connectivity as a tool for human connectomics: theory, properties, and optimization," *Journal of Neurophysiology*, vol. 103, no. 1, pp. 297–321, 2010.
- [5] D. M. Cole, S. M. Smith, and C. F. Beckmann, "Advances and pitfalls in the analysis and interpretation of resting-state fMRI data," *Frontiers in Systems Neuroscience*, vol. 4, article 8, 2010.
- [6] M. P. van den Heuvel and H. E. Hulshoff Pol, "Exploring the brain network: a review on resting-state fMRI functional connectivity," *European Neuropsychopharmacology*, vol. 20, no. 8, pp. 519–534, 2010.
- [7] B. T. Yeo, F. M. Krienen, J. Sepulcre et al., "The organization of the human cerebral cortex estimated by intrinsic functional connectivity," *Journal of Neurophysiology*, vol. 106, no. 3, pp. 1125–1165, 2011.
- [8] S. M. Smith, P. T. Fox, K. L. Miller et al., "Correspondence of the brain's functional architecture during activation and rest," *Proceedings of the National Academy of Sciences of the United States of America*, vol. 106, no. 31, pp. 13040–13045, 2009.
- [9] B. B. Biswal, "Resting state fMRI: a personal history," *NeuroImage*, vol. 62, no. 2, pp. 938–944, 2012.
- [10] E. S. van Oort, A. M. van Cappellen van Walsum, and D. G. Norris, "An investigation into the functional and structural connectivity of the default mode network," *Neuroimage*, vol. 90, pp. 381–389, 2013.
- [11] M. Filippi, M. P. van den Heuvel, A. Fornito et al., "Assessment of system dysfunction in the brain through MRI-based connectomics," *The Lancet Neurology*, vol. 12, no. 12, pp. 1189–1199, 2013.
- [12] R. L. Buckner, J. R. Andrews-Hanna, and D. L. Schacter, "The brain's default network: anatomy, function, and relevance to disease," *Annals of the New York Academy of Sciences*, vol. 1124, pp. 1–38, 2008.
- [13] M. D. Greicius, B. Krasnow, A. L. Reiss, and V. Menon, "Functional connectivity in the resting brain: a network analysis of the default mode hypothesis," *Proceedings of the National Academy of Sciences of the United States of America*, vol. 100, no. 1, pp. 253–258, 2003.
- [14] M. E. Raichle and A. Z. Snyder, "A default mode of brain function: a brief history of an evolving idea," *NeuroImage*, vol. 37, no. 4, pp. 1083–1090, 2007.
- [15] M. E. Raichle, A. M. MacLeod, A. Z. Snyder, W. J. Powers, D. A. Gusnard, and G. L. Shulman, "A default mode of brain function," *Proceedings of the National Academy of Sciences of the United States of America*, vol. 98, no. 2, pp. 676–682, 2001.
- [16] G. L. Shulman, D. L. W. Pope, S. V. Astafiev, M. P. McAvoy, A. Z. Snyder, and M. Corbetta, "Right hemisphere dominance during spatial selective attention and target detection occurs outside the dorsal frontoparietal network," *Journal of Neuroscience*, vol. 30, no. 10, pp. 3640–3651, 2010.
- [17] M. A. Silver, D. Ress, and D. J. Heeger, "Topographic maps of visual spatial attention in human parietal cortex," *Journal of Neurophysiology*, vol. 94, no. 2, pp. 1358–1371, 2005.
- [18] W. W. Seeley, V. Menon, A. F. Schatzberg et al., "Dissociable intrinsic connectivity networks for salience processing and executive control," *Journal of Neuroscience*, vol. 27, no. 9, pp. 2349–2356, 2007.
- [19] C. F. Beckmann, M. DeLuca, J. T. Devlin, and S. M. Smith, "Investigations into resting-state connectivity using independent component analysis," *Philosophical Transactions of the Royal Society B*, vol. 360, no. 1457, pp. 1001–1013, 2005.
- [20] A. R. Laird, P. M. Fox, S. B. Eickhoff et al., "Behavioral interpretations of intrinsic connectivity networks," *Journal of Cognitive Neuroscience*, vol. 23, no. 12, pp. 4022–4037, 2011.
- [21] D. S. Margulies, A. M. C. Kelly, L. Q. Uddin, B. B. Biswal, F. X. Castellanos, and M. P. Milham, "Mapping the functional connectivity of anterior cingulate cortex," *NeuroImage*, vol. 37, no. 2, pp. 579–588, 2007.
- [22] K. L. Ray, D. R. McKay, P. M. Fox et al., "ICA model order selection of task co-activation networks," *Frontiers in Neuroscience*, vol. 7, p. 237, 2013.
- [23] J. S. Damoiseaux and M. D. Greicius, "Greater than the sum of its parts: a review of studies combining structural connectivity and resting-state functional connectivity," *Brain Structure & Function*, vol. 213, no. 6, pp. 525–533, 2009.
- [24] R. L. Buckner, "Human functional connectivity: new tools, unresolved questions," *Proceedings of the National Academy of Sciences of the United States of America*, vol. 107, no. 24, pp. 10769–10770, 2010.
- [25] M. D. Greicius, K. Supekar, V. Menon, and R. F. Dougherty, "Resting-state functional connectivity reflects structural connectivity in the default mode network," *Cerebral Cortex*, vol. 19, no. 1, pp. 72–78, 2009.

- [26] F. Agosta, E. Canu, E. Stefanova et al., "Mild cognitive impairment in Parkinson's disease is associated with a distributed pattern of brain white matter damage," *Human Brain Mapping*, 2013.
- [27] M. H. Lee, C. D. Smyser, and J. S. Shimony, "Resting-state fMRI: a review of methods and clinical applications," *American Journal of Neuroradiology*, vol. 34, no. 10, pp. 1866–1872, 2013.
- [28] R. N. Spreng and G. R. Turner, "Structural covariance of the default network in healthy and pathological aging," *The Journal of Neuroscience*, vol. 33, no. 38, pp. 15226–15234, 2013.
- [29] F. Hoffstaedter, C. Grefkes, C. Roski, S. Caspers, K. Zilles, and S. B. Eickhoff, "Age-related decrease of functional connectivity additional to gray matter atrophy in a network for movement initiation," *Brain Structure and Function*, 2014.
- [30] D. H. Salat, D. S. Tuch, N. D. Hevelone et al., "Age-related changes in prefrontal white matter measured by diffusion tensor imaging," *Annals of the New York Academy of Sciences*, vol. 1064, pp. 37–49, 2005.
- [31] H. P. Müller and J. Kassubek, "Diffusion tensor magnetic resonance imaging in the analysis of neurodegenerative diseases," *Journal of Visualized Experiments*, no. 77, 2013.
- [32] H.-P. Müller, A. Unrath, A. C. Ludolph, and J. Kassubek, "Preservation of diffusion tensor properties during spatial normalization by use of tensor imaging and fibre tracking on a normal brain database," *Physics in Medicine and Biology*, vol. 52, no. 6, pp. N99–N109, 2007.
- [33] M. F. Folstein, S. E. Folstein, and P. R. McHugh, "Mini mental state". A practical method for grading the cognitive state of patients for the clinician," *Journal of Psychiatric Research*, vol. 12, no. 3, pp. 189–198, 1975.
- [34] E. Kalbe, J. Kessler, P. Calabrese et al., "DemTect: a new, sensitive cognitive screening test to support the diagnosis of mild cognitive impairment and early dementia," *International Journal of Geriatric Psychiatry*, vol. 19, no. 2, pp. 136–143, 2004.
- [35] F. Fazekas, J. B. Chawluk, A. Alavi, H. I. Hurtig, and R. A. Zimmerman, "MR signal abnormalities at 1.5 T in Alzheimer's dementia and normal aging," *American Journal of Roentgenology*, vol. 149, no. 2, pp. 351–356, 1987.
- [36] K. R. A. van Dijk, M. R. Sabuncu, and R. L. Buckner, "The influence of head motion on intrinsic functional connectivity MRI," *NeuroImage*, vol. 59, no. 1, pp. 431–438, 2012.
- [37] N. S. Altman, "An introduction to kernel and nearest-neighbor nonparametric regression," *American Statistician*, vol. 46, no. 3, pp. 175–185, 1992.
- [38] M. Brett, I. S. Johnsrude, and A. M. Owen, "The problem of functional localization in the human brain," *Nature Reviews Neuroscience*, vol. 3, no. 3, pp. 243–249, 2002.
- [39] J. Ashburner and K. J. Friston, "Nonlinear spatial normalization using basis functions," *Human Brain Mapping*, vol. 7, no. 4, pp. 254–266, 1999.
- [40] F. G. Ashby, *Statistical Analysis of FMRI Data*, MIT Press, Cambridge, Mass, USA, 1st edition, 2011.
- [41] A. Rosenfeld and A. C. Kak, *Digital Picture Processing Rosenfeld*, Academic Press, 2nd edition, 1982.
- [42] O. Friman, M. Borga, P. Lundberg, and H. Knutsson, "Detection and detrending in fMRI data analysis," *NeuroImage*, vol. 22, no. 2, pp. 645–655, 2004.
- [43] Q.-H. Zou, C.-Z. Zhu, Y. Yang et al., "An improved approach to detection of amplitude of low-frequency fluctuation (ALFF) for resting-state fMRI: fractional ALFF," *Journal of Neuroscience Methods*, vol. 172, no. 1, pp. 137–141, 2008.
- [44] X.-W. Song, Z.-Y. Dong, X.-Y. Long et al., "REST: a Toolkit for resting-state functional magnetic resonance imaging data processing," *PLoS ONE*, vol. 6, no. 9, Article ID e25031, 2011.
- [45] E. Y. Choi, B. T. Thomas Yeo, and R. L. Buckner, "The organization of the human striatum estimated by intrinsic functional connectivity," *Journal of Neurophysiology*, vol. 108, no. 8, pp. 2242–2263, 2012.
- [46] C. D. Hacker, J. S. Perlmutter, S. R. Criswell, B. M. Ances, and A. Z. Snyder, "Resting state functional connectivity of the striatum in Parkinson's disease," *Brain*, vol. 135, no. 12, pp. 3699–3711, 2012.
- [47] Y. Chao-Gan and Z. Yu-Feng, "DPARSF: a MATLAB toolbox for "pipeline" data analysis of resting-state fMRI," *Frontiers in Systems Neuroscience*, vol. 4, p. 13, 2010.
- [48] J. L. Whitwell, R. Avula, A. Master et al., "Disrupted thalamo-cortical connectivity in PSP: a resting-state fMRI, DTI, and VBM study," *Parkinsonism and Related Disorders*, vol. 17, no. 8, pp. 599–605, 2011.
- [49] J. L. Vincent, I. Kahn, A. Z. Snyder, M. E. Raichle, and R. L. Buckner, "Evidence for a frontoparietal control system revealed by intrinsic functional connectivity," *Journal of Neurophysiology*, vol. 100, no. 6, pp. 3328–3342, 2008.
- [50] V. I. Spormaker, P. M. Gleiser, and M. Czisch, "Frontoparietal connectivity and hierarchical structure of the brain's functional network during sleep," *Frontiers in Neurology*, vol. 3, article 80, 2012.
- [51] T. Wu, X. Long, Y. Zang et al., "Regional homogeneity changes in patients with parkinson's disease," *Human Brain Mapping*, vol. 30, no. 5, pp. 1502–1510, 2009.
- [52] T. Wu, X. Long, L. Wang et al., "Functional connectivity of cortical motor areas in the resting state in Parkinson's disease," *Human Brain Mapping*, vol. 32, no. 9, pp. 1443–1457, 2011.
- [53] A. Di Martino, A. Scheres, D. S. Margulies et al., "Functional connectivity of human striatum: a resting state fMRI study," *Cerebral Cortex*, vol. 18, no. 12, pp. 2735–2747, 2008.
- [54] N. C. Silver and W. P. Dunlap, "Averaging correlation coefficients: should Fisher's z transformation be used?" *Journal of Applied Psychology*, vol. 72, no. 1, pp. 146–148, 1987.
- [55] K. J. Friston, "Functional and effective connectivity in neuroimaging: a synthesis," *Human Brain Mapping*, vol. 2, no. 1-2, pp. 56–78, 1994.
- [56] S. M. Smith, M. Jenkinson, H. Johansen-Berg et al., "Tract-based spatial statistics: voxelwise analysis of multi-subject diffusion data," *NeuroImage*, vol. 31, no. 4, pp. 1487–1505, 2006.
- [57] H.-P. Müller, S. D. Süßmuth, G. B. Landwehrmeyer et al., "Stability effects on results of diffusion tensor imaging analysis by reduction of the number of gradient directions due to motion artifacts: an application to presymptomatic Huntington's disease," *PLoS Currents*, Article ID RRN1292, 2012.
- [58] A. L. Alexander, K. M. Hasan, M. Lazar, J. S. Tsuruda, and D. L. Parker, "Analysis of partial volume effects in diffusion-tensor MRI," *Magnetic Resonance in Medicine*, vol. 45, no. 5, pp. 770–780, 2001.
- [59] P. J. Basser and D. K. Jones, "Diffusion-tensor MRI: theory, experimental design and data analysis—a technical review," *NMR in Biomedicine*, vol. 15, no. 7-8, pp. 456–467, 2002.
- [60] H.-P. Müller, A. Unrath, A. D. Sperfeld, A. C. Ludolph, A. Riecker, and J. Kassubek, "Diffusion tensor imaging and tract-wise fractional anisotropy statistics: quantitative analysis in white matter pathology," *BioMedical Engineering Online*, vol. 6, article 42, 2007.

- [61] M. Strenziok, P. M. Greenwood, S. A. Santa Cruz, J. C. Thompson, and R. Parasuraman, "Differential contributions of dorso-ventral and rostro-caudal prefrontal white matter tracts to cognitive control in healthy older adults," *PLoS ONE*, vol. 8, no. 12, Article ID e81410, 2013.
- [62] J. Kassubek, H. P. Muller, K. Del Tredici et al., "Diffusion tensor imaging analysis of sequential spreading of disease in amyotrophic lateral sclerosis confirms patterns of TDP-43 pathology," *Brain*, 2014.
- [63] W. W. Orrison, *Atlas of Brain Function*, Thieme, New York, NY, USA, 2nd edition, 2008.
- [64] H. Ge, X. Yin, J. Xu et al., "Fiber pathways of attention subnetworks revealed with tract-based spatial statistics (TBSS) and probabilistic tractography," *PLoS ONE*, vol. 8, no. 11, Article ID e78831, 2013.
- [65] F. Oishi, A. V. Faria, P. C. M. van Zijl, and S. Mori, *MRI Atlas of Human White Matter*, Academic Press, Amsterdam, The Netherlands, 2nd edition, 2010.
- [66] C. Habas and E. A. Cabanis, "Cortical projections to the human red nucleus: a diffusion tensor tractography study with a 1.5-T MRI machine," *Neuroradiology*, vol. 48, no. 10, pp. 755–762, 2006.
- [67] F. Wang, Z. Sun, X. Du et al., "A diffusion tensor imaging study of middle and superior cerebellar peduncle in male patients with schizophrenia," *Neuroscience Letters*, vol. 348, no. 3, pp. 135–138, 2003.
- [68] T. Wu, L. Wang, Y. Chen, C. Zhao, K. Li, and P. Chan, "Changes of functional connectivity of the motor network in the resting state in Parkinson's disease," *Neuroscience Letters*, vol. 460, no. 1, pp. 6–10, 2009.
- [69] R. C. Helmich, L. C. Derikx, M. Bakker, R. Scheeringa, B. R. Bloem, and I. Toni, "Spatial remapping of cortico-striatal connectivity in parkinson's disease," *Cerebral Cortex*, vol. 20, no. 5, pp. 1175–1186, 2010.
- [70] Y. Kwak, S. Peltier, N. I. Bohnen, M. L. T. M. Müller, P. Dayalu, and R. D. Seidler, "Altered resting state cortico-striatal connectivity in mild to moderate stage Parkinson's disease," *Frontiers in Systems Neuroscience*, vol. 4, article 143, 2010.
- [71] A. Riecker, W. Grodd, U. Klose et al., "Relation between regional functional MRI activation and vascular reactivity to carbon dioxide during normal aging," *Journal of Cerebral Blood Flow and Metabolism*, vol. 23, no. 5, pp. 565–573, 2003.
- [72] M. D. Fox, A. Z. Snyder, J. L. Vincent, M. Corbetta, D. C. Van Essen, and M. E. Raichle, "The human brain is intrinsically organized into dynamic, anticorrelated functional networks," *Proceedings of the National Academy of Sciences of the United States of America*, vol. 102, no. 27, pp. 9673–9678, 2005.
- [73] S. R. Gohel and B. B. Biswal, "Functional integration between brain regions at "rest" occurs in multiple-frequency bands," *Brain Connectivity*, 2014.
- [74] M. D. Fox, D. Zhang, A. Z. Snyder, and M. E. Raichle, "The global signal and observed anticorrelated resting state brain networks," *Journal of Neurophysiology*, vol. 101, no. 6, pp. 3270–3283, 2009.
- [75] K. Murphy, R. M. Birn, D. A. Handwerker, T. B. Jones, and P. A. Bandettini, "The impact of global signal regression on resting state correlations: are anti-correlated networks introduced?" *NeuroImage*, vol. 44, no. 3, pp. 893–905, 2009.
- [76] A. Weissenbacher, C. Kasess, F. Gerstl, R. Lanzenberger, E. Moser, and C. Windischberger, "Correlations and anticorrelations in resting-state functional connectivity MRI: a quantitative comparison of preprocessing strategies," *NeuroImage*, vol. 47, no. 4, pp. 1408–1416, 2009.
- [77] G. D. Ruxton, "The unequal variance t-test is an underused alternative to Student's t-test and the Mann-Whitney U test," *Behavioral Ecology*, vol. 17, no. 4, pp. 688–690, 2006.
- [78] C. R. Genovese, N. A. Lazar, and T. Nichols, "Thresholding of statistical maps in functional neuroimaging using the false discovery rate," *NeuroImage*, vol. 15, no. 4, pp. 870–878, 2002.
- [79] A. Unrath, H.-P. Müller, A. Riecker, A. C. Ludolph, A.-D. Sperfeld, and J. Kassubek, "Whole brain-based analysis of regional white matter tract alterations in rare motor neuron diseases by diffusion tensor imaging," *Human Brain Mapping*, vol. 31, no. 11, pp. 1727–1740, 2010.
- [80] J. M. Segall, E. A. Allen, R. E. Jung et al., "Correspondence between structure and function in the human brain at rest," *Frontiers in Neuroinformatics*, no. 10, pp. 1–17, 2012.
- [81] S. M. Smith, D. Vidaurre, C. F. Beckmann et al., "Functional connectomics from resting-state fMRI," *Trends in Cognitive Sciences*, vol. 17, no. 12, pp. 666–682, 2013.
- [82] A. W. Toga, K. A. Clark, P. M. Thompson, D. W. Shattuck, and J. D. Van Horn, "Mapping the human connectome," *Neurosurgery*, vol. 71, no. 1, pp. 1–5, 2012.
- [83] Y. He, L. Wang, Y. Zang et al., "Regional coherence changes in the early stages of Alzheimer's disease: a combined structural and resting-state functional MRI study," *NeuroImage*, vol. 35, no. 2, pp. 488–500, 2007.
- [84] K. Mevel, G. Chételat, F. Eustache, and B. Desgranges, "The default mode network in healthy aging and Alzheimer's disease," *International Journal of Alzheimer's Disease*, vol. 2011, Article ID 535816, 9 pages, 2011.
- [85] Y. Stern, "What is cognitive reserve? Theory and research application of the reserve concept," *Journal of the International Neuropsychological Society*, vol. 8, no. 3, pp. 448–460, 2002.

Research Article

A Functional Polymorphism of the MAOA Gene Modulates Spontaneous Brain Activity in Pons

Hui Lei,¹ Xiaocui Zhang,¹ Xin Di,² Hengyi Rao,^{3,4} Qingsen Ming,¹ Jibiao Zhang,¹ Xiao Guo,¹ Yali Jiang,¹ Yidian Gao,¹ Jinyao Yi,¹ Xiongzhao Zhu,¹ and Shuqiao Yao¹

¹ The Medical Psychological Institute of the Second Xiangya Hospital, Central South University, Changsha, Hunan 410011, China

² Department of Biomedical Engineering, New Jersey Institute of Technology, Newark, NJ 07102, USA

³ Center for Functional Neuroimaging, Department of Neurology, University of Pennsylvania, Philadelphia, PA 19104, USA

⁴ Department of Psychology, Sun Yat-Sen University, Guangzhou, Guangdong 510275, China

Correspondence should be addressed to Shuqiao Yao; shuqiaoyao@163.com

Received 12 March 2014; Revised 13 May 2014; Accepted 14 May 2014; Published 25 May 2014

Academic Editor: Yong He

Copyright © 2014 Hui Lei et al. This is an open access article distributed under the Creative Commons Attribution License, which permits unrestricted use, distribution, and reproduction in any medium, provided the original work is properly cited.

Objective. To investigate the effects of a functional polymorphism of the monoamine oxidase A (MAOA) gene on spontaneous brain activity in healthy male adolescents. **Methods.** Thirty-one healthy male adolescents with the low-activity MAOA genotype (MAOA-L) and 25 healthy male adolescents with the high-activity MAOA genotype (MAOA-H) completed the 11-item Barratt Impulsiveness Scale (BIS-11) questionnaire and were subjected to resting-state functional magnetic resonance imaging (rs-fMRI) scans. The amplitude of low-frequency fluctuation (ALFF) of the blood oxygen level-dependent (BOLD) signal was calculated using REST software. ALFF data were related to BIS scores and compared between genotype groups. **Results.** Compared with the MAOA-H group, the MAOA-L group showed significantly lower ALFFs in the pons. There was a significant correlation between the BIS scores and the ALFF values in the pons for MAOA-L group, but not for the MAOA-H group. Further regression analysis showed a significant genotype by ALFF values interaction effect on BIS scores. **Conclusions.** Lower spontaneous brain activity in the pons of the MAOA-L male adolescents may provide a neural mechanism by which boys with the MAOA-L genotype confers risk for impulsivity and aggression.

1. Introduction

Monoamine oxidase (MAO) is a mitochondrial enzyme that was involved in degradation of neurotransmitters, including norepinephrine (NE), serotonin (5-HT), and dopamine [1]. There are two monoamine oxidase isozymes with distinct substrate specificities: MAOA and MAOB. MAOA provides the major enzymatic clearance of 5-HT and NE during brain development [1]. The MAOA-encoding gene (Xp11.4-Xp11.3) presents a well-characterized variable number tandem repeat (VNTR) functional polymorphism in the promoter region, with different length variants that influence protein transcription, and hence enzymatic activity, selectively [2, 3]. Enzyme expression is relatively higher in carriers of 3.5 or 4 repeats (MAOA-H allele) and lower in carriers of 2, 3, or 5 repeats (MAOA-L allele) [2]. Converging evidence indicates

that this functional polymorphism has a strong influence on serotonergic function *in vitro* and *in vivo* [2–4], with the high activity allele showing lower serotonergic responsivity [4].

Previous behavioral researches have indicated an important role for MAOA in human behavior and physiology. Caspi and colleagues found that males carrying MAOA-L alleles who experienced early-life adversity had a heightened risk of developing conduct disorder or antisocial personality and of exhibiting violent and antisocial behavior [5]. Besides, Samochowiec et al. found that the MAOA-L allele has been associated with antisocial behavior in male alcohol-dependent patients [6]. Huang et al. found a significant correlation of the MAOA-H allele with lower impulsivity in adult males who report early childhood abuse, further supported an association of MAOA-L allele and impulsivity in males [7]. Subsequent studies, including one meta-analysis

[8], have replicated the findings independently [9–11]. Conversely, the MAOA-H allele has been associated with an even greater propensity for antisocial behavior and impulsivity than the MAOA-L allele in males who experience early stress [12, 13]. Moreover, the MAOA-H allele has been associated with impulsive personality traits in normal male subjects [4]. Animal studies indicated that MAOA had an important effect on aggressive behavior. Aggression is increased in the male MAOA knockout mice [14] and monkeys with reared experience [15]. MAOA inhibition during brain development induced pathological aggression in mice [16].

These findings suggest that genetically driven variations in MAOA activity significantly influence impulsivity and aggression.

Using noninvasive neuroimaging techniques, including both positron emission tomography (PET) and functional magnetic resonance imaging (fMRI), previous studies have examined the effect of this polymorphism on brain function. Previous fMRI studies have demonstrated that individuals carrying MAOA-H alleles showed increased cingulate activation during conflict resolution [17] and increased orbitofrontal cortex activation during performing motor inhibition and working memory tasks [18, 19]. Meyer-Lindenberg et al. also reported that the MAOA polymorphism had a profound impact on the corticolimbic circuitry involved in emotional memory [20]. Structural MRI studies employing voxel-based morphometry (VBM) also produced conflicting findings with respect to the effect of MAOA genotypes on amygdala volume [20–22]. However, a positron emission tomography (PET) study found no differences in the glucose metabolism between MAOA-L and MAOA-H groups [23]. Currently, the neurobiological mechanisms underlying the effects of the MAOA polymorphism on impulsiveness are still unclear.

During the last decade, studies of spontaneous brain activity at resting states in normal individuals as well as patients with brain diseases have attracted enormous research interests. Biswal and colleagues firstly demonstrated in human subjects that spontaneous low-frequency (0.01–0.08 Hz) brain fluctuations measured by resting-state fMRI are physiologically meaningful [24]. The amplitude of low-frequency fluctuation (ALFF) of BOLD signals was developed by Zang and colleagues to provide another measurement of regional neural function during a resting-state [25]. Previous studies have suggested that ALFF is physiologically meaningful and reflective of regional spontaneous neuronal activity [25–27]. To date, ALFF analysis has been applied widely to the studies of different brain disorders, including epilepsy [28], schizophrenia [29, 30], major depressive disorder [31, 32], drug addiction [33], posttraumatic stress disorder [34], attention deficit hyperactivity disorder [25], and multiple sclerosis [35]. However, it remains unknown whether resting-state spontaneous brain activity would differ as a function of MAOA genetic variation. The purpose of this study is answering this question by comparing the ALFF in matched MAOA-L and MAOA-H male adolescents. Furthermore, ALFF measurements were correlated with impulsivity scores as measured by the Barratt Impulsiveness Scale (BIS) in both MAOA-L and MAOA-H genotypes, in order to examine

the neural bases underlying the effects of the MAOA polymorphism on impulsive behavior.

2. Materials and Methods

2.1. Participants. A total of 60 healthy male adolescents were recruited from a local middle school. All of them were Han Chinese. Only male adolescents were included because the MAOA VNTR polymorphism maps to an X-chromosome region suspected to escape the normal X-chromosome inactivation in females [36], making homozygous females not comparable to hemizygous males in terms of enzymatic activity. The inclusion criteria were an ability to give voluntary informed consent, an absence of concurrent neurological or psychiatric disorders, no history of head trauma, alcohol or drug abuse, no history of psychiatric illness or substance abuse on the basis of a SCID I assessment for DSM-IV criteria (1994), and no history of medical treatments relevant to cerebral blood flow and metabolism. The study was approved by the Ethics Committee of the Second Xiangya Hospital at Central South University in China, and all participants gave written informed consent to participate.

2.2. Neuropsychological Evaluation. The Italian version of the 11-item Barratt's Impulsivity Scale (BIS-11) was administered to obtain neuropsychological profiles of the subjects' impulsivity [37].

2.3. Genotyping. Samples of DNA were obtained by cheek swabbing. Polymerase chain reactions (PCRs) were performed in 25 μ L reaction volumes containing 1 μ L of DNA, GoTaq Green Master Mix (Promega Company, USA), 12.5 μ L of each of two primers (200 ng/L), and 9.5 μ L ddH₂O. The amplification protocol was as follows: 94°C for 3 min, 35 cycles of 95°C for 30 s, 58°C for 30 s, and 72°C for 45 s in a Gene Amp PCR system 2400 (Applied Biosystem, CA). PCR products were separated and electrophoresed on a 1.8% agarose gel and stained with Du Red (Biosharp, USA). They were then viewed under UV transillumination, and sizes were determined by comparison with a 50 bp DNA sequencing ladder. The MAOA-VNTR (MAOA promoter region polymorphism) was genotyped according to previously described methods [2]. Alleles with 2, 3, or 5 repeats were categorized as “low” activity, while those with 3.5 or 4 repeats were categorized as “high” activity.

2.4. Data Acquisition. All fMRI scans were obtained with a Philips Achieva 3-T scanner. The participants were instructed to keep their eyes closed and refrain from initiating goal-directed, attention-demanding activity during scanning. Foam pads were used to reduce head movements, and fitted ear plugs were used to reduce scanner noise. Resting-state fMRI scans were performed with an echo planar imaging sequence. Scan parameters were as follows: repetition time = 2000 ms; echo time = 30 ms; flip angle = 90°, matrix = 64 × 64; field of view = 240 mm; slice thickness = 4 mm; and slice gap = 0 mm. Each brain volume contained 36 axial slices, and each functional run contained 206 volumes. Before the functional

scan, high-resolution ($1 \times 1 \times 1 \text{ mm}^3$) anatomical images of 180 contiguous slices were obtained with a 3D MPRAGE sequence (repetition time = 8.5 ms, echo time = 3.7 ms, and flip angle = 8°).

2.5. Data Preprocessing. Image preprocessing and statistical analyses were performed with Statistical Parametric Mapping (SPM8, <http://www.fil.ion.ucl.ac.uk/spm/>). The first six volumes of the functional images were discarded for magnetization equilibrium and participants' adaptation to scanning noise. For each participant, functional images were motion corrected using the realignment function. Data from the subjects whose head motions exceeded 2 mm in the x , y , or z plane or whose rotation exceeded 2° during scanning were excluded.

Each subject's anatomical images were segmented using the new segment function, and deformation field maps were obtained. The deformation field maps were applied to all functional images to normalize them into the standard Montreal Neurological Institute (MNI) space with a resampling voxel size of $3 \times 3 \times 3 \text{ mm}^3$. Segmented anatomical images (unmodulated) were used to define white matter (WM) and cerebrospinal fluid (CSF) masks by thresholding the density images at a value of 0.99. For the time series of each voxel, the first eigenvector of the time series in the WM mask and the first eigenvector of the times series in the CSF mask, together with 24 motion parameters of Friston's model [38], were regressed out using linear regression. Finally, the time series of each voxel was filtered temporally using a band-pass filter (0.01–0.1 Hz) to reduce the effects of low-frequency drifts and of physiological high frequency respiratory and cardiac noises.

2.6. ALFF Analysis. The REST software package (REST, <http://resting-fmri.sourceforge.net>) was used to calculate ALFF values with a voxel-based approach. The filtered time series for each voxel were transformed to the frequency domain with a Fast Fourier Transform function, yielding a power spectrum. The square root of the power spectrum was calculated and then averaged across 0.01–0.08 Hz at each voxel. This averaged square root was taken as the ALFF [25]. To reduce global effects of variability across participants, the ALFF of each voxel was divided by the global mean ALFF value within the whole-brain mask obtained previously, and a standardized ALFF map of the whole brain was obtained. The ALFF maps were then smoothed spatially with an 8 mm, full width at half maximum (FWHM) Gaussian filter.

2.7. Analyses of Clinical Variables in relation to ALFF Data. To investigate the relationship between altered ALFF and impulsivity scores, the average ALFF values of all voxels were extracted separately, and then Pearson's correlation coefficients for ALFF values versus BIS-II total scores were computed for each group separately.

2.8. Statistical Analysis. Two-sample t -tests were applied to assess demographic and clinical data differences between MAOA genotype groups in SPSS 11.6 software (SPSS Inc.,

TABLE 1: Demographic information of subjects.

Characteristic	MAOA-H ($N = 25$)	MAOA-L ($N = 31$)	P value
Age, years: mean (s.d.)	15.92 (0.81)	15.55 (0.81)	0.09
Education, year: mean (s.d.)	10.56 (0.51)	10.52 (0.57)	0.77
BIS-II score: mean (s.d.)	69.16 (7.17)	66.71 (6.05)	0.17

Abbreviations: MAOA-H = high-activity MAOA genotype group; MAOA-L = low-activity MAOA genotype group; BIS-II = Italian version of the 11-item Barratt's Impulsivity Scale; s.d. = standard deviation.

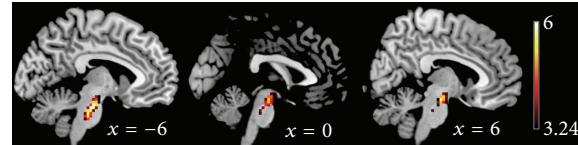


FIGURE 1: ALFF values using two-sample t -tests during resting state. Regions showing decreased ALFF values in male adolescents with MAOA-L compared to adolescents with MAOA-H were at the threshold $t > 3.24$, with correction for multiple comparisons applied at $P < .05$ (cluster-corrected with family wise error). Color bar indicates the T score.

Chicago, IL). To investigate ALFF differences between the two groups, two-sample t -tests were performed on the individual normalized ALFF maps in SPM8 software with age and educational level as nuisance covariates. The resulting statistical map was set at a combined threshold of $P < .001$ and a minimum cluster size of 50, which resulted in a cluster-corrected family-wise error $P < .05$.

3. Results

3.1. Genotyping and Participant Exclusions. The original cohort of 60 boys included 34 with the low-activity allele (57%) and 26 with the high-activity allele (43%). One high-activity allele and three low-activity allele subjects were excluded due to excessive head motion or rotation during scanning, leaving 31 low-activity allele and 25 high-activity allele subjects in the final analysis.

3.2. Demographic and Clinical Comparisons. The demographic and clinical data obtained for the two MAOA genotype groups are summarized in Table 1. There were no differences between the two genotype groups in terms of age, years of education, or BIS scores (all $P > 0.05$).

3.3. ALFF. Compared with MAOA-H carriers, adolescents carrying the MAOA-L allele showed significantly reduced ALFF values in the pons region of the brainstem (Table 2, Figure 1).

3.4. Behavioral Correlation. Although there were no differences in BIS scores between the MAOA genotype groups, only the MAOA-L group showed a significant correlation between the BIS score and the ALFF values in the pons

TABLE 2: Regions that showed significant differences in ALFF values between the high-activity and low-activity MAOA genotype groups in resting-state.

Bran region	Side	Peak MNI coordinates (mm)			Cluster size	Z score	P value*
		X	Y	Z			
MAOA-L < MAOA-H							
Pons	L	-6	-19	-23	130	4.38	<0.001
	R	6	-16	-17		4.12	
	L	-6	-25	-32		4.01	

Abbreviations: ALFF= amplitude of low-frequency fluctuations; MAOA-H = high-activity MAOA genotype group; MAOA-L = low-activity MAOA genotype group; L= left; R= right; MNI= Montreal Neurological Institute.

*Cluster-corrected with family-wise errors.

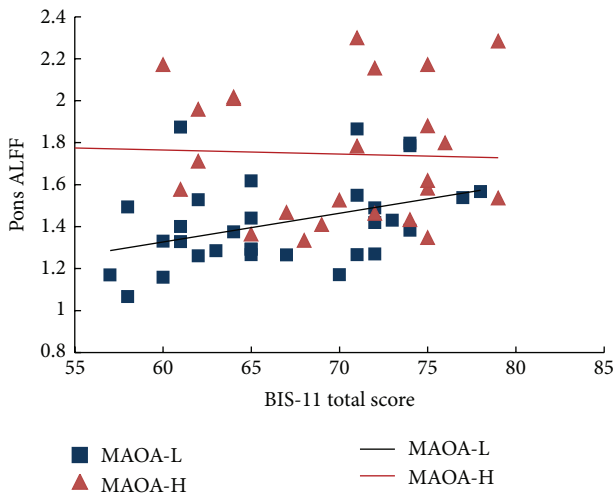


FIGURE 2: Correlations between BIS-II total scores and pons ALFF values in MAOA-L and MAOA-H genotype groups.

($r = 0.398$, $P = .02$, Figure 2), MAOA-H group showed no such correlation ($r = -0.044$, $P = .833$, Figure 2). Further regression analysis showed a significant genotype by ALFF values interaction effect on BIS scores ($\beta = 0.803$, $P < .05$).

4. Discussion

To our knowledge, the present study is the first to reveal the influence of MAOA genotype on brain regional spontaneous activity in male adolescents. We found that male adolescents with the MAOA-L genotype had significantly lower ALFF values in the pons than MAOA-H counterparts. Given that ALFF changes are suggestive of regional spontaneous neuronal activity [25], this difference is consistent with the possibility that boys carrying the MAOA-L may have a neural impairment in the pons and points to differential effects on spontaneous brain activity between the two MAOA genotypes. The allelic distribution observed in our sample population was similar to those reported previously in Asian populations [39, 40], and the approximate inverse of ratios reported for Caucasian populations (60–70% high activity allele and 30–40% low activity allele) [5, 22].

BIS-11 scores did not differ significantly between the groups, likely due to the small sample size in our study. Interestingly, however, we found that ALFF values in the pons correlated with BIS scores selectively in boys with a MAOA-L genotype but not in MAOA-H group, and a significant genotype by ALFF interactive effect on impulsiveness. These results suggest that MAOA genotype may modulate the association of impulsiveness and ALFF in pons, and the association was only shown in MAOA-L group.

The pons, a major component of the brainstem, serves mainly as a relay center between the spinal cord, cerebellum, and cerebral cortices and neural centers that control respiration, heartbeat, reflexes, sleep, equilibrium, and auditory and visual functions [41, 42]. Within the pons region, the locus coeruleus and raphe nuclei are important cranial nerve nuclei and are the principal sites for brain synthesis of NE and 5-HT, respectively. Using MAOA cDNA and oligonucleotide probes, Jahng et al. found that the pons (especially the locus coeruleus) is the region with the highest density of MAOA mRNA in the rat brain [43]. The MAOA gene polymorphism regulates the metabolism of NE and 5-HT [1]; animal and human studies indicate that the serotonin system has an important effect on aggressive and impulsive behavior [44, 45]. Therefore, it is possible that MAOA genotype-dependent modulation of 5-HT and NE neurotransmission underlie the MAOA gene effect to impulsiveness. Besides, it is possible that the influence of MAOA on spontaneous neuronal activity in pons is most likely mediated through its effects on serotonin and dopamine.

Previous research has implicated the role of pons in aggression. For example, pontine lesions have been associated with aggressive behaviors in animals [39, 40]. A human PET study showed reduced brain MAOA activity in the pons of participants who had high trait aggression compared with that in nonaggressive participants [41]. Indeed, several previous reports have pointed to the MAOA-L allele as a “risk” variant (allele) for impulsivity and aggression. Since Caspi and colleagues discovered that males carrying MAOA-L alleles who experienced early-life adversity were significantly likely to evince conduct disorder, an antisocial personality, and exhibit violent, antisocial behavior [5], a number of investigators have replicated the similar finding [9–11]. In addition, Huang et al. found that people with MAOA-L allele displayed more aggression and impulsive tendencies experienced abuse relative to their peers with MAOA-H allele

[7]. Our findings of low ALFF values in the pons of MAOA-L allele carriers, relative to those of MAOA-H allele carriers and selective correlation of BIS-11 scores with pons ALFF values in the MAOA-L group fit well the possibility that the MAOA-L allele may indeed be such a risk variant.

Our findings contrast with the results from a recent PET study showing no significant differences in resting brain glucose metabolism between the MAOA-L and MAOA-H genotypes [23]. However, previous fMRI studies have revealed significant effects of MAOA polymorphisms on brain activation in multiple corticolimbic regions, including anterior cingulate cortex, orbitofrontal cortex, and amygdala [17–20]. The inconsistent findings might be due to the different methodologies used and differences in the participants' characteristics, especially with respect to age composition.

There are some limitations of the current study that warrant consideration. First, the sample size is really small. We cannot rule out the possibility of false positive findings and the possibility of the gene effect on other brain regions. Second, only males were included in our study. We cannot determine whether the results are specific to males or also relate to females. Future studies should include both males and females with a larger sample size. In addition, the MAOA promoter polymorphism is likely not the only MAOA variant that has an effect on impulsiveness or brain function. We cannot rule out the potential interactive contribution of genotype-phenotype and gene-environment to impulsiveness or brain function.

5. Conclusions

In summary, in the present study, we obtained evidence showing that a well-characterized functional polymorphism in the MAOA gene modulates resting-state spontaneous brain activity in the pons in healthy male adolescents. Lower spontaneous brain activity in the pons of the MAOA-L male adolescents may provide a neural mechanism by which boys with the MAOA-L genotype confers risk for impulsivity and aggression.

Conflict of Interests

The authors declare that there is no conflict of interests in this paper with any trademark or software mentioned.

Authors' Contribution

Hui Lei and Xiaocui Zhang made equal contributions to this study.

Acknowledgments

This work was supported by a grant from the Ph.D. Programs Foundation of Ministry of Education of China (no. 20130162110043 awarded to Shuqiao Yao) and the Research Innovation Project for Postgraduate of Hunan Province, China (no. CX2011B068 awarded to Xiaocui Zhang). The authors are also very grateful to all volunteers who were

willing to participate in this study and for their compliance to the study protocol without receiving any financial incentive.

References

- [1] J. C. Shih and K. Chen, "MAO-A and -B gene knock-out mice exhibit distinctly different behavior," *Neurobiology*, vol. 7, no. 2, pp. 235–246, 1999.
- [2] S. Z. Sabol, S. Hu, and D. Hamer, "A functional polymorphism in the monoamine oxidase A gene promoter," *Human Genetics*, vol. 103, no. 3, pp. 273–279, 1998.
- [3] R. M. Denney, H. Koch, and I. W. Craig, "Association between monoamine oxidase A activity in human male skin fibroblasts and genotype of the MAOA promoter-associated variable number tandem repeat," *Human Genetics*, vol. 105, no. 6, pp. 542–551, 1999.
- [4] S. B. Manuck, J. D. Flory, R. E. Ferrell, J. J. Mann, and M. F. Muldoon, "A regulatory polymorphism of the monoamine oxidase-A gene may be associated with variability in aggression, impulsivity, and central nervous system serotonergic responsivity," *Psychiatry Research*, vol. 95, no. 1, pp. 9–23, 2000.
- [5] A. Caspi, J. McCray, T. E. Moffitt et al., "Role of genotype in the cycle of violence in maltreated children," *Science*, vol. 297, no. 5582, pp. 851–854, 2002.
- [6] J. Samochowiec, K.-P. Lesch, M. Rottmann et al., "Association of a regulatory polymorphism in the promoter region of the monoamine oxidase A gene with antisocial alcoholism," *Psychiatry Research*, vol. 86, no. 1, pp. 67–72, 1999.
- [7] Y. Y. Huang, S. P. Cate, C. Battistuzzi, M. A. Oquendo, D. Brent, and J. J. Mann, "An association between a functional polymorphism in the monoamine oxidase A gene promoter, impulsive traits and early abuse experiences," *Neuropsychopharmacology*, vol. 29, no. 8, pp. 1498–1505, 2004.
- [8] J. Kim-Cohen, A. Caspi, A. Taylor et al., "MAOA, maltreatment, and gene-environment interaction predicting children's mental health: new evidence and a meta-analysis," *Molecular Psychiatry*, vol. 11, no. 10, pp. 903–913, 2006.
- [9] D. L. Foley, L. J. Eaves, B. Wormley et al., "Childhood adversity, monoamine oxidase A genotype, and risk for conduct disorder," *Archives of General Psychiatry*, vol. 61, no. 7, pp. 738–744, 2004.
- [10] K. W. Nilsson, R. L. Sjöberg, M. Damberg et al., "Role of monoamine oxidase A genotype and psychosocial factors in male adolescent criminal activity," *Biological Psychiatry*, vol. 59, no. 2, pp. 121–127, 2006.
- [11] C. S. Widom and L. M. Brzustowicz, "MAOA and the 'cycle of violence': childhood abuse and neglect, MAOA genotype, and risk for violent and antisocial behavior," *Biological Psychiatry*, vol. 60, no. 7, pp. 684–689, 2006.
- [12] S. R. H. Beach, G. H. Brody, T. D. Gunter, H. Packer, P. Wernett, and R. A. Philibert, "Child maltreatment moderates the association of MAOA with symptoms of depression and antisocial personality disorder," *Journal of Family Psychology*, vol. 24, no. 1, pp. 12–20, 2010.
- [13] G. Guo, X.-M. Ou, M. Roettger, and J. C. Shih, "The VNTR 2 repeat in MAOA and delinquent behavior in adolescence and young adulthood: associations and MAOA promoter activity," *European Journal of Human Genetics*, vol. 16, no. 5, pp. 626–634, 2008.
- [14] O. Cases, I. Self, J. Grimsby et al., "Aggressive behavior and altered amounts of brain serotonin and norepinephrine in mice lacking MAOA," *Science*, vol. 268, no. 5218, pp. 1763–1766, 1995.

- [15] T. K. Newman, Y. V. Syagailo, C. S. Barr et al., "Monoamine oxidase a gene promoter variation and rearing experience influences aggressive behavior in rhesus monkeys," *Biological Psychiatry*, vol. 57, no. 2, pp. 167–172, 2005.
- [16] J. M. Mejia, F. R. Ervin, G. B. Baker, and R. M. Palmour, "Monoamine oxidase inhibition during brain development induces pathological aggressive behavior in mice," *Biological Psychiatry*, vol. 52, no. 8, pp. 811–821, 2002.
- [17] J. Fan, J. Fossella, T. Sommer, Y. Wu, and M. I. Posner, "Mapping the genetic variation of executive attention onto brain activity," *Proceedings of the National Academy of Sciences of the United States of America*, vol. 100, no. 12, pp. 7406–7411, 2003.
- [18] L. Passamonti, F. Fera, A. Magariello et al., "Monoamine oxidase-A genetic variations influence brain activity associated with inhibitory control: new insight into the neural correlates of impulsivity," *Biological Psychiatry*, vol. 59, no. 4, pp. 334–340, 2006.
- [19] A. Cerasa, M. C. Gioia, F. Fera et al., "Ventral-lateral prefrontal activity during working memory is modulated by MAO A genetic variation," *Brain Research*, vol. 1201, pp. 114–121, 2008.
- [20] A. Meyer-Lindenberg, J. W. Buckholtz, B. Kolachana et al., "Neural mechanisms of genetic risk for impulsivity and violence in humans," *Proceedings of the National Academy of Sciences of the United States of America*, vol. 103, no. 16, pp. 6269–6274, 2006.
- [21] A. Cerasa, M. C. Gioia, A. Labate et al., "MAO A VNTR polymorphism and variation in human morphology: a VBM study," *NeuroReport*, vol. 19, no. 11, pp. 1107–1110, 2008.
- [22] A. Cerasa, A. Quattrone, M. C. Gioia et al., "MAO A VNTR polymorphism and amygdala volume in healthy subjects," *Psychiatry Research—Neuroimaging*, vol. 191, no. 2, pp. 87–91, 2011.
- [23] N. Alia-Klein, A. Kriplani, K. Pradhan et al., "The MAO-A genotype does not modulate resting brain metabolism in adults," *Psychiatry Research—Neuroimaging*, vol. 164, no. 1, pp. 73–76, 2008.
- [24] B. Biswal, F. Z. Yetkin, V. M. Haughton, and J. S. Hyde, "Functional connectivity in the motor cortex of resting human brain using echo-planar MRI," *Magnetic Resonance in Medicine*, vol. 34, no. 4, pp. 537–541, 1995.
- [25] Y. F. Zang, Y. He, C. Z. Zhu et al., "Altered baseline brain activity in children with ADHD revealed by resting-state functional MRI," *Brain and Development*, vol. 29, pp. 83–91, 2007.
- [26] A. Shmuel and D. A. Leopold, "Neuronal correlates of spontaneous fluctuations in fMRI signals in monkey visual cortex: implications for functional connectivity at rest," *Human Brain Mapping*, vol. 29, no. 7, pp. 751–761, 2008.
- [27] S. I. Gonçalves, J. C. de Munck, P. J. W. Pouwels et al., "Correlating the alpha rhythm to BOLD using simultaneous EEG/fMRI: inter-subject variability," *NeuroImage*, vol. 30, no. 1, pp. 203–213, 2006.
- [28] Z. Zhang, G. Lu, Y. Zhong et al., "fMRI study of mesial temporal lobe epilepsy using amplitude of low-frequency fluctuation analysis," *Human Brain Mapping*, vol. 31, no. 12, pp. 1851–1861, 2010.
- [29] M. J. Hoptman, X. N. Zuo, P. D. Butler et al., "Amplitude of low-frequency oscillations in schizophrenia: a resting state fMRI study," *Schizophrenia Research*, vol. 117, no. 1, pp. 13–20, 2010.
- [30] X. Q. Huang, S. Lui, W. Deng et al., "Localization of cerebral functional deficits in treatment-naive, first-episode schizophrenia using resting-state fMRI," *NeuroImage*, vol. 49, no. 4, pp. 2901–2906, 2010.
- [31] Q. Jiao, J. Ding, G. Lu et al., "Increased activity imbalance in fronto-subcortical circuits in adolescents with major depression," *PLoS ONE*, vol. 6, no. 9, Article ID e25159, 2011.
- [32] X. C. Zhang, X. L. Zhu, X. Wang et al., "First-episode medication-naive major depressive disorder is associated with altered resting brain function in the affective network," *PLoS ONE*, vol. 9, Article ID e85241, 2014.
- [33] G. H. Jiang, Y. W. Qiu, X. L. Zhang et al., "Amplitude low-frequency oscillation abnormalities in the heroin users: a resting state fMRI study," *NeuroImage*, vol. 57, no. 1, pp. 149–154, 2011.
- [34] Y. Yin, L. Li, C. Jin et al., "Abnormal baseline brain activity in posttraumatic stress disorder: a resting-state functional magnetic resonance imaging study," *Neuroscience Letters*, vol. 498, no. 3, pp. 185–189, 2011.
- [35] M. J. Lowe, M. D. Phillips, J. T. Lurito, D. Mattson, M. Dzemidzic, and V. P. Mathews, "Multiple sclerosis: low-frequency temporal blood oxygen level-dependent fluctuations indicate reduced functional connectivity—initial results," *Radiology*, vol. 224, no. 1, pp. 184–192, 2002.
- [36] L. Carrel, A. A. Cottle, K. C. Goglin, and H. F. Willard, "A first-generation X-inactivation profile of the human X chromosome," *Proceedings of the National Academy of Sciences of the United States of America*, vol. 96, no. 25, pp. 14440–14444, 1999.
- [37] A. Fossati, A. Di Ceglie, E. Acquarini, and E. S. Barratt, "Psychometric properties of an Italian version of the Barratt Impulsiveness Scale-11 (BIS-11) in nonclinical subjects," *Journal of Clinical Psychology*, vol. 57, no. 6, pp. 815–828, 2001.
- [38] K. J. Friston, S. Williams, R. Howard, R. S. J. Frackowiak, and R. Turner, "Movement-related effects in fMRI time-series," *Magnetic Resonance in Medicine*, vol. 35, no. 3, pp. 346–355, 1996.
- [39] R. B. Lu, J. F. Lee, H. C. Ko et al., "No association of the MAO-A gene with alcoholism among Han Chinese males in Taiwan," *Progress in Neuro-Psychopharmacology and Biological Psychiatry*, vol. 26, pp. 457–461, 2002.
- [40] S. Y. Huang, W. W. Lin, F. J. Wan et al., "Monoamine oxidase-A polymorphisms might modify the association between the dopamine D2 receptor gene and alcohol dependence," *Journal of Psychiatry and Neuroscience*, vol. 32, no. 3, pp. 185–192, 2007.
- [41] M. B. Carpenter, "Gross anatomy of the brain," in *Core Text of Neuroanatomy*, pp. 31–43, Williams & Wilkins, Baltimore, Md, USA, 2nd edition, 1978.
- [42] W. J. Larsen, "Development of the brain and cranial nerves," in *Essentials of Human Embryology*, M. Strauss and D. Terry, Eds., pp. 273–302, Churchill Livingstone, New York, NY, USA, 2nd edition, 1998.
- [43] J. W. Jahng, T. A. Houpt, T. C. Wessel et al., "Localization of monoamine oxidase A and B mRNA in the rat brain by in situ hybridization," *Synapse*, vol. 25, pp. 30–36, 1997.
- [44] T. E. Moffitt, G. L. Brammer, A. Caspi et al., "Whole blood-serotonin relates to violence in an epidemiological study," *Biological Psychiatry*, vol. 43, no. 6, pp. 446–457, 1998.
- [45] S. Howell, G. Westergaard, B. Hoos et al., "Serotonergic influences on life-history outcomes in free-ranging male rhesus macaques," *The American Journal of Primatology*, vol. 69, no. 8, pp. 851–865, 2007.

Research Article

Quantifying Cerebellum Grey Matter and White Matter Perfusion Using Pulsed Arterial Spin Labeling

Xiufeng Li,¹ Subhendra N. Sarkar,² David E. Purdy,³ and Richard W. Briggs^{4,5,6}

¹ Department of Radiology and Center for Magnetic Resonance Research, University of Minnesota, 2021 Sixth Street SE, Minneapolis, MN 55455, USA

² Department of Radiology, Beth Israel Deaconess Medical Center, Harvard Medical School, Boston, MA 02215, USA

³ Siemens Healthcare, Malvern, PA 19355, USA

⁴ Department of Radiology, UT Southwestern Medical Center, Dallas, TX 75390, USA

⁵ Department of Internal Medicine, UT Southwestern Medical Center, Dallas, TX 75390, USA

⁶ Department of Physics & Astronomy, Georgia State University, Atlanta, GA 30302, USA

Correspondence should be addressed to Xiufeng Li; lix1607@umn.edu

Received 27 February 2014; Accepted 12 April 2014; Published 15 May 2014

Academic Editor: Danny Jiongjiong Wang

Copyright © 2014 Xiufeng Li et al. This is an open access article distributed under the Creative Commons Attribution License, which permits unrestricted use, distribution, and reproduction in any medium, provided the original work is properly cited.

To facilitate quantification of cerebellum cerebral blood flow (CBF), studies were performed to systematically optimize arterial spin labeling (ASL) parameters for measuring cerebellum perfusion, segment cerebellum to obtain separate CBF values for grey matter (GM) and white matter (WM), and compare FAIR ASST to PICORE. Cerebellum GM and WM CBF were measured with optimized ASL parameters using FAIR ASST and PICORE in five subjects. Influence of volume averaging in voxels on cerebellar grey and white matter boundaries was minimized by high-probability threshold masks. Cerebellar CBF values determined by FAIR ASST were 43.8 ± 5.1 mL/100 g/min for GM and 27.6 ± 4.5 mL/100 g/min for WM. Quantitative perfusion studies indicated that CBF in cerebellum GM is 1.6 times greater than that in cerebellum WM. Compared to PICORE, FAIR ASST produced similar CBF estimations but less subtraction error and lower temporal, spatial, and intersubject variability. These are important advantages for detecting group and/or condition differences in CBF values.

1. Introduction

The cerebellum is important for motor control, attention, language, and emotion [1, 2] and is compromised in a number of diseases, such as ataxia, autism, and cerebellar cognitive affective syndrome [3, 4]. Adequate perfusion of the tissue bed is important physiologically for tissue viability and function. Therefore, reliable assessments of cerebellum perfusion are valuable for studying the normal physiology of the cerebellum, diagnosing and providing information about pathology, and monitoring the efficacy of individualized therapy strategies [5, 6].

As a completely noninvasive perfusion imaging technique, arterial spin labeling (ASL) has been useful for both clinical [7–10] and research [11–13] studies. However, most of the technical developments and applications of ASL have

focused on the superior cortical part of the brain rather than inferior brain regions such as cerebellum. In addition to two abstracts with preliminary data from optimization experiments [14, 15] and a case study [16], only a handful of papers have reported cerebellum CBF values [17–22], and only one has reported separate CBF values for grey matter (GM) and white matter (WM) in cerebellum [17].

FAIR ASST [15, 17], by using preinversion and postinversion superior saturations, overcomes the FAIR confound of creating two labeled boluses, only one of which is temporally defined with QUIPSS [13] or Q2TIPS [23, 24]. FAIR ASST also reduces adverse venous artifacts generated by the intrinsic superior labeling of traditional FAIR when mapping CBF in middle and inferior brain regions. In this respect, FAIR ASST is similar to asymmetric PASL techniques such as PICORE (proximal inversion of magnetization with a control

for off-resonance effects) [13], in which only the inferiorly labeled blood is used for perfusion quantification; yet FAIR ASST retains the inherent control of magnetization transfer (MT) effects of symmetric FAIR methods. The aims of this study were to (1) systematically optimize ASL parameters for quantifying cerebellum CBF, (2) segment cerebellum to obtain separate CBF values for grey matter (GM) and white matter (WM), and (3) verify the hypothesis that FAIR ASST would be better than PICORE for quantifying cerebellum perfusion.

2. Materials and Methods

2.1. Subjects. Ten healthy male adults (age range 25–37 years, mean \pm S.D. = 29 ± 6 years) took part in four studies in three sessions to optimize the ASL sequences for the cerebellum: three subjects for the first study and session, four for the second study and session, and another three for the last two studies in the third session (see “ASL Optimization Studies” below). Five healthy male adults (age range 27–40 years, mean \pm S.D. = 35 ± 5 years) participated in the subsequent quantitative cerebellum perfusion study. Since caffeine is a vasoconstrictor, all subjects refrained from caffeine-containing coffee, tea, and soft drinks at least 8 hours before the studies. Subjects were instructed to avoid any movements of arms or legs and keep eyes closed but remain awake. Subjects’ heads were tightly restrained with foam padding. Studies were performed at approximately the same time in the early afternoon to avoid potential effects of circadian rhythms. Informed consent was obtained from all subjects prior to the studies, according to a protocol approved by the local Institutional Review Board.

2.2. MRI Scanner and Sequences. Studies were performed using a 3T Siemens Trio TIM whole-body scanner with 60 cm diameter magnet bore and SQ gradients (maximum gradient strength 45 mT/m in the z direction and 40 mT/m in the x and y directions, maximum slew rate 200 T/m/s). The body coil was used for transmission, and the Siemens 12-channel phased array head coil was used for reception.

For both FAIR ASST and PICORE sequences (Figure 1), a 15.36 ms hyperbolic secant inversion pulse with $22 \mu\text{T}$ RF amplitude and 95% labeling efficiency was used. The slab thickness for the inversion was adjusted by varying the slice-select gradient amplitude based on a reference value of 0.7 mT/m for a 100 mm slab [25]. Both sequences incorporated Q2TIPS method to define temporal bolus duration (TI_1) [24]. After a postlabeling time, imaging slices were acquired at total delay time (TI_2) by using echo planar imaging (EPI) as the readout. All saturation modules consisted of a 90-degree RF pulse followed by a spoiling gradient. The total duration of one saturation module was about 11 ms. Depending on the thickness of the saturation slab, an appropriate RF saturation pulse was automatically selected from a set of sinc RF pulses optimized for various thicknesses.

The FAIR ASST [15, 17] sequence used one preinversion and two postinversion superior saturation RF pulses to suppress the superior tagging of FAIR. The PICORE sequence

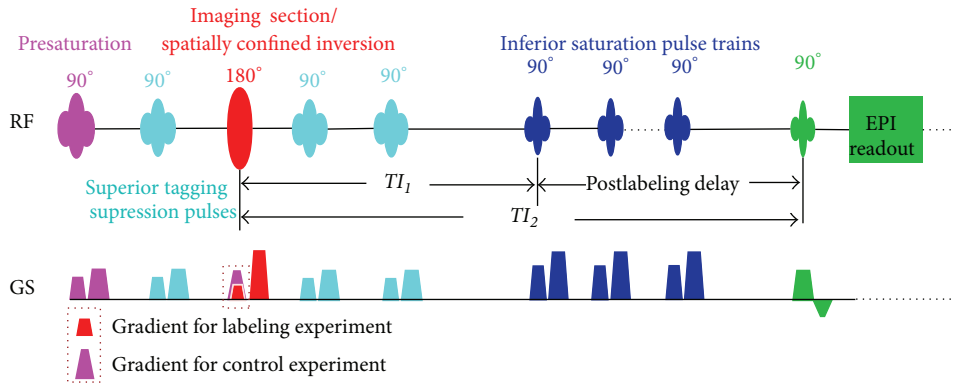
performed labeling image acquisition with proximal inversion and control image acquisition without slice-selective proximal inversion. Instead, the gradient used for slice-selective inversion in the labeling image acquisition was played out before the frequency-offset RF pulse [13], in the control image acquisition (Figure 1), to control for possible eddy current effects on slice acquisition.

2.3. Imaging Protocol. The Siemens coregistration tool AutoAlign was used to provide consistent slice orientation and position with respect to a standard head atlas across subjects and sessions. Axial ASL imaging slices were positioned to have the first inferior slice cover the lower edge of the cerebellum, oriented parallel to the anterior-posterior direction (Figure 1). Due to subject-dependent brain geometry, manual translation adjustment was helpful to ensure consistent slice position across subjects. The AutoAlign scout was followed by a gradient echo localizer, the T_1 -weighted high-resolution anatomic imaging sequence MPRAGE, and ASL scans with an EPI readout.

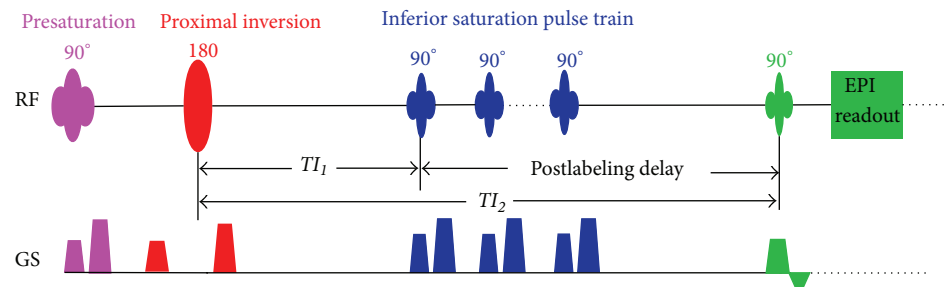
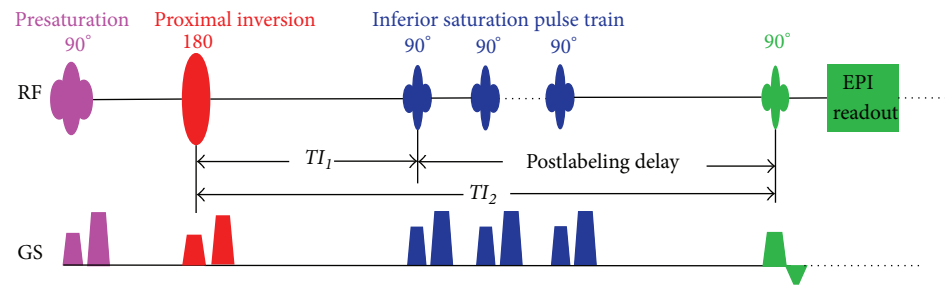
The MPRAGE sequence used the following parameters: TR/TE/TI = 2250/4/900 ms, flip angle = 9° , field of view (FOV) = $230 \times 230 \times 160 \text{ mm}^3$, matrix size = $256 \times 256 \times 160$, resolution = $0.9 \times 0.9 \times 1 \text{ mm}^3$, bandwidth = 160 Hz/pixel, GRAPPA iPAT factor = 2 with 24 reference lines, partial Fourier (PF) = 7/8, slice oversampling = 10%, slice orientation = sagittal, phase encoding direction = anterior to posterior, and total imaging time = 4 minutes and 38 seconds.

2.4. ASL Optimization Studies. The following ASL studies were performed to optimize FAIR ASST parameters for measuring cerebellar CBF: (1) a series of perfusion experiments, each with a different TI_2 value, to estimate arterial transit time (ATT) and bolus duration, the latter for properly setting the TI_1 value for the following experiments (Figure 1), (2) a perfusion study using the fixed optimal TI_1 value of 800 ms determined in (1) and varied postlabeling delay times to identify the proper delay to avoid intravascular artifacts, (3) a multiple-TR perfusion study to determine if a short TR significantly affects the refreshment of arterial blood at the labeling site, and (4) a study varying the number of inferior saturation pulses to find the minimum number necessary for effective suppression of residual labeled blood spins.

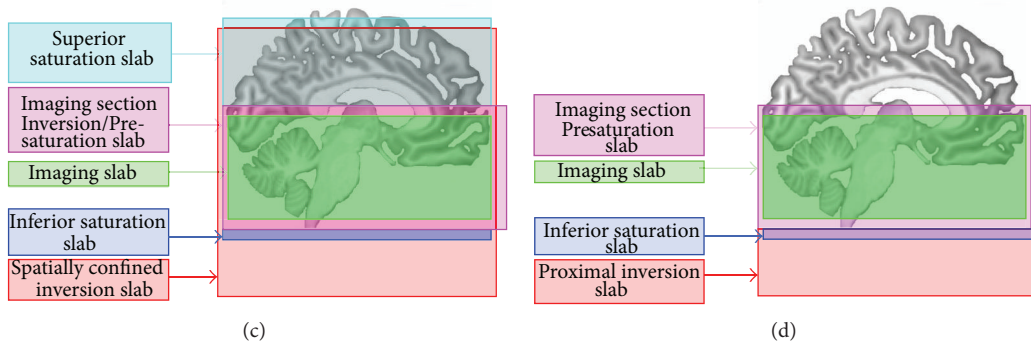
The variable TI_2 perfusion study employed the following MRI parameters: TR/TE = 4000/9.2 ms, FOV = $230 \times 230 \text{ mm}^2$, matrix size = 66×66 , in-plane resolution = $3.48 \times 3.48 \text{ mm}^2$, number of imaging slices = 12, slice thickness/gap = 5 mm/1 mm, imaging slab size = 71 mm, pairs of label and control measurements = 30, iPAT GRAPPA factor = 2 with 24 reference lines, and partial Fourier (PF) = 7/8. Imaging slices were acquired in ascending order. The slab sizes for the superior saturation, imaging section inversion, and spatially confined selective inversion were equal to 100 mm, 91 mm, and 271 mm, respectively. For each subject, the experiment was conducted twelve times using randomly ordered TI_2 values of 50, 300, 600, 900, 1200, 1500, 1800, 2100, 2400, 2700, 3000, and 3300 ms. The inferior saturation pulse



(a) FAIR ASST with Q2TIPS



(b) PICORE with Q2TIPS



(c)

(d)

FIGURE 1: Sequence diagrams for FAIR ASST (a) and PICORE (b) and spatial definitions for different slabs of FAIR ASST (c) and PICORE (d). Imaging section presaturation pulses (a, b in pink) were played out before the inversion RF pulses (in red); the imaging section slabs for the presaturations are presented in pink (c, d). Inferior saturation pulses and the corresponding saturation slab are indicated by dark blue. Superior tagging suppression pulses and the corresponding saturation slab, for FAIR ASST only, are displayed in cyan (a, c). For FAIR ASST (a, c), the stronger gradient (pink) for the imaging section control inversion and the weaker gradient (red) for the spatially confined labeling inversion are superposed on the sequence diagram and further denoted by the legends beneath the sequence diagram. For PICORE (b, d), the labeling was achieved by using proximal inversion (red) 10 mm below the imaging slab (green); in the labeling experiment (b, top), the slice-selective gradient was played out with an RF inversion pulse to create the proximal inversion slab (d), while in the control experiment (b, bottom), the gradient was played out before the control off-resonance RF inversion pulse, to control for possible gradient eddy current effects. The imaging slab was positioned to make the first inferior imaging slice cover the inferior edge of the cerebellum (c, d).

train was turned off. Total imaging time for ASL acquisitions was about 48 minutes.

The rest of the optimization studies used the same ASL parameters as those in the studies with varied TI_2 values, except as follows. Parameters for perfusion studies using varied postlabeling delay times were TR = 3000 ms, inferior saturation pulse interval/thickness = 25 ms/20 mm, TI_1 value/postlabeling times = 800/{200, 400, 600, 800, 1000, 1200, 1400} ms (randomized for each subject), inferior saturation pulse train lasting for the entire postlabeling delay period, and total ASL imaging time of about 21 minutes. In the perfusion studies exploring the effect of TR, parameters were TR = {2.5, 3.0, 3.5} s (randomized for each subject), $TI_1/TI_2 = 800$ ms/1800 ms, inferior saturation pulse interval/thickness/number = 25 ms/20 mm/40, and total imaging time of about 9 minutes. In the study evaluating the number of inferior saturations, parameters were TR = 3 s, $TI_1/TI_2 = 800$ ms/1800 ms, and inferior saturation pulse interval/thickness = 25 ms/20 mm. The number of inferior saturation pulses was varied from 0 to 40 in increments of 10, and the order of the imaging scans was randomized for each subject. The total imaging time for evaluating the sufficient number of inferior saturations was about 15 minutes.

2.5. Quantitative Cerebellum Perfusion Studies. The following ASL parameters were used for quantitative cerebellum perfusion studies: FOV = 180×180 mm², matrix size = 72×72 , slice thickness/gap = 3.5/0.7 mm, slice number = 16, in-plane resolution = 2.5×2.5 mm², slice thickness/gap = 3.5/0.7 mm, TR/TE = 2500/12 ms, pairs of label and control measurements = 90, iPAT GRAPPA factor = 2 with 24 reference lines, partial Fourier (PF) = 7/8, acquisition order = ascending (foot to head), $TI_1/TI_2 = 800$ ms/1800 ms, inferior saturation interval/thickness/number = 25 ms/20 mm/20, superior saturation slab thickness = 100 mm, selective inversion slab = 86.5 mm, and spatially confined inversion slab = 266.5 mm. For PICORE, a 100 mm slab, approximately the same as the effective inferior labeling slab size applied in FAIR ASST experiments, was used for proximal inversion, with a 10 mm gap between the imaging slab and the inversion slab. For each ASL scan, two proton density (M_0) images were acquired, one before and one after each ASL series, by using the same sequence with TR = 8 s, and the average M_0 image was used in subsequent model fits [25]. The total ASL imaging scan time was about 16 minutes with about 8 minutes for each method.

2.6. Data Processing Software. Image processing operations, such as motion correction and coregistration, were performed with SPM2 (Functional Imaging Laboratory, University College London). Four-parameter iterative nonlinear least squares model fitting was performed using scripts implemented in Matlab 7.1 (The MathWorks, Inc., Natick, Massachusetts) for perfusion signals from studies using multiple varied TI_2 values.

2.7. Image Preprocessing. Each ASL imaging series was first evaluated for subject motion, and whenever the translational motion was larger than 1 mm or the rotation around any axis

was larger than 1°, motion correction was performed using trilinear interpolation. Pairs of labeling and control images with motions larger than 2 mm in translation or 2° in rotation around any axis were excluded from further processing or analysis. A mean image of the ASL series was generated for later use in coregistration. Each ASL label-control image series was processed by pairwise subtraction to generate a perfusion-weighted imaging series, and images within the series were averaged to produce a mean perfusion-weighted image. The two M_0 images in each series were averaged to obtain a mean M_0 image.

2.8. Iterative Model Fitting. An iterative nonlinear least-squares model fitting was performed to fit ASL signals in the defined ROIs to the three-phase, single blood compartment model [26]:

$$\begin{aligned} \Delta M(t) &= 0, \quad 0 < t < \Delta t \\ &= 2\alpha M_{ob} \text{CBF} (t - \Delta t) \exp\left(-\frac{t}{T_{1b}}\right), \quad \Delta t < t < \tau + \Delta t \\ &= 2\alpha M_{ob} \text{CBF} \tau \exp\left(-\frac{t}{T_{1b}}\right), \quad \tau + \Delta t < t, \end{aligned} \quad (1)$$

where $\Delta M(t)$ is the measured ASL difference signal between label and control images in a specified ROI or voxel at inversion time t , Δt is the arterial transit time, τ is the bolus duration, CBF is the cerebral blood flow, M_{ob} is the fully relaxed magnetization of the blood, T_{1b} is the longitudinal relaxation time of the arterial blood, and α is the labeling efficiency, assumed to be 0.95 for the hyperbolic secant pulse used in this study [25].

To avoid the adverse effects of labeled blood signals from large arteries at short postlabeling delay times and of subtraction errors due to small motions, trimmed means of averaged ASL difference signals from the studies using varied TI_2 values were used for ASL model fitting, by excluding the 5% of voxels with the lowest values and the 5% with the highest values within GM and WM ROIs [27]. Perfusion signals were compensated for longitudinal relaxation differences between slices due to the incremental time of ~30 ms for sequential slice acquisition. To increase the signal-to-noise ratio (SNR) for perfusion signals measured with long TI_2 values, the GM perfusion signals of two adjacent imaging slices were averaged and fitted to the perfusion model.

2.9. CBF Quantification Using the Single-Subtraction Method. The mean perfusion-weighted image and the mean M_0 image were used to estimate CBF using the single blood compartment model [25, 28, 29]:

$$\text{CBF} = \frac{\Delta M}{(2\alpha M_{ob} TI_1 \exp(-TI_2/T_{1b}))}, \quad (2)$$

$$M_{ob} = \frac{M_0}{\lambda}, \quad (3)$$

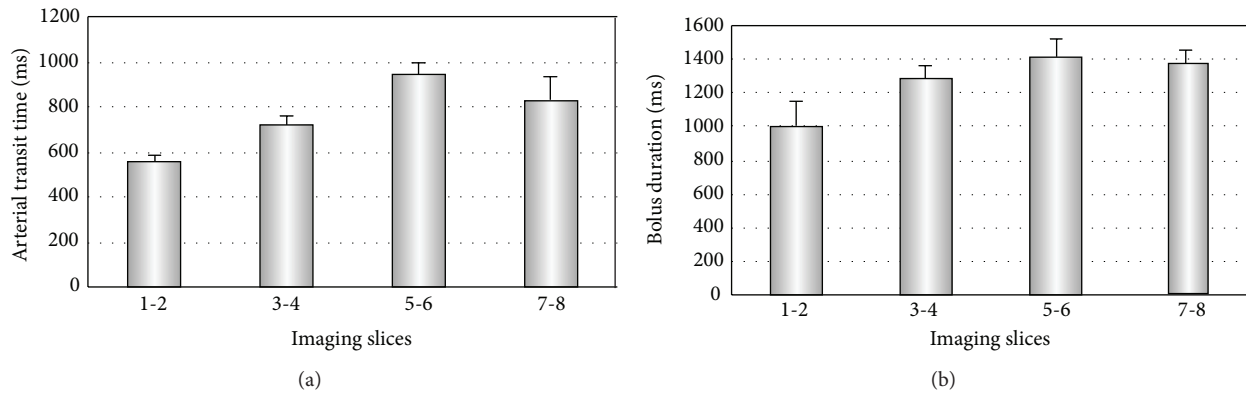


FIGURE 2: Estimated arterial transit time (a) and bolus duration (b) from perfusion studies using varied total delay times, TI_2 . Error bars represent standard deviations.

where ΔM is the mean ASL difference signal between labeling and control images, TI_2 is the total inversion time equal to the sum of TI_1 and the postlabeling delay, M_0 is the measured tissue proton density, and λ is the brain blood/tissue partition coefficient (assumed to be 0.9) [30].

2.10. Segmentation of Cerebellum GM and WM. Individual whole-brain GM and WM tissue masks were automatically generated using SPM with a probability threshold of 0.75. To obtain GM and WM masks constrained to cerebellum, a mask for cerebellum was manually traced from the high-resolution anatomic image for each subject, and a Boolean operation was then performed between the hand-drawn cerebellar ROIs and the probability-based GM and WM segmentation maps from SPM. GM and WM segmentation masks constrained to cerebellum obtained from that operation were coregistered to the mean image of the ASL scan series. The cerebellar GM and WM masks occasionally exhibited some nonbinary voxel values due to interpolation, and a few of these intermediate-valued voxels extended slightly beyond the cerebellum. In these cases, a threshold (typically equal to 0.9 for most subjects) was used to further conservatively limit the masks, based on individual inspection.

2.11. ROI-Based Cerebellum GM and WM CBF Analysis. For each subject, overall cerebellum GM and WM CBF values were estimated for the two PASL methods. Group mean CBF and standard deviation were calculated for cerebellum GM and WM. Interslice, spatial, and temporal variabilities were evaluated by computing the coefficient of variance (C.V.), or standard deviation divided by mean, expressed as percentage. Interslice variability was defined as the ratio between the standard deviation and the mean of slice mean CBF values. Spatial variability was calculated for all voxels within cerebellum GM and WM. The temporal variability was calculated by using the mean perfusion signals of four imaging slices near transverse sinuses.

Comparisons of GM CBF, WM CBF and perfusion signal variability between the two PASL methods were performed

using two-tailed paired t -tests; $P < 0.05$ was used as the threshold of statistically significant difference.

3. Results

3.1. Optimization Studies. Model-fitting the data from perfusion studies using varied TI_2 values indicated that the estimated bolus durations (ca. 800–1500 ms) and arterial transit times (ca. 550–1000 ms) varied from slice to slice in the cerebellum (Figure 2). For the inferior saturation pulse to effectively define the labeled bolus, TI_1 should be set less than the bolus duration τ [23]; a TI_1 of 800 ms was chosen for subsequent optimization studies and quantitative cerebellum CBF estimation using FAIR ASST and PICORE.

Typical perfusion-weighted imaging maps from studies using 800 ms TI_1 and varied postlabeling delay times showed that at short delay times, spurious hyperintense signals within big arteries dominated, whereas after a delay of 1000 ms, the perfusion-weighted imaging maps became spatially uniform without obviously hyperintense signals. With a longer delay of 1200 ms, the perfusion-weighted imaging maps only marginally improved in signal uniformity while SNR decreased (Figure 3). Intersubject variability and spatial variability minimized at a postlabeling delay time of about 1000 ms, also implying that the optimal postlabeling delay time should be 1000 ms (Figure 4).

CBF values measured using TR values of 2.5, 3.0, and 3.5 s were comparable for both GM and WM, indicating that blood at the labeling site is rapidly refreshed and that TR values as short as 2.5 s can be used for quantitative cerebellum perfusion studies at 3T (Figure 5(b)). Ten or more inferior saturation RF pulses were required for effective suppression; after 20 inferior saturation pulses, suppression remained almost unchanged when additional inferior saturation pulses were applied (Figure 5(a)).

3.2. Quantitative Perfusion Studies. Figure 6 shows, for a representative subject, a coregistered high-resolution anatomic image, the segmentation masks for cerebellum GM and

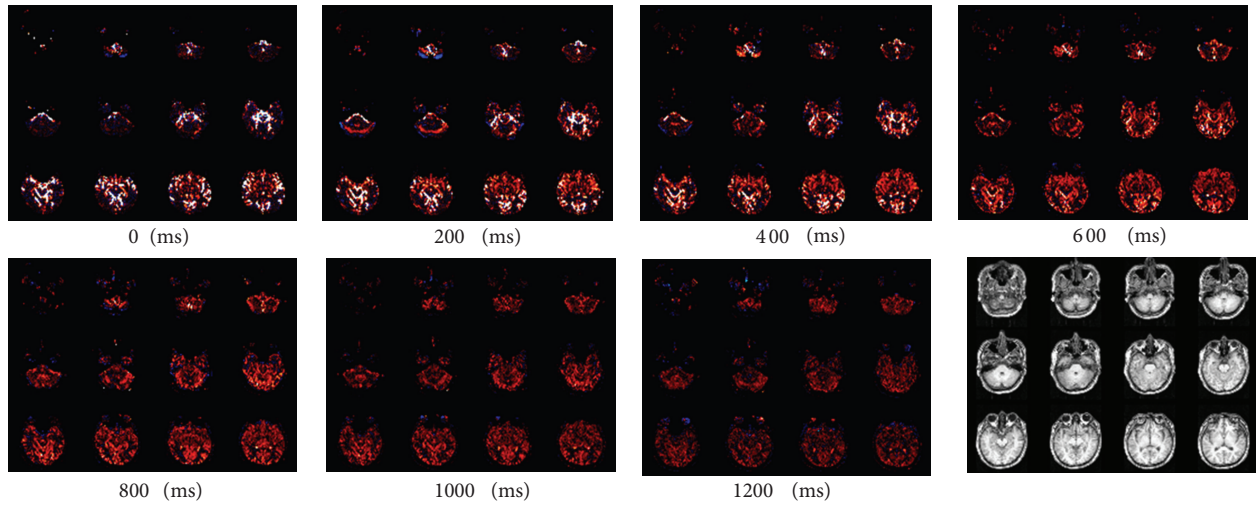


FIGURE 3: One typical subject's perfusion-weighted imaging maps and coregistered high-resolution anatomic images from the multiple-postlabeling-delay perfusion study with T_{I_1} equal to 800 ms. Postlabeling delay times (ms) for perfusion-weighted imaging maps are presented under corresponding panels.

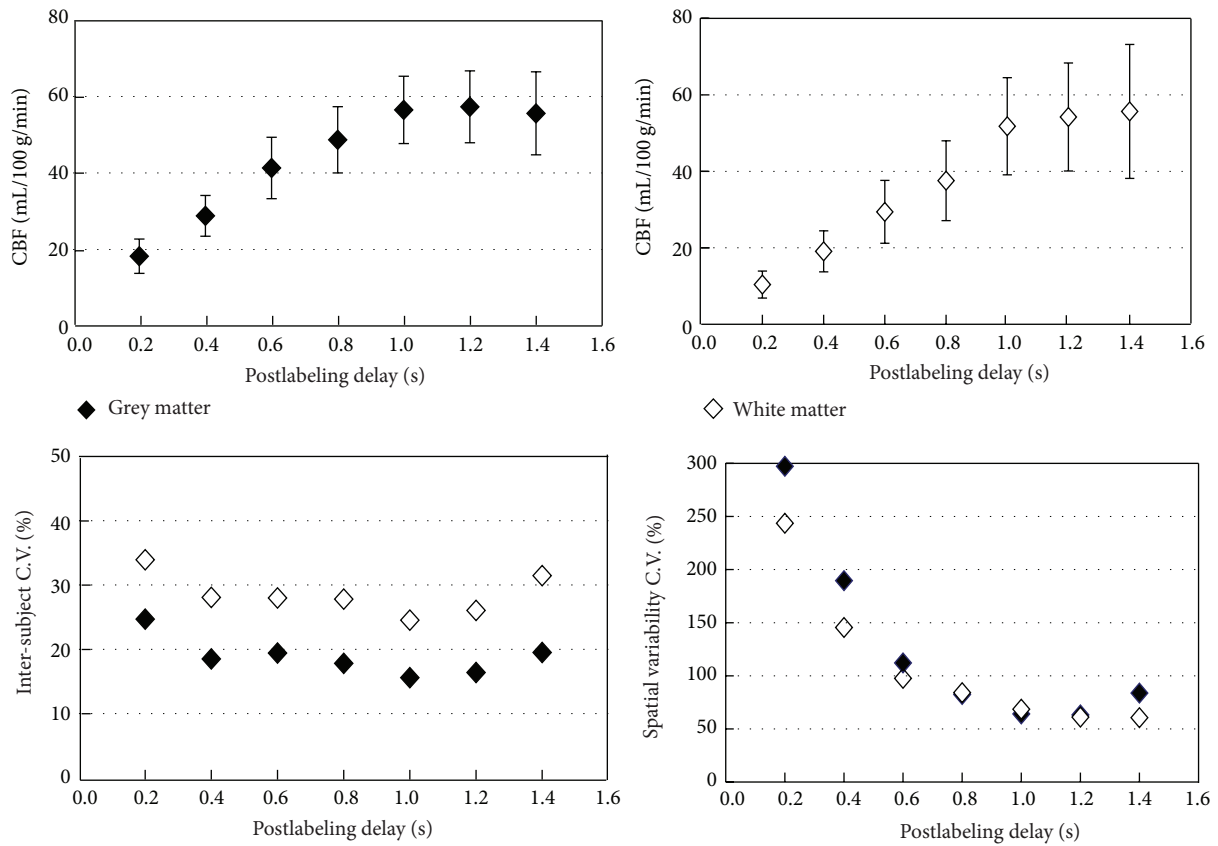


FIGURE 4: CBF values and intersubject and spatial variability of perfusion signals as a function of postlabeling delay time. Error bars represent standard deviation.

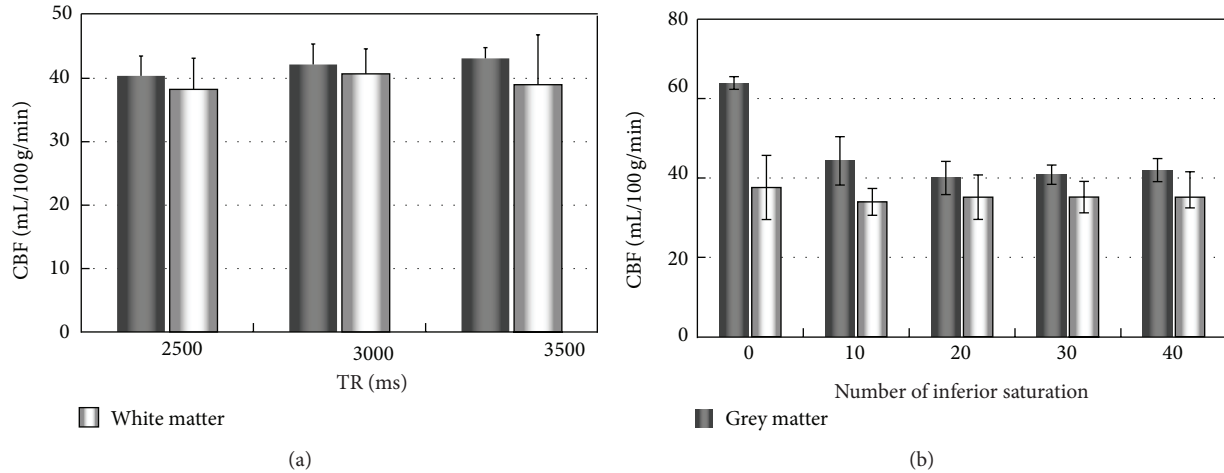


FIGURE 5: CBF values in cerebellum grey and white matter using different TRs (a) and different numbers of inferior saturation pulses (b). Error bars represent standard deviation.

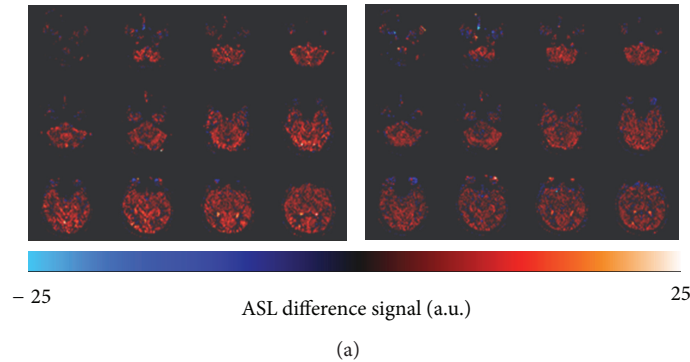


FIGURE 6: One typical subject's perfusion-weighted imaging maps in 12 slices from FAIR ASST ((a) left) and PICORE ((a) right), coregistered segmentation masks for cerebellum grey matter ((b) left) and white matter ((b) right), and corresponding high-resolution anatomic images (c).

WM, and the corresponding perfusion-weighted imaging maps from FAIR ASST and PICORE. Perfusion-weighted imaging maps from FAIR ASST have better uniformity than those from PICORE. The latter showed obvious hyperintense perfusion signal (especially in the inferior imaging slices) and more subtraction errors (as indicated by negative perfusion signals).

The mean CBF measured by FAIR ASST for cerebellum GM was 43.8 ± 5.1 mL/100 g/min, slightly higher but not significantly different ($P = 0.135$, paired two-tailed t -test) from the value of 40.35 ± 8.5 mL/100 g/min that was obtained using PICORE (Table 1). For cerebellum WM, the mean CBF from

FAIR ASST was 27.6 ± 4.5 mL/100 g/min, not significantly different ($P = 0.278$, paired two-tailed t -test) from the slightly lower value of 23.7 ± 7.5 mL/100 g/min from PICORE (Table 1). Mean grey-to-white matter ratios of cerebellum CBF (Table 1) obtained using the two PASL methods are similar ($P = 0.436$, paired two-tailed t -test). CBF measured by FAIR ASST gave lower intersubject (Table 1) and interslice (Figure 7(a)) variability and were more stable with time than data from PICORE (Figure 7(b)).

3.3. Susceptibility and Volume Averaging Effects. To check if signal reduction and image distortions arising from magnetic

TABLE I: Cerebellum CBF (mL/100 g/min) measured by FAIR ASST and PICORE*.

Subject number	FAIR ASST			PICORE		
	CBF _{GM}	CBF _{WM}	CBF _{GM} /CBF _{WM}	CBF _{GM}	CBF _{WM}	CBF _{GM} /CBF _{WM}
1	42.58	29.56	1.44	41.97	33.5	1.25
2	45.07	28.63	1.57	44.47	28.89	1.54
3	37.89	20.48	1.85	30.28	19.04	1.59
4	41.82	26.62	1.57	33.59	14.71	2.28
5	51.57	32.53	1.59	51.45	22.51	2.29
Mean	43.78*	27.56*	1.60*	40.35*	23.73*	1.79*
S.D.	5.06	4.49	0.15	8.52	7.53	0.47
C.V. (%)	11.6%	16.3%	9.4%	21.1%	31.7%	26.3%

*CBF_{GM} represents grey matter CBF; CBF_{WM}: white matter CBF; C.V.: coefficient of variance; and S.D.: standard deviation. No significant differences were found between the mean cerebellum CBF values obtained with FAIR ASST and PICORE, but the C.V. for FAIR ASST is about half that for PICORE.

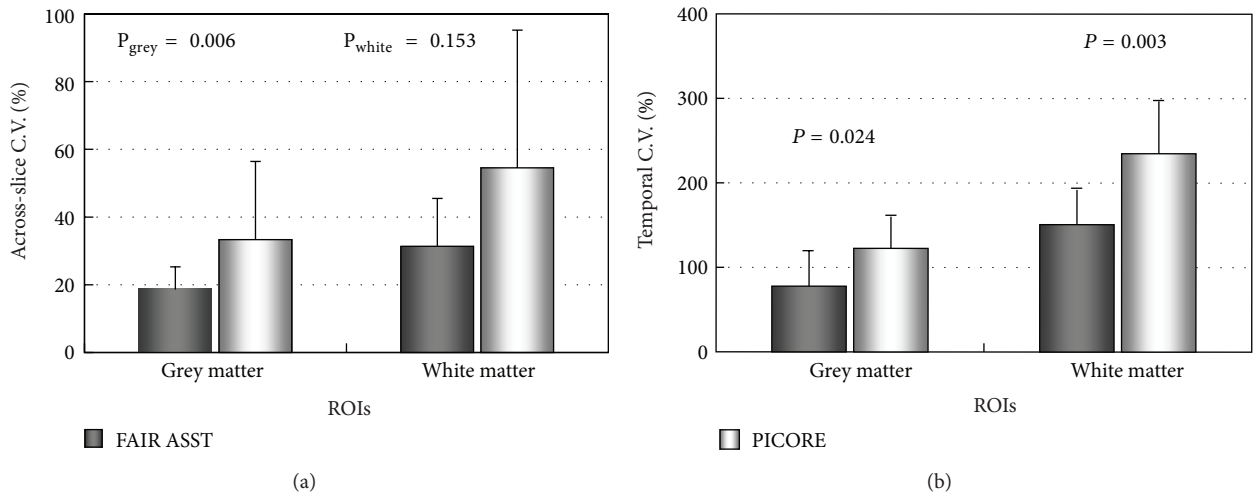


FIGURE 7: Across-slice and temporal variability of CBF values obtained with FAIR ASST and PICORE. Error bars represent standard deviations; P values are from two-tailed t -tests.

susceptibility gradients near the cerebellum [31] might be impacting CBF measurements of cerebellum GM or WM, scatter plots of CBF versus voxel intensity from the M_0 images were made (Figure 8(a)) and Pearson correlation tests were run on the data. No systematic correlation of CBF and M_0 voxel intensity was observed for WM ($R^2 = 0.022$); a slight correlation of CBF and M_0 voxel intensity for GM ($R^2 = 0.404$) disappeared when the 9.6% of GM voxels with intensities less than 800 were ignored ($R^2 = 0.029$). The correlation of CBF and M_0 voxel intensity for WM was only slightly affected by this threshold (1.6% of white matter voxels, $R^2 = 0.018$). The GM voxels with intensity < 800 were located almost entirely at the superficial cerebellar boundaries (Figure 8(b)), more suggestive of volume averaging (possibly exacerbated by slight motions) with the surroundings than of interfacial susceptibility mismatches. Histogram distribution plots for GM and WM M_0 voxel intensities were slightly skewed to high intensity for WM and to low intensity for GM, suggesting some averaging of intensities on the grey-white matter boundary (Figure 8(c)).

4. Discussion

Reliable perfusion measurements depend upon the proper selection of ASL parameters [26, 32, 33]. Optimization of parameters for cerebellum perfusion studies at 3T indicated that a temporal bolus width of 800 ms and a postlabeling delay of 1000 ms were suitable, that TR could be as short as 2.5 s without degrading SNR, and that 20 inferior saturation pulses were sufficient to suppress the residual labeled arterial blood. The postlabeling delay of 1.0 s is the same as that selected in a recent optimization study of cerebellar CBF [14].

Several previous quantitative measurements of cerebellar CBF by PET [33], SPECT [34], and ASL [14, 21] have yielded values in the range of 58–65 mL/100 g/min. The cerebellum GM CBF values of 63.6 ± 5.0 mL/100 g/min estimated using a PCASL multiple inversion time experiment with $3 \times 3 \times 7$ mm³ voxels [14] and of 58–62 mL/100 g/min estimated using PCASL with $3.44 \times 3.44 \times 5$ mm³ voxels [21] agree well with the cerebellum GM CBF value of 56.7 ± 5.0 mL/100 g/min for 6 subjects using FAIR with Q2TIPS

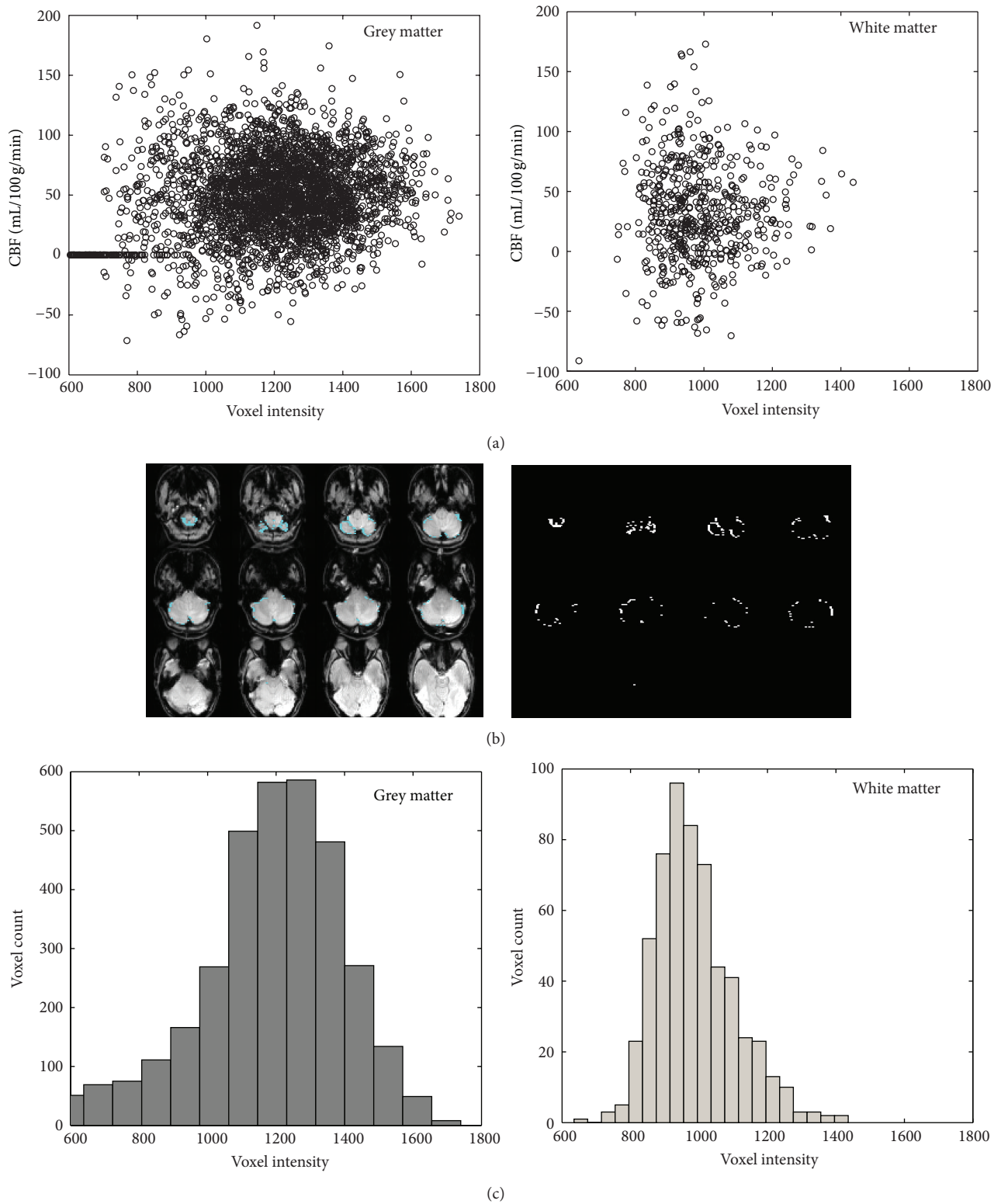


FIGURE 8: Analysis results for evaluating susceptibility and partial volume effects on cerebellar CBF measurements: (a) scatter plots of CBF versus M_0 voxel intensity for cerebellar grey matter (left) and white matter (right) from one typical subject show no relation between these two parameters; (b) grey matter voxels with intensity <800 were located almost entirely at the superficial cerebellar boundaries, as shown by images with (left) and without (right) anatomic underlays; (c) histogram distribution plots of cerebellar grey matter and white matter M_0 signal intensities from one typical subject showing high-intensity tail for WM and low-intensity tail for GM.

with $(3.5 \text{ mm})^3$ voxels [17] and the cerebellum GM CBF values of 55–65 mL/100 g/min obtained in the inferior saturation and postlabeling delay experiments of this study. PET [34], SPECT [35–37], and other ASL studies, one with $7 \times 3 \times 3 \text{ mm}^3$ voxels [20] and others with smaller voxels [16, 18, 19], have reported cerebellum CBF values of 30–48 mL/100 g/min, similar to those obtained with FAIR ASST in this study. The superior saturation of FAIR ASST reliably reduces contributions of inflow of superiorly labeled blood that artifactually enhance CBF estimates [15, 17] in FAIR, and thus it is not surprising that the cerebellar GM CBF of $43.8 \pm 5.1 \text{ mL/100 g/min}$ obtained using FAIR ASST with $2.5 \times 2.5 \times 3.5 \text{ mm}^3$ voxels in this study is lower than those obtained using traditional FAIR [17]. GM CBF measurements by FAIR ASST are comparable to, although insignificantly and slightly lower than, the literature values from PCASL [14, 20–22]; these slight differences of CBF measurements between FAIR ASST and PCASL can possibly be attributed to the use of different ASL techniques as well as CBF quantification models [22]. The cerebellar WM CBF of $27.6 \pm 4.5 \text{ mL/100 g/min}$ from this FAIR ASST study is also lower than the cerebellar WM CBF of $36.7 \pm 2.7 \text{ mL/100 g/min}$ from FAIR with Q2TIPS [17]. It should be noted that our data indicate volume averaging of GM and WM in some voxels (Figure 8(c)); if this were corrected [38], our average GM CBF values would be somewhat greater and our average WM CBF values would be slightly smaller.

Although it has been suggested that EPI-based ASL sequences for obtaining cerebellar perfusion might exhibit signal reduction and image distortions arising from magnetic susceptibility gradients near the cerebellum [31], these problems were not observed in this study or others recently reported [14, 15, 17]. One reason might be that in these cases, parallel imaging was employed with short TE that reduces susceptibility effects in EPI.

These studies were performed on young healthy adults in the age range 25–40 years. For elderly subjects and patients, the blood velocity is lower [39, 40], which will require longer postlabeling delay to allow the labeled blood to wash out from larger arteries. More inferior saturation RF pulses may also have to be performed in elderly or ill subjects in order to completely suppress slow-moving labeled blood spins.

Because the superior inflow of venous blood is suppressed at the outset in FAIR ASST, confounding venous inflow effects are minimized, resulting in perfusion images with more stable ASL signals, as indicated quantitatively by the temporal stability analysis (Figure 4). The amount and velocity of superiorly labeled venous blood are subject dependent, which may account for why CBF measurements by FAIR ASST gave consistently lower intersubject variability than those by PICORE (Table 1). The observed smaller subtraction errors and about 50% lower interslice variability in perfusion images from FAIR ASST compared to PICORE (Figure 4) may be due to the better control of MT effects with FAIR than PICORE. Although we have not compared the two methods on patient groups, these results suggest that FAIR ASST will be more sensitive and specific than PICORE in detecting abnormal CBF values in patient groups and disease conditions.

5. Conclusions

Using properly selected ASL parameters based on the results of ASL optimization studies, CBF values for cerebellum GM and WM were measured using FAIR ASST and PICORE. Results indicated that FAIR ASST is preferable to PICORE, giving similar CBF estimations but with lower intersubject and spatial variability, less subtraction error, and greater temporal stability. These are important advantages, which should make FAIR ASST more sensitive and specific than PICORE in detecting abnormal CBF values in different conditions and/or subject groups.

Disclosure

Richard W. Briggs would like to disclose that “Department of Physics & Astronomy, Georgia State University, Atlanta, GA 30302, USA” is his current address.

Conflict of Interests

The authors declare that there is no conflict of interests regarding the publication of this paper.

Acknowledgments

This study was supported by DoD Grant no. DAMD 17-01-1-0741 from the U.S. Army Medical Research and Materiel Command and by the VA IDIQ Contract VA549-P-0027 awarded and administered by the Dallas, TX VA Medical Center. The authors thank Robert W. Haley, M.D., PI of these grants, for his support and encouragement. The content does not necessarily reflect the position or the policy of the Federal government or the sponsoring agencies, and no official endorsement should be inferred. Research reported in this publication was also supported by the National Center for Advancing Translational Sciences of the National Institutes of Health Award no. UL1TR000114. The content is solely the responsibility of the authors and does not necessarily represent the official views of the National Institutes of Health.

References

- [1] E. J. Fine, C. C. Ionita, and L. Lohr, “The history of the development of the cerebellar examination,” *Seminars in Neurology*, vol. 22, no. 4, pp. 375–384, 2002.
- [2] U. Wolf, M. J. Rapoport, and T. A. Schweizer, “Evaluating the affective component of the cerebellar cognitive affective syndrome,” *The Journal of Neuropsychiatry and Clinical Neurosciences*, vol. 21, no. 3, pp. 245–253, 2009.
- [3] M.-U. Manto and M. Pandolfo, *The Cerebellum and Its Disorders*, Cambridge University Press, Cambridge, UK, 2002.
- [4] C. Ghez and S. Fahn, “The cerebellum,” in *Principles of Neural Science*, E. R. Kandel and J. H. Schwartz, Eds., Elsevier, New York, NY, USA, 2nd edition, 1985.
- [5] J. A. Detre, W. Zhang, D. A. Roberts et al., “Tissue specific perfusion imaging using arterial spin labeling,” *NMR in Biomedicine*, vol. 7, no. 1-2, pp. 75–82, 1994.

- [6] X. Golay, J. Hendrikse, and T. C. C. Lim, "Perfusion imaging using arterial spin labeling," *Topics in Magnetic Resonance Imaging*, vol. 15, no. 1, pp. 10–27, 2004.
- [7] J. A. Detre, O. B. Samuels, D. C. Alsop, J. B. Gonzalez-At, S. E. Kasner, and E. C. Raps, "Noninvasive magnetic resonance imaging evaluation of cerebral blood flow with acetazolamide challenge in patients with cerebrovascular stenosis," *Journal of Magnetic Resonance Imaging*, vol. 10, no. 5, pp. 870–875, 1999.
- [8] K. K. Oguz, X. Golay, F. B. Pizzini et al., "Sickle cell disease: continuous arterial spin-labeling perfusion MR imaging in children," *Radiology*, vol. 227, no. 2, pp. 567–574, 2003.
- [9] C. Warmuth, M. Günther, and C. Zimmer, "Quantification of blood flow in brain tumors: comparison of arterial spin labeling and dynamic susceptibility-weighted contrast-enhanced MR imaging," *Radiology*, vol. 228, no. 2, pp. 523–532, 2003.
- [10] D. C. Alsop, J. A. Detre, and M. Grossman, "Assessment of cerebral blood flow in Alzheimer's disease by spin-labeled magnetic resonance imaging," *Annals of Neurology*, vol. 47, no. 1, pp. 93–100, 2000.
- [11] S.-P. Lee, A. C. Silva, and S.-G. Kim, "Comparison of diffusion-weighted high-resolution CBF and spin-echo BOLD fMRI at 9.4 T," *Magnetic Resonance in Medicine*, vol. 47, no. 4, pp. 736–741, 2002.
- [12] F. Q. Ye, A. M. Smith, V. S. Mattay et al., "Quantitation of regional cerebral blood flow increases in prefrontal cortex during a working memory task: a steady-state arterial spin-tagging study," *NeuroImage*, vol. 8, no. 1, pp. 44–49, 1998.
- [13] E. C. Wong, R. B. Buxton, and L. R. Frank, "Implementation of quantitative perfusion imaging techniques for functional brain mapping using pulsed arterial spin labeling," *NMR in Biomedicine*, vol. 10, no. 4–5, pp. 237–249, 1997.
- [14] A. J. Huang, J. Hua, J. Farrell et al., "Quantification of cerebral blood flow using arterial spin labeling," in *Proceedings of the 19th Annual Meeting of ISMRM*, abstract 301, Montreal, Canada, 2011.
- [15] X. Li, S. N. Sarkar, D. E. Purdy, R. W. Haley, and R. W. Briggs, "Asymmetric FAIR—FAIR with active suppression of superior tagging (FAIR ASST)," in *Proceedings of the 18th Annual Meeting of ISMRM*, abstract 1737, Stockholm, Sweden, 2010.
- [16] T. Tsujikawa, T. Yamamoto, M. Ikawa, M. Yoneda, and H. Kimura, "Crossed cerebellar hyperperfusion after MELAS attack followed up by whole brain continuous arterial spin labeling perfusion imaging," *Acta Radiologica*, vol. 53, no. 2, pp. 220–222, 2012.
- [17] X. Li, S. N. Sarkar, D. E. Purdy, R. W. Haley, and R. W. Briggs, "Improved quantification of brain perfusion using FAIR with active suppression of superior tagging (FAIR ASST)," *Journal of Magnetic Resonance Imaging*, vol. 34, no. 5, pp. 1037–1044, 2011.
- [18] A. Pfefferbaum, S. Chanraud, A.-L. Pitel et al., "Volumetric cerebral perfusion imaging in healthy adults: regional distribution, laterality, and repeatability of pulsed continuous arterial spin labeling (PCASL)," *Psychiatry Research: Neuroimaging*, vol. 182, no. 3, pp. 266–273, 2010.
- [19] A. Pfefferbaum, S. Chanraud, A.-L. Pitel et al., "Cerebral blood flow in posterior cortical nodes of the default mode network decreases with task engagement but remains higher than in most brain regions," *Cerebral Cortex*, vol. 21, no. 1, pp. 233–244, 2011.
- [20] N. Khalili-Mahani, M. J. P. van Osch, E. Baerends et al., "Pseudocontinuous arterial spin labeling reveals dissociable effects of morphine and alcohol on regional cerebral blood flow," *Journal of Cerebral Blood Flow & Metabolism*, vol. 31, no. 5, pp. 1321–1333, 2011.
- [21] Q. Zou, H. Gu, D. J. J. Wang, J.-H. Gao, and Y. Yang, "Quantification of load dependent brain activity in parametric N-back working memory tasks using pseudo-continuous arterial spin labeling (pCASL) perfusion imaging," *Journal of Cognitive Science*, vol. 12, no. 2, pp. 127–210, 2011.
- [22] Q. Qin, A. J. Huang, J. Hua, J. E. Desmond, R. D. Stevens, and P. C. van Zijl, "Three-dimensional whole-brain perfusion quantification using pseudo-continuous arterial spin labeling MRI at multiple post-labeling delays: accounting for both arterial transit time and impulse response function," *NMR in Biomedicine*, vol. 27, no. 2, pp. 116–128, 2014.
- [23] E. C. Wong, R. B. Buxton, and L. R. Frank, "Quantitative imaging of perfusion using a single subtraction (QUIPSS and QUIPSS II)," *Magnetic Resonance in Medicine*, vol. 39, no. 5, pp. 702–708, 1998.
- [24] W. M. Luh, E. C. Wong, P. A. Bandettini, and J. S. Hyde, "QUIPSS II with thin-slice T1 periodic saturation: a method for improving accuracy of quantitative perfusion imaging using pulsed arterial spin labeling," *Magnetic Resonance in Medicine*, vol. 41, no. 6, pp. 1246–1254, 1999.
- [25] J. Wang, D. J. Licht, G.-H. Jahng et al., "Pediatric perfusion imaging using pulsed arterial spin labeling," *Journal of Magnetic Resonance Imaging*, vol. 18, no. 4, pp. 404–413, 2003.
- [26] R. B. Buxton, L. R. Frank, E. C. Wong, B. Siewert, S. Warach, and R. R. Edelman, "A general kinetic model for quantitative perfusion imaging with arterial spin labeling," *Magnetic Resonance in Medicine*, vol. 40, no. 3, pp. 383–396, 1998.
- [27] B. J. MacIntosh, K. T. S. Pattinson, D. Gallichan et al., "Measuring the effects of remifentanyl on cerebral blood flow and arterial arrival time using 3D GRASE MRI with pulsed arterial spin labelling," *Journal of Cerebral Blood Flow & Metabolism*, vol. 28, no. 8, pp. 1514–1522, 2008.
- [28] R. B. Buxton, "Quantifying CBF with arterial spin labeling," *Journal of Magnetic Resonance Imaging*, vol. 22, no. 6, pp. 723–726, 2005.
- [29] L. M. Parkes, "Quantification of cerebral perfusion using arterial spin labeling: two-compartment models," *Journal of Magnetic Resonance Imaging*, vol. 22, no. 6, pp. 732–736, 2005.
- [30] D. A. Roberts, R. Rizi, R. E. Lenkinski, and J. S. Leigh Jr., "Magnetic resonance imaging of the brain: blood partition coefficient for water: application to spin-tagging measurement of perfusion," *Journal of Magnetic Resonance Imaging*, vol. 6, no. 2, pp. 363–366, 1996.
- [31] A. Boss, P. Martirosian, U. Klose, T. Nägele, C. D. Claussen, and F. Schick, "FAIR-TrueFISP imaging of cerebral perfusion in areas of high magnetic susceptibility differences at 1.5 and 3 Tesla," *Journal of Magnetic Resonance Imaging*, vol. 25, no. 5, pp. 924–931, 2007.
- [32] D. C. Alsop and J. A. Detre, "Reduced transit-time sensitivity in noninvasive magnetic resonance imaging of human cerebral blood flow," *Journal of Cerebral Blood Flow & Metabolism*, vol. 16, no. 6, pp. 1236–1249, 1996.
- [33] H. Ito, I. Kanno, M. Ibaraki, J. Hatazawa, and S. Miura, "Changes in human cerebral blood flow and cerebral blood volume during hypercapnia and hypocapnia measured by positron emission tomography," *Journal of Cerebral Blood Flow & Metabolism*, vol. 23, no. 6, pp. 665–670, 2003.
- [34] H. Ito, K. Inoue, R. Goto et al., "Database of normal human cerebral blood flow measured by SPECT: I. Comparison between I-123-IMP, Tc-99m-HMPAO, and Tc-99m-ECD as referred with

- O-15 labeled water PET and voxel-based morphometry," *Annals of Nuclear Medicine*, vol. 20, no. 2, pp. 131–138, 2006.
- [35] J. Decety, H. Sjöholm, E. Ryding, G. Stenberg, and D. H. Ingvar, "The cerebellum participates in mental activity: tomographic measurements of regional cerebral blood flow," *Brain Research*, vol. 535, no. 2, pp. 313–317, 1990.
- [36] N. Miyazawa, K. Toyama, A. S. Arbab, K. Koizumi, T. Arai, and H. Nukui, "Evaluation of crossed cerebellar diaschisis in 30 patients with major cerebral artery occlusion by means of quantitative I-123 IMP SPECT," *Annals of Nuclear Medicine*, vol. 15, no. 6, pp. 513–519, 2001.
- [37] S. Yoshinari, S. Hamano, N. Eda, M. Sakamoto, and Y. Takahashi, "Development of regional cerebral blood flow during childhood studied with iodine-123 IMP SPECT," *Jikeikai Medical Journal*, vol. 53, no. 2, pp. 87–92, 2006.
- [38] I. Asllani, A. Borogovac, and T. R. Brown, "Regression algorithm correcting for partial volume effects in arterial spin labeling MRI," *Magnetic Resonance in Medicine*, vol. 60, no. 6, pp. 1362–1371, 2008.
- [39] P. Pantano, J. C. Baron, P. Lebrun-Grandié, N. Duquesnoy, M. G. Bousser, and D. Comar, "Regional cerebral blood flow and oxygen consumption in human aging," *Stroke*, vol. 15, no. 4, pp. 635–641, 1984.
- [40] T. G. Shaw, K. F. Mortel, J. S. Meyer, R. L. Rogers, J. Hardenberg, and M. M. Cutaja, "Cerebral blood flow changes in benign aging and cerebrovascular disease," *Neurology*, vol. 34, no. 7, pp. 855–862, 1984.

Research Article

Tract-Based Spatial Statistics: Application to Mild Cognitive Impairment

Yau-Yau Wai,^{1,2} Wen-Chuin Hsu,^{3,4} Hon-Chung Fung,³ Jiann-Der Lee,⁵ Hsiao-Lung Chan,⁵ Ming-Lun Tsai,² Yu-Chun Lin,^{1,2} Yih-Ru Wu,³ Leslie Ying,^{6,7} and Jiun-Jie Wang^{1,2,8,9,10}

¹ Department of Medical Imaging and Radiological Sciences, Chang Gung University, Taoyuan County, Taiwan

² Department of Radiology and Intervention, Chang Gung Memorial Hospital, 5 FuHsing Street, Linkou, Taoyuan County, Taiwan

³ Department of Neurology, Chang Gung Memorial Hospital, Chang-Gung University College of Medicine, Linkou, New Taipei 333, Taiwan

⁴ Dementia Center, Chang Gung Memorial Hospital, 5 FuHsing Street, Linkou, Taoyuan County, Taiwan

⁵ Department of Electrical Engineering, Chang Gung University, 259 WenHua 1st Road, Taoyuan County, Taoyuan, Taiwan

⁶ Department of Biomedical Engineering, University at Buffalo, The State University of New York, Buffalo, NY 14260, USA

⁷ Department of Electrical Engineering, University at Buffalo, The State University of New York, Buffalo, NY 14260, USA

⁸ Neuroscience Research Center, Chang Gung Memorial Hospital, 5 FuHsing Street, Linkou, Taoyuan County, Taiwan

⁹ Institute of Radiological Research, Chang Gung University, Chang Gung Memorial Hospital, 5 FuHsing Street, Linkou, Taoyuan County, Taiwan

¹⁰ Healthy Aging Research Center, Chang Gung University, 259 WenHua 1st Road, Taoyuan County, Taoyuan, Taiwan

Correspondence should be addressed to Jiun-Jie Wang; jwang@mail.cgu.edu.tw

Received 10 January 2014; Accepted 10 April 2014; Published 12 May 2014

Academic Editor: Hengyi Rao

Copyright © 2014 Yau-Yau Wai et al. This is an open access article distributed under the Creative Commons Attribution License, which permits unrestricted use, distribution, and reproduction in any medium, provided the original work is properly cited.

Rationale and Objectives. The primary objective of the current investigation was to characterize white matter integrity in different subtypes of mild cognitive impairment (MCI) using tract-based spatial statistics of diffusion tensor imaging. *Materials and Methods.* The study participants were divided into 4 groups of 30 subjects each as follows: cognitively healthy controls, amnesic MCI, dysexecutive MCI, and Alzheimer's disease (AD). All subjects underwent a comprehensive neuropsychological assessment, apolipoprotein E genotyping, and 3-tesla MRI. The diffusion tensor was reconstructed and then analyzed using tract-based spatial statistics. The changes in brain white matter tracts were also examined according to the apolipoprotein E $\epsilon 4$ status. *Results.* Compared with controls, amnesic MCI patients showed significant differences in the cerebral white matter, where changes were consistently detectable in the frontal and parietal lobes. We found a moderate impact of the apolipoprotein E $\epsilon 4$ status on the extent of white matter disruption in the amnesic MCI group. Patients with AD exhibited similar but more extensive alterations, while no significant changes were observed in dysexecutive MCI patients. *Conclusion.* The results from this study indicate that amnesic MCI is the most likely precursor to AD as both conditions share significant white matter damage. By contrast, dysexecutive MCI seems to be characterized by a distinct pathogenesis.

1. Introduction

Dementia refers to a clinical syndrome of acquired intellectual disturbances produced by brain dysfunction [1]. Mild cognitive impairment (MCI) is considered to be the clinical transition stage between normal aging and dementia [2].

Evidence suggests that subjects with MCI tend to progress to probable Alzheimer's disease (AD) at a rate of approximately 10% to 15% per year [2]. However, MCI is a clinically heterogeneous syndrome, with some patients showing isolated memory impairments (i.e., amnesic MCI) and others with isolated executive function impairments (i.e., dysexecutive

MCI). Importantly, Yaffe et al. [3] demonstrated that dysexecutive MCI patients are less likely to convert to dementia but have higher 5-year mortality rates than amnesic MCI.

MRI studies of dementia have been mainly focused on the assessment of hippocampal and entorhinal atrophy [4–6]. Global brain atrophy on conventional MRI has been proposed as a marker for advanced MCI [7, 8], but the low specificity limits its clinical value [9, 10]. Similarly, neuropsychological tests can be considered as screening tools for MCI but are not adequate for diagnosis. Diffusion tensor imaging (DTI) is MRI technique that can noninvasively measure macroscopic axonal organization in the central nervous system [11, 12]. Because of the potential for investigating white matter integrity and fiber connectivity *in vivo*, this technique has been widely applied to study brain disorders [13, 14].

Three eigenvalues and three corresponding eigenvectors can be derived from the diffusion tensor. The largest eigenvalue is often referred to as the axial diffusivity (longitudinal diffusivity (LD), in the study, in order not to be confused with Alzheimer's disease) and the average of the second and third eigenvalues as radial diffusivity (RD) [15]. In white matter, diffusion tensor is usually modeled as cylindrically symmetric [16, 17]. The increase of the mean diffusivity (MD) can be related to an increase in either LD or RD. The reduction of FA can be related to either a decrease of diffusion in the longitudinal direction (AD) or an increase in the transverse direction (RD). Many studies attributed the changes in RD as related axonal injury or demyelination process [18].

Conventional DTI data are often analyzed in a region of interest approach. Because the directional information is encoded by the signal intensity, great care is required for all imaging processing procedures (e.g., registration and normalization). Tract-based spatial statistics (TBSS) [19, 20] is a new whole brain voxelwise analysis method that provides more reliable alignment of the white matter tracts and less bias from smoothing than conventional voxel-based methods. The data-driven approach of TBSS is particularly useful in a disorder like MCI, for which regional patterns of brain abnormalities are not fully determined. Thus, the aim of the present study was to investigate white matter changes in two MCI subgroups, dysexecutive MCI and amnesic MCI, using a TBSS approach. Imaging patterns were also compared with those of AD patients and cognitively healthy controls.

2. Materials and Methods

The study was approved by our institutional review board and complied with the tenets of the Declaration of Helsinki. Each participant or participant's legal guardian gave written informed consent for participation.

2.1. Participants and Clinical Workup. The study participants ($n = 120$) were divided into 4 clinical groups of 30 subjects each as follows: cognitively healthy controls, amnesic MCI, dysexecutive MCI, and AD. The clinical workup included a thorough medical history, physical examination, and neuropsychological testing. Four key cognitive domains

were assessed: memory, executive function, language, and visuospatial skills. All subjects were screened for the presence of depressive symptoms using either the Hamilton depression rating scale (healthy control) or the Cornell scale for depression in dementia (AD, amnesic MCI, and dysexecutive MCI). Patients with depression were excluded.

The diagnosis of AD was made using the NINCDS-ADRDA criteria [21]. The clinical dementia rating was used to quantify the severity of symptoms of dementia. MCI patients were diagnosed after an extensive clinical evaluation. The clinical phenotype of MCI was determined according to the criteria by Petersen [1]. The amnesic MCI group exhibited an isolated memory impairment without deficits in other cognitive domains. Patients with dysexecutive MCI had a relatively focal dysfunction in the executive domain, while memory, language, and visuospatial skills remained within the normal range. Cognitively healthy controls were free of cognitive impairment as judged by clinical assessment, neuropsychological testing, and clinical dementia rating.

2.2. Apolipoprotein E Genotyping. Genomic DNA was extracted from leukocytes in samples of whole blood, following a standard salting-out technique. Apolipoprotein E genotypes were detected by polymerase chain reaction followed by restriction fragment length polymorphism analysis.

2.3. Image Acquisition. Images were acquired using a 3-tesla MR scanner (Magnetom Trio with TIM, Siemens, Erlangen, Germany). T2WI FLAIR and T1WI magnetization-prepared rapid acquisition gradient echo images were acquired to rule out concomitant neurological disorders. DTI was acquired using a spin-echo EPI sequence with the following parameters: TR/TE/flip angle = 7500 ms/83 ms/90°, field of view = 256 mm², and matrix size = 128 × 128. Diffusion-weighting gradients were applied in 64 noncollinear directions with a diffusion weighting of 1000 s/mm². Sixty-four contiguous axial slices were obtained to cover the majority of the brain with an isotropic voxel size of 2 mm. The single average acquisition time was 8 minutes 47 seconds.

2.4. Image Processing and Analysis. Diffusion analysis was performed and the white matter skeleton was identified using TBSS, part of FSL (<http://fsl.fmrib.ox.ac.uk/fsl/fsl4.0/tbss/index>). In brief, the reconstructed fractional anisotropy [16, 17] of each individual was initially aligned to the MNI template. The parameters from the nonlinear registration were then applied to the diffusion indices, including MD/LD/RD [16, 17]. The spatial normalization was achieved by 12-parameter affine transformation. Both followed the recommended procedures and parameters by TBSS. The aligned diffusion indices were then projected onto a fiber tract-derived skeleton and fed into the voxelwise cross-subject statistics. Data from each of the diffusion indices were compared by the Randomise 2.1 software [22, 23]. Multiple comparison correction was done by the familywise error correction with a threshold of $P < 0.05$. We identified abnormal white matter tracts based on the atlas prepared

TABLE 1: General characteristics of the study participants.

	Controls	Dysexecutive	Amnesic	AD
Number of subjects	30	30	30	30
Age (years)	67.2 ± 5.6	65.9 ± 7.6	68.6 ± 8.3	73.9 ± 9.4
Range	61–80	50–84	56–84	54–83
Median	65.5	65	69	76.5
Sex (males/females)	18/12	12/18	17/13	12/18
Education (years)	10.1 ± 4.7	8.0 ± 3.5	8.3 ± 5.3	7.3 ± 6.4
Clinical dementia rating score	0.00 ± 0.00	0.12 ± 0.22	0.47 ± 0.13	1.00 ± 0.57
Apolipoprotein E status				
ε4 carriers	2	4	11	5
ε4 noncarriers	28	23	16	23
Unknown	0	3	3	2

Data are given as means ± standard deviation or counts, as appropriate.

TABLE 2: Neuropsychological test scores.

	Controls	Apolipoprotein E ε4 noncarriers	Amnesic MCI apolipoprotein E ε4 carriers	Sum	Dysexecutive MCI	AD
Mean global score						
Mini-mental status examination	28.23 (1.30)	25.25 (3.87)	25.09 (4.18)	25.10 (3.87)	27.63 (1.47)	15.07 (6.34)
Mean memory score						
Word sequence learning-recall	3.17 (1.93)	0.47 (0.64)	0.55 (0.93)	0.45 (0.74)	2.00 (1.68)	0.04 (0.20)
Logic memory II	11.60 (2.72)	8.25 (3.66)	8.18 (4.21)	7.97 (3.72)	9.87 (2.42)	3.15 (1.87)
Mean executive function score						
Semantic association of verbal fluency	33.40 (6.82)	31.81 (4.04)*	25.73 (7.16)*	29.57 (6.03)	32.83 (7.37)	14.55 (6.20)
Wisconsin card sorting test Completed Categories	5.20 (1.13)	3.67 (1.91)	3.82 (1.89)	3.69 (1.77)	2.60 (1.35)	1.88 (2.76)
Mean visuospatial score						
3D block construction models	28.6 (0.77)	27.31 (2.60)	26.91 (4.11)	27.27 (3.1)	28.03 (1.65)	18.41 (10.50)
Mean language score						
Object naming test	16.00 (0.00)	15.94 (0.25)	16.00 (0.00)	15.97 (0.18)	15.97 (0.18)	13.13 (3.65)

Data are given as means (standard deviation); *Significant differences at $P < 0.05$ ($P = 0.0225$).

at Johns Hopkins University [24]. The correlation between neuropsychiatry measures and the diffusion indices was assessed using the regression model in the SPM (Wellcome Trust Centre for Neuroimaging, UK). The effect of the apolipoprotein E ε4 allele was determined by dividing participants in either apolipoprotein E ε4 (ε2/ε4, ε3/ε4, and ε4/ε4) or non-ε4 (ε2/ε2, ε2/ε3, and ε3/ε3) carriers. Cognitive performances were compared between carriers and noncarriers using Student's t -test. The TBSS approach was also applied to compare the imaging patterns according to the apolipoprotein E ε4 carrier status.

3. Results

Table 1 shows the general characteristics of the study participants. The neuropsychological tests are reported in Table 2. The results from TBSS analysis did not identify significant

white matter changes in dysexecutive MCI patients compared with cognitively healthy controls. Figure 1 shows the changes in fractional anisotropy along the white matter skeleton of patients with amnesic MCI (a) and AD (b) compared with healthy controls. Both groups of patients exhibited a widespread fractional anisotropy decrease within the white matter tracts. Changes in the amnesic MCI group were restricted to the frontal and parietal lobes, while AD patients consistently exhibited more extensive damage which was suggestive of a progressive disease process.

Figure 2 shows an increase in RD along the white matter skeleton of both amnesic MCI (a) and AD (b) patients compared with healthy controls. The location was consistent but significantly smaller than the corresponding areas identified in Figure 1. The arrows indicate the location of the most significant areas of increased RD. These results suggest that an increased RD was presumably driving a reduction of fractional anisotropy in both AD and amnesic MCI patients.

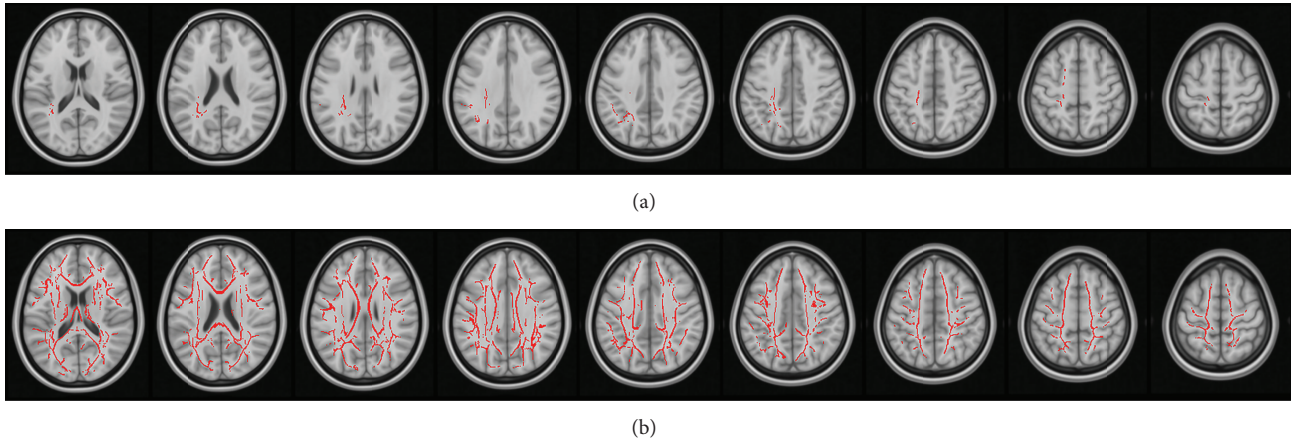


FIGURE 1: Fractional anisotropy in the white matter regions of the study participants. Compared with normal controls, fractional anisotropy is reduced within the white matter skeleton of both patients with amnesic MCI (a) and AD (b). The left of the figure corresponds to the subject's right side.

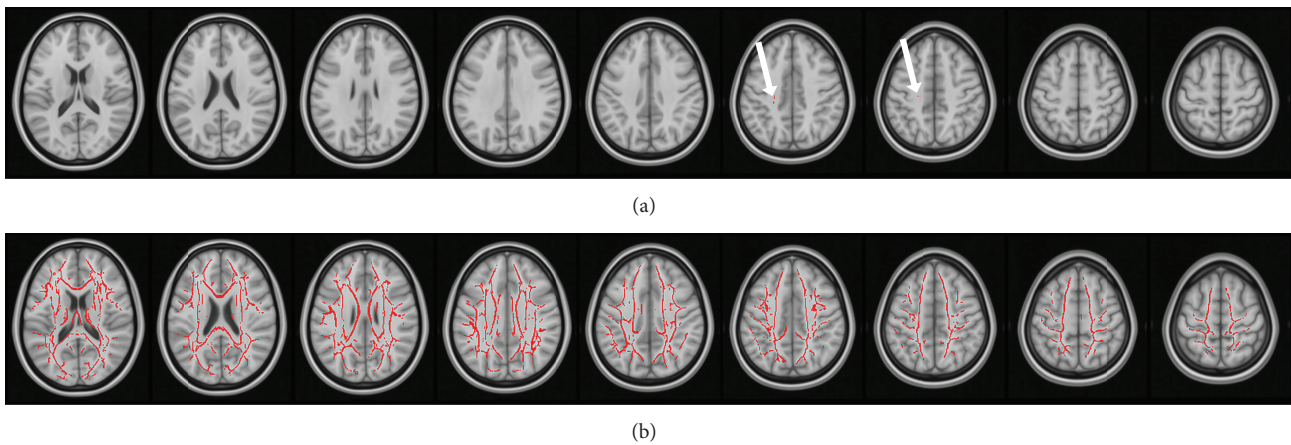


FIGURE 2: Radial diffusivity in the white matter regions of the study participants. Compared with normal controls, radial diffusivity is increased within the white matter skeleton of both patients with amnesic MCI (a) and AD (b). The pattern of such changes is consistent with the observed reductions in fractional anisotropy. The arrows indicate the locations of the fiber tracts showing significant changes.

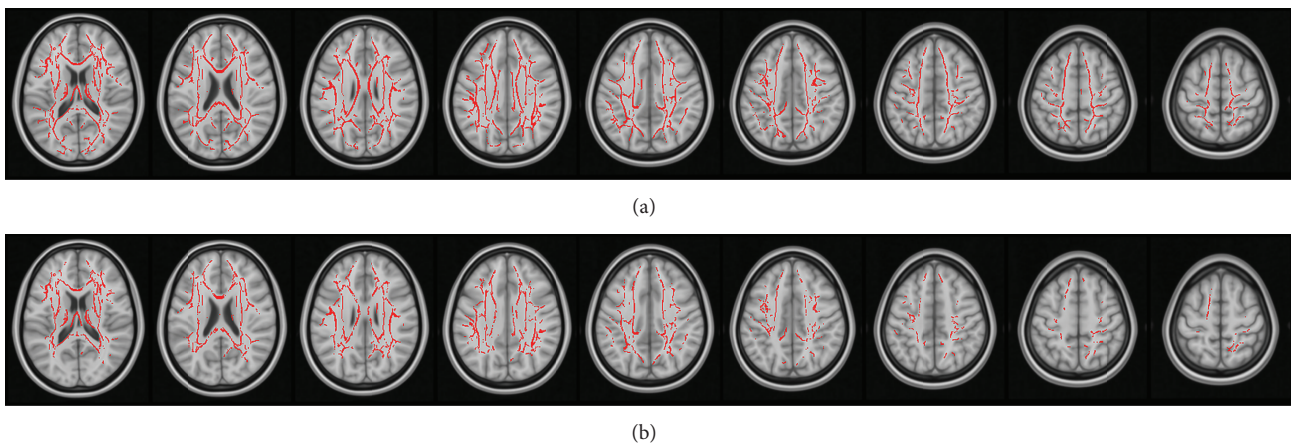


FIGURE 3: MD and longitudinal diffusivity in the white matter regions in patients with AD. Compared with normal controls, MD (a) and longitudinal diffusivity (b) are significantly increased within the white matter skeleton of patients with AD. The observed increases are largely consistent with the corresponding reductions in fractional anisotropy.

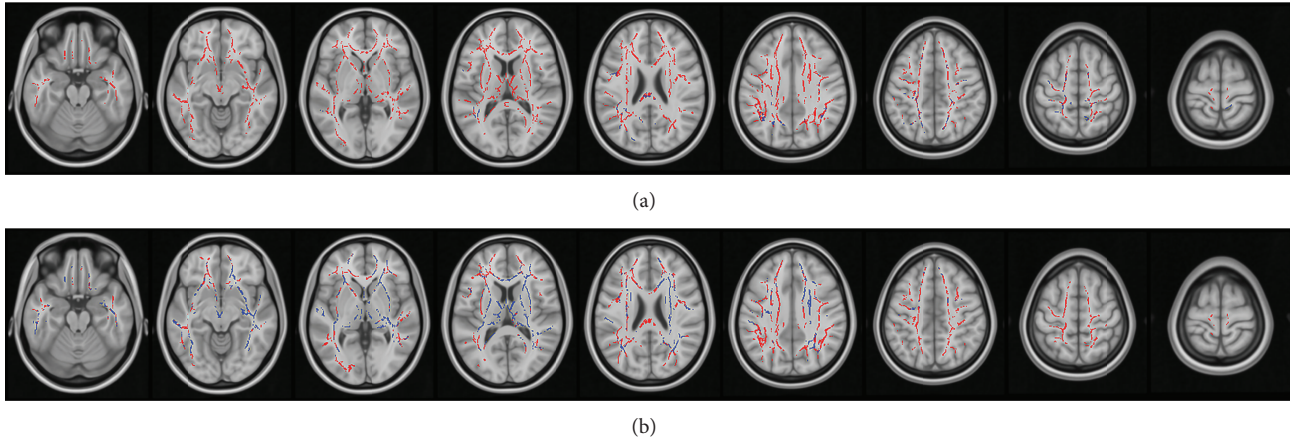


FIGURE 4: Effect of the apolipoprotein E $\epsilon 4$ status on white matter changes in amnesic MCI patients. The diffusion indices are examined in amnesic MCI patients after stratification according to apolipoprotein E $\epsilon 4$ status. In (a), the decrease of fractional anisotropy is marked in blue, while the increase in MD is reported in red. In (b), the increases of LD and RD are marked in blue and red, respectively.

Figure 3 shows the corresponding increases of MD (a) and LD (b) in AD patients. No significant changes of these parameters were found in the amnesic MCI group. The observed increase of MD in AD patients was largely in accordance with the corresponding fractional anisotropy changes (depicted in Figure 1(b)). The pattern of LD increases was similarly consistent, with the only exception being the absence of significant changes in the occipital lobe.

The effect of the apolipoprotein E $\epsilon 4$ allele on white matter changes in amnesic MCI patients is shown in Figure 4. In (a), the decrease of fractional anisotropy is marked in blue, while the increase in MD is reported in red. In (b), the increases of LD and RD are marked in blue and red, respectively. Compared with healthy subjects, amnesic MCI patients without the apolipoprotein E $\epsilon 4$ allele exhibited larger and more striking changes in both fractional anisotropy and RD. Similarly, more extensive areas of MD and LD changes were evident in apolipoprotein E $\epsilon 4$ noncarriers.

In all study groups, we found no correlation between changes in diffusion indices and neuropsychiatric measurements, even after allowance for age and/or education levels.

4. Discussion

There are three main findings in this study. First, we have shown that AD and amnesic MCI may share a common neurodegenerative substrate which impairs white matter integrity. The results from this study indicate that this process can be efficiently visualized in a noninvasive manner using DTI-TBSS. Second, AD patients showed more extensive white matter damage compared with amnesic MCI subjects, supporting the view that amnesic MCI is the most likely precursor to AD. Third, the apolipoprotein E $\epsilon 4$ carrier status affected the extent of white matter involvement in amnesic MCI patients. Importantly, we found no evidence of significant white matter damage in dysexecutive MCI, suggesting highly distinct pathways of neurodegeneration

compared with amnesic MCI. Moreover, there was no correlation between diffusion indices and neuropsychological test scores, suggesting no direct association between DTI-TBSS findings and MCI.

4.1. White Matter Changes in AD and MCI. Diffusion tensor imaging is sensitive to white matter damage and has been previously used to examine entire neural networks and their integrity in AD and MCI [25, 26]. The observed changes in diffusion indices have been mainly attributed to alterations in the white matter structure. Compared with normal controls, both amnesic MCI and AD are characterized by increases in RD and MD and a reduction in fractional anisotropy. The increase in RD has generally been ascribed to alterations in myelin sheaths, which can be related to the observed changes in both MD and fractional anisotropy. As these indices are altered in amnesic MCI and AD, it is feasible that both conditions are characterized by an altered brain myelination.

The results from this study indicate a significant overlap between the affected regions of amnesic MCI and AD patients. The changes in amnesic MCI patients were chiefly located in the frontal and parietal regions. However, the extension of damage was significantly greater in AD patients, suggesting that amnesic MCI is the most likely precursor to AD.

LD did not differ in both amnesic and dysexecutive MCI, while AD patients showed an increase of both LD and RD. In normal aging, an increased LD reflects a reduced axonal packing in white matter structures due to thinning of myelin or decrease in axonal diameter. This phenomenon in turn results in an increased diffusivity in all orientations within a voxel [25, 27]. Using MRS, Meyrhoff et al. provided suggestive evidence of diffuse axonal injury and membrane alterations in AD patients [28]. Our results indicate that LD changes seem to be restricted to AD patients.

We found no significant association between neuropsychological testing and the results of DTI-TBSS analysis.

However, these results should be interpreted cautiously as cognitive performances were assessed only at the study admission; additionally, all neuropsychological scores were distributed in a narrow range. In any case, it is noteworthy that white matter changes on DTI-TBSS do not necessarily reflect changes in cortical functions.

In this study, there were no significant alterations in diffusion indices of dysexecutive MCI patients, suggesting that changes in white matter structure do not play a major role in this condition. Alternatively, such alterations could be so subtle that they escaped detection by means of DTI-TBSS. Further studies are necessary to shed more light on the neuroradiological alterations specific to dysexecutive MCI.

4.2. Impact of APOE $\epsilon 4$ Carrier Status on White Matter Changes. The apolipoprotein E $\epsilon 4$ allele is the most widely recognized genetic risk factor for sporadic AD [29] and affects, even for nondemented elders, the levels of cognitive performance [30]. In the present study, amnesic MCI patients who carried at least one apolipoprotein E $\epsilon 4$ allele showed a nonsignificant trend toward lower scores on the executive function and memory measures compared with those without. In contrast, we found no impact of the apolipoprotein E $\epsilon 4$ status on both visuospatial and language processing.

The results from the DTI-TBSS analysis demonstrated that the apolipoprotein E $\epsilon 4$ status had a moderate impact on the extent of white matter disruption in amnesic MCI patients. In subjects without the apolipoprotein E $\epsilon 4$ allele, we found that RD and LD were significantly increased, which can be related to the observation of an increased MD and a reduced fractional anisotropy. It is noteworthy that the impact of the apolipoprotein E $\epsilon 4$ status on cognitive functions may vary in different ethnic groups [31, 32]. Interestingly, the apolipoprotein E $\epsilon 4$ allele is less prevalent in people of Chinese ancestry [33]. This variability has been shown to influence the association of this polymorphism with different phenotypes [33, 34]. For this reason, the observed association between the apolipoprotein E $\epsilon 4$ status and the extent of white matter disruption in our amnesic MCI patients should be confirmed in multiethnic populations. In addition, future studies should assess how the presence of white matter abnormalities reflects associative cortical functioning in MCI patients.

4.3. Comparison with Previous Studies. Bosch et al. [35] have previously identified a general neural network which seems to be specifically disrupted in AD. However, the authors failed to identify specific white matter changes in amnesic MCI patients compared with healthy controls. In contrast, Zhuang et al. [36] reported a significant fractional anisotropy reduction in the frontal, temporal, and parietal lobes of amnesic MCI patients. The fractional anisotropy changes identified in our study are similar to those reported by Zhuang et al. [36], albeit being located in a smaller region. This discrepancy can be attributed to the different sample sizes used in the studies. It is also important to note that MCI is not a diagnostic entity as AD is; consequently, a number of

studies use the term MCI but do not use Petersen's criteria [1]. Between-study heterogeneity in MCI severity may also explain the discrepancy. In accordance with Zhuang et al. [36], our study identified significant signal changes of the white matter in amnesic MCI patients. This result deserves further independent scrutiny.

4.4. Study Limitations. The findings of our study should be interpreted within the context of the following limitations. First, a well-established model for tensor signal processing in the gray matter is still lacking. For this reason, we limited our DTI-TBSS analysis to the white matter skeleton. The analysis of gray matter diffusion properties may be challenging, but this knowledge may ultimately help define the correlation between white matter changes and cortical functioning in amnesic MCI and AD patients. Furthermore, the observed changes in LD/RD, as detected in the white matter skeleton, can be controversial noticeably in the region where the fiber distribution is complicated or where the fibers cross [37, 38]. Therefore, the interpretation of the observed white matter change should be exercised with great care.

Second, in this study we did not correlate *in vivo* imaging findings with postmortem analysis of brain tissue. Furthermore, given the cross-sectional design, we cannot infer causality between white matter changes and the conversion of amnesic MCI to AD. Notwithstanding these limitations, the results from this study indicate that amnesic MCI is the most likely precursor to AD as both conditions share significant white matter damage. By contrast, dysexecutive MCI seems to be characterized by a distinct pathogenetic mechanism.

5. Conclusion

Amnesic MCI is the most likely precursor to Alzheimer's disease because both conditions share significant white matter damage as assessed by tract-based spatial statistics. Dysexecutive MCI seems to be characterized by a distinct pathogenesis.

Conflict of Interests

The authors declare that there is no conflict of interests regarding the publication of this paper.

Authors' Contribution

Yau-Yau Wai and Wen-Chiun Hsu contributed equally to the paper.

Acknowledgments

This work was supported by the Ministry of Science and Technology, Taiwan (102-2325-B-182-008) and Chang Gung Memorial Hospital, Linkou (CMRPD1C0292 and CMRPD3D0011). The imaging facility was supported by the Molecular Imaging Center and Neuroscience Research Center, Chang Gung Memorial Hospital, Linkou. The funding source had no involvement in the collection, analysis, and

interpretation of data; in the writing of the report; or in the decision to submit the paper for publication.

References

- [1] R. C. Petersen, "Mild cognitive impairment as a diagnostic entity," *Journal of Internal Medicine*, vol. 256, no. 3, pp. 183–194, 2004.
- [2] J. Pa, A. Boxer, L. L. Chao et al., "Clinical-neuroimaging characteristics of dysexecutive mild cognitive impairment," *Annals of Neurology*, vol. 65, no. 4, pp. 414–423, 2009.
- [3] K. Yaffe, R. C. Petersen, K. Lindquist, J. Kramer, and B. Miller, "Subtype of mild cognitive impairment and progression to dementia and death," *Dementia and Geriatric Cognitive Disorders*, vol. 22, no. 4, pp. 312–319, 2006.
- [4] A. Convit, J. De Asis, M. J. De Leon, C. Y. Tarshish, S. De Santi, and H. Rusinek, "Atrophy of the medial occipitotemporal, inferior, and middle temporal gyri in non-demented elderly predict decline to Alzheimer's disease," *Neurobiology of Aging*, vol. 21, no. 1, pp. 19–26, 2000.
- [5] A. Convit, M. J. De Leon, C. Tarshish et al., "Specific hippocampal volume reductions in individuals at risk for Alzheimer's disease," *Neurobiology of Aging*, vol. 18, no. 2, pp. 131–138, 1997.
- [6] J. L. Whitwell, M. M. Shiung, S. A. Przybelski et al., "MRI patterns of atrophy associated with progression to AD in amnesic mild cognitive impairment," *Neurology*, vol. 70, no. 7, pp. 512–520, 2008.
- [7] S. M. de la Monte, "Quantitation of cerebral atrophy in preclinical and end-stage Alzheimer's disease," *Annals of Neurology*, vol. 25, no. 5, pp. 450–459, 1989.
- [8] M. J. de Leon, J. Golomb, A. E. George et al., "The radiologic prediction of Alzheimer disease: the atrophic hippocampal formation," *American Journal of Neuroradiology*, vol. 14, no. 4, pp. 897–906, 1993.
- [9] G. D. Jackson, R. I. Kuzniecky, and G. D. Cascino, "Hippocampal sclerosis without detectable hippocampal atrophy," *Neurology*, vol. 44, no. 1, pp. 42–46, 1994.
- [10] A. Pitkänen, M. Laakso, R. Kälviäinen et al., "Severity of hippocampal atrophy correlates with the prolongation of MRI T₂ relaxation time in temporal lobe epilepsy but not in Alzheimer's disease," *Neurology*, vol. 46, no. 6, pp. 1724–1730, 1996.
- [11] S. G. Horowitz, P. Skudlarski, and J. C. Gore, "Correlations and dissociations between BOLD signal and P300 amplitude in an auditory oddball task: a parametric approach to combining fMRI and ERP," *Magnetic Resonance Imaging*, vol. 20, no. 4, pp. 319–325, 2002.
- [12] B. W. Müller, P. Stude, K. Nebel et al., "Sparse imaging of the auditory oddball task with functional MRI," *NeuroReport*, vol. 14, no. 12, pp. 1597–1601, 2003.
- [13] M. Fushimi, N. Matsubuchi, and A. Sekine, "Progression of P300 in a patient with bilateral hippocampal lesions," *Clinical Neurophysiology*, vol. 116, no. 3, pp. 625–631, 2005.
- [14] E. B. Myers and S. E. Blumstein, "The neural bases of the lexical effect: an fMRI investigation," *Cerebral Cortex*, vol. 18, no. 2, pp. 278–288, 2008.
- [15] S.-K. Song, S.-W. Sun, M. J. Ramsbottom, C. Chang, J. Russell, and A. H. Cross, "Dysmyelination revealed through MRI as increased radial (but unchanged axial) diffusion of water," *NeuroImage*, vol. 17, no. 3, pp. 1429–1436, 2002.
- [16] P. J. Basser and C. Pierpaoli, "Microstructural and physiological features of tissues elucidated by quantitative-diffusion-tensor MRI," *Journal of Magnetic Resonance B*, vol. 111, no. 3, pp. 209–219, 1996.
- [17] C. Pierpaoli and P. J. Basser, "Toward a quantitative assessment of diffusion anisotropy," *Magnetic Resonance in Medicine*, vol. 36, no. 6, pp. 893–906, 1996.
- [18] M. D. Budde, M. Xie, A. H. Cross, and S.-K. Song, "Axial diffusivity is the primary correlate of axonal injury in the experimental autoimmune encephalomyelitis spinal cord: a quantitative pixelwise analysis," *The Journal of Neuroscience*, vol. 29, no. 9, pp. 2805–2813, 2009.
- [19] S. M. Smith, H. Johansen-Berg, M. Jenkinson et al., "Acquisition and voxelwise analysis of multi-subject diffusion data with tract-based spatial statistics," *Nature Protocols*, vol. 2, no. 3, pp. 499–503, 2007.
- [20] S. M. Smith, M. Jenkinson, H. Johansen-Berg et al., "Tract-based spatial statistics: voxelwise analysis of multi-subject diffusion data," *NeuroImage*, vol. 31, no. 4, pp. 1487–1505, 2006.
- [21] G. McKhann, D. Drachman, M. Folstein, R. Katzman, D. Price, and E. M. Stadlan, "Clinical diagnosis of Alzheimer's disease: report of the NINCDS-ADRDA work group under the auspices of Department of Health and Human Services Task Force on Alzheimer's disease," *Neurology*, vol. 34, no. 7, pp. 939–944, 1984.
- [22] E. T. Bullmore, J. Suckling, S. Overmeyer, S. Rabe-Hesketh, E. Taylor, and M. J. Brammer, "Global, voxel, and cluster tests, by theory and permutation, for a difference between two groups of structural mr images of the brain," *IEEE Transactions on Medical Imaging*, vol. 18, no. 1, pp. 32–42, 1999.
- [23] T. E. Nichols and A. P. Holmes, "Nonparametric permutation tests for functional neuroimaging: a primer with examples," *Human Brain Mapping*, vol. 15, no. 1, pp. 1–25, 2002.
- [24] S. Wakana, H. Jiang, L. M. Nagae-Poetscher, P. C. M. van Zijl, and S. Mori, "Fiber tract-based atlas of human white matter anatomy," *Radiology*, vol. 230, no. 1, pp. 77–87, 2004.
- [25] E. V. Sullivan, T. Rohlfing, and A. Pfefferbaum, "Quantitative fiber tracking of lateral and interhemispheric white matter systems in normal aging: relations to timed performance," *Neurobiology of Aging*, vol. 31, no. 3, pp. 464–481, 2010.
- [26] A. Stadlbauer, E. Salomonowitz, G. Strunk, T. Hammen, and O. Ganslandt, "Age-related degradation in the central nervous system: assessment with diffusion-tensor imaging and quantitative fiber tracking," *Radiology*, vol. 247, no. 1, pp. 179–188, 2008.
- [27] C. D. Smith, H. Chebrolu, D. R. Wekstein, F. A. Schmitt, and W. R. Markesbery, "Age and gender effects on human brain anatomy: a voxel-based morphometric study in healthy elderly," *Neurobiology of Aging*, vol. 28, no. 7, pp. 1075–1087, 2007.
- [28] D. J. Meyerhoff, S. MacKay, J.-M. Constans et al., "Axonal injury and membrane alterations in Alzheimer's disease suggested by in vivo proton magnetic resonance spectroscopic imaging," *Annals of Neurology*, vol. 36, no. 1, pp. 40–47, 1994.
- [29] X. He, K. Cooley, C. H. Y. Chung, N. Dashti, and J. Tang, "Apolipoprotein receptor 2 and XI α / β mediate apolipoprotein E-induced endocytosis of amyloid- β precursor protein and β -secretase, leading to amyloid- β production," *The Journal of Neuroscience*, vol. 27, no. 15, pp. 4052–4060, 2007.
- [30] R. A. Honea, E. Vidoni, A. Harsha, and J. M. Burns, "Impact of APOE on the healthy aging brain: a voxel-based MRI and DTI study," *Journal of Alzheimer's Disease*, vol. 18, no. 3, pp. 553–564, 2009.
- [31] G. I. Korovaitseva, T. V. Sherbatich, N. V. Selezneva et al., "Association between the apolipoprotein E (APOE) gene and various forms of Alzheimer's disease," *Genetika*, vol. 37, no. 4, pp. 529–535, 2001.

- [32] S. G. Post, P. J. Whitehouse, R. H. Binstock et al., "The clinical introduction of genetic testing for Alzheimer disease: an ethical perspective," *The Journal of the American Medical Association*, vol. 277, no. 10, pp. 832–836, 1997.
- [33] S. Y. S. Wong, E. M. C. Lau, M. Li, T. Chung, A. Sham, and J. Woo, "The prevalence of Apo E4 genotype and its relationship to bone mineral density in Hong Kong Chinese," *Journal of Bone and Mineral Metabolism*, vol. 23, no. 3, pp. 261–265, 2005.
- [34] H.-C. Liu, C. J. Hong, S. J. Wang et al., "ApoE genotype in relation to AD and cholesterol: a study of 2,326 Chinese adults," *Neurology*, vol. 53, no. 5, pp. 962–966, 1999.
- [35] B. Bosch, E. M. Arenaza-Urquijo, L. Rami et al., "Multiple DTI index analysis in normal aging, amnesic MCI and AD. Relationship with neuropsychological performance," *Neurobiology of Aging*, vol. 33, no. 1, pp. 61–74, 2012.
- [36] L. Zhuang, W. Wen, W. Zhu et al., "White matter integrity in mild cognitive impairment: a tract-based spatial statistics study," *NeuroImage*, vol. 53, no. 1, pp. 16–25, 2010.
- [37] D. K. Jones, T. R. Knosche, and R. Turner, "White matter integrity, fiber count, and other fallacies: the do's and don'ts of diffusion MRI," *Neuroimage*, vol. 73, pp. 239–254, 2013.
- [38] C. A. M. Wheeler-Kingshott and M. Cercignani, "About "axial" and "radial" diffusivities," *Magnetic Resonance in Medicine*, vol. 61, no. 5, pp. 1255–1260, 2009.